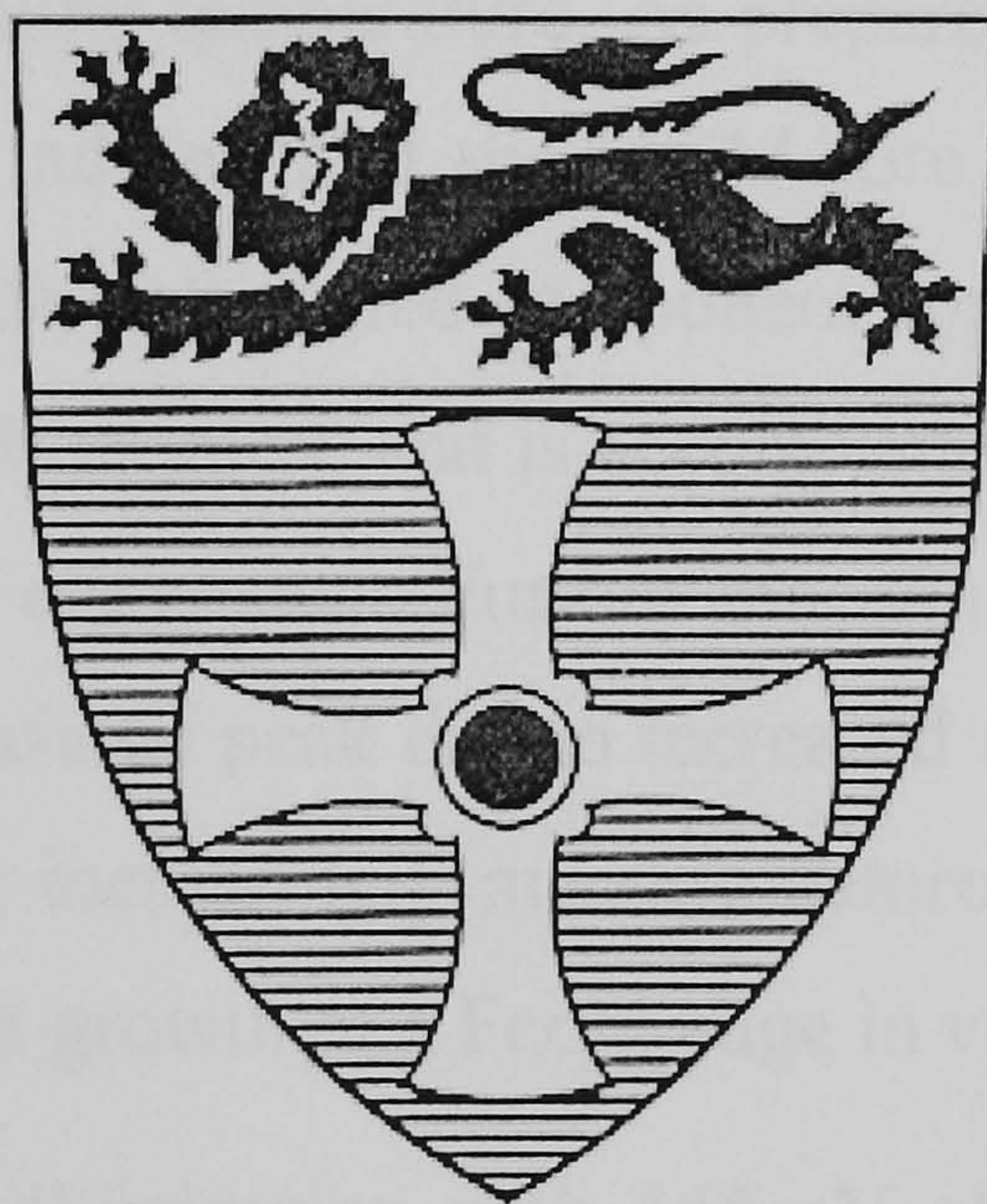


Electronic and Optical Properties of Nanostructured Materials

Thesis submitted to the University of Newcastle upon Tyne
for the degree of Doctor of Philosophy

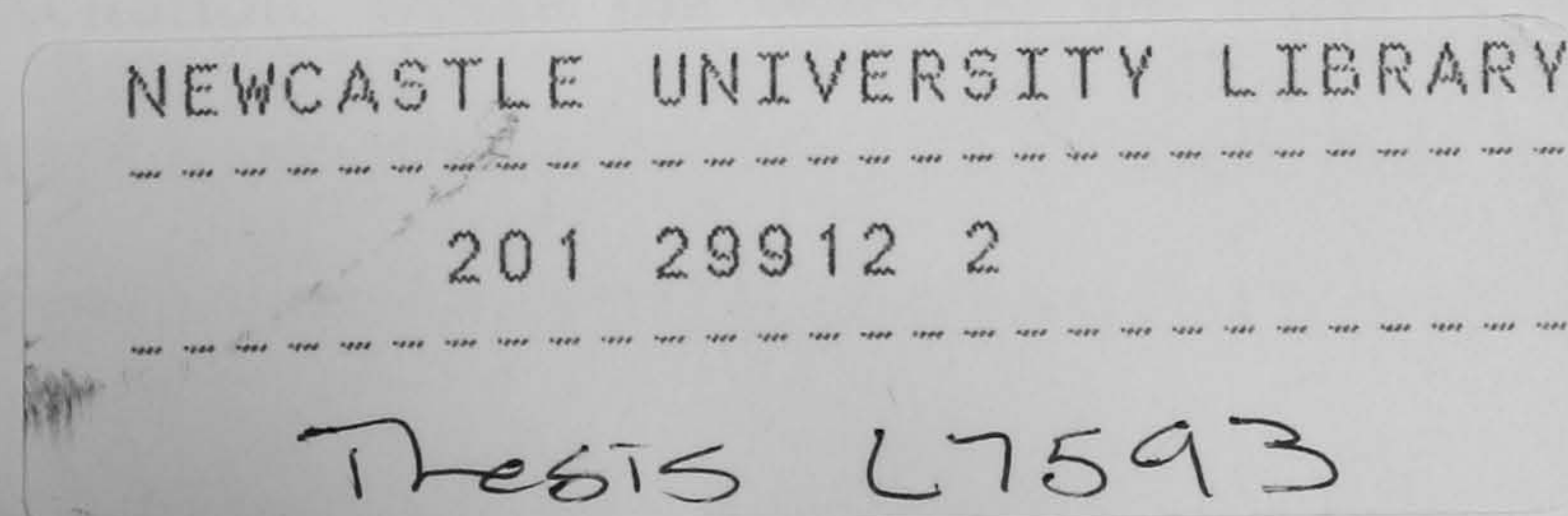
By

Yimin Chao



Nanotechnology
School of Chemical Engineering and Advanced Materials
University of Newcastle upon Tyne

November 2003



Abstract

Three types of nanostructured materials have been investigated: C₆₀ on InP (100), Indium clusters on InP (100) and luminescent alkylated-Si quantum dots.

The growth model and electronic structure of C₆₀ molecules adsorbed on InP (100) were studied by XPS and UPS as a function of coverage and annealing temperature. The C *1s*, P *2p*, In *4d* core levels and the valence band spectra point to the presence of a localized covalent bond between C₆₀ molecules and the substrate. No filling of the lowest unoccupied molecular orbit derived bands was observed. The absence of any change in the surface components of In *4d* core level upon C₆₀ adsorption indicated that the chemisorption bond exists between the fullerene molecules and phosphorus atoms rather than between C₆₀ molecules and indium atoms. This assertion is supported by the simultaneous desorption of both C₆₀ and P upon annealing to 640 K and above.

The evolution of clean, In-terminated InP (100)-(2 × 4) surfaces is investigated by SRPES as a function of annealing temperature. As-prepared InP (100)-(2 × 4) surface are found to be free of metallic indium, and the In *4d* core level shows two clear surface components. A third, indium-cluster-related component appears after annealing above 360 ± 10 °C, due to phosphorous desorption, and is accompanied by a corresponding reduction in intensity in the In-P surface component. Further annealing leads to a decrease in binding energy of the indium cluster related peak due to increased metallicity and hence core-hole screening in the clusters. The increasingly metallic nature of the indium clusters is also revealed by the appearance and growth of a Fermi edge in valence band spectra.

During the course of illumination with 145 eV photons we have monitored the evolution of the Si *2p* core level, and observed in real time a splitting and growth of a new Si *2p* component assigned to the Si⁴⁺ ionic state of Si. This new peak is attributed to in situ oxidation of Si quantum dots caused by photo-induced reaction with water, multilayers of which are present on the surface of the as-introduced quantum dots. X-ray excited optical luminescence (XEOL) reveals that two bands are active upon soft X-ray photon excitation. Surprisingly the 390 nm band (blue light) is the most intense, which is quite different to the result for UV photoexcitation, where the 600-700 nm band is the most prominent one (orange light). The orange light originated from Si-Si bond, blue light from Si-C bond. The ageing phenomenon of photoluminescence is observed but it is reversible.

Acknowledgements

There are many people to whom I am very thankful for their support and help when preparing this thesis.

First of all, I would like to thank my supervisor Dr. Lidija Šiller for this great opportunity to carry out my Ph D work in her group. It has been an extremely interesting and worthwhile time. I would also like to thank Dr. Michael Hunt for his excellent physical insights and intelligent conversation, and Dr Vin Dhanak for his patient and valuable advise and support during the plenty beam-time in Daresbury Laboratory.

I am also grateful to the scholarship panel of the University of Newcastle for award of a Development Trust Bursary throughout my research.

Thanks must go to my friends and colleagues, past and present—Satheesh, Lars, Mossimo, Chris, Diny, George, Lissy.

Last but not least, I thank my beloved wife Yajuan and talented energetic son Yueyang for always being there for me, and my parents—they were forced to put up with my absence for a long time, for something which really is no where near as important as being with them.

Contents

Abstract	i
Acknowledgements	ii
Chapter 1 General Background and Motivations	1
1.1 Photoemission Spectroscopy (PES)	2
1.2 The screening effect	10
1.3 Near edge X-ray absorption fine structure (NEXAFS)	13
1.4 X-ray excited optical luminescence (XEOL).....	18
1.5 Nanostructured systems	20
1.5.1 Metal clusters—Indium clusters.....	21
1.5.2 Semiconductor clusters— Silicon quantum dots.....	23
1.5.3 The nanoscale carbon structure— C_{60}	26
1.6 Some motivations	32
1.6.1 Chemisorption of C_{60} on InP (100) surface	32
1.6.2 Indium clusters on InP (100) surface.....	33
1.6.3 Luminescent Alkylated Silicon Quantum Dots.....	36
1.7 References.....	38
Chapter 2 Experimental.....	50
2.1 Ultra High Vacuum (UHV) system.....	51
2.2 Synchrotron radiation source (SRS) and beamline optics	54
2.2.1 Station 4.1 in Daresbury Lab	58
2.2.2 Beamline I511 in MAX Lab	61
2.3 Photoemission spectroscopy acquirement	63
2.3.1 Geometry of the measurements.....	66
2.3.2 Binding Energy Calibrations.....	67
2.4 Sample Preparation	68
2.4.1 InP (100) Surface Treatment.....	68
2.4.2 Si-Quantum Dots	69
2.5 C_{60} Evaporation and Coverage Calibrations.....	71
2.6 Temperature Measurements.....	72
2.7 Photoluminescence Spectroscopy	73
2.7.1 Photon Spectrometer and Photomultiplier Tubes.....	74
2.7.2 KEITHLEY Programmable Electrometer and HP VEE Control Programme ..	76
2.8 Description of Atomic Force Microscope	78
2.9 References.....	82
Chapter 3 Chemisorption of C_{60} on InP (100) Surface.....	84
3.1 Growth Models	85

3.2	Adsorption Models	87
3.3	The evolution of core levels and valence band as C ₆₀ coverage.....	88
3.3.1	The evolution of C 1s as C ₆₀ coverage.....	88
3.3.2	The evolution of valence band as C ₆₀ coverage	89
3.3.3	The evolution of P 2p as coverage of C ₆₀	91
3.3.4	The In 4d core level spectra in different C ₆₀ coverage	94
3.4	The evolution of core levels and valence band as annealing temperature.....	96
3.4.1	The evolution of core level C 1s and valence band as annealing temperature ..	97
3.4.2	The components of core level In 4d spectrum at high annealing temperature..	98
3.5	Summary.....	101
3.6	Reference:	102
Chapter 4 Nanometre scale Indium clusters on InP (100) surface		104
4.1	The evolution of In-terminated InP (100)-(2 × 4) as a function of temperature.....	106
4.2	In 4d components: bulk, surface and Indium clusters	108
4.3	The evolution of components as a function of temperature	112
4.4	Valence band evolution	114
4.5	Angle Resolved Photoemission Spectroscopy of Indium clusters.....	116
4.6	AFM images of indium clusters.....	124
4.7	Summary.....	126
4.8	References.....	127
Chapter 5 Luminescent Alkylated Si Quantum Dots		130
5.1	Some aspects of silicon quantum dots synthesis and STM image.....	131
5.2	Core level spectra: line shape and shift	139
5.3	NEXAFS of Alkylated silicon quantum dots	151
5.4	Photoluminescence Spectra	152
5.5	Summary.....	156
5.6	References.....	157
Chapter 6 Future Work		160
6.1	Intensive investigation on unique optical property related electronic structure of Si-QDs.....	161
6.2	Evolution of Indium clusters electronic structure as a function of annealing temperature—at different cluster size.....	162
6.3	Reconstruction of InP (100) (2 × 4) with C ₆₀ on the surface.....	162
6.4	References.....	163
Appendix A: Fittings parameters of core level spectra		164
Appendix B: List of papers.....		166

Chapter 1 General Background and Motivations

This chapter gives an introduction into the basic concepts and background, such as principle of photoemission spectra (PES), three step model of photoemission process, the screening effect, the mechanism of near edge X-ray adsorption fine structure (NEXAFS), three nanostructured systems, and X-ray excited optical luminescence (XEOL); review and motivations to this work are also given.

1.1	Photoemission Spectroscopy (PES)	2
1.2	The screening effect	10
1.3	Near edge X-ray absorption fine structure (NEXAFS)	13
1.4	X-ray excited optical luminescence (XEOL).....	18
1.5	Nanostructured systems	20
1.5.1	Metal clusters—Indium clusters.....	21
1.5.2	Semiconductor clusters— Silicon quantum dots.....	23
1.5.3	The nanoscale carbon structure— C ₆₀	26
1.6	Some motivations	32
1.6.1	Chemisorption of C ₆₀ on InP (100) surface.....	32
1.6.2	Indium clusters on InP (100) surface.....	33
1.6.3	Luminescent Alkylated Silicon Quantum Dots.....	36
1.7	References.....	38

1.1 Photoemission Spectroscopy (PES)

One of the most powerful experimental tools for examining the electronic structure of a solid or film is photoemission spectroscopy [1]. Photoemission spectroscopy (PES) is a much applied experimental technique when it comes to extracting information about the occupied electronic structure of solids and their surfaces. The principle behind PES is the photoelectric effect where an electron is emitted from a solid, molecule, or atom upon the absorption of a photon. Basically, in photoemission spectroscopy the kinetic energy, and to some extent, angle-resolved distribution of the photoemitted electrons is measured. A very basic prerequisite for doing PES (meaningfully) is an answer to the question: How does the PES spectra actually relate to the electronic structure of the material?

When a surface is irradiated by a monochromatic photon beam, electrons are emitted by the photoelectric field, see Fig. 1.1. With equipped analyser, the electrons are energy analysed. The energy spectrum of the photoemitted electrons provides us with information on the occupied electronic states of the surface.

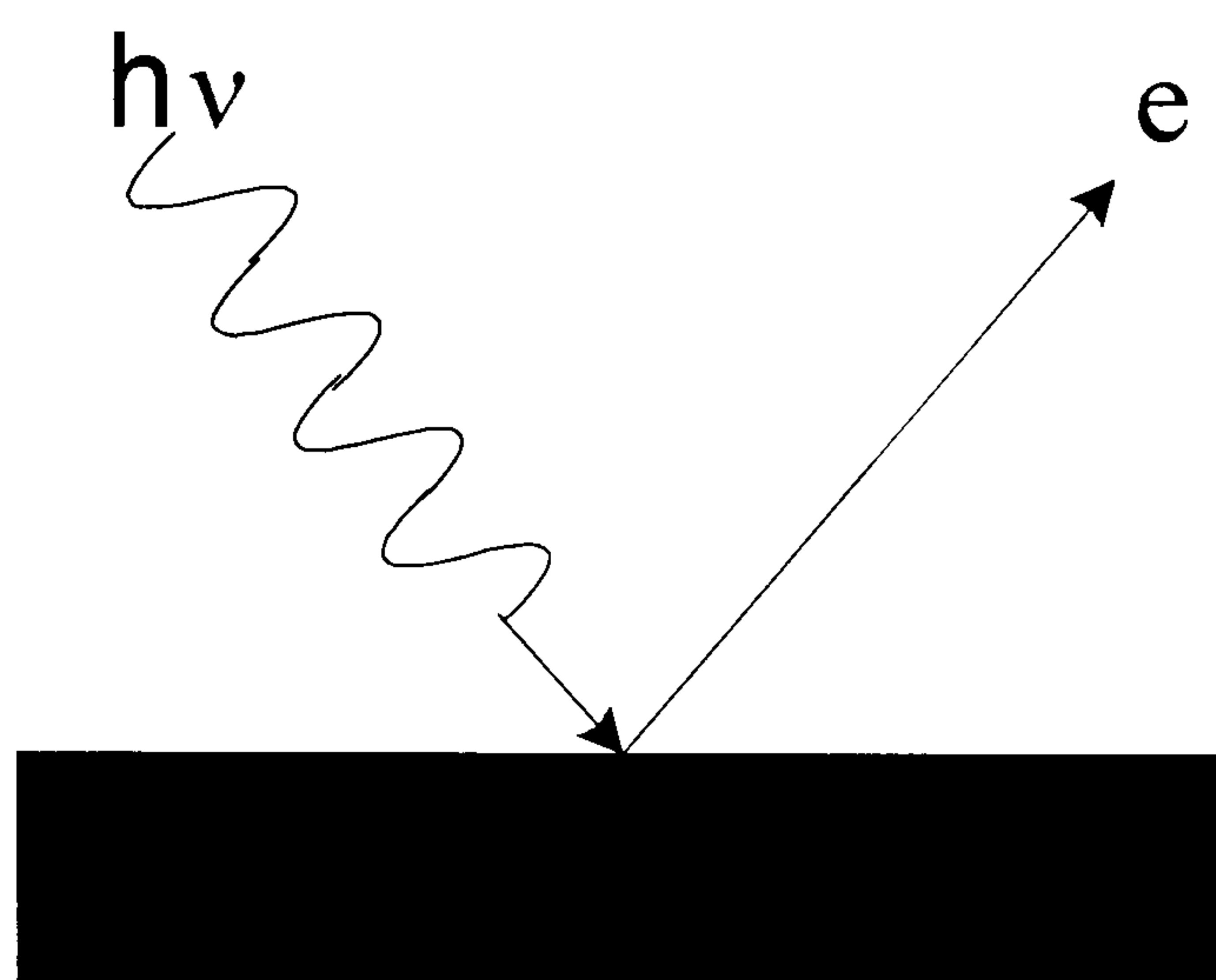


Fig. 1. 1 Schematic illustration of photoelectron emitted by monochromatic photon beam

Traditionally photoemission is divided into two regimes. These regimes arise from the energy ranges available from laboratory-based photon sources. One is Ultra-violet Photoemission Spectroscopy (UPS), which employs photons in the ultra-violet energy range (Typically two spectral lines from He discharge, He I: 21.2eV and He II: 40.8eV). The low photon energy enables us only to access valence band states. Another regime is X-ray Photoemission Spectroscopy (XPS) also known as Electron Spectroscopy for Chemical Analysis (ESCA), which uses X-rays to excite the surface (Typical X-ray lines used are Al $K\alpha$ with $h\nu = 1486.6$ eV and Mg $K\alpha$ with $h\nu = 1253.6$ eV), can access both core and valence electrons, although the latter typically with a low cross-section. Core lines can provide chemical composition and information on bonding in addition to information about some aspects of electronic structure.

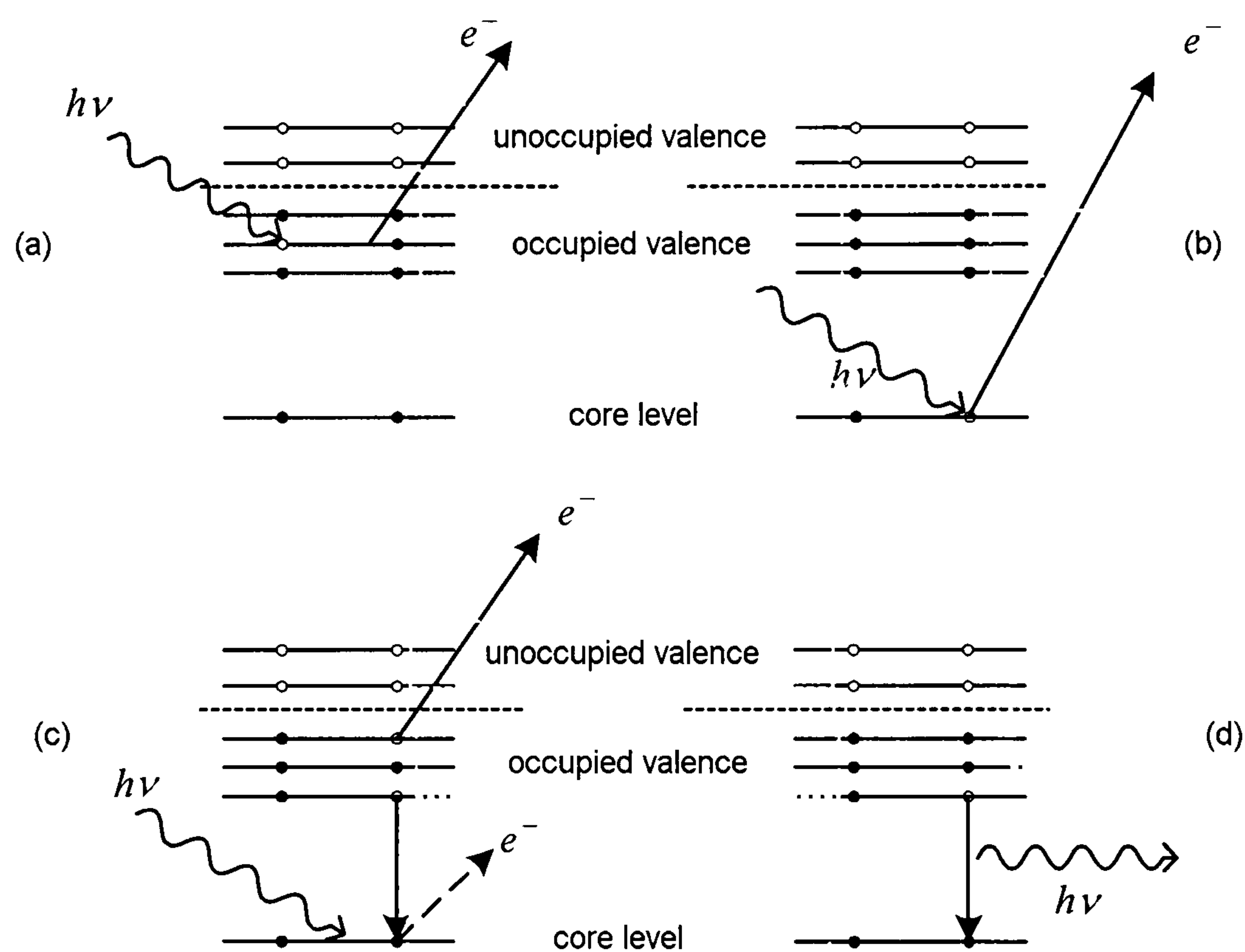


Fig. 1. 2 X-ray interaction with the electrons: photoemission (a) UPS and (b) XPS, (c) Auger electron emission and (d) X-ray emission

But, now synchrotron radiation has come to play a vital role in photoemission spectroscopy. Synchrotron Radiation Sources (SRS) typically provide a continuum for photoemission from the far infrared to the hard ($h\nu > 10$ keV) X-rays regime, and with suitable monochromator photoemission spectroscopy can be performed at any energy in this range. Detailed description of synchrotron radiation source and beamline optics can be found in section 2.2.

In addition to photoemission, there are two other types of the photon interaction with electrons: Auger electron emission and X-ray emission, although X-ray emission has not been detected in this work. Fig 1.2 illustrates the photon interaction with electrons: photoemission (UPS and XPS), Auger electron spectroscopy (AES) and X-ray emission spectroscopy (XES).

A fully rigorous theoretical model of photoemission requires a process of electron removal through to detection to be treated quantum mechanically as a fully coherent process. This approach approaches the photoemission experiment from the viewpoint of a one-step process [2].

A less accurate approach is to model the photoemission process in three steps—the three steps model. This approach is both simpler and more instructive. In the three-step model we artificially divide photoemission into three independent steps [2]:

1. Optical excitation of the electron within the crystal
2. Propagation of the excited electron to the surface
3. Emission of the electron into the vacuum. During this last process the electron traverses the surface.

Step1: Excitation

Fermi Golden Rule gives the transition probability for optical excitation.

$$\begin{aligned}
 W_{fi} &= \frac{2\pi}{\hbar} \left| \langle \Psi_{K_f} | H | \Psi_{K_i} \rangle \right|^2 \delta(E_f(K_f) - E_i(K_i) - \hbar\omega) \\
 &= \frac{2\pi}{\hbar} M_{fi}^2 \delta(E_f - E_i - \hbar\omega)
 \end{aligned}
 \tag{1. 1}$$

where i stands for initial state, f stands for final state, $\hbar\omega$ is the energy of incident photons. E_f and K_f , are the energy and momentum of final state respectively; E_i and K_i , the energy and momentum of initial state.

The perturbation exciting the system is given by the momentum operator \mathbf{p} and the vector potential \mathbf{A} of incident electromagnetic wave (dipole approximation)

$$H = \frac{e}{2m} (\mathbf{A} \cdot \mathbf{p} + \mathbf{p} \cdot \mathbf{A}) \approx \frac{e}{m} \mathbf{A} \cdot \mathbf{p} \quad (1.2)$$

(\mathbf{A} can be approximated as commuting with \mathbf{p})

The current of photoexcited electrons with energy E which propagates towards the surface is:

$$I^{\text{int}}(E, \hbar\omega, \mathbf{k}) \approx \frac{2\pi}{\hbar} \sum_{f,i} M_{fi} f(T, E_i) \delta(E_f(\mathbf{k}_f) - E_i(\mathbf{k}_i) - \hbar\omega) \delta(E - E_f(\mathbf{k}_f)), (k_{\perp} > 0) \quad (1.3)$$

The function $f(T, E_i)$ is the Fermi distribution function. It ensures that the initial state with E_i is occupied.

Step 2: Propagation

Once excited the electron must reach the surface. The transport probability $D(E, \mathbf{k})$ is proportional to the electron mean free path, λ , and is a measure of the probability that the electron can reach the surface without undergoing inelastic scattering.

$$D(E, \mathbf{k}) \propto \lambda(E, \mathbf{k}) \quad (1.4)$$

where λ is the electron mean free path, the average distance of electrons running between two collisions.

The process of inelastic scattering causes all information about the electronic structure of the sample carried by the electron to be lost. The scattered electrons contribute to a strong spectral background called the secondary electron background. The small inelastic mean free path of the electrons leads to the high surface sensitivity of the photoemission technique even when highly penetrating X-rays are used as the exciting radiation. Fig. 1.3 gives the “universal curve” of surface sensitivity, mean free path of

electrons vs. kinetic energy of electrons. The form of the curve arises from the following: at low energy (up to a fraction of an eV) excitation of lattice vibrations (phonons) dominate; between 5-25 eV electron-electron scattering takes over in the form of plasmon (collective electron density fluctuations) excitation; at higher energies the photoelectron can excite bound electrons into unoccupied levels of the solid and the ionisation continuum. From this figure we see that typically electrons would escape from several nm beneath the surface.

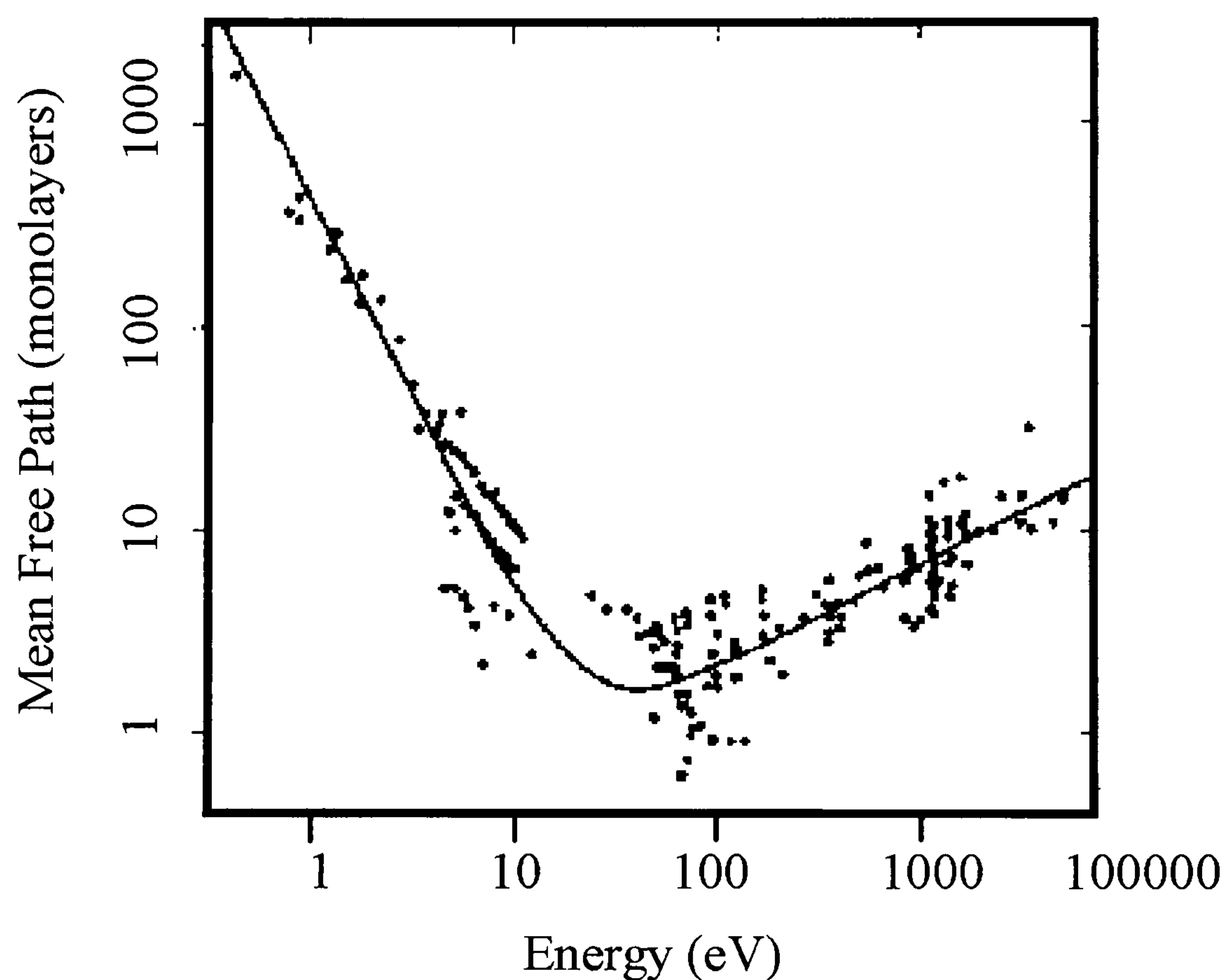


Fig. 1. 3 Universal curve of surface sensitivity, which is mean free path of electrons in solid as a function of their energy; a compilation of a variety of experimental data [2, 3]

Step 3 Transmission

Because of the 2D translational symmetry, the transmission of the electron through the surface into the vacuum requires conservation of its wave-vector component parallel to the surface, but k_{\perp} is not conserved (see Fig. 1.4).

$$k_{//}^{ex} = k_{//}^{int} + G_{//}. \quad (1.5)$$

$$k_{\perp}^{ex} \neq k_{\perp}^{int} + G_{\perp} \quad (1.6)$$

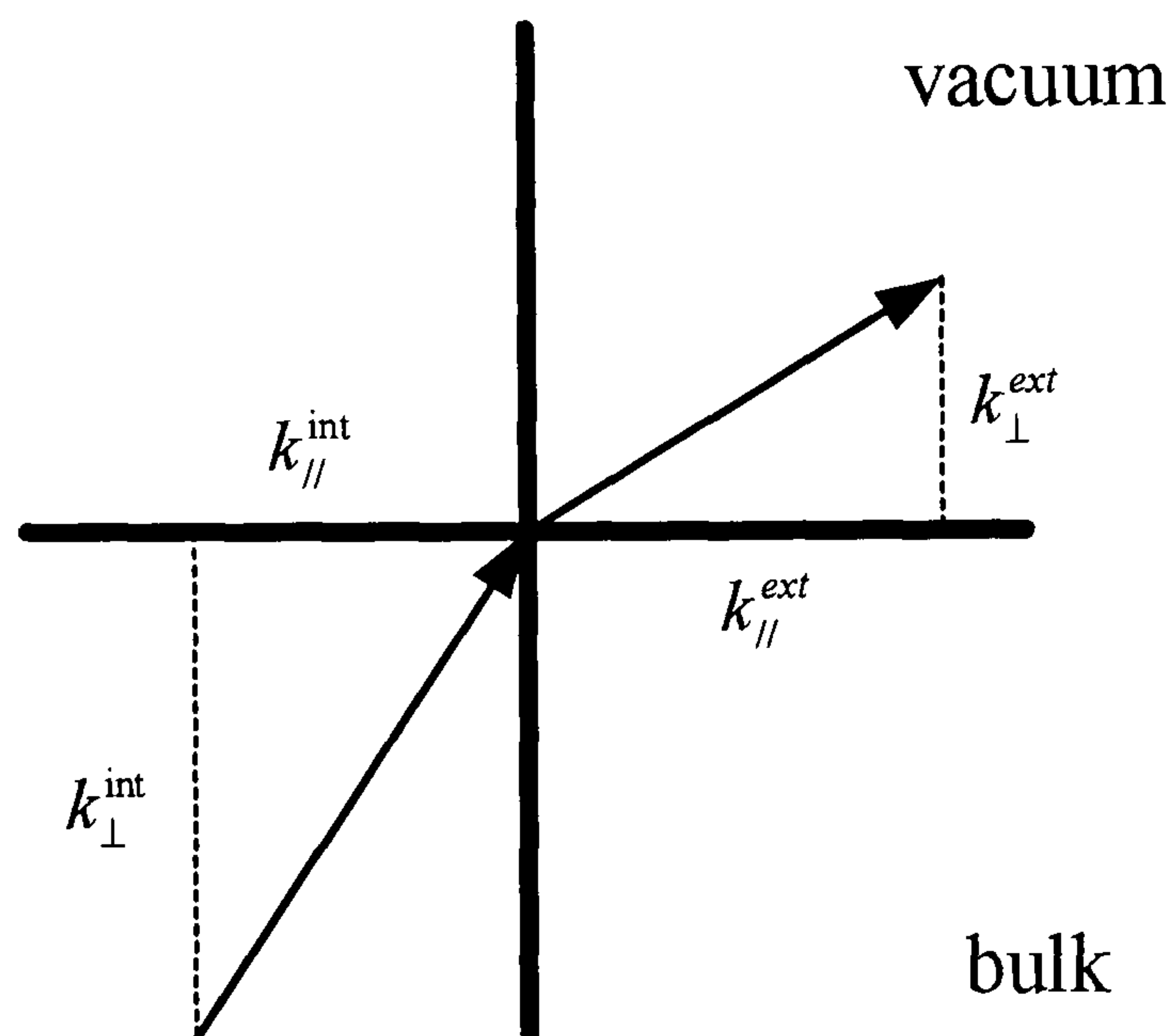


Fig. 1. 4 Conservation of the wave vector component $k_{//}$ (parallel to the surface) upon transmission of the emitted electron through the surface

For the external electron on the vacuum side, the k_{\perp}^{ex} value is determined by the energy conservation requirement

$$E_{kin} = \frac{\hbar^2 (k^{ex})^2}{2m} = \frac{\hbar^2}{2m} [(k_{\perp}^{ex})^2 + (k_{//}^{ex})^2] = E_f - E_{vac} \quad (1.7)$$

where E_{kin} is the kinetic energy of the photoemitted electron under consideration (see Fig. 1.5)

$$\phi = E_{vac} - E_F \quad (1.8)$$

and let E_B be the initial state binding energy referred to the Fermi level, thus

$$\hbar\omega = E_f - E_i = E_{kin} + \phi + E_B \quad (1.9)$$

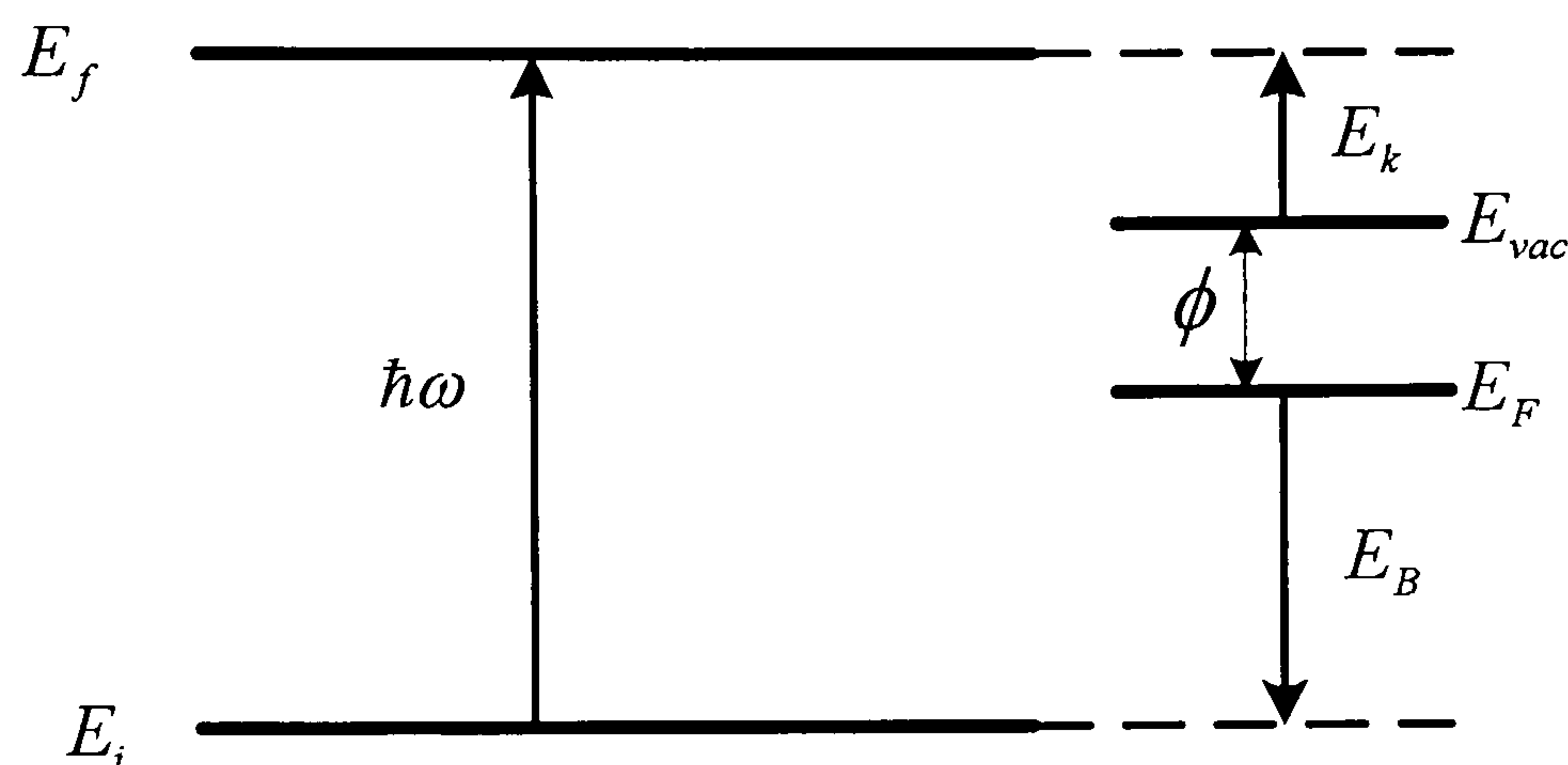


Fig. 1. 5 Energy conservation relationship when an electron is transmitted through a surface.

Transmission through the surface is formally given by a transmission probability

$$T(E, \mathbf{k}) \delta(\mathbf{k}_{//} + \mathbf{G}_{//} - \mathbf{k}_{//}^{ex}) \quad (1. 10)$$

in the simplest fashion, only electrons propagating outwards can be observed, i.e.

$$T(E, \mathbf{k}) = 0 \quad \text{when } k_{\perp}^{ex} < 0$$

$$T(E, \mathbf{k}) = R \quad \text{when } k_{\perp}^{ex} > 0$$

where R is a positive constant.

Putting all the terms together, the detected photocurrent is simply the product of the terms which have examined individually

$$\begin{aligned} I^{ex}(E, \hbar\omega, \mathbf{k}) &= I^{int}(E, \hbar\omega, \mathbf{k}) D(E, \mathbf{k}) T(E, \mathbf{k}) \delta(\mathbf{k}_{//} + \mathbf{G}_{//} - \mathbf{k}_{//}^{ex}) \\ &\propto \sum_{f,i} M_{fi} f(T, E_i) \delta(E_f(\mathbf{k}) - E_i(\mathbf{k}) - \hbar\omega) \delta(E - E_f(\mathbf{k})) \\ &\quad \times \delta(\mathbf{k}_{//} + \mathbf{G}_{//} - \mathbf{k}_{//}^{ex}) D(E, \mathbf{k}) T(E, \mathbf{k}_{//}) \end{aligned} \quad (1. 11)$$

The measured photoelectron intensity $I^{ex}(E, \hbar\omega, \mathbf{k})$ may therefore be evaluated (i) for a determination of the chemical composition, (ii) for an analysis of the atomic binding conditions, and (iii) for a depth-profiling of the sample constituents in the near-surface region.

(i) Due to its occupied atomic orbitals each atom exhibits different ionizable energy levels, which are reflected as element-specific peaks in the x-ray photoelectron spectrum. As these emissions, which are characterized by their binding energies, simply overlay each other in compounds or mixtures, ESCA (*Electron Spectroscopy for Chemical Analysis*) measurements allow the identification of all participating elements by determination of their atomic core level lines. If additional information concerning the cross section of the electronic transition, the mean free path of the electrons and the spectrometer efficiency is provided, even a determination of the chemical stoichiometry is possible [4].

(ii) The exact peak position of core level emissions in XPS spectra are governed by the oxidation level of the emitting atom and the electric field generated by adjacent atoms [5]. Generally, in case of coordination with more electronegative ligands the core level electrons of a central atom appear at higher binding energy making them more difficult to excite. This so-called *chemical shift* may influence the energetic position of the emission peak up to 10 eV [4], which enables an identification of binding partners and a distinction of single or double covalent bonds. Therefore, high-resolution x-ray photoelectron spectroscopy is the preferred technique to trace chemical reactions or redox processes.

(iii) Keeping the sample orientation to the light source unchanged a variation of the detection angle θ in the XPS environment allows to tune the averaged information depth $z \propto \cos\theta$ of the emitted photoelectrons. Using the analyzer angle θ as a parameter the peak ratio of elemental core level emissions mirrors an eventual concentration gradient perpendicular to the surface. From the statistical error and from the number of angular-dependent spectra a depth-resolved profile of the atomic distribution may be derived with defined accuracy [6]. A suitable electron energy ensures a sufficient variation of the escape depth for different emission angles, so that a distinction between intercalates and adsorbates becomes possible.

1.2 The screening effect

Although the core electrons are not involved directly in chemical bonding, their binding energies are not entirely independent of the local environment, and so-called chemical shifts can cause variation of several electron volts. Such shifts can be divided into two types: initial state effects, resulting from changes in the local electric field; and final state effects, due to the way in which the valence electrons rearrange themselves to screen the core hole—screening effect [7].

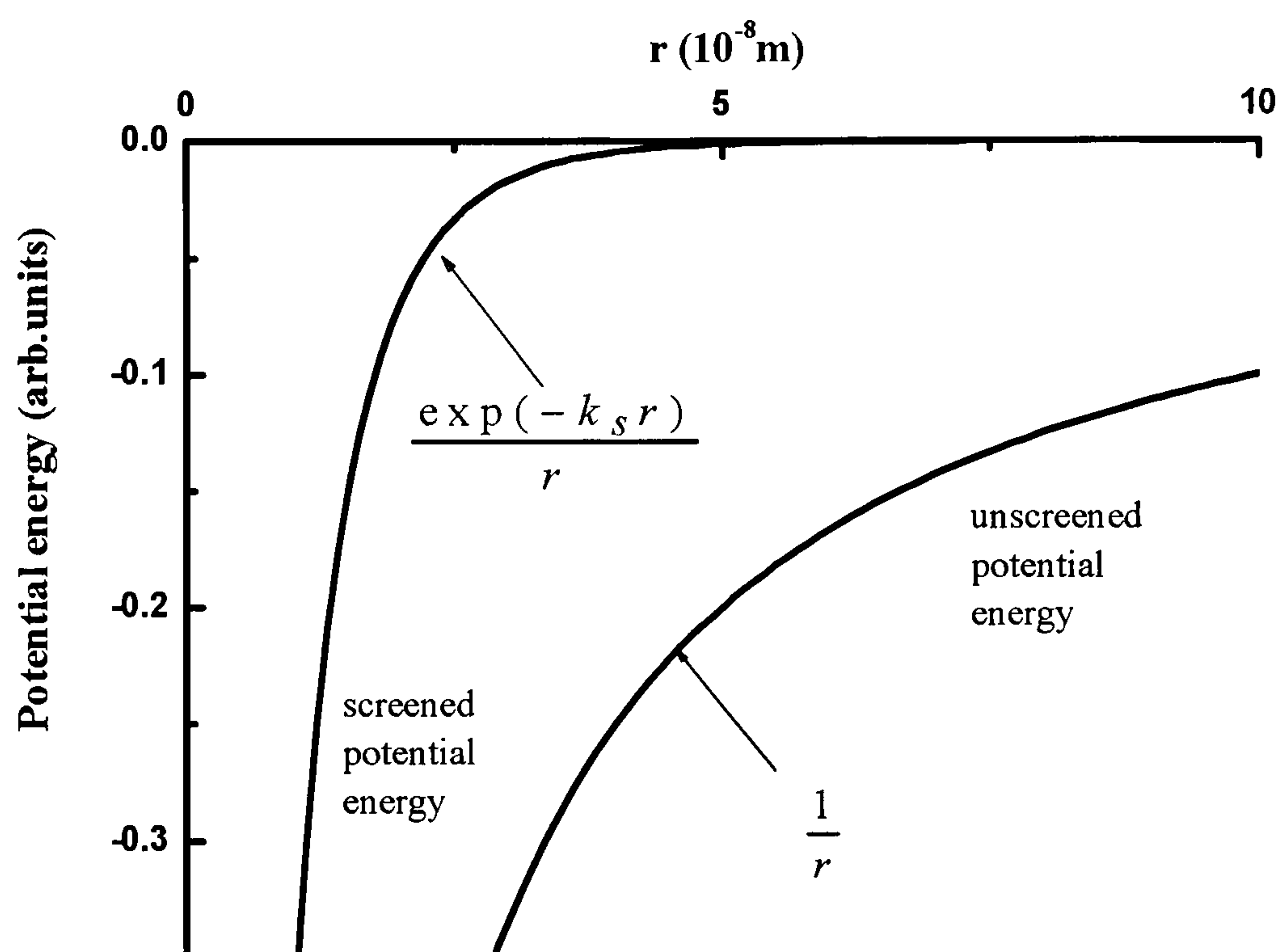


Fig. 1. 6 Comparison of screened and unscreened Coulomb potentials of a static unit positive charge. The screening length $1/k_s$ is set equal to unity [7].

During the photoemission experiments, when electrons emitted by photoelectric field, the left holes are equivalent to positive charges. The electric field of a positive charge embedded in an electron gas, e.g. in metal, falls off with increasing r faster than $1/r$, because the electron gas tends to gather around and thus to screen the positive charge.

We consider a point charge q placed in a sea of conduction electrons. The Poisson equation for the unscreened Coulomb potential is [7]

$$\nabla^2 \phi_0 = -q\delta(r) \quad (1.12)$$

and we know that $\phi_0 = -q/4\pi r$. But with the screening effect, the Coulomb potential is

$$\phi(r) = -\frac{q}{4\pi r} \exp(-k_s r) \quad (1.13)$$

where k_s is the screening parameter [7].

Fig. 1. 6 plots the comparison of screened and unscreened Coulomb potentials of a static unit positive charge. The screening length $1/k_s$ is set equal to unity.

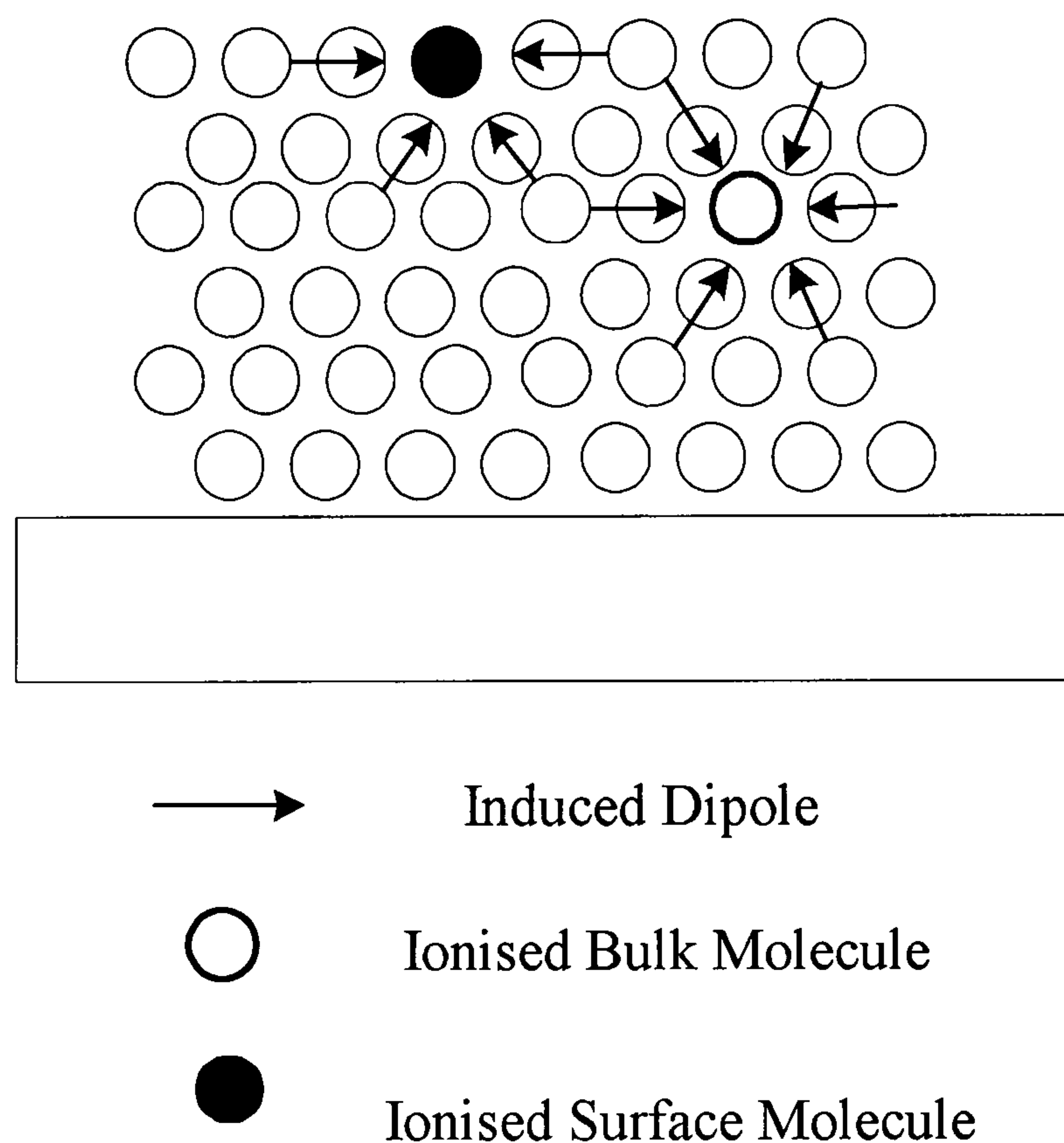


Fig. 1. 7 Screening of the final state at the surface and in the bulk

A good example of the screening effect is surface core level shift (SCLS)—a special kind of binding energy shift. This is equal to the difference in binding energy

between core electrons bound to the atoms deep in the bulk of an infinitely thick film and those at the surface. It results from differences in screening of the ionic final states in the bulk and at the surface, through polarisation of the molecules surrounding the ionised site. A molecule at the surface has a lower number of nearest neighbours and it is therefore less efficiently screened than one which is in the bulk, see Fig.1.7. In Chapter 4 we can see the core level In $4d$ fitted by three or four components, one is from bulk, two from surface, another one from metallic indium clusters. Detailed discussion can be found in Chapter 4.

For a thick layer an increasing in measured core level binding energy is observed by changing the electron emission angle from normal to grazing [8, 9]. This is because in grazing emission, electrons almost exclusively from the surface layer will be recorded (this is due to the extreme surface sensitivity of photoemission as discussed in Sec.1.1). In normal emission a large number of electrons from the bulk will also contribute to the observed spectrum.

In Chapter 3 we recorded C $1s$ spectra always in normal emission angle, but as the increasing of coverage of C_{60} on the substrate the C $1s$ peak position shifted to higher binding energy. This means the polarisation screening effect in fullerene film reduced as the increasing of the C_{60} coverage. The reason is the thick C_{60} solid film was regarded as an insulator, see section 1.5.3. Detailed discussion is given in Chapter 3.

1.3 Near edge X-ray absorption fine structure (NEXAFS)

X-ray absorption spectra (XAS) are generally characterized by many fine spectral features near the absorption edge. Near edge X-ray absorption fine structure (NEXAFS), which is also sometimes referred to as X-ray absorption near edge structure (XANES), typically represents the energy region from the absorption edge to about 50eV above the edge. NEXAFS spectra provide important information about the electronic and structural properties [10].

The potential utilization of near edge features for the structural determination of matters was first recognized in 1920 by Kossel [11]. However, research effort in this area was limited primarily due to difficulties in obtaining intense light sources for excitations and due to the complexity in data analysis. During the 1970s, the availability of bright, polarized, and tuneable synchrotron light sources, as well as the development of scattering theories for the interpretation of near edge features, made EXAFS a powerful tool for structural determinations. By the mid-1980s, NEXAFS had become a powerful surface spectroscopy, especially in elucidating the electronic and structural properties of molecules on surfaces [10].

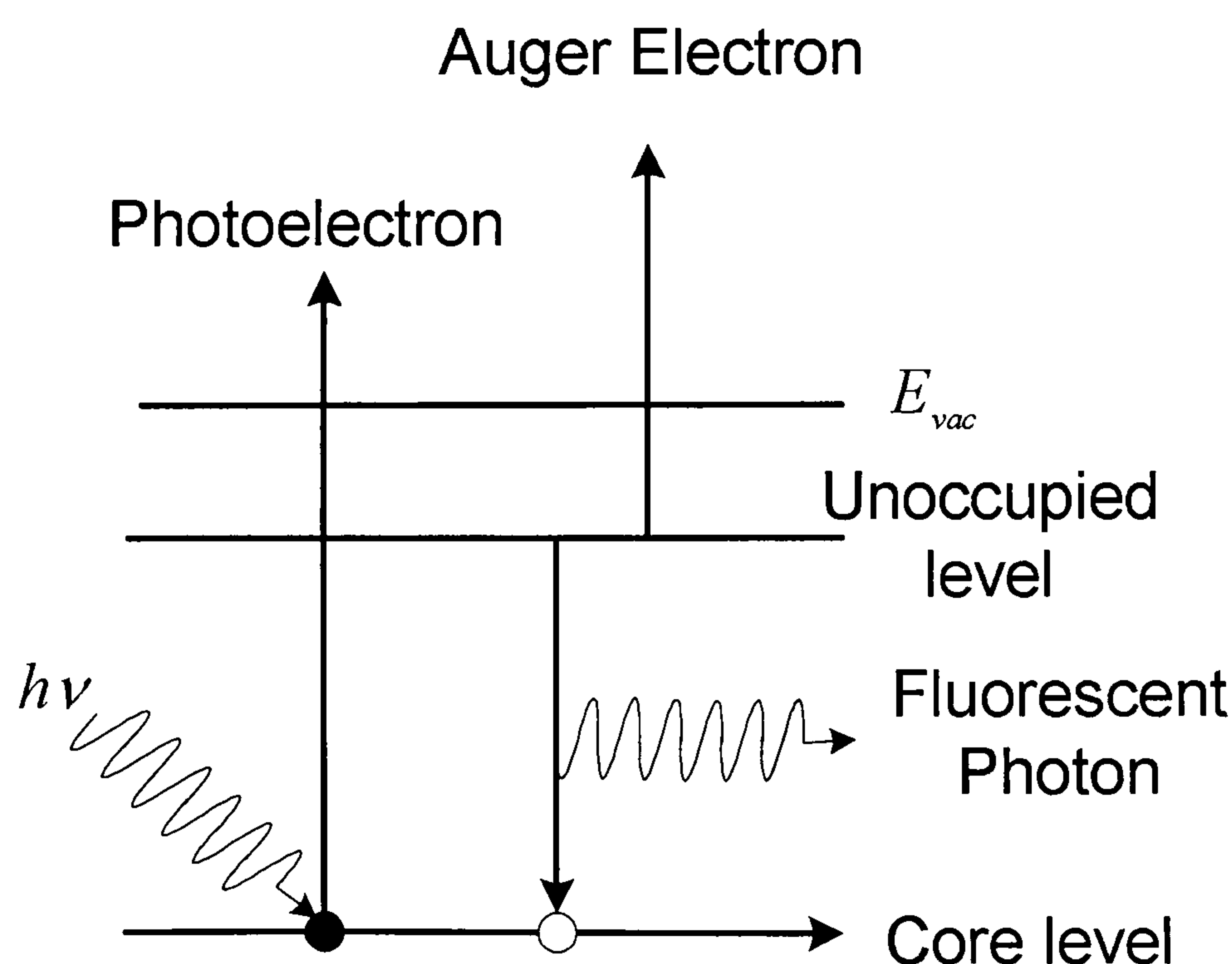


Fig. 1. 8 Schematics of creation and annihilation of a core hole as a result of X-ray absorption.

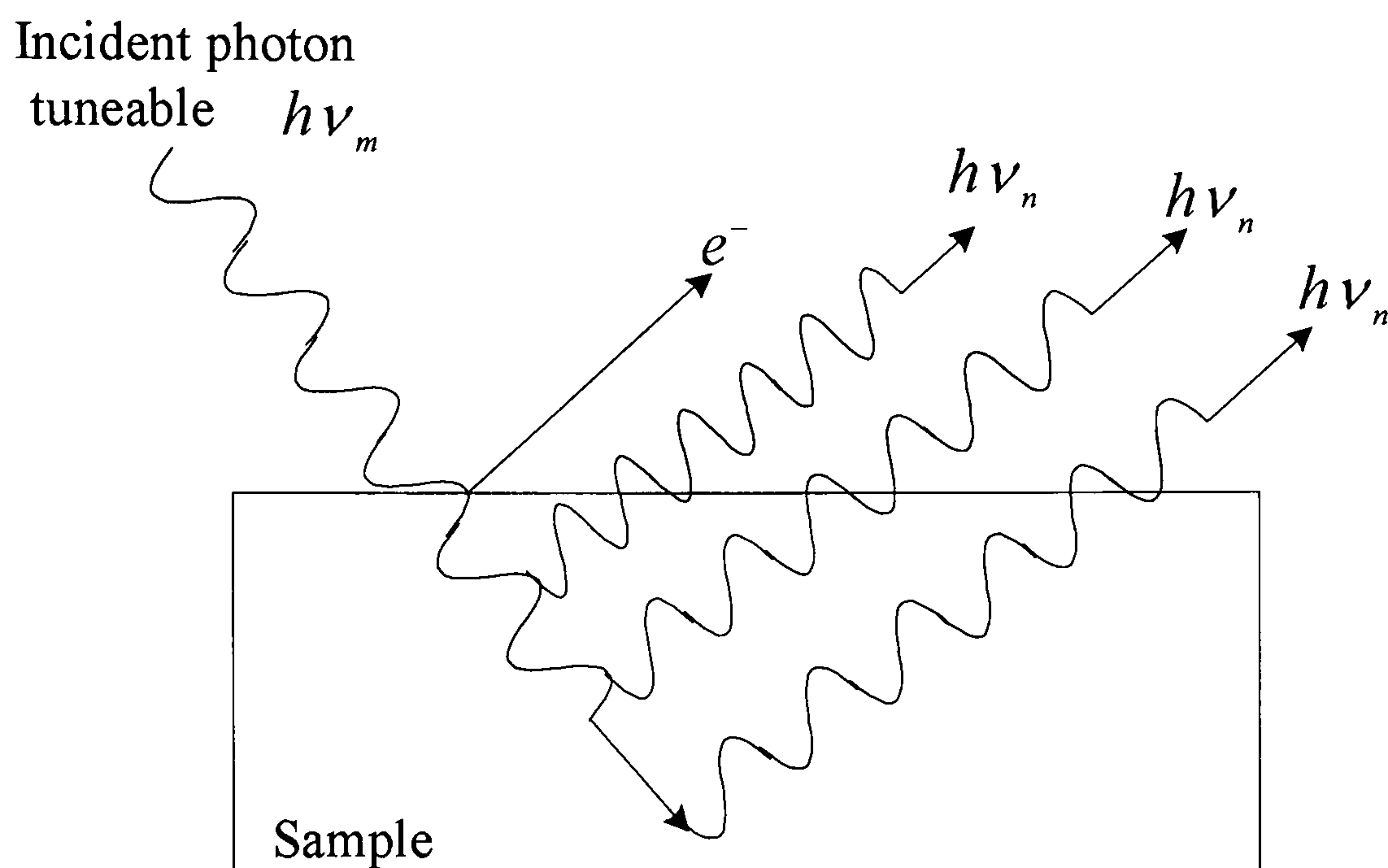


Fig. 1. 9 NEXAFS measurements are carried out by following the de-excitation process, which generates either an Auger electron or a fluorescence photon.

The absorption of an X-ray photon, with a resonance energy $h\nu$, gives rise to an electronic excitation from the core level to an unoccupied state. As shown in Fig. 1. 8, a core hole is created as a result of the resonance excitation. In NEXAFS measurements, the resonance transition is measured by following the annihilation, instead of the creation, of core holes. The energy gained by annihilation can be released by either the radiation of fluorescence photons or by the emission of Auger electrons. In this process photoelectrons are always there, thus the ejected electrons include photoelectrons and Auger electrons. NEXAFS spectra can be recorded by measuring either the electron yield or fluorescence yield as a function of incident photon energy, see Fig. 1. 9.

The X-ray absorption spectra of gaseous materials can at least in principle be measured in transmission mode, recording the changes in the “transparency” as a function of the incident photon energy: Due to the extremely short attenuation lengths of soft X-rays in solids, this is not possible in solids (except possibly in some cases for ultra-thin films). Instead, the incident photon energy dependence of the yield of secondary particles (electrons or photons), which are produced during the decay of the core excitation, can then be used in order to get information on the energy –dependence of the absorption

cross-section [10]. Due to practical reasons these techniques are favoured even when recording gas-phase NEXAFS, and due to the relatively longer escape depths of photons, the photon yield measurements can also be used on liquids.

To obtain an experimental spectrum which is more or less directly corresponding to the absorption cross-section, total or partial electron or photon yields can be recorded. These different options generally use different detectors, and have advantages and limitations, which are reviewed below.

First, total electron yield (TEY) can be obtained most simply by recording the sample drain current, as electrons are photo-emitted from the sample upon interaction with incident light either directly or due to decaying of an auto-ionising state. The drain current setup essentially consists of a wire, which connects the sample holder, isolated from the ground, through a vacuum feed-through to a pico-amp meter. An obvious advantage of this technique is the simplicity of the setup, while the results for metallic or even semi-conducting samples are nevertheless as good as for the more sophisticated setups. However, applicability to conducting samples only and the shallowness of the surface layer of the sample that is probed can sometimes make it necessary to use a different setup. Other possibilities for recording the TEY signal are to use a channeltron detector or a multi-channel plate (MCP).

Second, the total photon yield, alias total fluorescence yield (TFY) signal can be recorded by using a channeltron detector, a MCP detector or, as a less efficient option, by using the X-ray emission (XE) spectrometer in zero order diffraction. Being a photon-in-photon-out technique, this method can reach considerably larger probe depths (on the order of 1000Å) and is less sensitive to possible surface contamination. It can also be used to measure absorption in buried layers (e.g. in samples covered by a layer of material protecting the sample from oxidation during transfer).

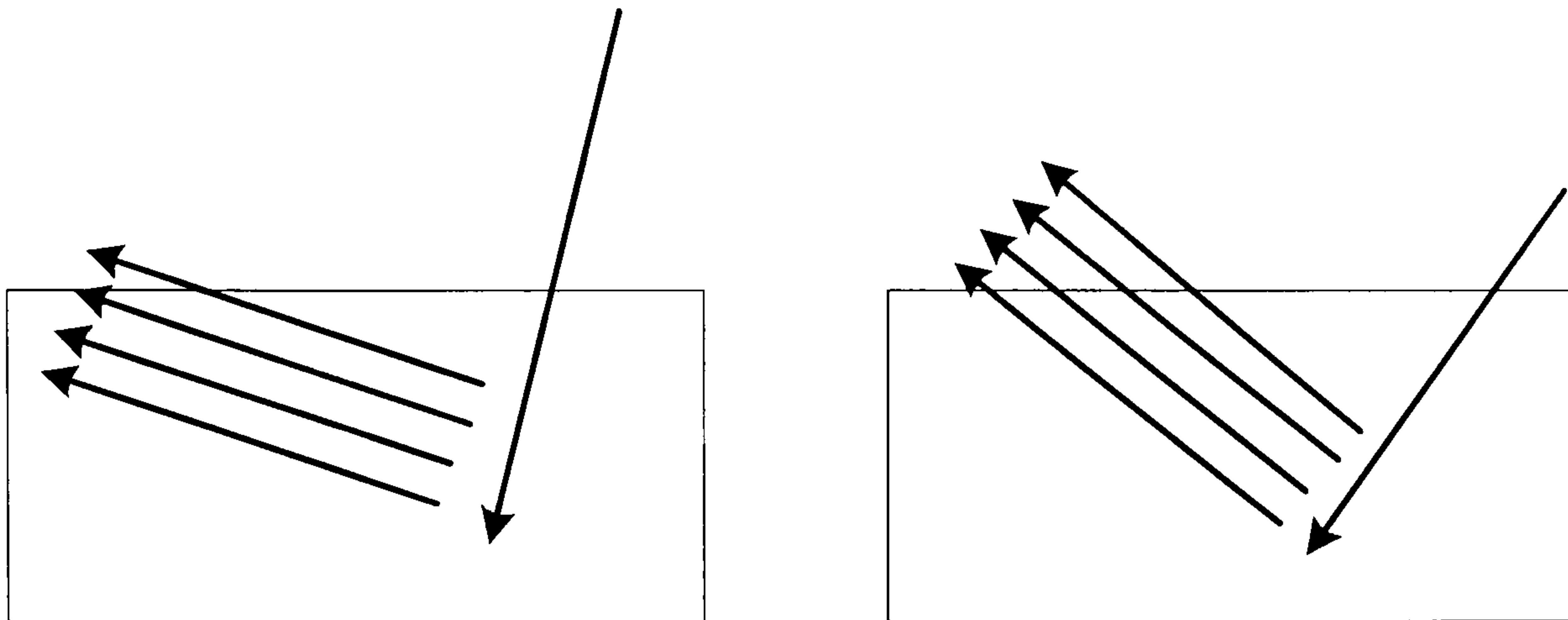


Fig. 1. 10 Saturation effect in TFY (absorption) spectroscopy: due to the large photon escape depth, the photon yield recorded with near-normal exit angles may at different energies (for different energy-dependent absorption cross-sections) contain contribution from different depths in the sample, neutralising the effect of the absorption cross-section. At near-normal detection angles, the light at energies with smaller absorption coefficient can originate from deeper in the sample than at energies with large absorption cross-section. The total intensity observed can at the same time be almost constant [12].

When using this technique, however, one should be careful considering the effects of self-absorption, and the fact that the absorption cross-section need in many cases not be proportional to the photon yield signal. The effect of self-absorption is illustrated in Fig.1.10. For a bulk sample or a thick film, all of the incoming light gets absorbed, although the effective absorption length depends on the energy-dependent cross-section. If the TFY signal is then recorded at a near-normal (exit) angle, the secondary photons come from different depths in the sample for different incident energies, but due to the long escape depth these photons are still capable of leaving the sample and the dependence of the total number of emitted photons can in the extreme case be constant (independent of energy and only dependent of the incident intensity). The best way to prevent this from happening is to use near-normal incidence angles and grazing exit angles, so that photons emitted only from a thin surface layer are detected.

This signal should then be proportional to photons absorbed in the same layer of limited thickness, and the total number of the absorbed, and emitted, photons should be proportional to the absorption cross-section. The amount of self-absorption differs from material to material between the extremes of a flat line (constant) in the spectrum to negligible effects. The technique can still be very useful, especially in the cases when this is only option, e.g. for buried layers or liquids in a containing cell quipped with a window [12].

Third, partial electron yield (PEY) can be measured using a photoelectron spectrometer and choosing an energy window (and integrating the total count rate within the window). This will give the decay rate via a certain transition. A less sophisticated alternative to this is to use a total yield detector in combination with one or several retarding grid(s) in order to set a low kinetic energy limit for the electrons which can reach the detector. Using the PEY instead of TEY enables to enhance the element-specificity to some extent (in case of a composite sample) and gives some flexibility to choose the probe depth by recording decay channels with quite different kinetic energies.

Fourth, partial fluorescence yield (PFY) measures the decay rates (of an energy-dependent magnitude of a core-excited population) via a specific fluorescent decay channel. Although this technique usually suffers from extremely low count rates, the capability to discriminate more strictly against (the approximately constant background) fluorescence from other elements in a composite sample make it in certain cases useful. The signal can be detected by choosing a suitable energy window in the spectrometer and integrating the count rate for each incoming photon energy step [9].

In our experiments, we acquired the partial electron yield from silicon quantum dots as a function of incident photon energy (See Chapter 5).

1.4 X-ray excited optical luminescence (XEOL)

X-ray excited optical luminescence (XEOL) is essentially an energy-transfer event in which the absorption of the X-ray photon produces a large number of energetic electrons (photoelectron and Auger electron, see Fig. 1.2 in Section 1.1 and Fig. 1.8 in Section 1.3). These electrons in turn cause further ionization and excitation. The energy is transferred to luminescent centres through inelastic processes which lead to the creation of holes in the valence band and electrons in the conduction band in semiconductor nanostructures, for example, or holes and electrons in the occupied and unoccupied molecular orbital (MO) of organic molecules, respectively. The recombination of holes and electrons will emit light. This is the well-known scintillation process [13].

XEOL is a photon in – photon out technique. Using laboratory soft X-rays such as Mg K α (1253.6eV) and Al K α (1486.6eV), and visible UV and soft X-ray (10eV—3keV) from a tuneable synchrotron light source, it is often possible to conduct site and sampling depth selective measurement [14-16]. The sampling depth selectivity comes from the energy-dependent penetration depth of the photons and the site selectivity comes from the tunability of the source. For example, when the photon energy is tuned to the silicon L-edge, the photon will be absorbed preferentially by the silicon atom. This channel selective excitation will greatly facilitate the identification of the origin of luminescence [13].

Radiative recombination of an electron with a hole across the bandgap of semiconductors produces luminescence. The emitted photons have energy equal to the bandgap energy and a momentum that is negligible. Thus, the electron and the hole must be located at the same point in the Brillouin zone, which is the case in direct gap semiconductors such as GaAs. Under these conditions, the radiative recombination rate is large and the radiative lifetime is short (typically of the order of a few nanoseconds for a dipole-allowed transition). To obtain large luminescence efficiency, the nonradiative recombination rate must be smaller than the radiative recombination rate. The efficiency is defined by

$$\eta = \tau_{\text{nonrad}} / (\tau_{\text{nonrad}} + \tau_{\text{rad}}) \quad (1.14)$$

where η is the quantum efficiency, τ_{rad} is the radiative lifetime, and τ_{nonrad} is the nonradiative lifetime [17]. Nonradiative recombination occurs at the surface (surface recombination) and in the bulk (Auger recombination; recombination at defects). To minimize it, the surface should be well passivated and the bulk must be free of defects that act as radiation killers. The efficiency of direct gap III-V semiconductors such as GaAs exceeds 1% at room temperature and 10% at cryogenic temperature [17].

Silicon (Si) is an indirect gap semiconductor, in which electrons and holes are found at different locations in the Brillouin zone. Therefore, recombination by emission of single photons is not possible. Photon emission is possible only if another particle, such as a phonon, capable of carrying a large momentum is involved. In this case, both energy and momentum can be conserved in the radiation transition. The participation of a third particle in addition to the electron and the hole makes the rate of the process substantially lower and the radiation lifetime is typically on the millisecond regime. Thus, the efficiency drops by several orders of magnitude, even for high purity materials and good surface passivation. At room temperature, the efficiency of crystalline Si (c-Si) is usually of the order of 10^{-4} to $10^{-5}\%$, which makes it unattractive for light emitting devices (LEDs) [18]. Several attempts have been made to improve the luminescence efficiency of Si and Si-based alloys. They include the use of Si-Ge alloys and superlattices [19] and isoelectronic impurities [20] in a manner similar to N in GaP. The strategy in these attempts can be divided into two classes: increasing the radiative rate or decreasing the nonradiative rate [17]. The former can be achieved by “bandgap engineering” or “defect engineering” which essentially consists of “convincing” the electron and hole that they do not need a phonon to recombine radiatively. This can be accomplished through zone folding in thin superlattices or with isoelectronic impurities whose energy level extends throughout the Brillouin zone. The later consists of confining the electron and the hole to a small volume where the probability of finding a nonradiative centre is equal to zero. Fabrication of silicon quantum dots (Si-QDs) is the example of this attempt. The discussion in quantum confinement in Si-QDs can be found in section 1.5.2.

1.5 Nanostructured systems

In this thesis three types of nanostructured systems are discussed: metal clusters—indium clusters, semiconductor clusters—silicon quantum dots, and nanoscale carbon structure— C_{60} .

Clusters do not represent a fifth state of matter as proposed earlier [21], instead, they are intermediate between atoms on the one hand and the solid or liquid state on the other hand. They represent an important kind of condensed matter of its own, full of surprising, outstanding, and otherwise not observed physical properties. They deserve interest not only due to the fundamental aspects of how condensed matter is formed from atoms, but also because of their often underrated importance in nature and technology. We believe that cluster matter as a representative of novel materials hides plenty of undiscovered and obscured properties and potential future applications, in particular for nanotechnologies.

A cluster is an entity, consisting of between 3 and 10^7 atoms of uniform or mixed chemical composition, packed densely with arbitrary external shape and structural arrangement [21].

Although clusters are usually generated experimentally by condensing atoms into clusters, there is the option (although seldom used in experiments) of cleaving, splitting, or grinding matter. Fig. 1.11 schematically illustrates these possible approaches to the cluster region.

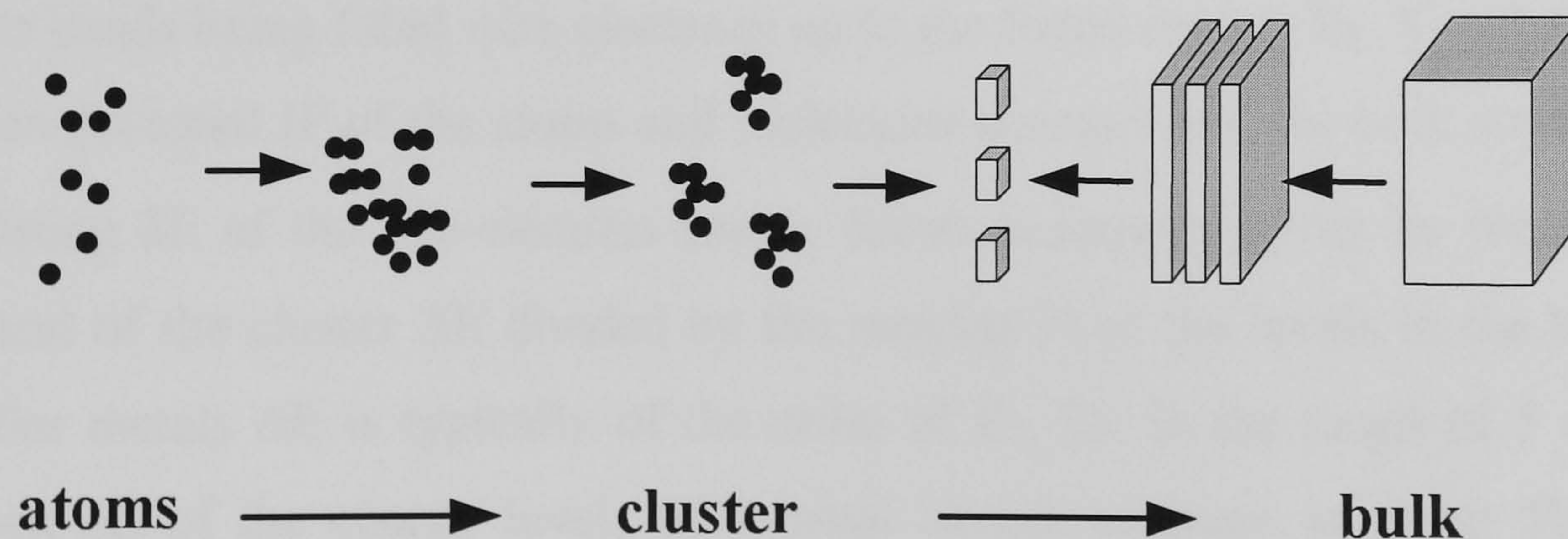


Fig. 1. 11 Two different concepts to approach clusters: nucleation or cleavage of macroscopic material

1.5.1 Metal clusters—Indium clusters

In order to classify them, three size regimes of clusters are defined in Table 1.1. In addition, the corresponding ratios of surface to volume atoms N_s/N_v are given.

Table 1. 1 Classifications of clusters according to the number N of atoms per cluster [21]

Very small clusters	Small clusters	Large clusters
$2 < N \leq 20$	$20 \leq N \leq 500$	$500 \leq N \leq 10^7$
Surface and inner volume not separable	$0.5 \leq N_s/N_v \leq 0.9$	$N_s/N_v \leq 0.5$

Clusters do not represent a uniform state of matter. Instead, experimental and theoretical results vary widely as a function of size. Quantum-size effects are due to the extraordinary spectra of electron energy levels which are predicted to be quantized.

Fig. 1. 12 gives a schematic example of the one-electron energy levels of atoms, clusters and bulk material. The original energy levels of the atom split into two components, if a diatomic molecule is formed. The levels continue to split for larger and larger clusters and finally merge into the quasi-continuous band structure of the bulk solid, the bands being filled with electrons up to the Fermi energy E_F . Simultaneously, the ionization potential IP of the atoms and molecules changes into the bulk work function ϕ . The splitting δE of the one-electron energy levels is roughly given by the width of the quasi band of the cluster ΔE divided by the number N of the levels in the band: $\delta E = \Delta E/N$. For metals ΔE is typically of the order of E_F , i.e. in the range of 5 eV, thus the separation δE of the energy levels of a metal cluster amounts to about 50 meV for a cluster with $N=100$ atoms.

Detailed discussion for semiconductor clusters can be found in next section.

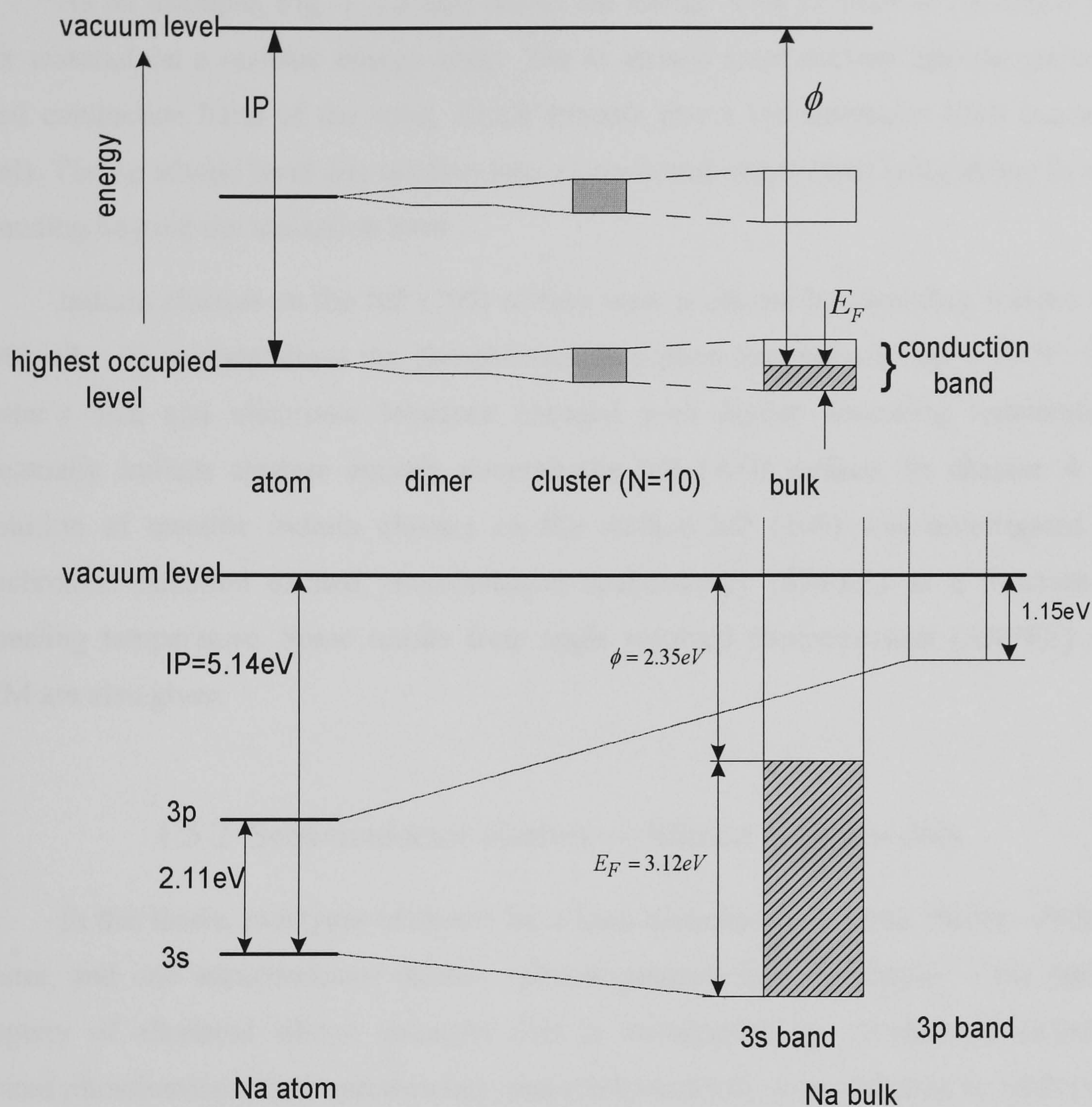


Fig. 1. 12 Schematic energy level diagram of atoms, dimers, clusters and bulk material (up) and realistic level scheme for sodium atoms and bulk material (low). The dashed lines indicate the splitting of the energy levels; IP, ϕ , and E_F denote the ionization potential, the bulk work function, and the Fermi energy, respectively [21].

As an example, Fig. 1. 12 also shows the energy level scheme of Na atoms and bulk material on a realistic energy scale. The 3s atomic level evolves into the partially filled conduction band of the solid, which extends above the ionization limit (vacuum level). The 3p atomic level also evolves into a very broad empty band lying above E_F and extending beyond the ionization limit.

Indium clusters on the InP (100) surface were produced by annealing a clean InP (100) $-(2 \times 4)$ surface above the phosphorous desorption temperature 360 ± 10 °C. The cluster's size and electronic structure changed with higher annealing temperature. Eventually indium clusters entirely covered the InP (100) surface. In chapter 4 the evolution of metallic indium clusters on the surface InP (100) was investigated by synchrotron radiation excited photoemission spectroscopy (SRPES) as a function of annealing temperature. Some results from angle resolved photoemission (ARPES) and AFM are also given.

1.5.2 Semiconductor clusters — Silicon quantum dots

In this thesis, two types of cluster have been discussed: one metal cluster—indium cluster, and one semiconductor cluster—silicon quantum dots. In chapter 5 the optical property of alkylated silicon quantum dots is investigated by synchrotron radiation excited photoluminescence spectroscopy, and electron structure investigated by SRPES.

When Si nanostructures become smaller than 20-30 nm, the transport, electronic, and optical properties of bulk silicon start to be influenced significantly by quantum confinement effects [22]. For example, the PL energy of luminescent porous silicon (LEP-Si) should equal the bandgap minus the binding energy of the excitation [17]. The bandgap of crystallite silicon (c-Si) is 1.12 eV, but the PL energy is much bigger than this value, see Chapter 5 for detailed PL energy. One explanation is that the bandgap of LEP-Si is much bigger than that of c-Si. That means due to quantum confinement the conduction band energy risen up and valence band energy reduced.

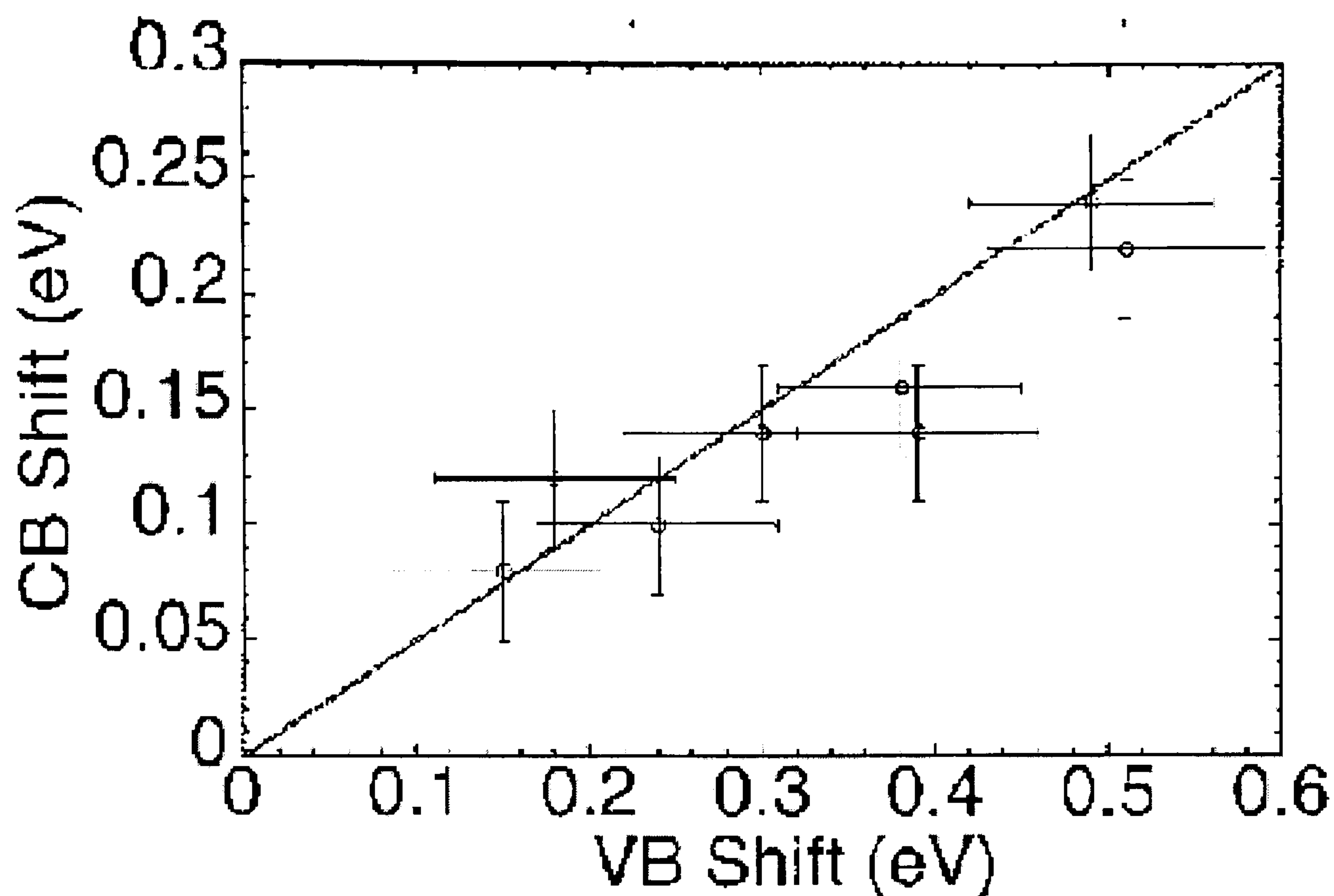


Fig. 1. 13 The CB shift versus the VB shift for a series of silicon nanoclusters. The solid line represents a 2:1 ratio between VB shift and the CB shift [23].

Fig. 1.13 shows the conduction band edge shift determined from L-edge data as a function of the valence band shift determined from photoemission, for a series of different samples [23]. Careful inspection indicated that the confinement decreases the valence band edge twice as much as it increases the conduction band edge, in agreement with effective mass theory [24]. Fig. 1.14 illustrates this relationship. Since the VB shift is equal to twice the CB band, the bandgap of π -Si samples is obtained from [23]:

$$E_{\text{gap}} = \Delta E_{\text{vb}} + \Delta E_{\text{cb}} + 1.12 \text{ eV} = 3\Delta E_{\text{cb}} + 1.12 \text{ eV} \quad (1.15)$$

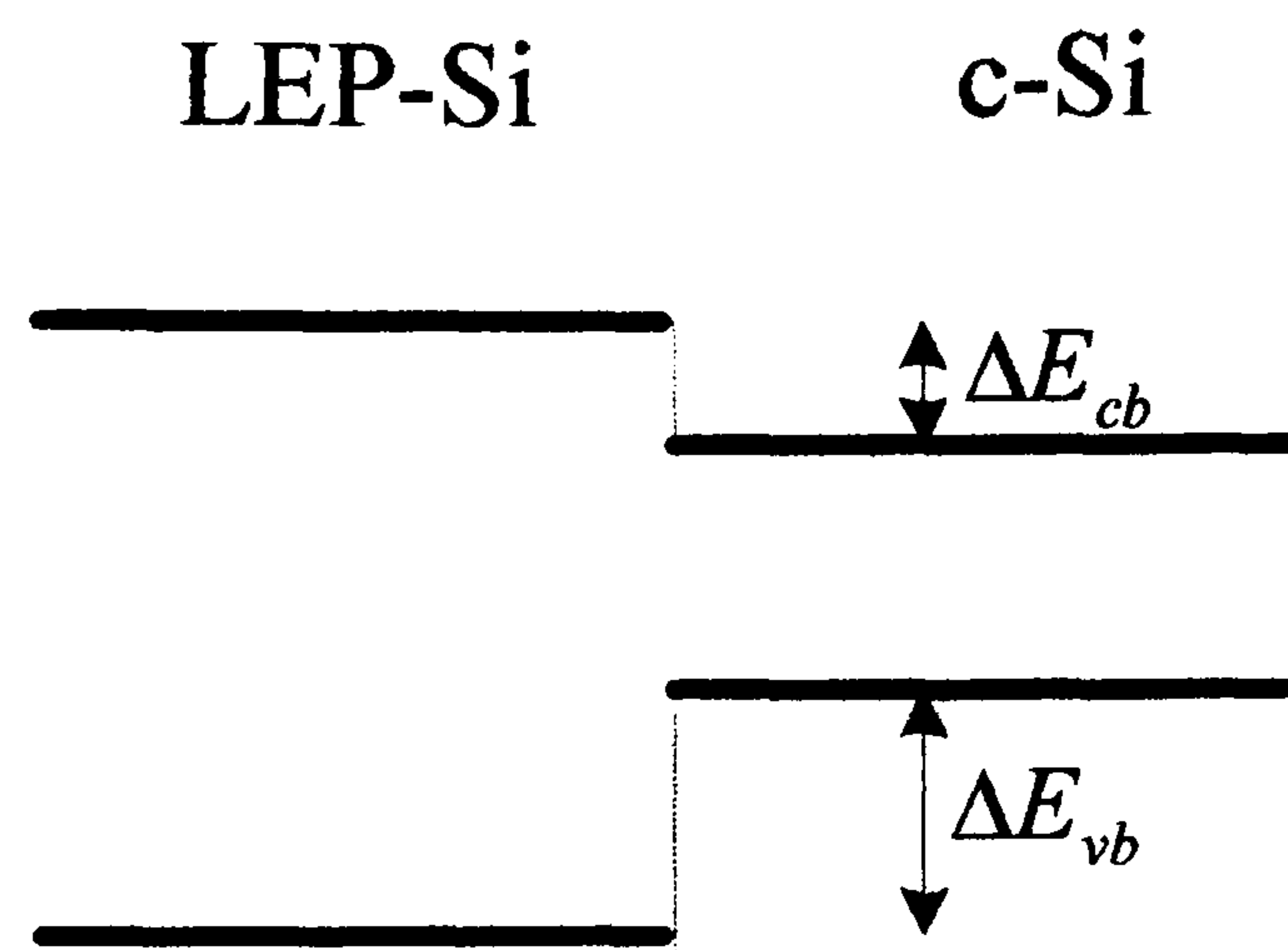


Fig. 1. 14 Increase in the conduction band energy versus decrease in the valence band energy for different π -Si samples. The effect of quantization in the valence band is twice as large as in the conduction band

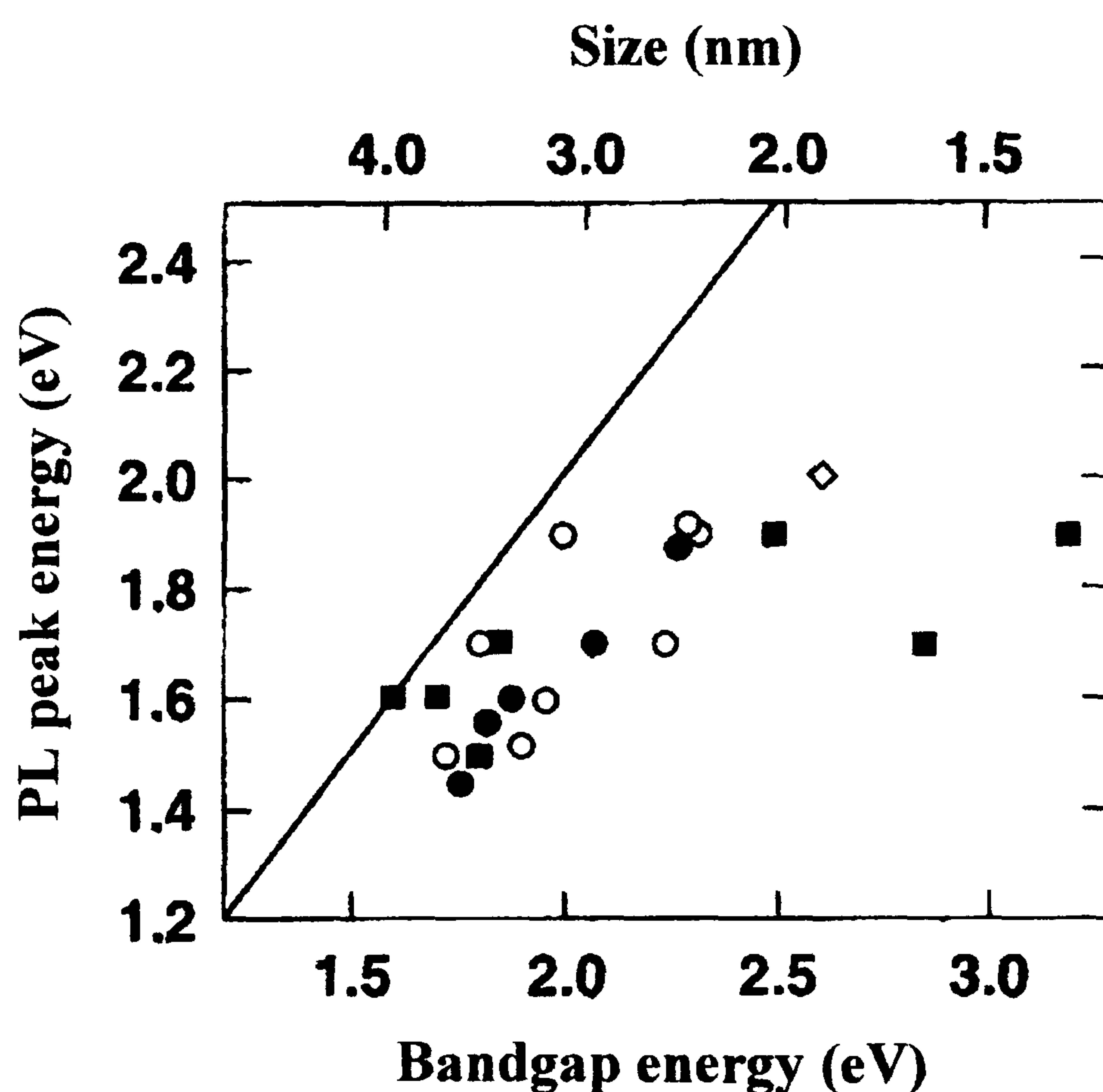


Fig. 1. 15 Photoluminescence peak energy versus bandgap energy in π -Si. If the PL and bandgap energies were the same, the data would fall on the solid line [17].

The difference between bandgap energy and photoluminescence energy is called Stokes shift. For example, π -Si samples having a peak PL energy of 2 eV (orange), the conduction band edge increased by 0.5 eV and valence band edge decreased by 1 eV compared to bulk c-Si. Thus, the bandgap of these samples was 2.6 eV, while the PL was at 2 eV. Fig. 1.15 is a compilation of several experimental and theoretical results and shows that the Stokes shift between bandgap and PL energies increases with decreasing size.

For size above 3 nm, the difference between bandgap and PL energies remains below 300 meV, a value that could be attributed to exciton binding energy in small crystallites; however, below 3 nm, the difference appears to be too large (up to 1 eV and more) to be explained by the expected increase in the free exciton binding energy. It seems likely that the luminescence does not coincide with the bandgap and thus involves surface states [17].

1.5.3 The nanoscale carbon structure— C_{60}

C_{60} , or “Buckminsterfullerene” after the famous architect Buckminster Fuller, is the most abundant member of a family of recently discovered carbon molecules [25, 26], referred to as fullerenes. A fullerene is defined as a closed cage carbon molecule containing 12 pentagonal faces and any number of hexagonal faces, of which C_{60} has 20.

Remarkably, the discovery of C_{60} really came from the field of astrophysics. To try to find how C might contribute to interstellar, bands, studies of the infra-red (IR) absorption of its clusters were underway. Using a laser to evaporate C, it was found that under certain circumstances a particular abundance of clusters with the mass of 720 atomic mass units (a.m.u) occurred, implying that an extremely stable molecule consisting 60 C atoms was being produced. Such high stability would only be expected if each atom in such a molecule had all four of its covalent bonds used. Three dimensional spheroid structures which would not leave any bonds unsaturated at the edges were

therefore considered, and the truncated icosahedron shown in Fig. 1.16 was proposed [25].

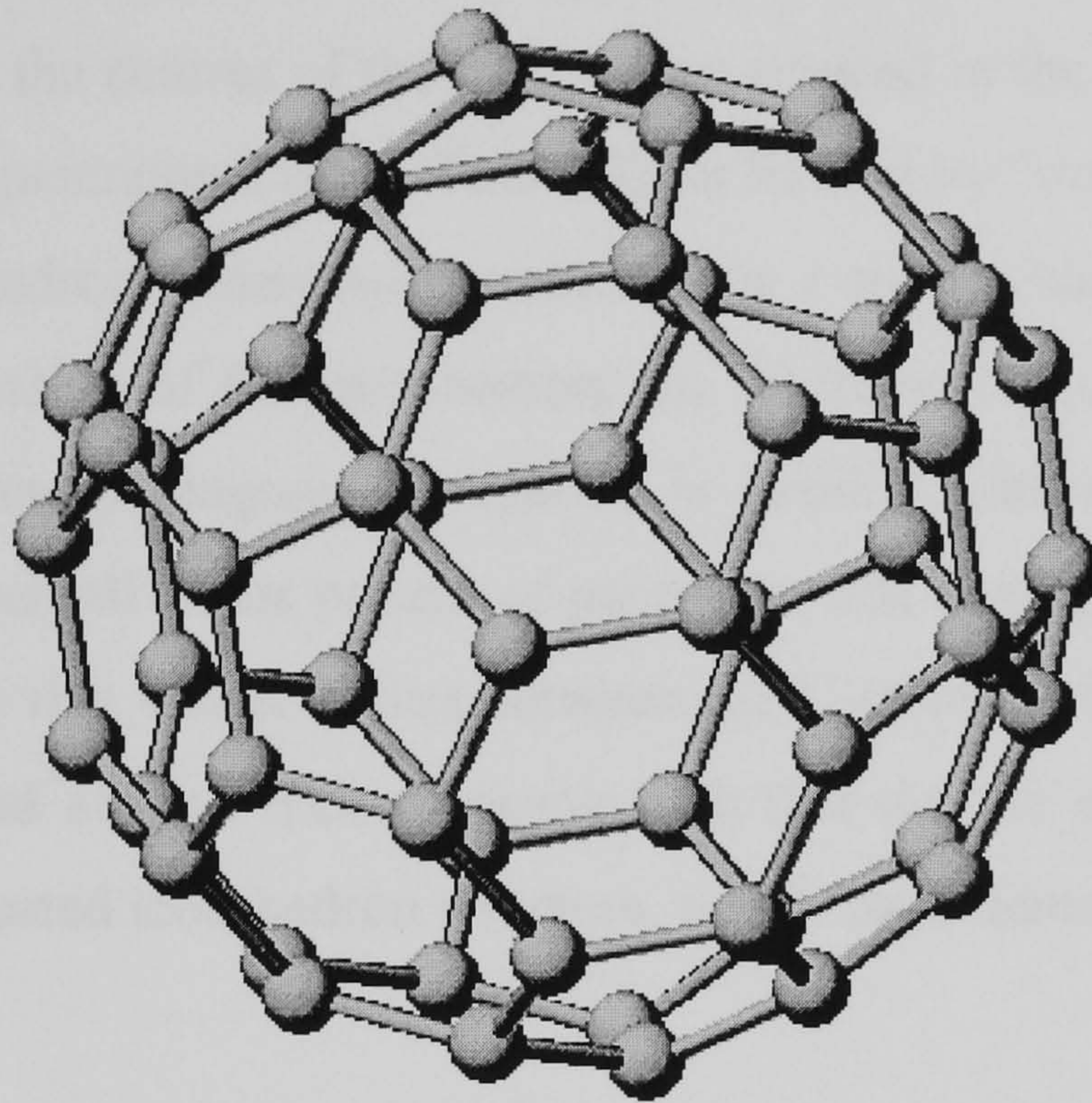


Fig. 1. 16 Schematic diagram of the structure of C_{60} molecule, known as Buckminsterfullerene. It has the shape of a truncated icosahedron, a solid that has 12 pentagonal and 20 hexagonal faces, with a carbon atom at every vertex. (Adapted from an image available at the Sussex Fullerene Centre's Fullerene Gallery website:

<http://www.sussex.ac.uk/Users/kroto/FullereneCentre/gallery/c60.html>)

C_{60} was first produced by laser vaporisation of graphite into a He carrier gas [25]; however this only resulted in minute quantities. The essential data needed to confirm the suggested structure demanded the use of nuclear magnetic resonance (NMR) and IR absorption, requiring much larger quantities of the new molecule than were available. Several groups therefore worked on the development of methods to produce macroscopic quantities of C_{60} in the laboratory. In 1990 an alternative method of production [27] was found, in which carbon rods were vaporised by resistive heating in an inert He atmosphere produced larger quantities. This method, combined with procedure to isolate

C₆₀ from other compounds [28, 29], has enabled high purity C₆₀ (>99.5%) to be produced in gram quantities for use in experiments.

The truncated icosahedron is now generally accepted as the correct structural model for C₆₀, which the centres of the 60 C atoms situated in the position of the corners of the hexagonal and pentagonal faces. This solid is formed by “truncating” (chopping the corner off) an icosahedron, where an icosahedron is a solid whose faces are 20 regular triangles. Upon truncation of the icosahedron, the 20 triangles become hexagons, while the 12 vertices become pentagons. Everybody is familiar with the football, known in America as the “soccerball”. The pattern of pentagons and hexagons found on a football is in fact the same as that which occurs between the C atoms in the C₆₀ molecules. The hexagons are arranged around each pentagon such that no two pentagons are adjacent. This results in a truncated icosahedron structure, with a cage diameter of 7.1 Å, shown in Fig. 1. 16.

There are only two different C-C bond lengths within the C₆₀ molecule; the bonds separating 2 hexagons are $1.40 \pm 0.01\text{\AA}$ long, and those between hexagons and pentagons are $1.45 \pm 0.01\text{\AA}$ long. Each atom has an identical set of two long and one short bond. The hexagons are all therefore irregular, while the pentagons are regular.

Carbon is a very special element, and the way in which it forms molecules is a remarkable example of the theory of hybridisation. The electronic ground state of a C atom is $1s^2 2s^2 2p_x 2p_y$. However, by promoting one 2s electron into p_z orbital, so called sp-hybrids can be formed, in which the s and p wave-functions mix together resulting in four linear combinations per C atom. Such hybrids form strong covalent bonds, as for example in the tetrahedral diamond structure where the three p electrons hybridise with the remaining 2s electron to form four sp^3 -hybrid orbitals. Since all three dimensions of p-orbitals are used, this results three dimensional bonding so that the nearest neighbours to each C atom are at the positions of the corners of a tetrahedron with the original atom in the centre [30].

If only two p electrons are hybridised with the remaining s electron, sp^2 hybrids occur, resulting in two dimensional structures. The most well known example of these is graphite, where the three sp^2 hybrids form σ bonds in a plane with an angle of 120°

between them. The remaining p orbitals, one in each C atom, are directed perpendicular to the plane, and interact broadside with each other forming π bonds, with each atom thus possessing one double bond [30]. The bonding between graphite sheets is much weaker than that within each sheet, and predominantly van der Waals in nature. This weak inter-plane bonding is responsible for the special properties of graphite as a lubricant, and in pencils—adjacent layers slide against each other.

Each C atom in neutral C_{60} possesses six electrons, making a total of 360 per molecule. Of these, 120 are 1s core electrons localised in individual C atoms, while the remaining 240 are the valence electrons responsible for the covalent bonding which holds the molecule together. C_{60} can be approximated by a curved sheet of graphite, and the bonding between the atoms therefore has predominantly sp^2 character. However, because the molecule is curved the valence electron wave functions have some sp^3 character resulting in a σ and π mixture in entire valence states, with the occupied orbitals becoming more π -like as their energy increases [30].

The simplest approximation to C_{60} is that of a sphere, and much progress can be made in understanding the molecule's electronic structure by using such a model [31-33]. The solutions to the Schrödinger equation for a particle on a sphere are the spherical harmonics, denoted Y_{lm} [34], where l is a quantum number associated with the angular momentum of the particle, and m can take integer values from $-l$ to $+l$. For C_{60} , each molecular orbital (MO) consists predominantly of linear combinations of spherical harmonics with the same value of l . In practice, the value of the following integral gives the degree to which a wave-function is described by a given set of spherical harmonics:

$$F_l(r) = \sum_m \left| \int_S Y_{lm}^*(r) \Psi(r) d\Omega \right|^2 \quad (1.16)$$

The integration is carried out over the surface S of a sphere of radius r centred at the middle of the C_{60} cage, and $\Psi(r)$ is a wave-function obtained from model calculations. The value of $F_l(r)$ obtained for each MO's wave-function is an order of magnitude higher for one particular value of l than for all others, and the orbitals can then be designated by an l quantum number. Consideration of the radial variation of the wave-functions divides

method [32, 33]. The five-fold degenerate h_u level which can accommodate 10 electrons, is filled in the ground state, while the t_{1u} and t_{1g} orbitals, which were also represented with $l=5$ in the spherical model, are unoccupied.

C_{60} forms a solid called Fullerite. At room temperature (300 K), the molecules stack in a face centred cubic (f.c.c.) lattice [30], with a nearest neighbour distance (NND) of 10.04 Å. This can be compared to the diameter of the C_{60} molecule, 7.1 Å, and the short and long C-C distances for the covalently bonded carbon atoms within a C_{60} cage, 1.40 Å and 1.45 Å, respectively. The closest distance between two C atoms on adjacent fullerenes is therefore more than double the C-C distance within a molecule, and is closer to the interplane separation in graphite. We might therefore expect C_{60} molecules also to be bonded each other through the van der Waals force. The sublimation temperature of this solid is ~ 450 K, and at a temperature of ~ 260 K it undergoes a phase transition to simple cubic structure [30].

From general considerations of the bonding between the C_{60} molecules, one can build up a simple model of the electronic structure of fullerite. When the fullerenes are put together in a solid, their wave-functions overlap and perturb each other. This perturbation will be relatively weak in a van der Waals bonded solid in which the molecules are well separated. The electron wave functions will delocalise throughout the solid, and the single electron energy levels of the molecule will be broadened into bands. The bandwidth is dependent on the extent of the overlap of the wave-functions on adjacent molecules, and for C_{60} , we therefore expect rather narrow bands [30]. Since calculations predict the HOMO-LUMO separation is ~ 1.6 eV, we would expect the solid to have a bandgap between the occupied and unoccupied states, and to be an insulator [30].

1.6 Some motivations

1.6.1 Chemisorption of C_{60} on InP (100) surface

The growth of C_{60} films on many kinds of surfaces has become a topic of great interest in recent years [26]. The interaction of C_{60} with semiconductor surfaces, such as Ge [35], Si [36-42], and GaAs (110) [43-46] has been the subject of intense experimental investigation because of the potential industrial applications of these systems. The interaction of C_{60} with Si is predominantly covalent and strong [36-42] the substrate-adsorbate interactions tend to dominate the weak C_{60} - C_{60} interactions, and the molecules are immobile at room temperature (RT), forming structures with no long-range order [38, 41, 42]. Moreover, the fullerene molecules do not desorb from the low-index Si surfaces even at 1000 K, while above this temperature they fragment to form a SiC film [36, 37, 40, 47]. Normally, the interaction of fullerenes with GaAs (110) surfaces is so weak that the fullerene-fullerene interaction dominates the observed structure, resulting in the growth of an fcc (111) face. Only in the case of the GaAs (001)-(4 × 2) As-rich surface, a second “strained” fullerene structure is observed for which an ionic type of bonding has been suggested, stronger than the bond formed with the other GaAs (110) surfaces [44-46, 48]. Photoemission studies demonstrated that C_{60} adsorption on GaAs (110) did not affect As 3*d* and Ga 3*d* core levels but led only to a slight change of the width of the C 1*s* level [46].

With respect to possible applications in devices, the InP (100) surface is also of major interest. To our knowledge, however, no study has been made of the interaction of C_{60} with InP (100). In this work we investigate the nature of bonding between adsorbed C_{60} and InP by means of photoemission. We present a detailed analysis of the changes in C 1*s*, P 2*p* and In 4*d* levels as well as in the valence-band spectra as a function of coverage and annealing. The results reveal evidence of covalent bonding between the fullerene and InP surface, the existence of a preferential chemisorption bond between C_{60} molecules and P atoms rather than between C_{60} molecules and In atoms, and significant desorption of C_{60} coupled with the growth of metallic indium clusters when annealing temperature was increased to 640 K and above.

1.6.2 Indium clusters on InP (100) surface

Despite the large body of literature regarding the composition and structure of the In rich- InP (100)-(2×4) [49-55] surface there is still disagreement in several areas. For example, in photoemission studies it has been difficult to assign the number of low binding energy components of the In4*d* core line that are associated with ‘free’ indium in an unambiguous way. The In4*d* core level has been fitted with three surface and one bulk component by some groups [49, 50], while others have fitted with two surface components and one bulk component [52, 53, 55]. Perhaps the main problem is that researchers are unable to distinguish the low binding energy component(s) related directly to the surface reconstruction from that due to ‘free’ indium (by ‘free’ indium we mean indium in excess of that required for a perfect 2×4 reconstruction) found in the form of clusters on the surface. An additional difficulty in the unambiguous assignment of a particular In4*d* component to indium clusters is that, as we shall demonstrate in this paper, the binding energy of the cluster related component changes according to the size, and hence screening efficiency, of the indium clusters.

The above debate about possible models for the In rich (2×4) InP (100) surface reconstruction arises from the discovery that this surface does not behave analogously to the GaAs(100) surface [56]. It has recently been suggested on the basis of STM studies [54, 57], total energy calculations [58, 59], and angle resolved photoemission spectroscopy [56, 59] that simple In-In dimers or trimers are not solely present on this surface, as originally expected, but that there is evidence that there is also a considerable fraction mixed In-P dimers [54, 56-59] or even P-P dimers [54, 60] present. Our recent studies of the chemisorption of C₆₀ on InP (100)-(2 × 4)[61] are in agreement with these findings – chemisorption of a fullerene leads to changes in the spectral features of both the fullerene and phosphorous but not of the indium. This result requires the presence of phosphorous atoms at the outermost layer of the InP (100)-(2 × 4) surface, which are likely to desorb from the surface in the initial stages of annealing.

In addition to providing further insight into the way in which the InP(100)-(2×4) surface changes under annealing, information gleaned about the nature of the indium clusters is important in its own right. The properties of clusters have been the focus of much research interest over the years [43, 62-64] partly due to the desire to understand the transition from the atomic to bulk solid state [65], and partly due to the potential applications of clusters in fields as diverse as heterogeneous catalysis [66], non-linear optics [67, 68], and nanoscale electronics [21, 69]. There are a number of ways of growing clusters on substrates, such as in-situ size and energy selected cluster deposition [70], thermal evaporation [71, 72], and ex-situ chemical preparation [73]. In the case of III-V semiconductors, clusters of the group III elements are formed simply by heating, sputtering or reaction with atomic hydrogen [62, 72, 74-76]. Once prepared and then oxidised, indium clusters, for example, might become important in the formation of InO_x thin films, widely known as sensor elements [77, 78].

In air the InP (100) surface naturally oxidises so that ion bombardment and annealing treatment are necessary in order to obtain an In-rich (2×4) reconstruction, and has been studied in the past [79-81]. The periodicity of the surface has been confirmed by LEED and STM [54]. Indium clusters produced by annealing oxidised InP (100) over a wide temperature range ($250^\circ\text{C} - 550^\circ\text{C}$), have been observed by photoemission spectroscopy (PES) [79]. No detailed study of the In clusters was made since the emphasis of that work was mainly to investigate the influence of Sb deposition on the surface thermal stability. Reflection electron microscopy (REM)[80] has also been used, to study the growth of indium clusters on InP (110) at 650°C (above the thermal decomposition temperature - 370°C - of the InP surface [76]). PES has also been used to investigate argon ion bombardment treated InP (110) surfaces over a wide temperature range [81]. The starting surface in that work was already cluster covered, due to preferential phosphorous sputtering above ion energies of 60eV [82]. To our knowledge, no work has been done on the growth of clusters of indium starting with cluster free In-terminated InP (100)-(2×4) surfaces. In this work we study the effects of heating a perfect (to within experimental sensitivity) InP (100)-(2×4) surface in a temperature range between 360°C and 500°C , and present a detailed analysis of the changes induced in $\text{In}4d$ and valence band spectra. Clean InP (100) as a high carrier mobility material has rising

technological potential, and its surface core level shifts (SCLS) and morphology has been studied widely by X-ray photoemission spectroscopy (XPS), SRPES, STM [49-54, 81, 83-88]. In studies of the InP (100)-(2×4) surface the proposed number of In4*d* core level components for the clean surface varies, as mentioned above, with the presence of three surface and one bulk component suggested by some groups [49, 50], while others use two surface components and one bulk component [52, 53, 55]. The aim of this work is to try directly to identify and assign the low binding energy component of the In4*d* core line by following its development as a function of temperature. In addition, STM work suggests that the most probable model for InP (100)-(2×4) surface is a two phosphorus dimer – two missing dimer model, with the prediction of a highly mobile second layer of In-In dimers which may decompose to form the In clusters [54].

1.6.3 Luminescent Alkylated Silicon Quantum Dots

Semiconductor nanocrystallites, or quantum dots, are potential building blocks of future nanoelectronic and nanophotonic devices. When Si nanostructures become smaller than 20-30 nm, the transport, electronic, and optical properties of bulk silicon start to be influenced significantly by quantum confinement effects [22]. Therefore, it is desirable to develop techniques for fabrication of silicon nanocrystallites (Si-NCs) and to understand their physical and chemical properties. The intensive investigation of Si nanostructures is linked to potential application in light-emitting devices integrated on a chip [89, 90]. Recently, optical gain in silicon nanocrystals embedded in a silicon dioxide matrix has been shown; this brings fabrication of a silicon laser a significant step closer [91]. Compared to the weak IR luminescence of bulk silicon (observed only at low temperatures), the efficiency of photoluminescence (PL) from Si nanostructures is strongly increased due to the greater overlap of electron-hole pairs [92, 93]. Numerous models have been proposed to explain photoluminescence from silicon nanocrystals: recombination of quantum confined electron-hole pairs at siloxenes, amorphous Si phases, and/or surface states related to silicon-oxygen or hydrogen bonds [22, 94, 95], etc. However, detailed studies of the PL mechanism are hampered due to the broad PL band resulting from inhomogeneous broadening (omnipresent in ensembles of NCs). Certain improvements can be achieved by size-selection methods [96], although ultimately single-dot spectroscopy (SDS) is needed to reveal the detailed PL mechanism [22].

Several approaches for the preparation of silicon nanocrystallites are known in the literature, including electrochemical etching [94, 97], reactive sputtering [98], sol-gel techniques [99], ultrasonic dispersion of porous silicon [100], gas-phase decomposition of silanes [101], laser ablation/immobilization on self-assembled monolayers [102], thermal vaporization [23] and solution methods [103]. The surface of these silicon nanoparticles can be passivated or terminated by hydrogen [104], oxide [101, 105, 106], alkoxide [107] or alkylated [97, 108, 109]. It has recently been shown that an alkyl-modified silicon core is an efficient fluorophore which is stable in aqueous/biological media, non-toxic, and emits photons (wavelength 600-700 nm with 513 nm excitation) and does not interact

strongly with most biological molecules [110]. Such properties mean that these passivated nanocrystallites might also be potentially important as nanoscale sensors inside living cells.

In this work we made a detailed study [111], using scanning tunnelling microscopy (STM), soft X-ray photoemission and X-ray excited optical luminescence (XEOL), which aims to determine the composition of alkylated silicon nanocrystallites and to understand their reactivity upon irradiation. To our knowledge, there are no investigations in the literature which explore the interaction of photons in the VUV/XUV energy region with any kind of Si-NCs. Chemical changes induced by illumination of the nanocrystallites may well be involved in ageing processes. For this reason the VUV/XUV photon energy range is particularly interesting because the Si2*p* core levels are accessible allowing both reactivity and luminescence to be followed simultaneously, and their relationship to be determined.

The effects of ageing in porous silicon have been studied over the past decade [112-115] and is still a subject of interest in many investigations which aim to discover appropriate capping layers [116-118] to suppress ambient ageing and prepare porous silicon for industrial applications. However, studies of ageing of Si nanocrystallites are much rarer. We have found only few indirect study of ageing in Si nanocrystallites [94, 119]. The lack of ageing studies on Si-NCs may possibly be due to difficulties in preparation of these materials in sufficient (milligram) quantities for study by macroscopic techniques.

1.7 References

- [1] J. C. Woicik, E. J. Nelson, D. Heskett, J. Warner, L. E. Berman, B. A. Karlin, I. A. Vartanyants, M. Z. Hasan, T. Kendelewicz, Z. X. Shen, and P. Pianetta, Phys. Rev. B **64**, 125115 (2001).
- [2] H. Luth, *Surfaces and interfaces of solids* (Springer-Verlag, 1993).
- [3] M. P. Seah and W. A. Dench, Surf.Interf.Anal. **1**, 2 (1979).
- [4] C. Wagner, W. Riggs, L. Davis, and J. Moulder, in *Handbook of X-ray photoelectron spectroscopy*, edited by G. E. Muilenberg (Perkin Elmer Corporation, Eden Prairie, Minnesota, 1997).
- [5] P. Bagus, F. Illas, and F. Parmingiani, J. Electron Spectrosc. Relat. Phenom. **100**, 215 (1999).
- [6] P. Cumpson, Appl.Surf. Sci. **144-145**, 16 (1999).
- [7] C. Kittel, *Introduction to solid state physics* (John Wiley & Sons, Inc., 1996).
- [8] E. Rotenberg, C. Enkvist, P. A. Bruhwiler, A. J. Maxwell, and N. Martensson, Phys. Rev. B **54**, R5279 (1996).
- [9] G. Gensterblum, K. Hevesi, B. Y. Han, L. M. Yu, J. J. Pireaux, P. A. Thiry, R. Caudano, A. A. Lucas, D. Bernaerts, S. Amelinckx, G. Vantendeloo, G. Bendele, T. Buslaps, R. L. Johnson, M. Foss, R. Feidenhansl, and G. Lelay, Phys. Rev. B **50**, 11981 (1994).

- [10] J. G. Chen, Surface Science Reports **30**, 1 (1997).
- [11] J. Stohr, *NEXAFS Spectroscopy* (Springer, New York, 1992).
- [12] T. Käämbre, in *Physcis* (Uppsala, 2002).
- [13] T. K. Sham, R. Sammynaiken, Y. J. Zhu, P. Zhang, I. Coulthard, and S. J. Naftel, Thin Solid Films **363**, 318 (2000).
- [14] T. K. Sham, D. T. Jiang, I. Coulthard, J. W. Lorimer, X. H. Feng, K. H. Tan, S. P. Frigo, R. A. Rosenberg, D. C. Houghton, and B. Bryskiewicz, Nature **363**, 331 (1993).
- [15] D. T. Jiang, I. Coulthard, T. K. Sham, J. W. Lorimer, S. P. Frigo, X. H. Feng, and R. A. Rosenberg, J. Appl. Phys. **74**, 6335 (1993).
- [16] I. Coulthard and T. K. Sham, Solid State Commun. **110**, 203 (1999).
- [17] P. M. Fauchet, in *Light Emission in Silicon From Physics to Devices*, edited by D. J. Lockwood (Academic Press, New York, 1998), Vol. 49, p. 205.
- [18] S. S. Iyer and Y.-H. Xie, Science **260**, 40 (1993).
- [19] J. C. Sturm, Mat. Res. Soc. Symp. Proc. **358**, 665 (1993).
- [20] P. L. Bradfield, T. G. Brown, and D. G. Hall, Appl. Phys. Lett. **55**, 100 (1989).
- [21] U. Kreibig and M. Vollmer, *Optical Properties of Metal Clusters* (Springer-Verlag, 1995).

- [22] J. Valenta, R. Juhasz, and J. Linnros, Appl. Phys. Lett. **80**, 1070 (2002).
- [23] T. van Buuren, L. N. Dinh, L. L. Chase, W. J. Siekhaus, and L. J. Terminello, Phys. Rev. Lett. **80**, 3803 (1998).
- [24] T. van Buuren, T. Tiedje, J. R. Dahn, and B. M. May, Appl. Phys. Lett. **63**, 2911 (1993).
- [25] H. W. Kroto, J. R. Heath, S. C. O'Brien, R. F. Curl, and R. E. Smalley, Nature **318**, 162 (1985).
- [26] A. V. Hamza, *Fullerenes Chemistry, Physics and Technology* (John & Sons, New York, 2000).
- [27] W. Kratschmer, L. D. Lamb, K. Fostiropoulos, and D. R. Huffman, Nature **347**, 354 (1990).
- [28] D. S. Bethune, G. Meijer, W. C. Tang, and H. J. Rosen, Chem. Phys. Lett. **174**, 219 (1990).
- [29] R. Taylor, J. P. Hare, A. K. Abdulsada, and H. W. Kroto, J. Chem. Soc.-Chem. Commun., 1423 (1990).
- [30] A. J. Maxwell, in *Physics* (Uppsala University, 1996).
- [31] N. Troullier and J. L. Martins, phys.Rev. B **46**, 1754 (1992).
- [32] M. Ozaki and A. Takahashi, Chem. Phys. Lett. **127**, 242 (1986).

- [33] R. C. Haddon, L. E. Brus, and K. Raghavachari, Chem. Phys. Lett. **5**, 459 (1986).
- [34] P. W. Atkins, *Molecular Quantum Mechanics* (Oxford University Press, Oxford, 1983).
- [35] A. Goldoni, C. Cepek, M. De Seta, J. Avila, M. C. Asensio, and M. Sancrotti, Surf. Sci. **454-456**, 514 (2000).
- [36] M. De Seta, D. Sanvitto, and M. Evangelisti, Phys. Rev. B **59**, 9878 (1999).
- [37] C. Cepek, P. Schiavuta, and M. Sancrotti, Phys. Rev. B **60**, 2068 (1999).
- [38] P. Moriarty, D. Upward, Y.-R. Ma, P. H. Beton, and D. Teehan, Phys. Rev. B **57**, 362 (1998).
- [39] J. Schmidt, M. R. C. Hunt, P. Miao, and R. E. Palmer, Phys. Rev. B **56**, 9918 (1997).
- [40] M. R. C. Hunt, J. Phys. Condens. Matter **8**, L229 (1996).
- [41] X. W. Yao, T. G. Ruskell, R. K. Workman, D. Sarid, and D. Chen, Surf. Sci. **366**, L743 (1996).
- [42] T. Sakurai, X. D. Wang, Q. K. Xue, Y. Hasegawa, T. Hashizume, and H. Shinohara, Prog. Surf. Sci. **51**, 263 (1996).
- [43] D. Dalacu, E. Jolanta, E. Klemberg-Sapieha, and L. Martinu, Surf. Sci. **472**, 33 (2001).

- [44] J. C. Duphy, D. Klyachko, H. Xu, and D. M. Chen, *Surf. Sci.* **383**, L760 (1997).
- [45] T. Sakurai, Q. Xue, T. Hashizume, and Y. Hasagawa, *J. Vacuum Sci. Technol. B* **15**, 1628 (1997).
- [46] T. R. Ohno, Y. Chen, S. E. Harvey, G. H. Kroll, J. H. Weaver, R. E. Haufler, and R. E. Smalley, *Phys. Rev. B* **44**, 13747 (1991).
- [47] A. V. Hamza, M. Balloch, and M. Moalem, *Surf. Sci.* **317**, L1129 (1994).
- [48] M. Shimomura, N. Sanada, S. Ichikawa, Y. Fukuda, Nagoshi, and P. J. Moller, *J. Appl. Phys.* **83**, 3071 (1998).
- [49] V. Chab, L. Pekarek, I. Ulrych, J. Suchy, K. C. Prince, M. Peloi, M. Evans, C. Comicioli, M. Zacchigna, and C. Crotti, *Surf. Sci.* **377**, 261 (1997).
- [50] M. Shimomura, N. Sanada, G. Kaneda, T. Takeuchi, Y. Suzuki, Y. Fukuda, W. R. A. Huff, T. Abukawa, S. Kono, H. W. Yeom, and A. Kakizaki, *Surf. Sci.* **413**, 625 (1998).
- [51] D. Pahlke, J. Kinsky, C. Schultz, M. Pristovsek, M. Zorn, N. Esser, and W. Richter, *Phys. Rev. B* **56**, R1661 (1997).
- [52] R. K. Gebhardt, A. B. Preobrajenski, and T. Chasse, *Phys. Rev. B* **61**, 9997 (2000).
- [53] S. Sloboshanin, R. K. Gebhardt, J. A. Schaefer, and T. Chasse, *Surf. Sci.* **431**, 252 (1999).

- [54] Q. Guo, M. E. Pemble, and E. M. Williams, *Surf. Sci.* **433-435**, 410 (1999).
- [55] W. G. Schmidt, F. Bechstedt, N. Esser, M. Pristovsek, C. Schultz, and W. Richter, *Phys. Rev. B* **57**, 14596 (1998).
- [56] W. R. A. Huff, M. Shimomura, N. Sanada, G. Kaneda, Y. Suzuki, H. W. Yeom, T. Abukawa, S. Kono, and Y. Fukuda, *Phys. Rev. B* **57**, 10132 (1998).
- [57] M. Shimomura, N. Sanada, Y. Fukuda, and P. J. Moller, *Surf. Sci.* **359**, L451 (1996).
- [58] W. G. Schmidt and F. Bechstedt, *Surf. Sci.* **409**, 474 (1998).
- [59] A. M. Frisch, P. Vogt, S. Visbeck, T. Hannappel, F. Willig, W. Braun, W. Richter, J. Bernholc, W. G. Schmidt, and N. Esser, *Appl. Surf. Sci.* **166**, 224 (2000).
- [60] W. G. Schmidt, E. L. Briggs, J. Bernholc, and F. Bechstedt, *Phys. Rev. B* **59**, 2234 (1999).
- [61] Y. Chao, K. Svensson, D. Radosavkic, V. R. Dhanak, L. Šiller, and M. R. C. Hunt, *Phys. Rev. B* **64**, 235331 (2001).
- [62] T. D. Lowes and M. Zinke-Allmang, *Phys. Rev. B* **49**, 16678 (1994).
- [63] G. K. Wertheim and S. B. DiCenzo, *phys.Rev. B* **37**, 844 (1988).
- [64] G. K. Wertheim, S. B. Dicenzo, and D. N. E. Buchanan, *Phys. Rev. B* **33**, 5384 (1986).

- [65] W. A. de Heer, Rev. Mod. Phys. **65**, 611 (1993).
- [66] M. Valdem, X. Lai, and D. W. Goodman, Science **281**, 1647 (1998).
- [67] H. B. Liao, R. F. Xiao, J. S. Fu, H. Wang, K. S. Wong, and G. K. L. Wong, Opt. Lett. **23**, 388 (1998).
- [68] D. Ricard, P. Roussignol, and C. Flytzanis, Opt. Lett. **10**, 511 (1985).
- [69] S. H. M. Persson and L. Olofsson, Appl. Phys. Lett. **74**, 2546 (1999).
- [70] C.-M. Grimaud, L. Šiller, M. Anderson, and R. E. Palmer, Phys.Rev.B **59**, 9874 (1999).
- [71] I. Goldfarb, P. T. Hayden, J. H. Owen, and G. A. D. Briggs, Phys. Rev. B **56**, 10459 (1997).
- [72] G. R. Carlow, R. J. Bartel, Zinke-Allmanag, and M., Phys. Rev. B **56**, 12519 (1997).
- [73] J. P. Wilcoxon, P. P. Provencio, and G. A. Samara, Phys. Rev. B **64**, 035417 (2001).
- [74] S. Nannarone, S. Daddato, M. G. Betti, U. delPennino, Y. Chen, P. Samonto, and G. J. Lapeyre, Phys. Rev. B **43**, 9818 (1991).
- [75] R. delPennino, R. Biagi, C. Mariani, L. Šiller, A. Amoddeo, F. Proix, and C. A. Sebenne, Physica Stat. Solid A -Appl. Res. **159**, 205 (1997).

- [76] J. C. Tsang, A. Kahn, and P. Mark, *Surf. Sci.* **97**, 119 (1980).
- [77] H. Yamaura, T. Jinkawa, J. Tamaki, K. Moroya, N. Miura, and N. Yamazoe, *Sensors and Actuators B* **35-36**, 325 (1996).
- [78] N. G. Patel, K. K. Makhija, C. J. Panchal, D. B. Dave, and V. S. Vaishnav, *Sensors and Actuators B* **23**, 49 (1995).
- [79] P. Soukiassian, P. S. Mangat, Y. Huttel, Z. Hurych, B. Gruzza, and A. Porte, *J. Vac. Sci. Technol. B* **11**, 1603 (1993).
- [80] M. Gajdardziska-Josifovska, M. H. Malay, and D. J. Smith, *Surf. Rev. Lett.* **4**, 655 (1997).
- [81] W. M. Lau, R. N. S. Sodhi, B. J. Finn, K. H. Tan, and G. M. Bancroft, *Appl. Phys. Lett.* **51**, 177 (1987).
- [82] J. B. Malhebre and W. O. Barnard, *Surf. Sci.* **255**, 309 (1991).
- [83] R. W. M. Kwok and W. M. Lau, *J. Vac. Sci. Technol. A-Vac. Surf. Films* **10**, 2515 (1992).
- [84] R. K. Gebhardt, S. Sloboshanin, J. A. Schaefer, and T. Chasse, *Appl. Surf. Sci.* **142**, 94 (1999).
- [85] C. Ottaviani, M. Capozzi, C. Quaresima, M. Matteucci, and C. Crotti, *J. Electron Spectroscopy and Related Phenomena* **76**, 139 (1995).

- [86] C. Schultz, A. M. Frisch, K. Hinrichs, J. Kinsky, T. Herrmann, U. Rossow, N. Esser, and W. Richter, *J. Vac. Sci. Technol. B* **15**, 1260 (1997).
- [87] T. X. Zhao, H. Ji, Q. Liang, X. P. Wang, P. S. Xu, E. D. Lu, J. X. Wu, and C. C. Hsu, *J. Vac. Sci. Technol.* **13**, 1967 (1995).
- [88] W. G. Wilke, V. Hinkel, W. Theis, and K. Horn, *Phys. Rev. B* **40**, 9824 (1989).
- [89] F. Cunin, T. A. Schmedake, J. R. Link, Y. Y. Li, J. Koh, S. N. Bhatia, and M. J. Sailor, *Nature Materials* **1**, 39 (2002).
- [90] M. Buchez, M. Moronne, P. Gin, S. Weiss, and A. P. Alivisatos, *Science* **281**, 2013 (1998).
- [91] L. Pavesi, L. Dal Negro, C. Mazzoleni, G. Franzo, and F. Priolo, *Nature* **408**, 440 (2000).
- [92] J. A. Bruce, T. Murahashi, and M. S. Wrighton, *J. Phys. Chem.* **86**, 1552 (1982).
- [93] D. Kovalev, H. Heckler, M. Ben-Chorin, G. Polisski, M. Schwartzkopff, and F. Koch, *Phys. Rev. Lett.* **81**, 2803 (1998).
- [94] M. V. Wolkin, J. Jorne, P. M. Fauchet, G. Allan, and C. Delerue, *Phys. Rev. Lett.* **82**, 197 (1999).
- [95] Z. Ding, B. M. Quinn, S. K. Haram, L. E. Pell, B. A. Korgel, and A. J. Bard, *Science* **296**, 1293 (2002).
- [96] W. L. Wilson, P. F. Szajowski, and L. E. Brus, *Science* **262**, 1242 (1993).

- [97] L. H. Lie, M. Duerdin, E. M. Tuite, A. Houlton, and B. R. Horrocks, J. Electroanal. Chem. **538**, 183 (2002).
- [98] S. Furukawa and T. Miyasato, Phys. Rev. B **38**, 5726 (1988).
- [99] L. Zhang, J. L. Coffey, and T. W. Zerda, J. Sol-Gel Sci. Technol. **11**, 267 (1998).
- [100] J. L. Heinrich, C. L. Curtis, G. M. Credo, K. L. Kavanagh, and M. J. Sailor, Science **255**, 66 (1992).
- [101] L. E. Brus, P. F. Szajowski, W. L. Wilson, T. D. Harris, S. Schuppler, and P. H. Citrin, J. Am. Chem. Soc. **117**, 2915 (1995).
- [102] K. Hata, S. Yoshida, M. Fujita, S. Yasuda, T. Makimura, K. Murakami, and H. Shigekawa, Journal of Physical Chemistry B **105**, 10842 (2001).
- [103] J. R. Heath, Science **258**, 1131 (1992).
- [104] P. E. Batson and J. R. Heath, Phys. Rev. Lett. **71**, 911 (1993).
- [105] K. A. Littau, P. F. Szajowski, A. J. Muller, and L. E. Brus, J. Phys. Chem. **97**, 1224 (1993).
- [106] A. Fojtik, H. Weller, S. Fiechter, and A. Henglein, Chem. Phys. Lett. **134**, 477 (1987).
- [107] Bley, R. A. and S. M. Kauzlarich, J. Am. Chem. Soc. **118**, 12461 (1996).

- [108] R. K. Baldwin, K. A. Pettigrew, J. C. Garno, P. P. Power, G.-Y. Liu, and S. M. Kauzlarich, *J. Am. Chem. Soc.* **124**, 1150 (2002).
- [109] C. S. Yang, R. A. Bley, S. M. Kauzlarich, H. W. H. Lee, and D. G. Delgado, *J. Am. Chem. Soc.* **121**, 5191 (1999).
- [110] M. J. Sailor and E. J. Lee, *Adv. Mater.* **9**, 783 (1997).
- [111] Y. Chao, S. Krishnamurthy, M. Montalti, L. H. Lie, A. Houlton, B. R. Horrocks, L. Kjeldgaard, V. R. Dhanak, M. R. C. Hunt, and L. Šiller, *J. Chem. Phys.* **submitted** (2003).
- [112] B. Huy, P. H. Binh, B. Q. Diep, and P. V. Luong, *Physica E-Low-Dimensional Systems & Nanostructures* **17**, 134 (2003).
- [113] H. Elhouichet and M. Oueslati, *Appl. Surf. Sci.* **191**, 11 (2002).
- [114] M. A. Butturi, M. C. Carotta, G. Martinelli, L. Passari, G. M. Youssef, A. Chiorino, and G. Ghiotti, *Solid State Commun.* **101**, 11 (1997).
- [115] Y. Kanemitsu, T. Ogawa, K. Shiraishi, and K. Takeda, *Phys. Rev. B* **48**, 4883 (1993).
- [116] X. J. Li, D. L. Zhu, Q. W. Chen, and Y. H. Zhang, *Appl. Phys. Lett.* **74**, 389 (1999).
- [117] T. Giaddui, L. G. Earwaker, K. S. Forcey, A. Loni, and L. T. Canham, *J. Phys. D-Appl. Phys.* **31**, 1131 (1998).

- [118] T. Giaddui, K. S. Forcey, L. G. Earwaker, A. Loni, L. T. Canham, and A. Halimaoui, J. Phys. D-Appl. Phys. **29**, 1580 (1996).
- [119] Y. Kanemitsu, H. Uto, Y. Masumoto, T. Matsumoto, T. Futagi, and H. Mimura, Phys. Rev. B **48**, 2827 (1993).

Chapter 2 Experimental

The following chapter describes the apparatus and experimental techniques used during the experiments in this thesis. A description of the ultra-high-vacuum systems, beamlines and AFM is presented. Methods used to prepare samples are described along with the InP (100)-(2 × 4) reconstruction. A self-written HP-VEE control programme is also given.

2.1	Ultra High Vacuum (UHV) system	51
2.2	Synchrotron radiation source (SRS) and beamline optics.....	54
2.2.1	Station 4.1 in Daresbury Lab	58
2.2.2	Beamline I511 in MAX Lab	61
2.3	Photoemission spectroscopy acquirement.....	63
2.3.1	Geometry of the measurements	66
2.3.2	Binding Energy Calibrations	67
2.4	Sample Preparation	68
2.4.1	InP (100) Surface Treatment	68
2.4.2	Si-Quantum Dots.....	69
2.5	C ₆₀ Evaporation and Coverage Calibrations	71
2.6	Temperature Measurements	72
2.7	Photoluminescence Spectroscopy.....	73
2.7.1	Photon Spectrometer and Photomultiplier Tubes	74
2.7.2	KEITHLEY Programmable Electrometer and HP VEE Control Programme..	76
2.8	Description of Atomic Force Microscope.....	78
2.9	References	82

The technical demands for doing photoemission spectroscopy (PES) experiments were divided into three parts: First, refinement of ultra-high-vacuum (UHV) techniques and methods for preparing clean and well-defined samples *in situ*; Second, the development of high resolution, high sensitivity, angle-resolved electrostatic electron spectrometers which allowed measurements in a reasonable time; Third, development of high intensity light sources (e.g. He I radiation from a discharge lamp), and later the advent of synchrotron radiation facilities as a tunable high intensity light sources. Today various implementations of PES have become established methods for investigating the electronic structure of materials in the solid state. The following sections are about the experimental details related to this thesis.

2.1 Ultra High Vacuum (UHV) system

Ultra high vacuum (UHV) is required for most surface science experiments for two principal reasons:

1. To enable atomically clean surfaces to be prepared for study, and such surfaces to be maintained in a contamination-free state for the duration of the experiment.
2. To permit the use of low energy electron and ion-based experimental techniques without undue interference from gas phase scattering.

Let's look at the variation of various parameters with pressure. Sticking coefficient is defined as the ratio of the rate of *adsorption* to the rate at which the *adsorptive* strikes the total surface, i.e. covered and uncovered. It is usually a function of surface coverage, of temperature and of the details of the surface structure of the *adsorbent*. If we assume sticking coefficient $S = 1$, the Flux (F) of atoms or molecules striking our surface is related to the pressure P, temperature T and the molecule mass M:

[1]

$$F = \frac{N_A P}{\sqrt{2\pi M R T}} \quad (2.1)$$

In unit atoms/cm² s,

$$F = 3.51 \times 10^{22} \frac{P(\text{Torr})}{\sqrt{M(\text{g/mol})T}} \quad (2.2)$$

For example CO, at room temperature $T = 300\text{K}$ and pressure 1×10^{-6} Torr,

$$F = 3.51 \times 10^{22} \frac{1 \times 10^{-6}(\text{Torr})}{\sqrt{28(\text{g/mol})300(\text{K})}} \approx 10^{15} (\text{atoms/cm}^2 \text{ s}) \quad (2.3)$$

If we assume surface density $\sigma_{\text{surf}} = 10^{15}$ atoms/cm², to cover a surface in 1 second with a monolayer of gas, we need a gas exposure of

$$1 \text{ L (Langmuir)} = 1 \times 10^{-6} (\text{Pressure/Torr}) \cdot (\text{Time/s}) \quad (2.4)$$

To have a control of the atomic composition of a surface for i.e. 3 hours (10800s), the pressure must be lower than $P = 10^{-10}$ Torr. This can be obtained in an ultra high vacuum (UHV) system, where the number of gas atoms or molecules incident onto a surface is small compared to atmospheric pressure. Such a vacuum, with a pressure $< 10^{-8}$ Torr, can be achieved with an arrangement of stainless steel chambers attached to suitable pumps.

Fig. 2.1 and Fig. 2.5 show the same UHV system in beamline 4.1, Daresbury, under the different angle, it only has one big main chamber with a load-lock for the exchange of samples between air and UHV. Fig. 2.6 is the photo of the UHV system used in I511, Max-Lab. It consists of one main analysis chamber and one preparation chamber.

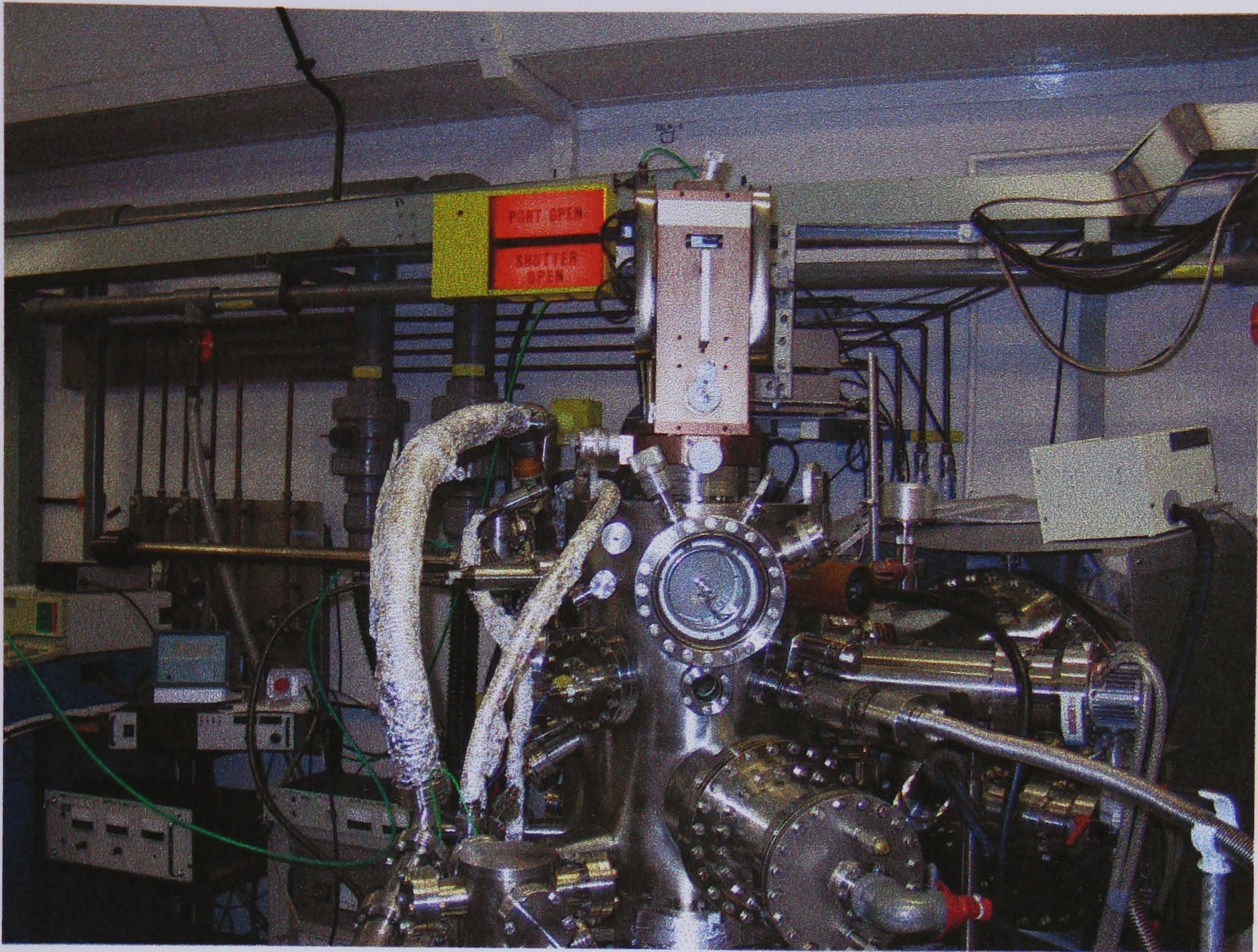


Fig. 2. 1 UHV system in station 4.1, Daresbury

2.2 Synchrotron radiation source (SRS) and beamline optics

For most studies in this thesis, tuneable high brilliance radiation sources at synchrotron are a prerequisite. Synchrotron radiation is generated when a charged particle, moving at relativistic speeds, is deflected by a magnetic field. The deflection can be achieved either by bending magnets (circular motion) or by periodic magnetic structures (sinusoidal motion). Synchrotron radiation provides a bright and polarized photon beam as the excitation source. In general, synchrotron radiation is several orders of magnitude more intense, and more importantly, covers a much broader energy range than the conventional X-ray sources. These characteristics are essential for achieving reliable and high quality photoemission (PES), near edge X-ray adsorption fine structure (NEXAFS) and X-ray excited optical luminescence (XEOL) measurement, because the cross section of emission for each element and energy level varies with the excitation photon energy, see Chapter 1.

Three types of radiation sources on the storage ring are distinguished (see Fig. 2.2): the bending magnet, the wiggler and the undulator. The bending magnet is a dipole magnet placed at a vertex of the synchrotron “ring” (or more precisely: a polygon), generating forward-directed cone of light, and has a characteristic frequency, which is determined by the electron energy and the field strength. A wiggler is mounted on a straight section and consists of several “bending-magnet”—poles to gain intensity. The most selective and bright source is the undulator, which like a wiggler is a periodic magnetic structure, but the number of poles is considerably larger, and their distance and the field strength are chosen so that the light is generated coherently at different bending stages and interferes with itself. The interference of light from different periods concentrates the intensity from an undulator source into narrow spectral regions, the “undulator” peaks, which are the result of interference in different orders.

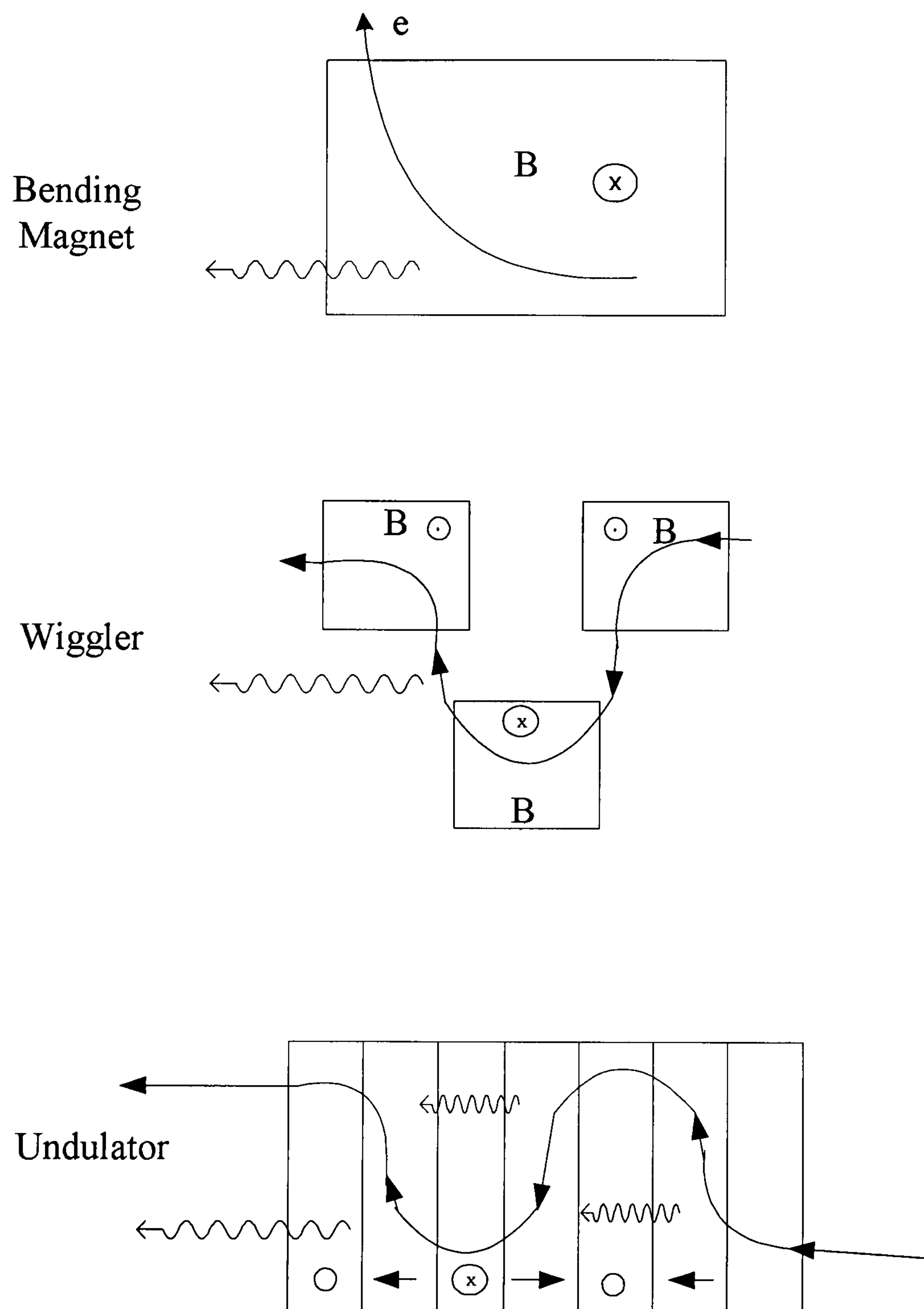


Fig. 2. 2 Working principles of radiative elements on a synchrotron ring: bending magnet, wiggler and undulator

The synchrotron measurements presented in this thesis were carried out using either bending magnet (4.1, Daresbury) or undulator radiation sources (I511, Max II).

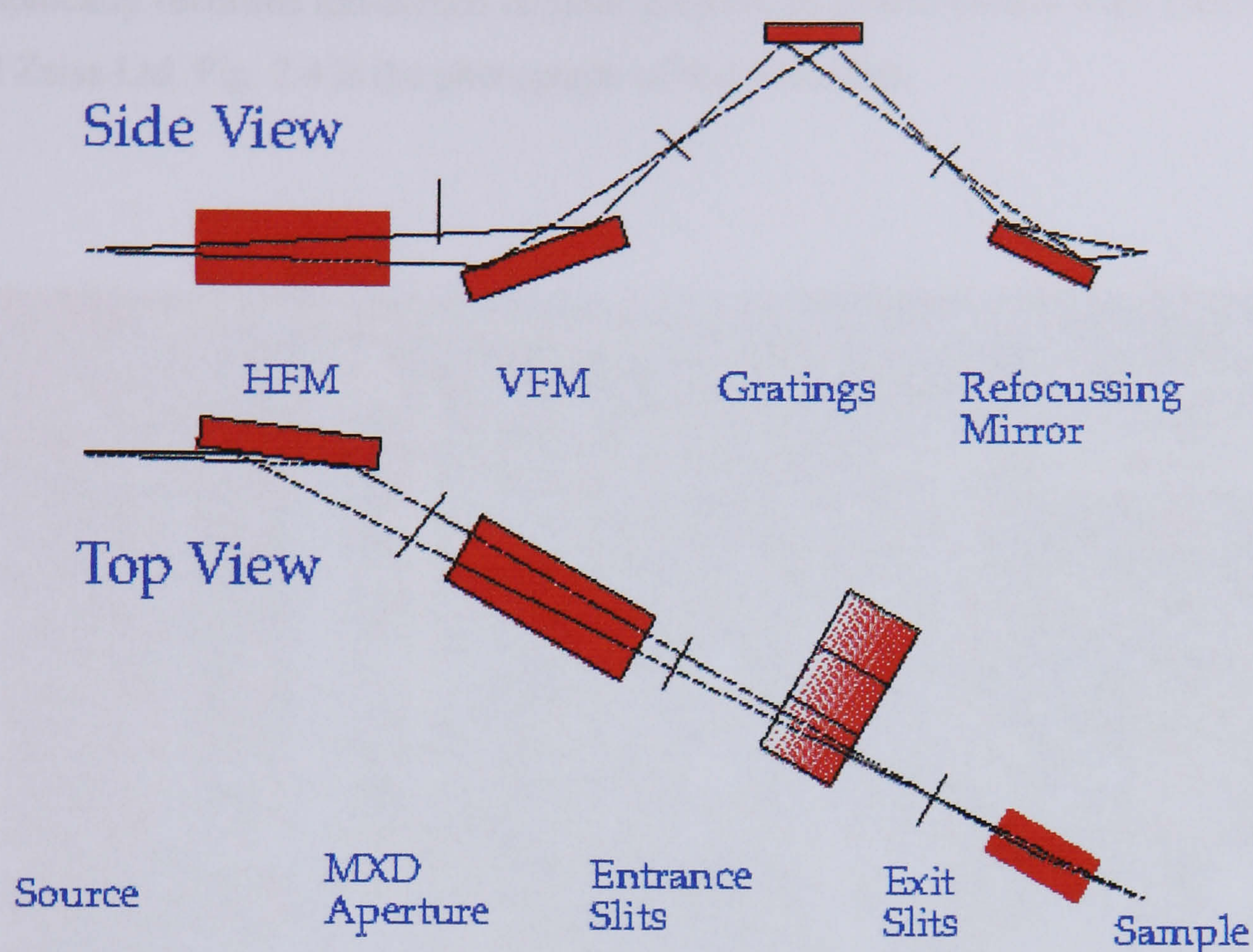


Fig. 2. 3 Schematic Layout of Beamline 4.1, Daresbury

Fig. 2.3 illustrates the layout of beamline 4.1 in Daresbury. At the left are two pre-mirrors close to each other. The focussing function of the two mirrors is decoupled. The one closest to the source is the horizontally focussing mirror (HFM) and the second is the vertically focussing mirror (VFM). The HFM is water cooled since it serves as a heat and radiation sink, protecting the other optical elements in the line. It collects 6 mrad of the available synchrotron radiation at dipole 4, deflects the beam sideways and focusses the source horizontally in the non-dispersive direction at the mean position of the monochromator exit slit. The VFM deflects the beam upwards and focusses vertically in the dispersive direction at the monochromator entrance slit. An aperture (MXD) upstream of the VFM is located to allow selection of circular polarised light in the upper or lower part of the photon beam in the vertical direction for dichroism experiments.

After the entrance slit, one of three in-situ interchangeable gratings diffracts and focusses the photon beam vertically at the exit slit. The Au coated spherical gratings are

holographically recorded ion-etched laminar profiles on quartz blanks were manufactured by Carl Zeiss Ltd. Fig. 2.4 is the photograph of this beamline.

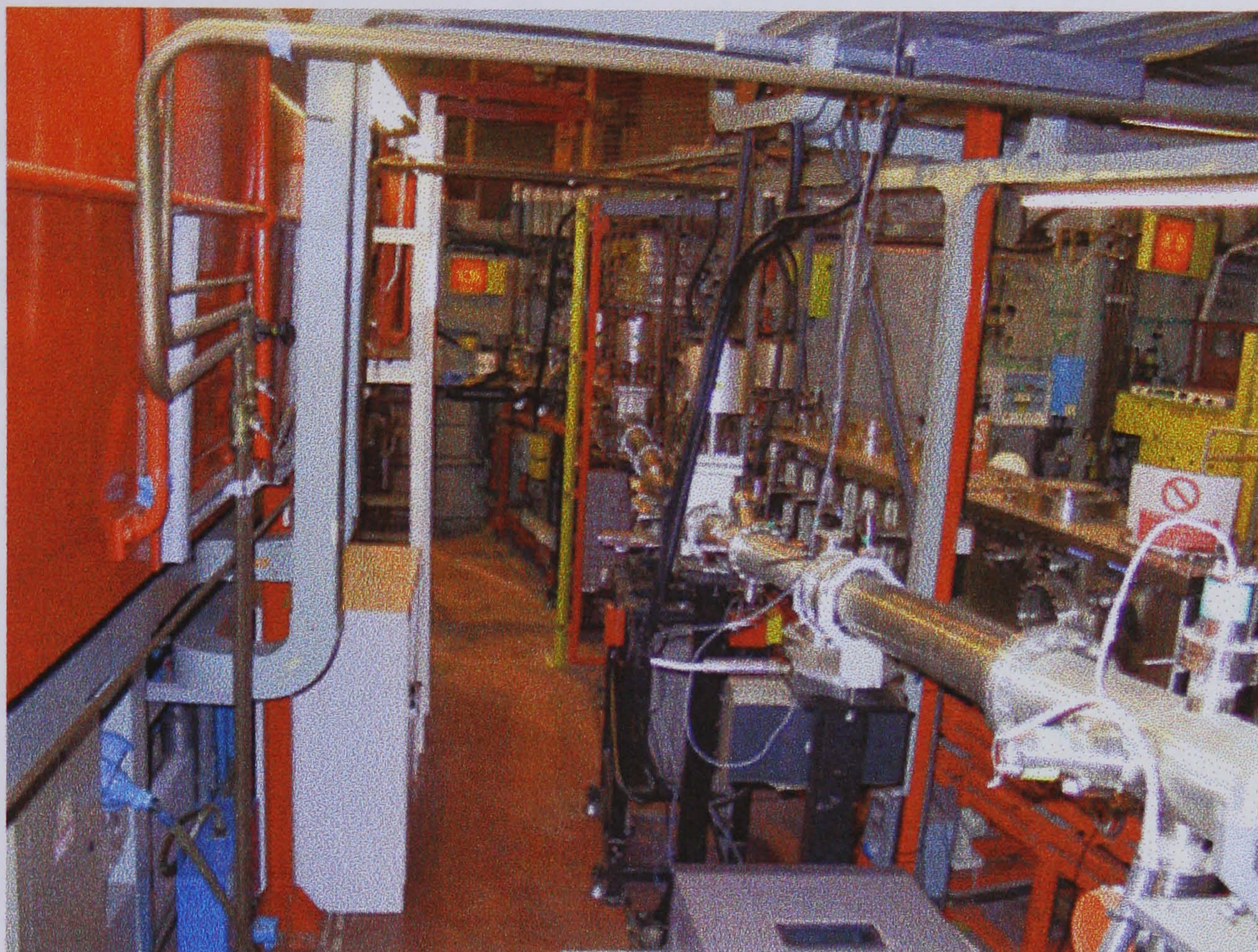


Fig. 2. 4 A glance at beamline 4.1, Daresbury

2.2.1 Station 4.1 in Daresbury Lab

Station 4.1 comprises of a UHV beamline (see Fig. 2.4) with a spherical grating monochromator and associated control and data acquisition systems. The photon energy range covered is 14-170 eV, using three interchangeable diffraction gratings. The surface science end station is equipped with a Scienta SES200 hemispherical electron energy analyser. An Omicron LEED/Auger system is also available on this system, as well as sample cleaning and gas dosing facilities. A Helium lamp and X-ray Source may also be available. The samples can be mounted on a motorised VG Omniax manipulator with azimuthal rotation, liquid nitrogen cooling and electron-beam heating.

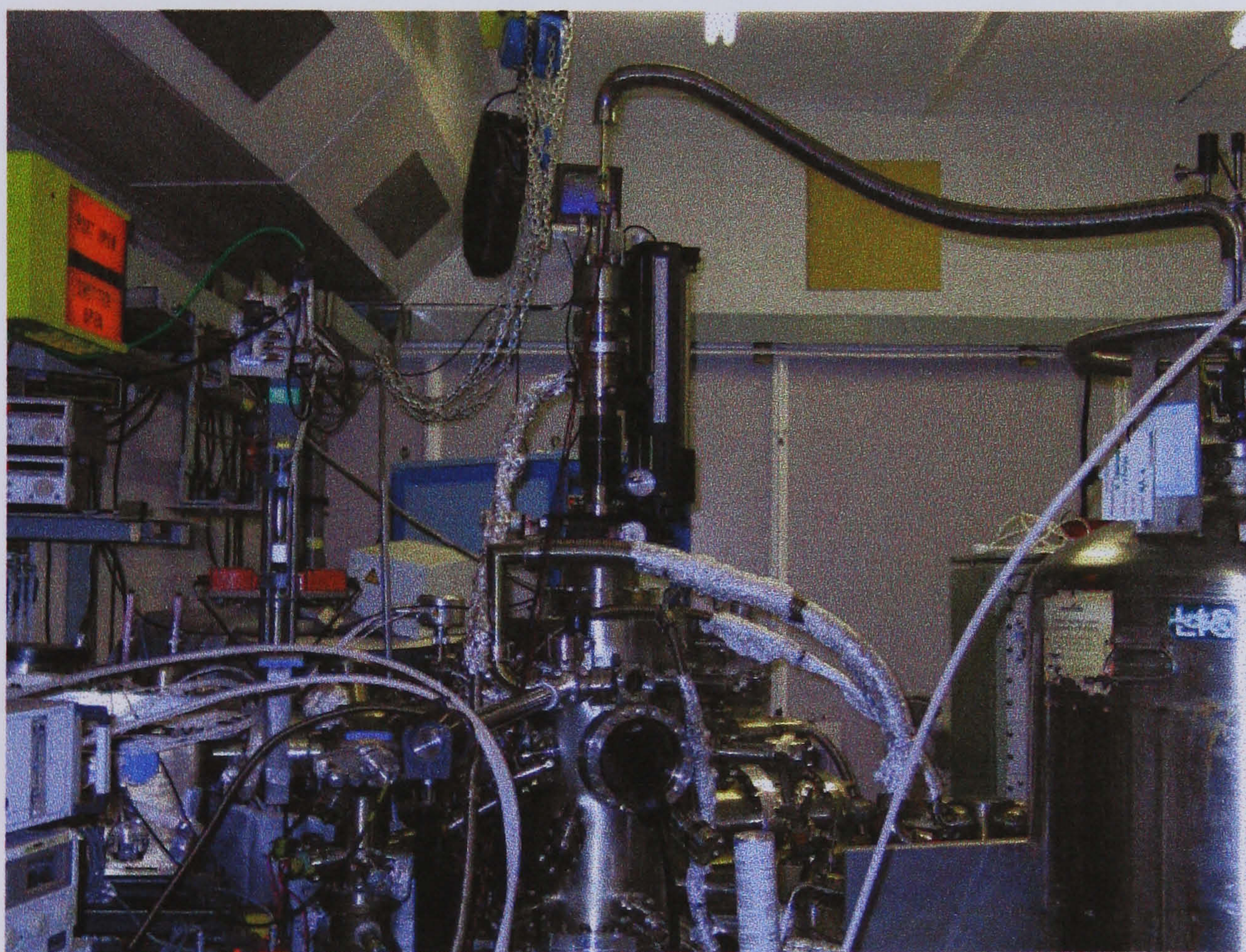


Fig. 2. 5 UHV system equipped with liquid helium cooling system

The SES200 hemispherical electron energy analyser is a full hemisphere with a mean radius of 200 mm; the spectrometer incorporates highly stable voltage supplies and

is equipped with a multidetection system. The magnetic field in the analyser is kept at a safe, low level by the use of double 3 mm μ -metal shields surrounding the whole electron-optical system with tight connections between different parts [2]. Fig. 2.6 is the photograph of the electron spectrometer.

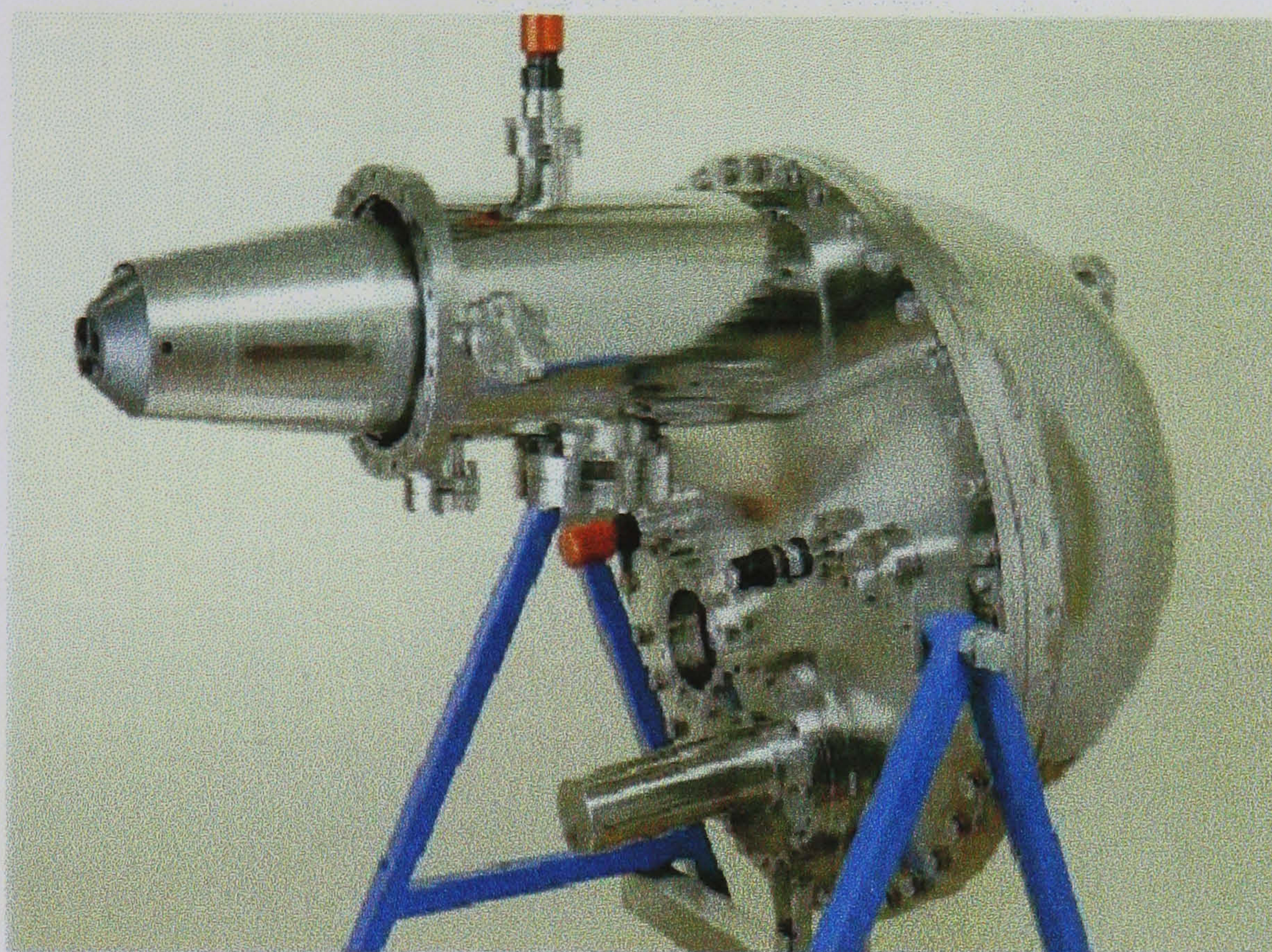


Fig. 2. 6 Photograph of the electron spectrometer

The electron lens can be operated in different modes, optimizing transmission, spatial resolution or angle resolution. The pass energy of the analyser can be chosen between 1 and 1000 eV. The lens voltages are continuously varied during the recording of a spectrum. In principle, the related retarding energy equals the difference between kinetic energy (E_K) of excited electron and the pass energy (E_P) of the analyser, i.e.

$$\text{Ret.} = E_K - E_P \quad (2. 5)$$

The voltages are defined by a set of tables, which for each pass energy give the correct voltages for a moderate number of initial energies (kinetic energies before the lens), and the appropriate voltages for intermediate initial energies are calculated by a

cubic spline interpolation [2]. Fig. 2.7 is the schematic electron optical system of the electron spectrometer [3].

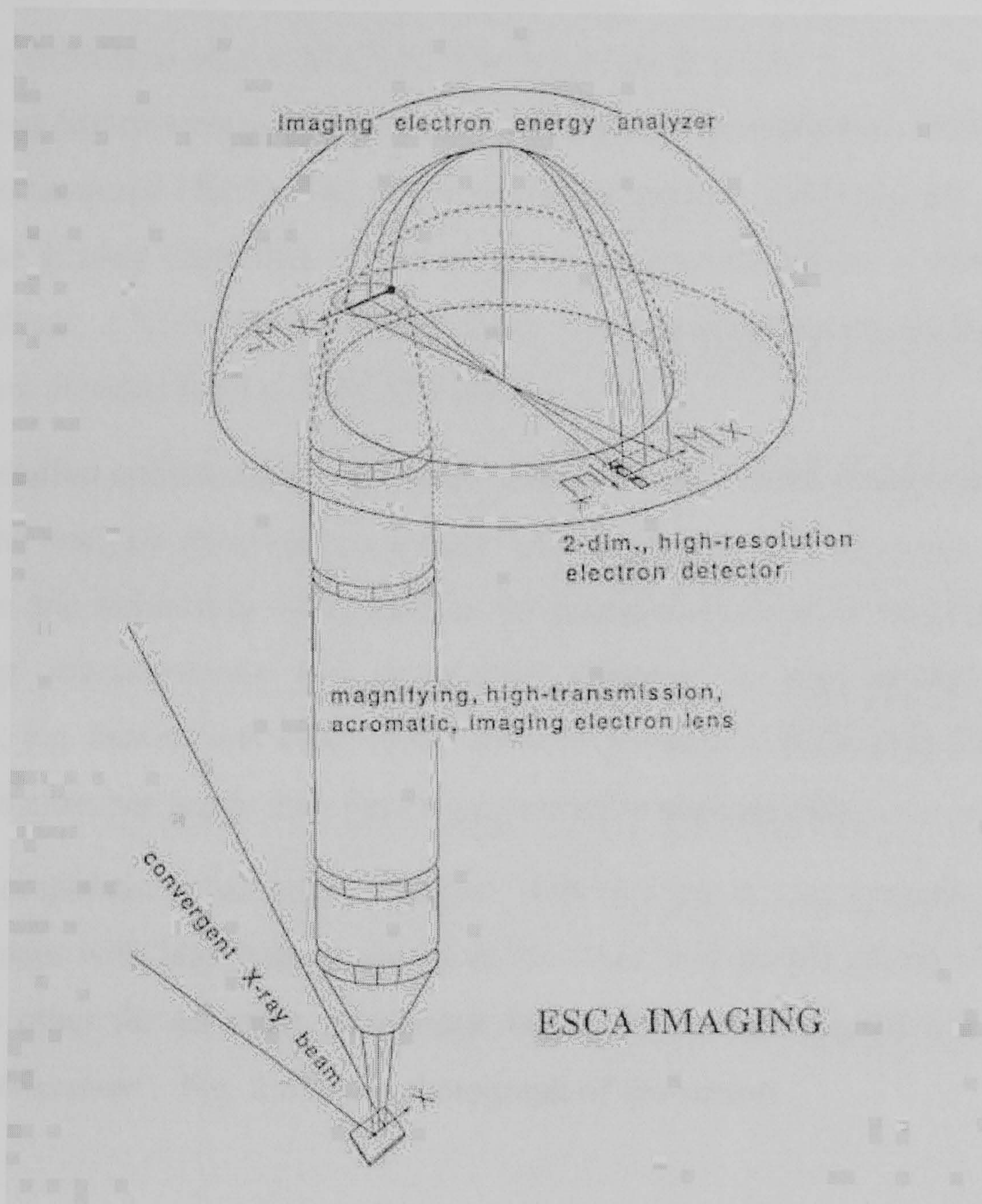


Fig. 2. 7 Electron optical system of the electron spectrometer consists of a hemispherical analyser with a Herzog-plate termination and an accelerating-retarding multielement electrostatic lens [3]

2.2.2 Beamline I511 in MAX Lab

Beamline I511 is an undulator based VUV, soft X-ray beamline at the 3rd generation synchrotron source MAX-II. The beamline is aimed at high resolution X-ray Photoemission Spectroscopy (XPS), X-ray Absorption Spectroscopy (XAS) and X-ray emission spectroscopy (XES). The effective energy range is 100-1100 eV, using a Zeiss SX700 plane grating high flux monochromator. It also comprises a Scienta SES-200 electron analyser, a XES-300 spherical grating X-ray emission spectrometer, and a MCP based electron detector for e.g. NEXAFS studies.

The station consists of a preparation chamber with various options and an analysis chamber. The analysis chamber is a strictly UHV system due to its direct connection to the beamline and refocusing optics (and as the preparation chamber must be open to the main during measurements the preparation chamber is also strictly UHV). All preparations, e.g. heating and evaporation are to be performed in the preparation chamber - the analysis chamber is just that, for the purpose of measuring only.

The preparation chamber is equipped with two gas dosing systems; one for non-toxic substances with high vapour pressures (i.e. inert and simple gases) called the "*gas system*", the other for all other substances, but mainly water, liquids and hydrocarbon gases "*liquids system*". Fig. 2.8 is the photograph of the station.

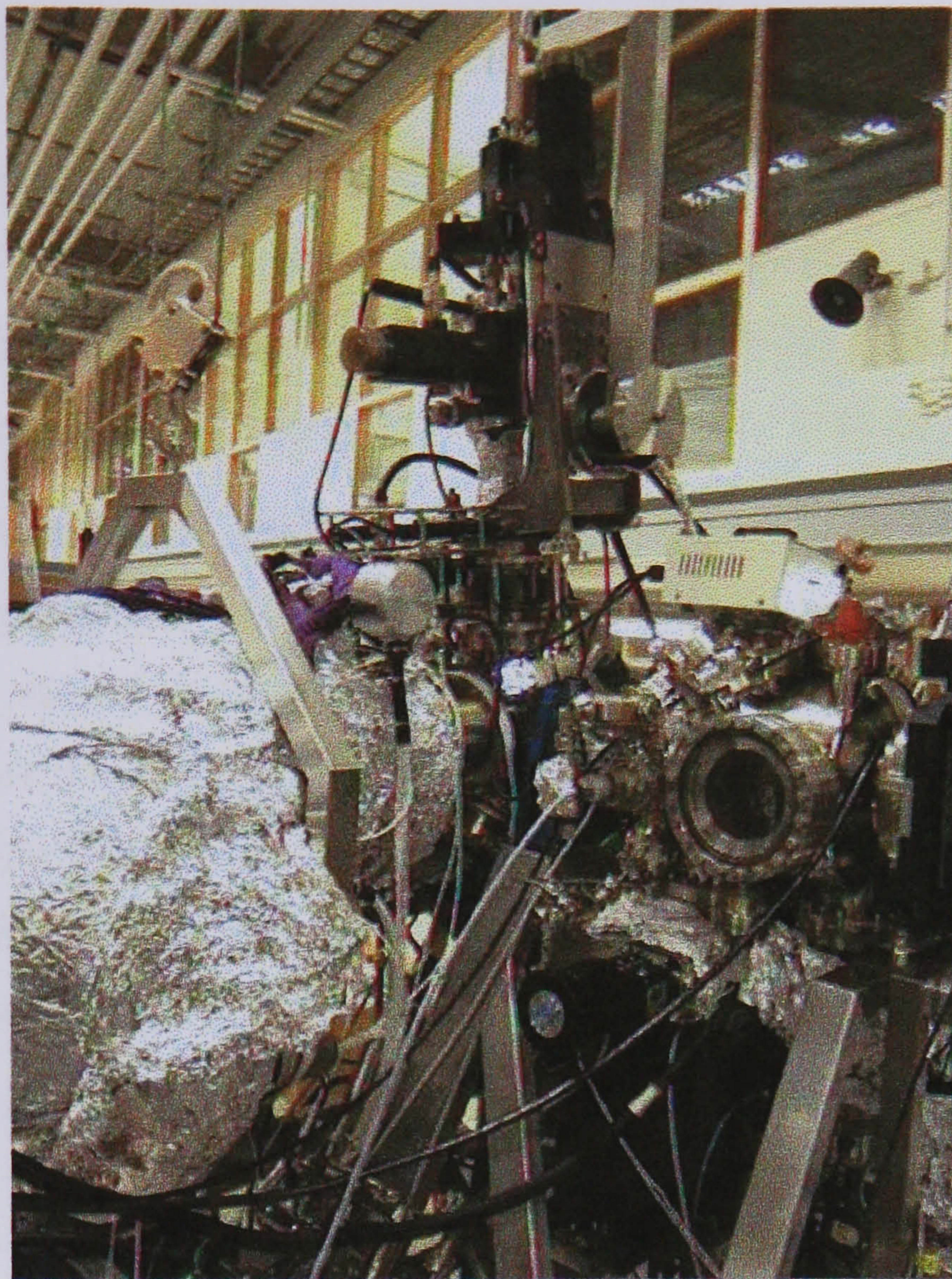


Fig. 2. 8 Station I511, Max-Lab

2.3 Photoemission spectroscopy acquirement

X-ray photoelectron spectroscopy (XPS) for core level, ultraviolet photoemission spectroscopy (UPS) for valence band and synchrotron radiation photoemission spectra (SREPS), NEXAFS were acquired with a SCIENTA SES-200 analyser using beam line 4.1 of the synchrotron radiation source (SRS) Daresbury and I511 in Maxlab.

For the photoemission study of chemisorption of C_{60} on InP (100), the spectra were acquired using $MgK\alpha$ X-rays for core levels $C1s$, $P2p$; and a helium discharge lamp for core level $In4d$, valence band and Fermi edge. The experiment resolution was 0.85 eV for XPS and 0.09 eV for UPS respectively [4]. Fig. 2.9 gives an example of Fermi edge spectrum from which the resolution information can be obtained. The overall resolution can be defined as the distance between the two points in the energy axis corresponding to the 10% and 90% height of Fermi edge spectrum respectively. For example, $\Delta \sim 0.09$ eV is the resolution in Fig. 2.9.

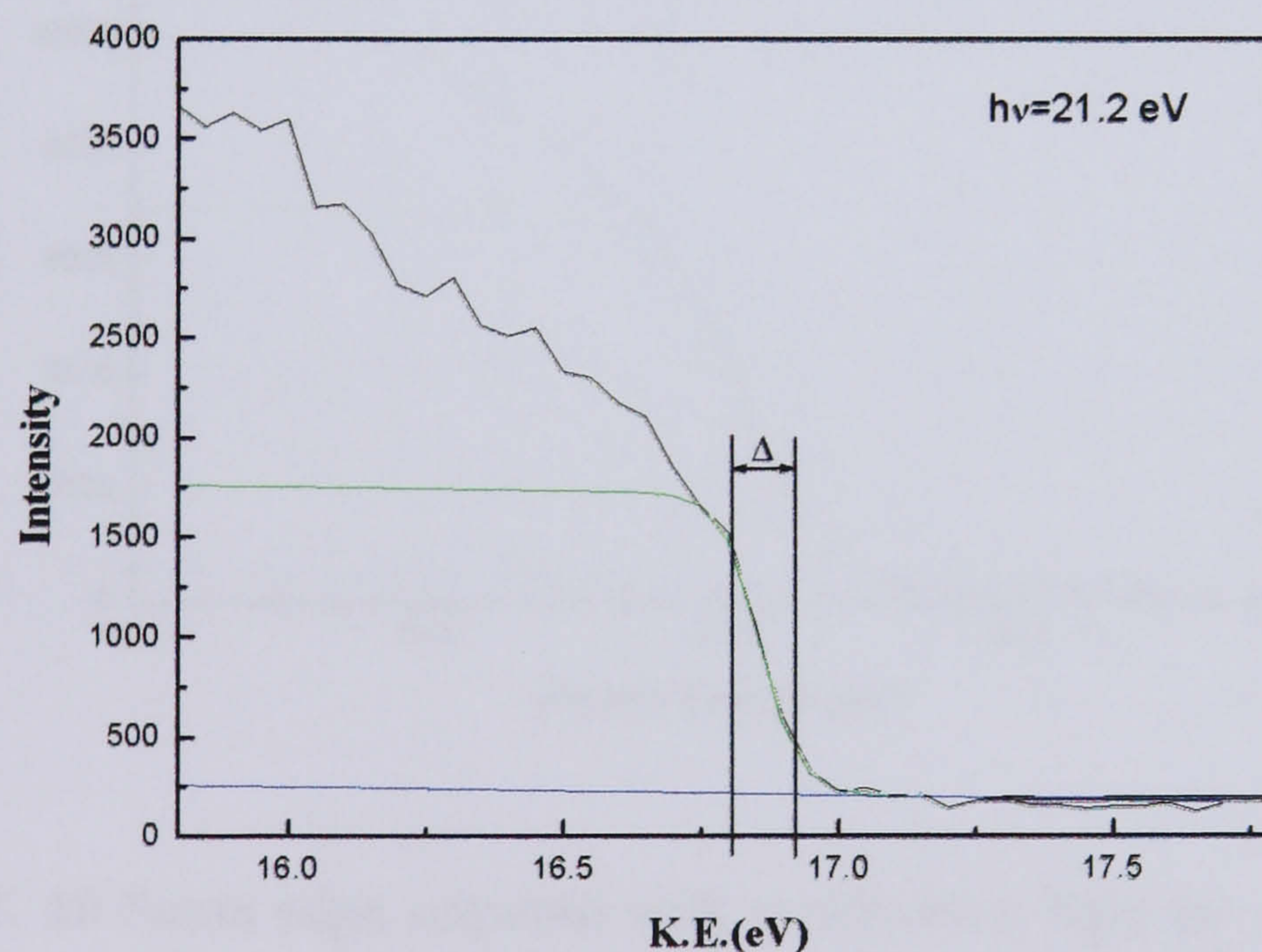


Fig. 2. 9 Fermi edge acquired with He-I UV light 21.2 eV and fitting with Fermi-Dirac additive and linear background, from which the experiment resolution can be obtained, about 0.09 eV.

For the photoemission study of indium clusters on InP (100) – (2 × 4) surface, all In4*d* spectra acquired with synchrotron radiation were obtained with 50 eV photon energy. All spectra were acquired in normal emission with the synchrotron light incident at 60 degrees to the normal. The overall resolution of spectra acquired using synchrotron radiation is estimated at ~ 0.3 eV, using the Fermi edge of the metallic clusters. In addition we acquired spectra with He II radiation from a discharge lamp where the overall resolution was improved to ~ 0.09 eV [5]. Spectra acquired at this improved resolution were used to determine initial fitting parameters such as number of surface components, their energy position and the position and width of the bulk In4*d* component. Fig. 2.10 gives an example Fermi edge acquired with synchrotron light photon energy 50 eV, from which the experiment resolution information can be obtained.

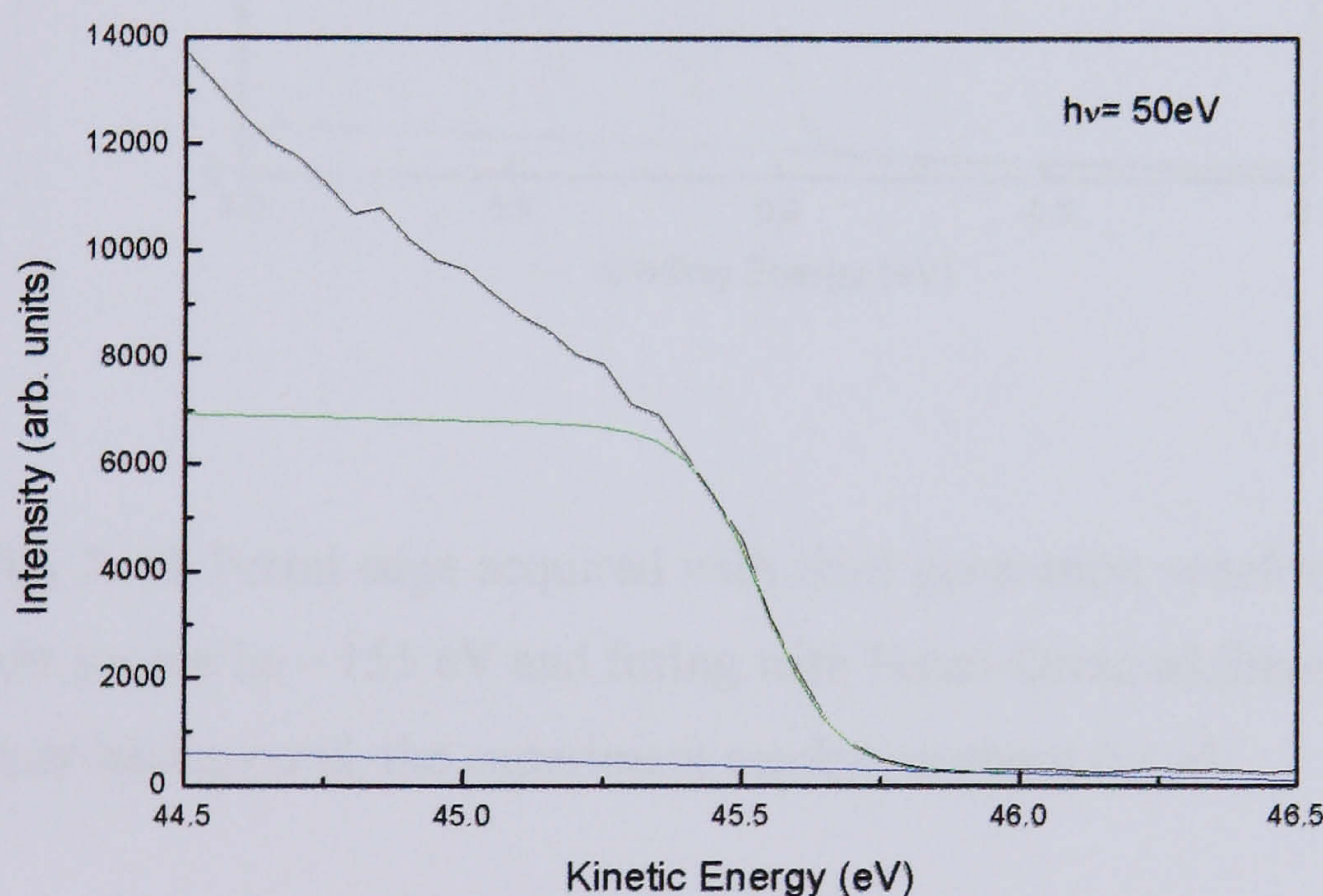


Fig. 2. 10 Fermi edge acquired with synchrotron light $h\nu = 50$ eV and fitting with Fermi-Dirac additive and linear background, from which the experiment resolution can be obtained, which is about 0.3 eV.

For luminescent alkylated silicon quantum dots, core level Si2*p* spectra acquired with synchrotron radiation were obtained with photon energy 145 eV or 155 eV. Core

level *C1s*, *O1s* were obtained with 633 eV. Valence band spectra were obtained with 145 eV. Some of them were got in I511 Maxlab, which is higher resolution third generation synchrotron source. Experimental resolution was about 0.1 eV (see Fig. 2.11 below).

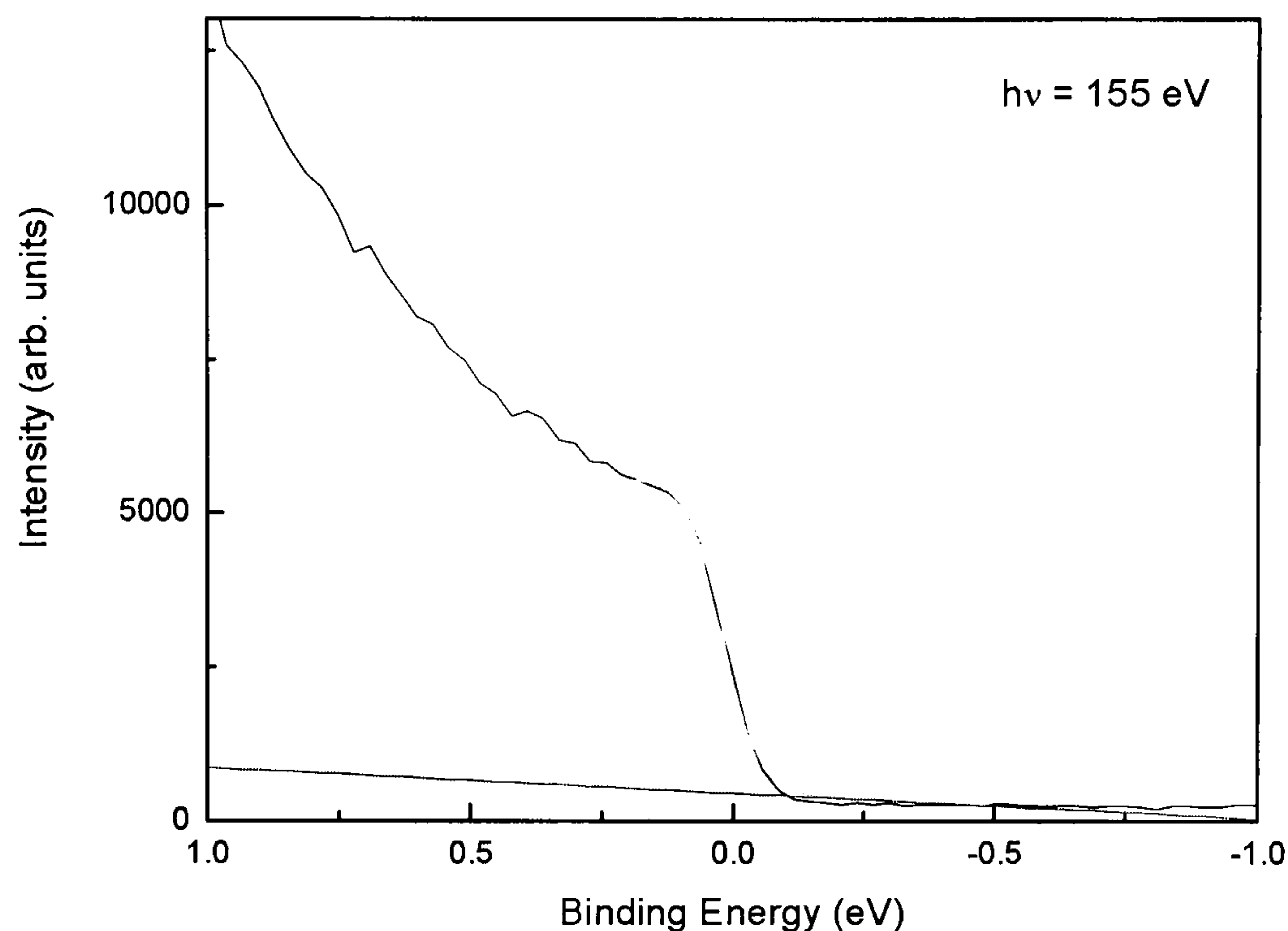


Fig. 2. 11 Fermi edge acquired with third generation synchrotron light source $h\nu = 155$ eV and fitting with Fermi-Dirac additive and linear background, the experiment resolution about 0.1 eV

2.3.1 Geometry of the measurements

Fig. 2.12 shows the schematic drawing of photoemission experimental geometry. The manipulator mounted on the chamber can adjust the parameters: θ , Φ and so on. For example, if we need to acquire spectra in the normal emission direction, the sample should be adjusted to face analyzer, i.e. $\theta=0$. At station 4.1, Daresbury, the angle between analyser and beamline is 60° , thus the sample should be rotated to $\theta_{hv}=60^\circ$.

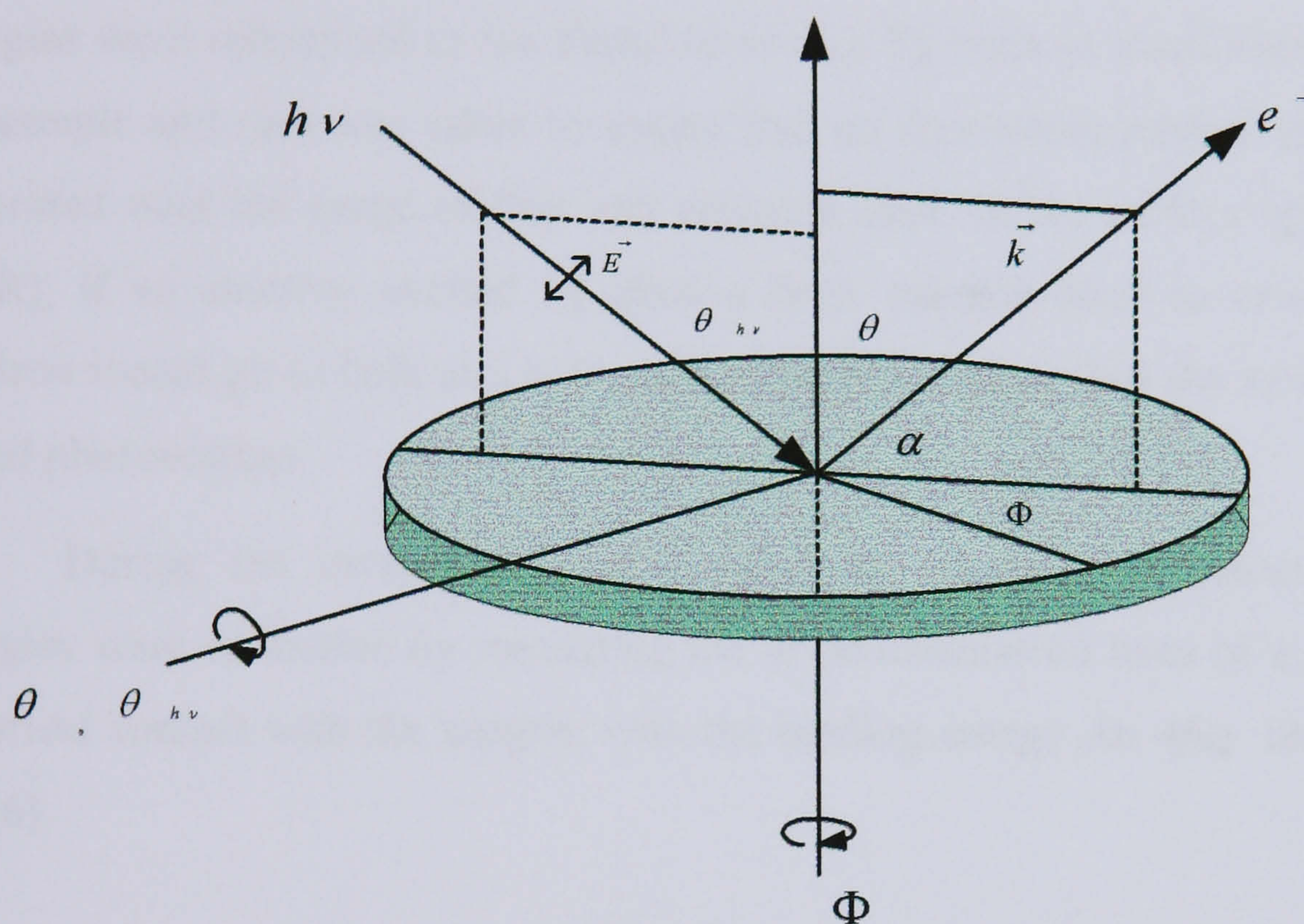


Fig. 2. 12 Schematic drawing of the photoemission experimental geometry

2.3.2 Binding Energy Calibrations

During the investigation of chemisorption of C_{60} on InP (100), binding energies for UPS spectra were referenced to the Fermi level of a Ta plate at the base of, and in electrical contact with, the sample holder. XPS binding energies were calibrated using the bulk In4*d* line employing the binding energy value obtained from the corresponding HeII spectrum.

During the investigation of surface- and cluster-related In4*d* lines, binding energies were referenced to the Fermi level of a Ta plate in good electrical contact with the sample and care was taken to ensure that no observable surface photovoltages were generated over the range of flux and energies used. In the surface space-charge region (SCR), if an electron excited by photon from valence band to conduction band, the electron would go to bulk and hole goes to surface region, thus the established voltage is called photovoltage.

During the investigation of luminescent alkylated-Si quantum dots, binding energies were calibrated by measuring the 4*f* photoemission lines of a gold foil in direct electrical contact with the sample, with the binding energy Au 4*f*_{7/2} line defined as 84.0 eV [6].

2.4 Sample Preparation

2.4.1 InP (100) Surface Treatment

The InP (100) samples were cut from polished *n*-type InP (100) wafers (S-doped with $n = 2 \times 10^{17}$, wafer thickness 400 μm ; the reported resistivity was $1.5 \times 10^{-2} \Omega \text{ cm}$; purchased from Wafer Technology Ltd). The samples were cleaned by a chemical etching treatment using a sulphuric acid and hydrogen peroxide solution (H_2SO_4 : H_2O_2 : H_2O (3:1:1)) for 10 min at 60°C [7, 8]. They were then rinsed with deionised (DI) water and dipped in an $(\text{NH}_4)_2\text{S}_x$ solution for 20 min at 65°C to avoid oxide formation. Subsequently, they were again rinsed in running DI water and then rapidly introduced into an ultrahigh vacuum (UHV) chamber at a pressure below 5×10^{-10} mbar. An In-terminated InP (100)-(2 \times 4) reconstruction [7-9] was prepared by performing several cycles of sputtering (Ar^+ ions, 0.5 keV beam energy, 1 μA sample current) and annealing, until no impurities could be detected by photoemission, and sharp low-energy electron diffraction (LEED) patterns characteristic of the clean surface were observed [7, 8].

2.4.2 Si-Quantum Dots

The Si-quantum dots (Si-QDs) were prepared in the lab of Dr Ben Horrocks. This electrochemical method was developed by his group in The University of Newcastle upon Tyne [10].

Photoluminescent porous silicon layers were formed by galvanostatic anodization of boron-doped p-Si (100) oriented wafer ($10\ \Omega\cdot\text{cm}$ resistivity, Compart Technology, Peterborough, UK) in a 1:1 v/v solution of 48% aqueous HF and ethanol solution. The electrochemical cell was machined from PTEE and circular in cross-section (1 cm diameter). The silicon wafer was sealed to the base using a VitonTM O-ring. The counter electrode was a piece of tungsten wire coiled into a loop to improve the uniformity of the current distribution and the etching was carried out using a constant current source made in-house. See Fig.2.13. A layer of luminescent porous silicon was made at high current density (30 min at $480\text{--}560\ \text{mA}\cdot\text{cm}^{-2}$) and cleaved from the surface by a subsequent “electropolishing” treatment (1 min, $800\ \text{mA}\cdot\text{cm}^{-2}$). The solution was decanted and the fluorescing silicon powder was dried under the vacuum of a rotary pump. The dry, hydrogen-terminated silicon powder was then transferred into a Schlenk flask on a grease-free vacuum line (employing Young’s taps) and refluxed overnight in a dry toluene solution (Merck, distilled over Na) containing 1 M of the alkene (1-hexene, 1-octene, 1-undecene or 1,9-decadiene, Merck) or dimethoxytrityl-protected undecenol (prepared by reaction of undecenol with dimethoxytrityl chloride according to standard procedures [11, 12]). Dimethoxytrityl is abbreviated as DMT throughout the text. Undissolved silicon particles were filtered off before all solvent and unreacted alkene was removed under reduced pressure with a rotary pump. Fig. 2.14 illustrates the process of Si-QD synthesis. Just prior to introduction to the main vacuum chamber, the quantum dots powder was redissolved by stirring in dichloromethane and a few drops were put onto the substrate (graphite, metal), then rapidly introduced into an ultrahigh vacuum (UHV) chamber at a pressure below 5×10^{-10} mbar. We made attempt to measure HRTEM of this material and although we could not get the exact size we can certainly say that they are smaller than 6 nm, in particular we found very difficult to disperse them

probably due to very small size [13]. The estimated size of Q-dot is about 2.4 nm from the very recent STM and AFM results [14], see Chapter 5.

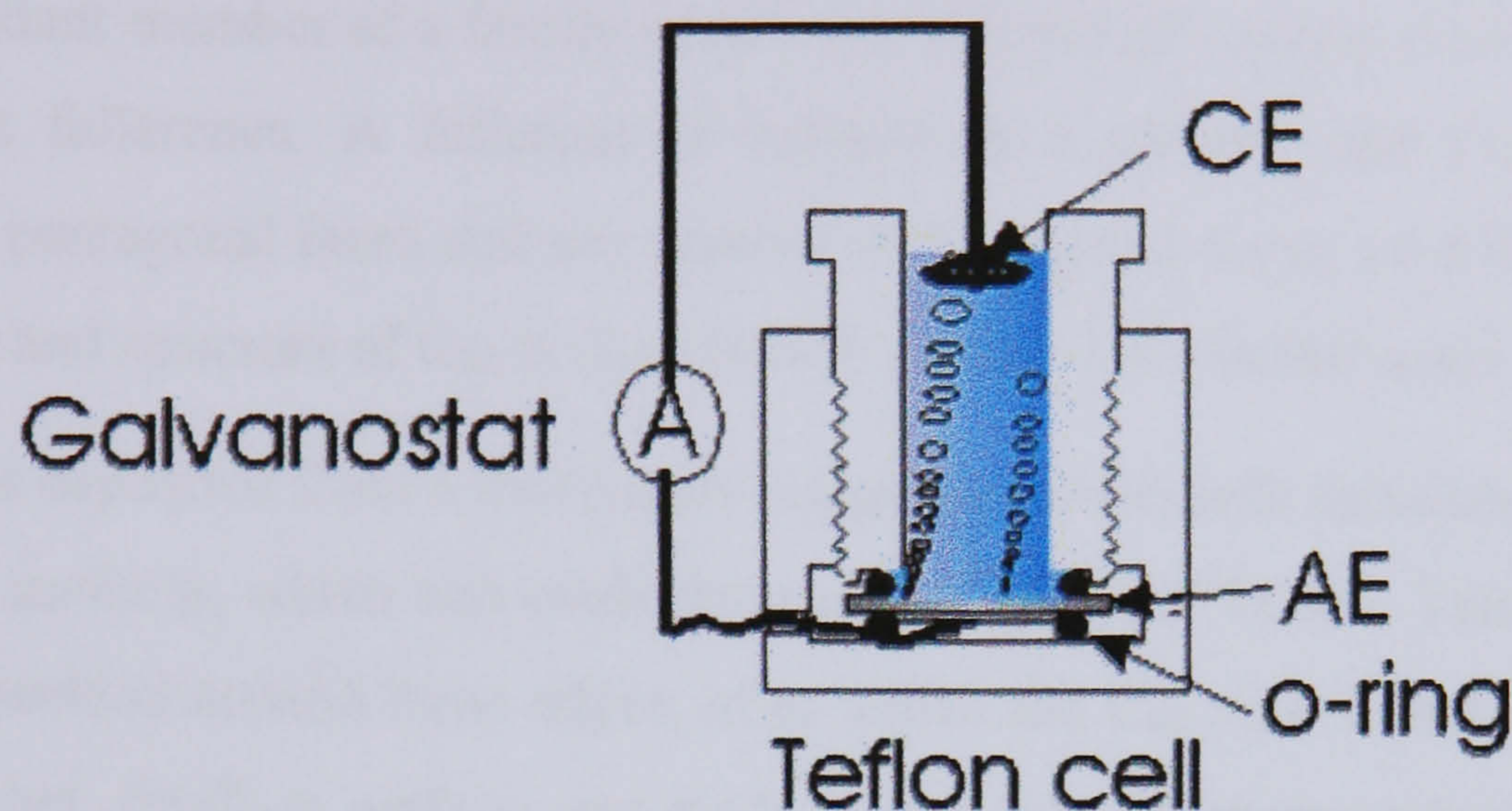


Fig. 2. 13 Schematic of electrochemical etching cell

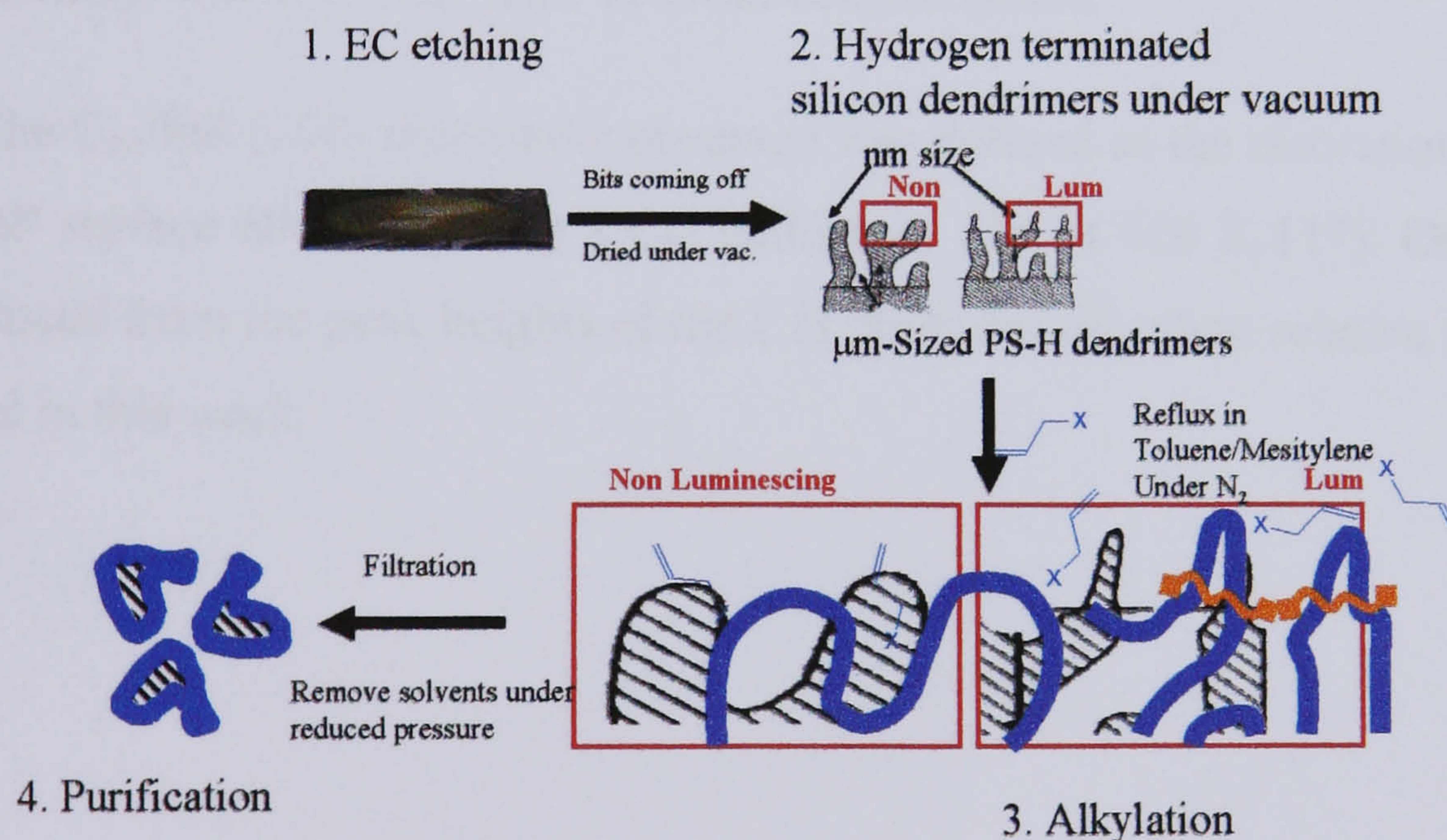


Fig. 2. 14 Synthesis of Si-QD: 1) electrochemical etching; 2) hydrogen terminated silicon bits dried under vacuum; 3) alkylation; 4) purification

2.5 C₆₀ Evaporation and Coverage Calibrations

C₆₀, or “Buckminsterfullerene” after the famous architect Buckminster Fuller, is the most abundant member of a family of recently discovered carbon molecules [15, 16], referred to as fullerenes. A fullerene is defined as a closed cage carbon molecule containing 12 pentagonal faces and any number of hexagonal faces, of which C₆₀ has 20. The discovery and structure of C₆₀ is discussed in section 1.5.3 in this work.

C₆₀ was deposited from a thoroughly outgassed home-built tantalum Knudsen cell onto the clean surfaces, which was made from a small sheet of Ta foil. This was folded in two and spot-welded around three edges, after which the C₆₀ was inserted and the forth edge spot-welded; finally a pinhole was made in one side. A thermocouple is also spot-welded directly onto the Knudsen cell, so that temperature can be monitored. The evaporations were made at temperature 690K, but Fullerene deposition was carried out with the sample at room temperature (RT). During C₆₀ sublimation, the chamber pressure was maintained below 3×10^{-9} Torr to avoid contamination.

The C₆₀/InP (100) monolayer coverage was defined as the saturation coverage left on the InP surface after annealing a C₆₀ multilayer film at 600 K [17]. Other coverages were deduced from the peak heights of the C1s photoemission line relative to those of the In3d level in this work.

2.6 Temperature Measurements

Sample temperatures were measured by a K-type thermocouple, (Nickel - Chromium & Nickel – Aluminium, measured temperature range from -200 °C to 1250 °C) in close proximity to the sample holder, using slow heating and cooling to ensure proper temperature equilibration. This measurement applied both in Daresbury and Max-lab. For example, Fig. 2.15 shows the two thermocouples attached to the sample holder which we used in I511, Max-lab.

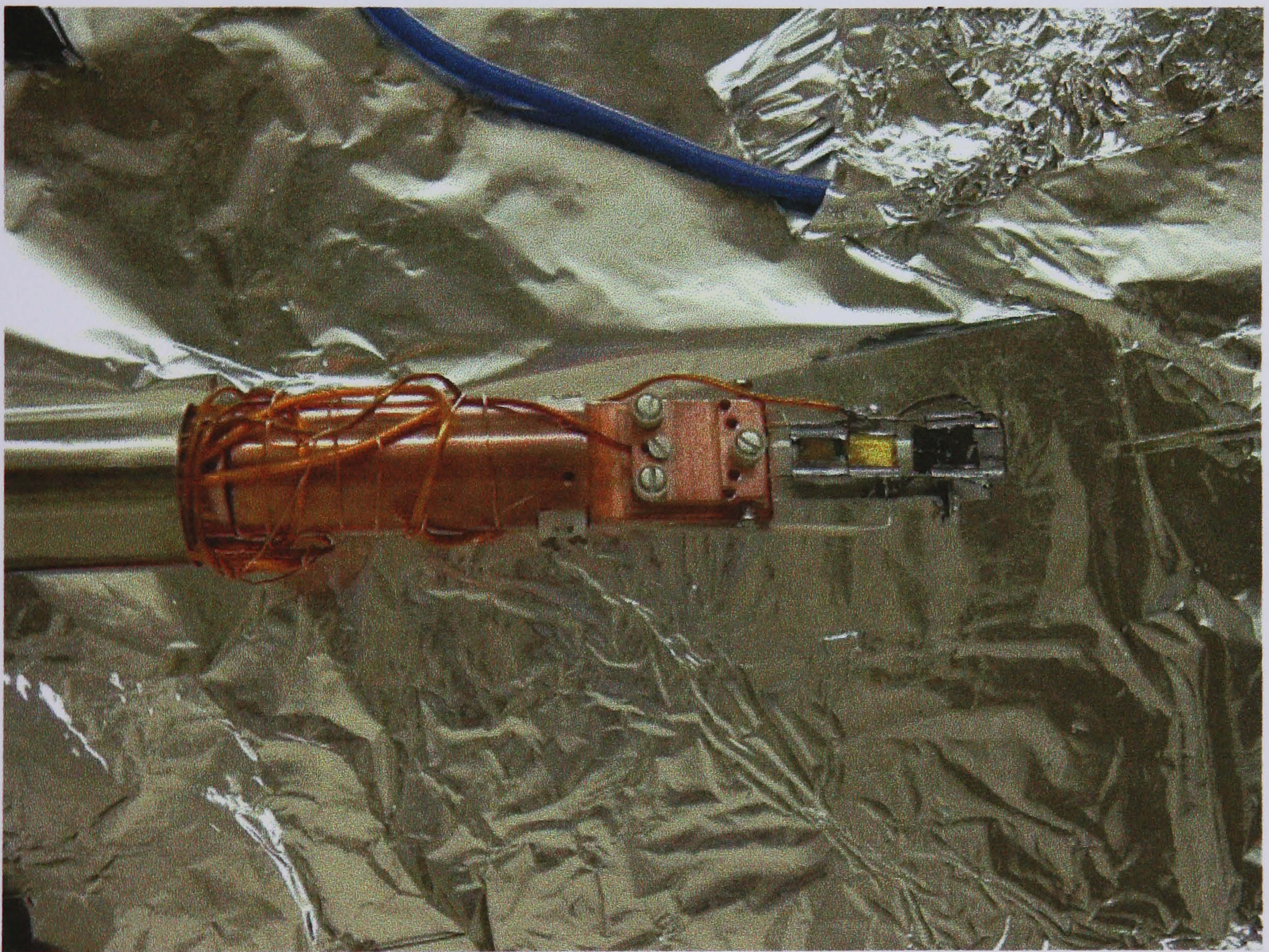


Fig. 2. 15 The sample holder with two attached K-type thermocouple which we used in I511, Max-lab

2.7 Photoluminescence Spectroscopy

Photoluminescence spectra were acquired by SPEX 1681B 0.22m Spectrometer and KEITHLEY-617 Programmable Electrometer controlled by a self-written HP-VEE programme, with a Model H957 photomultiplier module (Built-in PMT R928), manufactured by Hamamatsu. The overview of the experiment arrangement is given in Fig. 2.16. One IEEE488.2 Interface Board, Model KPCI-488 has been plugged in the computer.

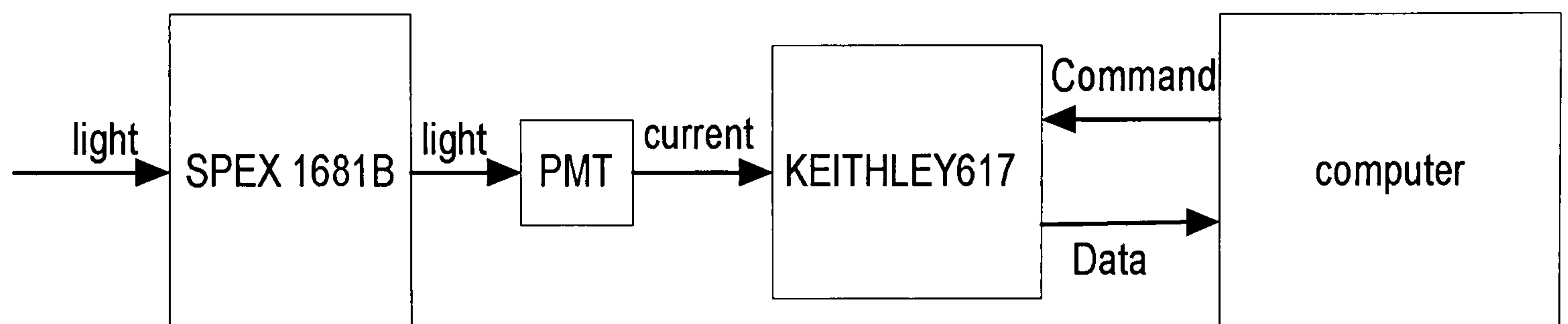


Fig. 2. 16 Overview of experiment arrangement for photoluminescence spectroscopy

2.7.1 Photon Spectrometer and Photomultiplier Tubes

SPEX 1681B 0.22m spectrometer is a compact, general- purpose spectrometer that can deliver radiation in the region between 185 and 1000 nm without sacrificing throughput. As shown in the optical diagram (Fig. 2.17), incoming light focused onto the entrance slit is directed by a 45 ° mirror (M1) to collimating mirror (M2). From here, light is dispersed by the grating (G) onto mirror M3. Since the grating sorts light according to wavelength depending on the grating angle, only a narrow, specific band of light will be directed out the exit slit by the last mirror (M4). The narrowness of that bandpass is determined by the slit width. The specification resolution is 0.25 nm at 546 nm with 50 μm slits and 1200gr/mm grating. In our case, in order to obtain the maximum intensity of the photoluminescence light, the both slits were set to 8 mm, thus the overall bandpass was about 26 nm.

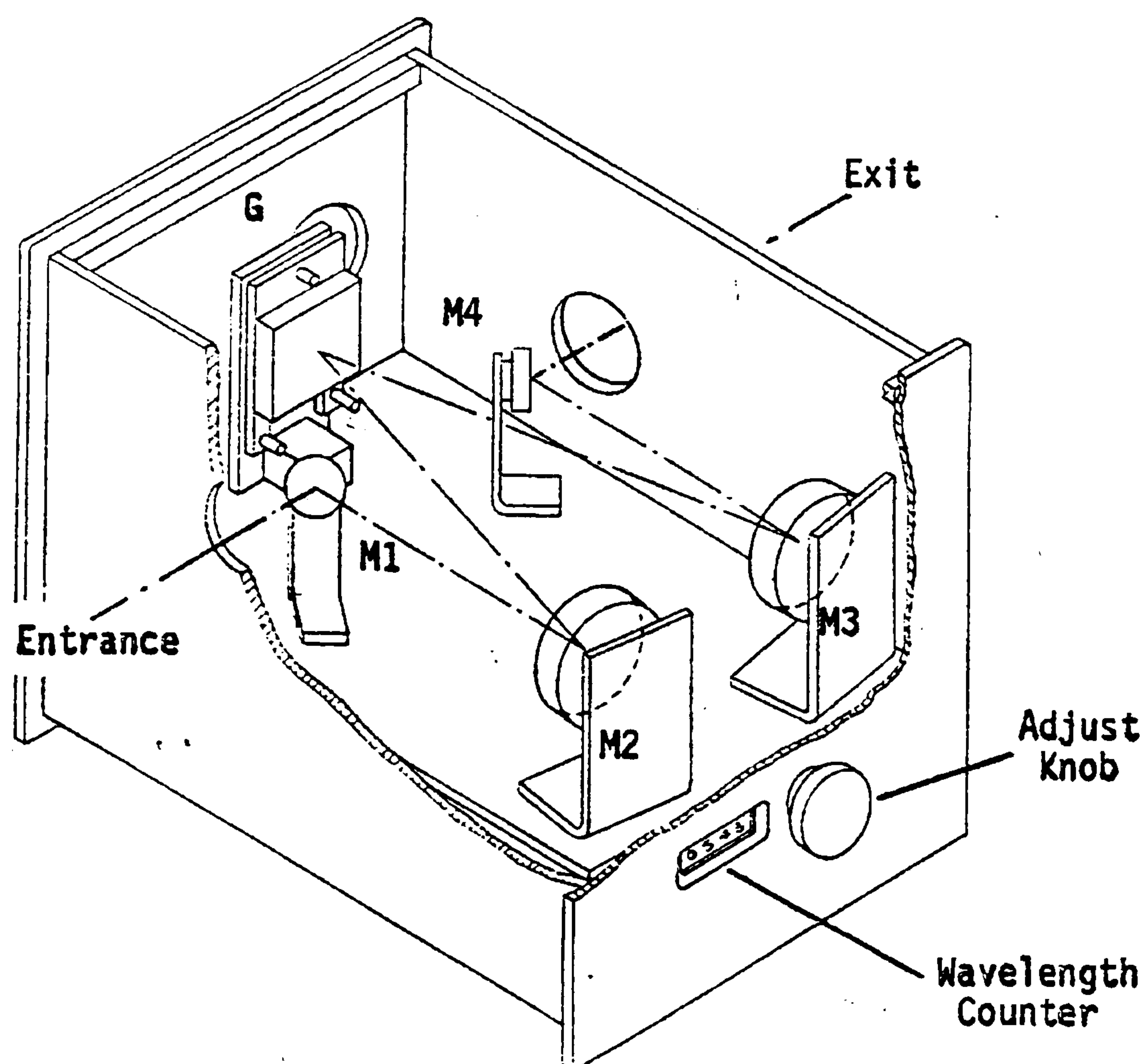


Fig. 2. 17 Optical diagram of SPEX-1681B spectrometer

Photomultiplier tube is the most important component in this experiment, whose photocathode response characteristics affects the quality of final photoluminescence spectroscopy. Fortunately, we got Model R943-02 photomultiplier tube manufactured by Hamamats, which is a flat line of photocathode radiant sensitivity with wavelength in a wide range between 300 and 800 nm, see Fig. 2.18. The dark current is less than 0.1 pA from our experiments.

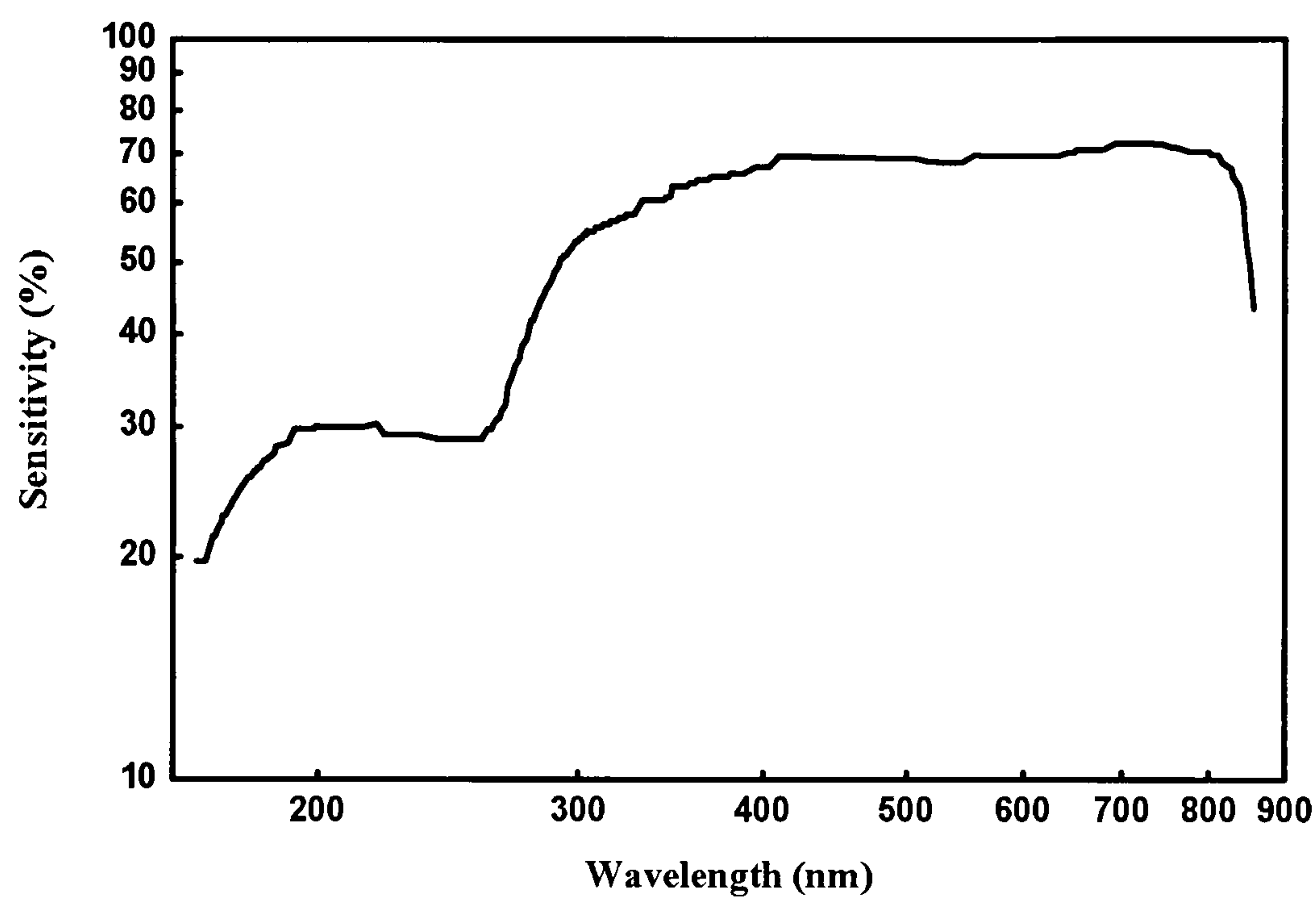


Fig. 2. 18 characteristic of the Photomultiplier tube

2.7.2 KEITHLEY Programmable Electrometer and HP VEE Control Programme

The Keithley Model 617 Programmable Electrometer is a highly sensitive instrument designed to measure voltage, current, charge, and resistance. Here I used it to measure current from photomultiplier tube. With a Model KPCI-488 interface board, the communication between the electrometer and computer is controlled by a Hewlett – Packard Visual Engineering Environment (HP VEE) programme which I wrote for the purpose.

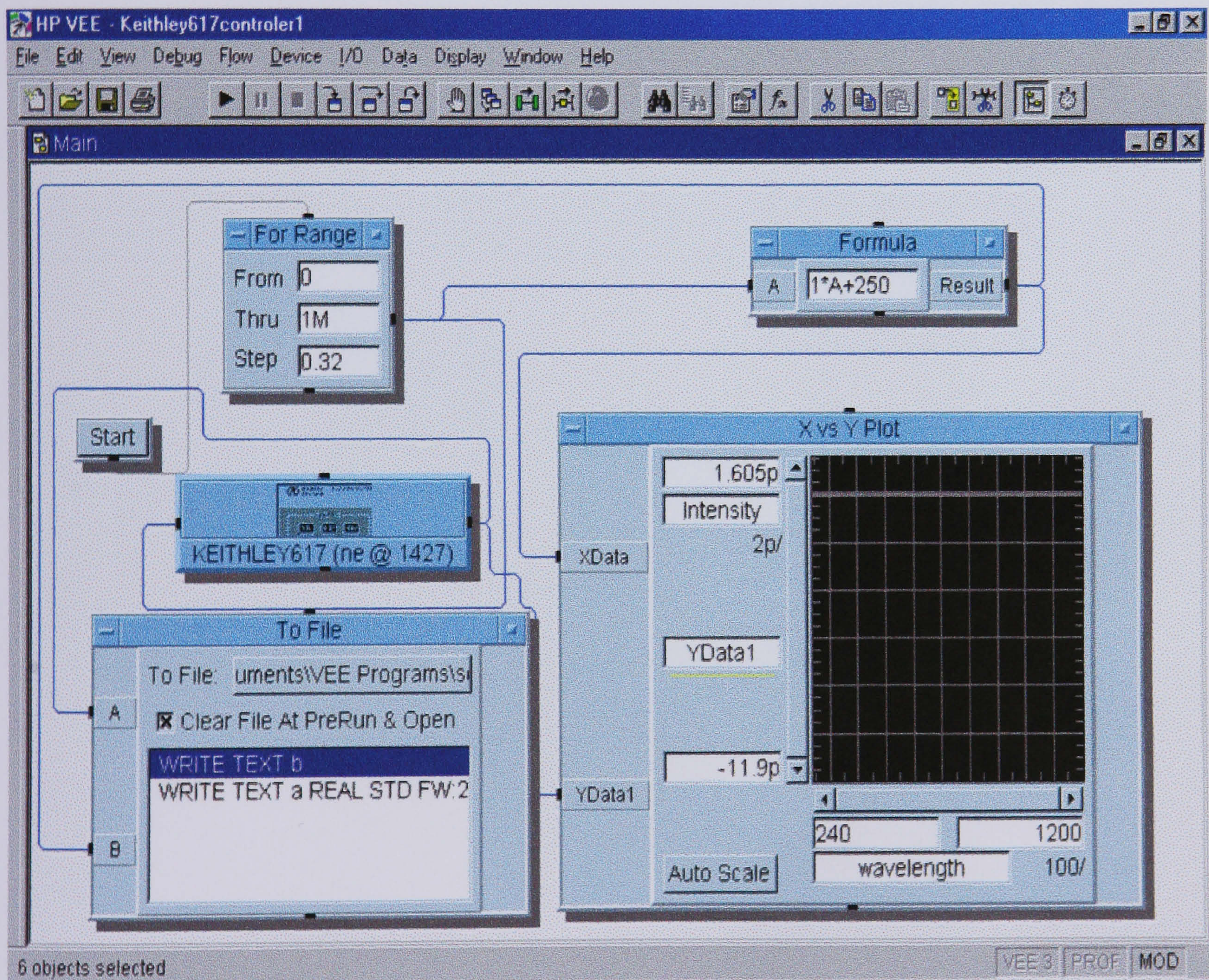


Fig. 2. 19 HP VEE programme for the control and data acquisition of Keithley

HP VEE is a visual programming language that produces dramatic reductions in test development time. Programs are constructed by connecting icons together on the screen [18]. The resulting HP VEE programme – which resembles a block diagram – may be run like a programme in a textual language such as C or Visual Basic.

Fig. 2.19 is the aspect of my Keithley control and data acquisition programme. The photoluminescence spectrum can be displayed in real time during the experiment; meanwhile, the data also stored in a preset folder in ASCII format.

2.8 Description of Atomic Force Microscope

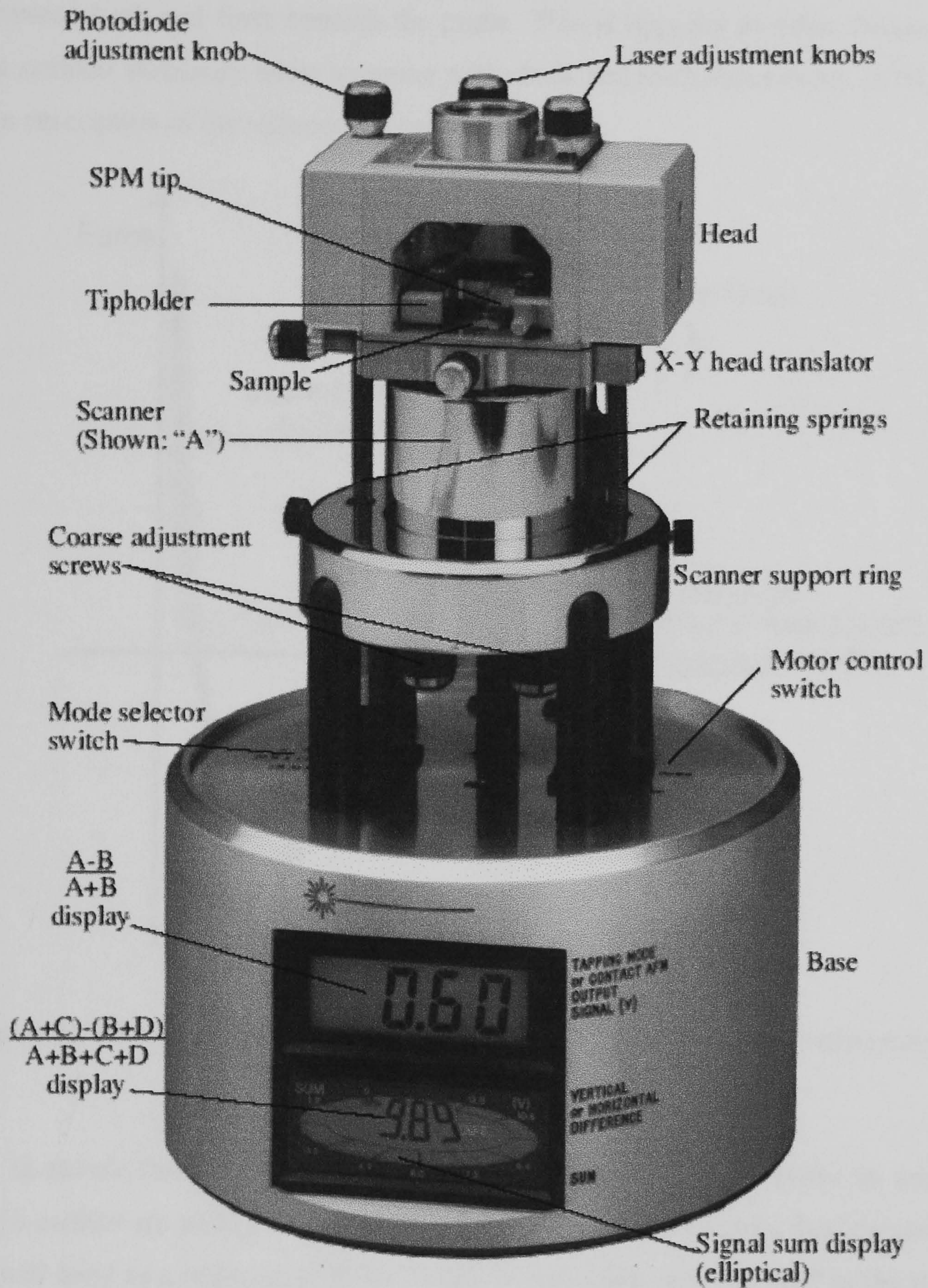


Fig. 2. 20 MultiModel SPM [19]

The MultiModel SPM has been used to study indium clusters and silicon quantum dots topography in this thesis. It is designed around a stationary probe. That is, samples are scanned back and forth beneath the probe. This is opposite to other designs, which mount samples stationary while scanning probe back and forth above them. In this section a basic description of the technique is presented

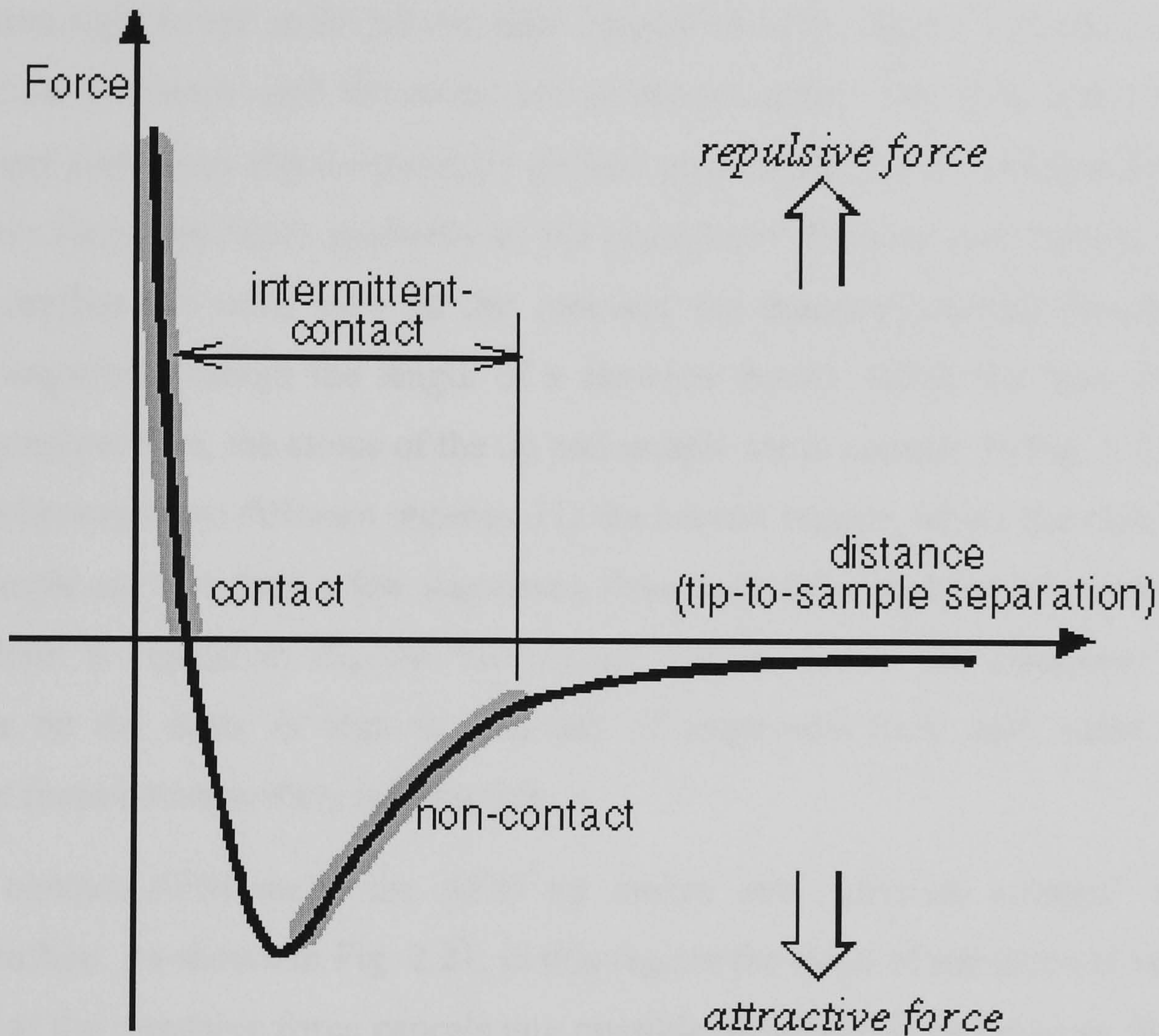


Fig. 2. 21 Variation of the Van der Waals force with the tip to sample distance [20]

In atomic force microscope, the forces between atoms in the probe tip and in the sample's surface are measured. The probe tip is located at the end of a flexible cantilever, which will bend as a response to these forces. A deflection sensor placed in the scanning head measure the bending of the cantilever. The scanner is a tube made of a piezoelectric material, which means that it will expand or contract with applied voltage and it can be used to move the probe with extremely fine precision in the x, y and z direction. In order to keep the cantilever deflection constant, the scanner must move the cantilever up or

down. Since the scanner motion therefore corresponds to the surface topography of the sample (convoluted with tip shape), it is used to generate an image of the sample surface.

Both attractive and repulsive contributions are associated with the forces on the cantilever [21]. Fig. 2.21 shows the variation of the force with the distance between the tip and the sample's surface. As the distance between the tip and the sample decreases (moving from right to left in the curve), their respective atoms begin to attract each other. This attraction increases until the atoms are so close together that their electron clouds begin to repel each other electro-statically (lowest point of the curve). From this point on, the repulsive forces increases gradually as the interatomic distance continues to decrease and force reaches the value zero. At this moment, the distance between the atoms is a couple of angstroms (about the length of a chemical bond). When the Van der Waals force becomes positive, the atoms of the tip and sample are in contact. In Fig. 2.21 we can distinguish between two different regimes: (1) the contact regime, where the cantilever tip and the sample are less than a few angstroms from each other and the interatomic force between them is repulsive; (2) the non-contact regime, where the cantilever and the sample are on the order of tens to hundreds of angstroms from each other and the interatomic force between them is attractive.

In contact AFM mode the AFM tip makes soft “physical contact” with the sample's surface. As shown in Fig. 2.21, in this regime the slope of the curve is very high, meaning that the repulsive force cancels any possible attractive force between the atoms. This means that when the cantilever pushes the AFM tip against the sample, it is the cantilever itself that bends rather than moving the tip atoms closer to the sample atoms.

In addition to the Van der Waals force, two other forces must be accounted for in contact AFM mode: i) a capillary force due to the thin water layer often found on the sample surface in an ambient environment; and ii) a force due to the cantilever itself. The capillary applies a strong attractive force ($\sim 10^{-8}$ N) that holds the tip in contact with the surface and its magnitude depends upon the distance between the tip and the sample [22]. However, this force should be constant as long as the tip and the sample are in contact due to the fact that it is not possible to reduce the distance between the tip and the sample.

The force applied by the cantilever is variable and depends upon the deflection of the cantilever and its spring constant.

In non-contact mode, an AFM tip is vibrated near the surface of the sample allowing imaging sample topography with little or no contact between the tip and the sample. The total force between the tip and the sample is very low ($\sim 10^{-12}$ N), which is of great advantage for studying soft or elastic samples [22]. Also, it allows samples like silicon wafers not to be contaminated through contact with the tip.

Non-contact AFM mode requires stiffer cantilevers than contact AFM mode, so they can not be pulled in contact with the sample surface. This cantilever is vibrated near its resonant frequency with amplitude of a few tens to hundreds of angstroms and any changes in the resonant frequency or vibration amplitude are detected as the tip moves close to the sample surface. Changes in the resonant frequency of the cantilever are related to changes in the force gradient experienced by the cantilever, which at the same time varies with the tip-to-sample separation, or sample topography.

In intermittent-contact AFM mode the cantilever tip is brought closer to the sample than in non-contact AFM mode, so that it “taps” the sample as it scans through it. This mode is also called “tapping mode”.

Intermittent-contact AFM is less likely to damage the sample than contact AFM because it eliminates lateral forces, such as friction, between the tip and the sample.

In intermittent-contact AFM mode, surface topography images are obtained by monitoring the changes in the resonant frequency of the cantilever as this is moved across the surface of the sample, similarly as in non-contact AFM mode.

2.9 References

- [1] D. P. Woodruff and T. A. Delchar, *Modern technique of surface science* (Cambridge University Press, Cambridge, 1986).
- [2] N. Martensson, P. Baltzer, P. A. Bruhwiler, J.-O. Forsell, A. Nilsson, A. Stenborg, and B. Wannberg, *J. Electron Spectrosc. Relat. Phenom.* **70**, 117 (1994).
- [3] U. Gelius, B. Wannberg, P. Baltzer, H. Hellner-Feldegg, G. Carlsson, C.-G. Johansson, J. Larsson, P. Munger, and G. Vegerfors, *J. Electron Spectrosc. Relat. Phenom.* **52**, 747 (1990).
- [4] Y. Chao, K. Svensson, D. Radosavkic, V. R. Dhanak, L. Šiller, and M. R. C. Hunt, *Phys. Rev. B* **64**, 235331 (2001).
- [5] Y. Chao, K. Svensson, D. Radosavkic, V. R. Dhanak, M. R. C. Hunt, and L. Šiller, *Phys. Rev. B* **66**, 075323 (2002).
- [6] *X-ray data booklet* (Lawrence Berkeley National Lab, Berkeley, 2001).
- [7] W. R. A. Huff, M. Shimomura, N. Sanada, G. Kaneda, Y. Suzuki, H. W. Yeom, T. Abukawa, S. Kono, and Y. Fukuda, *Phys. Rev. B* **57**, 10132 (1998).
- [8] M. Shimomura, N. Sanada, S. Ichikawa, Y. Fukuda, Nagoshi, and P. J. Moller, *J. Appl. Phys.* **83**, 3071 (1998).
- [9] W. G. Schmidt, F. Bechstedt, N. Esser, M. Pristovsek, C. Schultz, and W. Richter, *Phys. Rev. B* **57**, 14596 (1998).
- [10] L. H. Lie, M. Duerdin, E. M. Tuite, A. Houlton, and B. R. Horrocks, *J. Electroanal. Chem.* **538**, 183 (2002).
- [11] K. L. Agarwal, A. Yamazaki, P. J. Cashion, and H. G. Khorana, *Angew. Chem. Int Ed. Engl.* **11**, 451 (1972).

- [12] M. Smith, D. H. Ramler, I. H. Goldberg, and H. G. Khorana, *J. Am. Chem. Soc.* **84**, 430 (1963).
- [13] Y. Butenko, V. Kuznetsov, and L. Siller, unpublished.
- [14] L. H. Lie and B. R. Horrocks, unpublished (2003).
- [15] H. W. Kroto, J. R. Heath, S. C. Obrien, R. F. Curl, and R. E. Smalley, *Nature* **318**, 162 (1985).
- [16] A. V. Hamza, *Fullerenes Chemistry, Physics and Technology* (John & Sons, New York, 2000).
- [17] M. R. C. Hunt, A. Rajogopal, R. Caudano, and P. Rudolf, *Surf. Sci.* **454-456**, 267 (2000).
- [18] R. Helsel, *Visual Programming with HP VEE* (Prentice Hall PTR, New Jersey, 1998).
- [19] *MultiModd™SPM Instruction Manual* (Digital Instruments Veeco Metrology Group, 1997).
- [20] I. Acre-Garcia, in *Materials* (Newcastle University, Newcastle, 2002).
- [21] C. Kittel, *Introduction to solid state physics* (John Wiley & Sons, Inc., 1996).
- [22] R. Howland and L. Benatar, *A Practical Guide to Scanning Probe Microscopy* (Park Scientific Instruments, 1993).

Chapter 3 Chemisorption of C₆₀ on InP (100) Surface

In this Chapter, the growth models and criteria of chemisorption are described. The evolutions of core level and valence band as function of C₆₀ coverage/annealing temperature are discussed. The growth model and electronic structure of C₆₀ molecules adsorbed on InP (100) were studied by X-ray photoemission spectroscopy (XPS) and ultraviolet photoemission spectroscopy (UPS) as a function of coverage and annealing temperature. The C 1s, P 2p, In 4d core levels and the valence band spectra point to the presence of a localized covalent bond between C₆₀ molecules and the substrate. No filling of the lowest unoccupied molecular orbit derived bands was observed. The absence of any change in the surface components of In 4d core level upon C₆₀ adsorption indicated that the chemisorption bond exists between the fullerene molecules and phosphorus atoms rather than between C₆₀ molecules and indium atoms. This assertion is supported by the simultaneous desorption of both C₆₀ and P upon annealing to 640K and above.

3.1	Growth Models	85
3.2	Adsorption Models.....	87
3.3	The evolution of core levels and valence band as C ₆₀ coverage.....	88
3.3.1	The evolution of C 1s as C ₆₀ coverage	88
3.3.2	The evolution of valence band as C ₆₀ coverage.....	89
3.3.3	The evolution of P 2p as coverage of C ₆₀	91
3.3.4	The In 4d core level spectra in different C ₆₀ coverage.....	94
3.4	The evolution of core levels and valence band as annealing temperature	96
3.4.1	The evolution of core level C 1s and valence band as annealing temperature	97
3.4.2	The components of core level In 4d spectrum at high annealing temperature	98
3.5	Summary	101
3.6	Reference:.....	102

Since fullerenes were discovered in the environment, many methods for their production have been investigated [1-3]. The formation of C_{60} monolayer (ML) films on many kinds of surfaces is a topic of great interest.

In this work we demonstrate (a) hybridisation between the fullerene and InP; (b) the existence of a chemisorption bond between C_{60} molecules and P atoms rather than between C_{60} molecules and indium atoms; (c) the presence of metallic indium clusters when annealing temperature is increased to 640K.

The experiments were carried out in station 4.1, Daresbury. The sample preparation can be found in section 2.4.1. Photoemission spectra were acquired with a SCIENTA SES-200 analyser using $MgK\alpha$ X-rays and a helium-discharge lamp for core-level (X-ray photoelectron spectroscopy (XPS)) and valence-band (ultraviolet photoemission spectroscopy (UPS)) spectra, respectively. The experimental resolution was 0.85 eV (0.09 eV) for XPS (UPS) photoemission spectra [4]. Binding energy calibration can be found in section 2.3.2. C_{60} deposition and coverage calibration can be found in section 2.5.

3.1 Growth Models

Extensive experimental results point to the existence of three distinct equilibrium growth models [5], each named after investigators associated with their initial description: Frank-Van der Merwe (FV) growth, Stranski-Krastanov (SK) growth and Volmer-Weber (VW) growth. FV growth follows the layer-by-layer scenario, one monolayer after the next, up to some desired thickness of overlayer material. However, one often finds that the deposited material “balls up” into three-dimensional clumps, which only later coalesce into a thick polycrystalline film. VW growth is just the opposite of the FV model. Three-dimensional crystallites nucleate immediately upon contact and the overlayer may not completely cover the exposed substrate surface until a great many atoms have been deposited. SK growth lies in between: a few monolayers adsorb in layer-by-layer fashion before three-dimensional clumps begin to form. Fig 3.1 shows schematical illustration of three types of growth models: (a) Frank-Van der Merwe (FV); (b) Stranski-Krastanov (SK) growth; (c) Volmer-Weber (VW) growth.

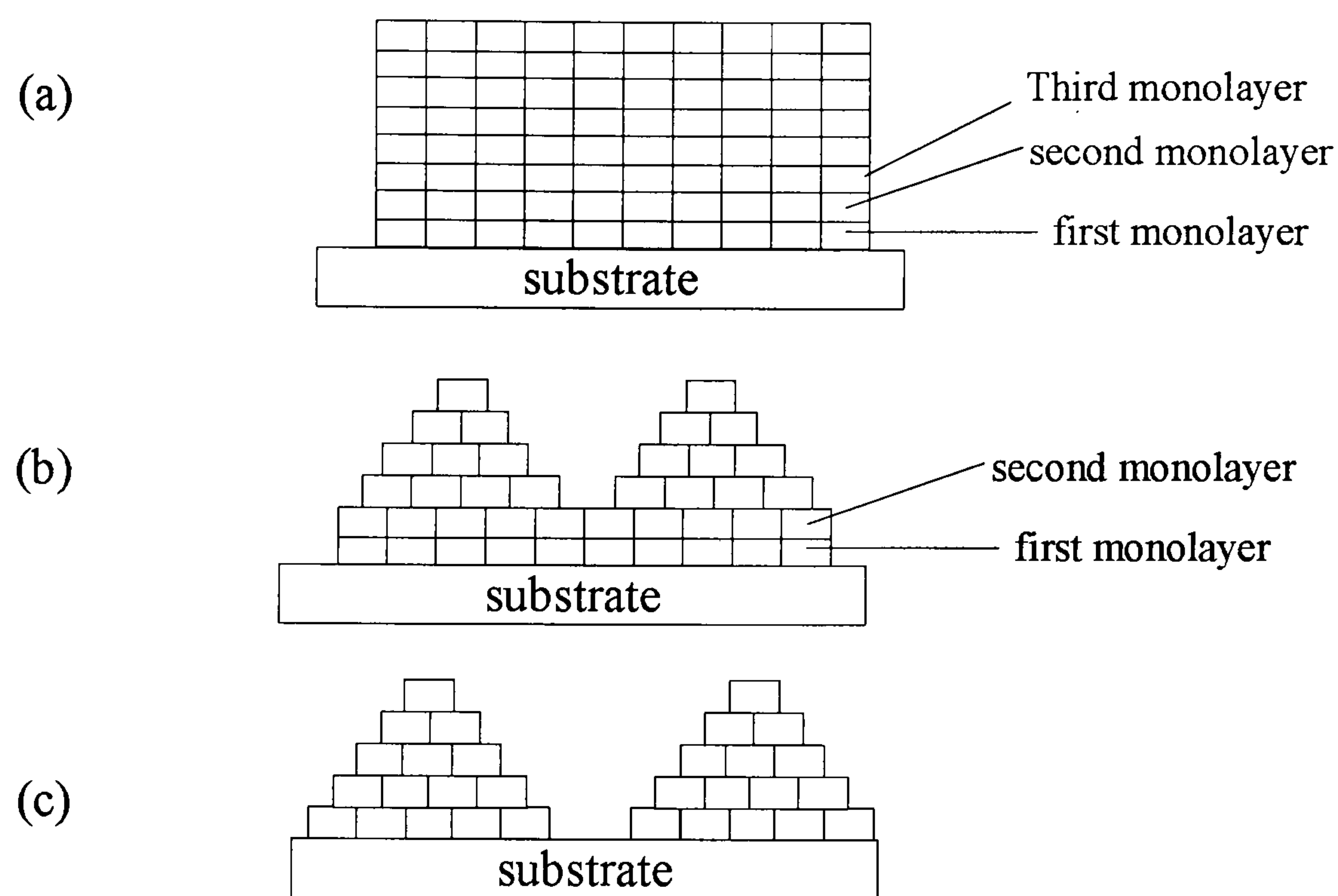


Fig. 3. 1 Schematic illustration of three types of growth models: (a) Frank-Van der Merwe (FV); (b) Stranski-Krastanov (SK) growth; (c) Volmer-Weber (VW) growth [5]

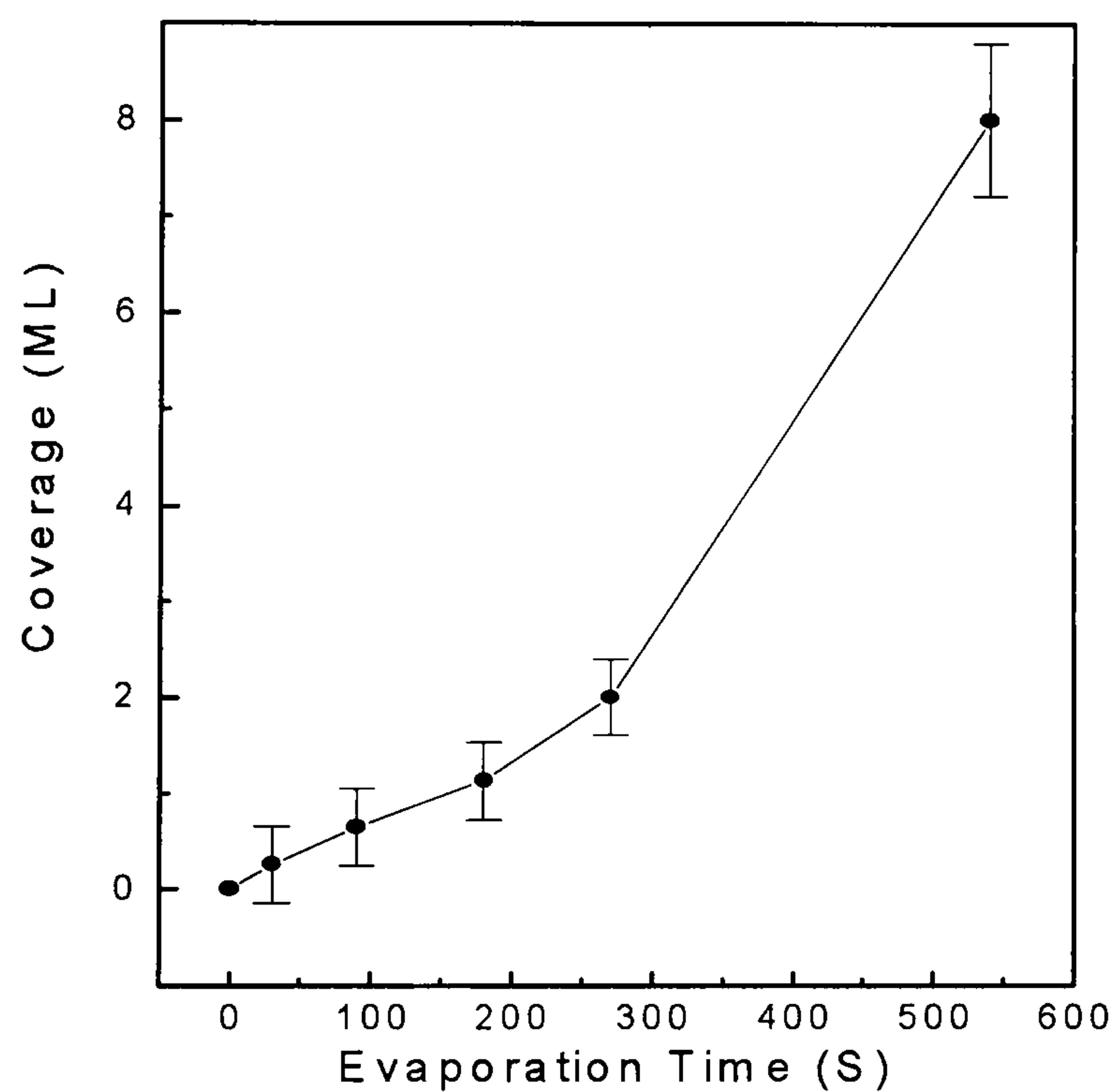


Fig. 3. 2 Fullerene coverage vs. evaporation time. 1 ML coverage was defined as the saturation coverage left on clean InP (100) surface after annealing a C₆₀ multilayer film at 600 K. Other coverages were deduced from the peak heights of the C 1s photoemission line relative to those of the In 3d level [4].

The growth model information could be obtained from the relationship between the coverage of adsorbate and evaporation time. Fig.3.2 shows the relationship between C_{60} coverage and evaporation time: it exhibits the typical 3-D (Vollmer-Weber) growth model behaviour. The same growth model has been observed by STM [6] for C_{60} on GaAs (110). Further information about the growth model and C_{60} -InP interaction can be gained from the C $1s$ photoemission line in section 3.3. An asymmetric lineshape is observed even above monolayer coverage resulting from the 3-D growth model at room temperature - molecules in several incomplete layers are probed, the core hole in each layer experiencing a different degree of screening and hence displaying slightly different binding energies [7]. The three-dimensional growth results in changes to the P $2p$ lineshape even above a nominal 1 ML coverage as well (section 3.3).

3.2 Adsorption Models

There are two principal modes of adsorption of molecules on surfaces: Physical adsorption (Physisorption) and Chemical adsorption (Chemisorption). The basis of distinction is the nature of the bonding between the molecule and the surface.

The weakest form of adsorption to a solid surface is called physical adsorption, or physisorption. It is characterized by the lack of a true chemical bond between adsorbate and substrate. The attractive force that binds a gas phase species to a solid is van der Waals interaction [5]. There is no significant redistribution of electron density in either the molecule or at the substrate surface.

However, chemical bonds exist in chemisorption, involving substantial rearrangement of electron density, is formed between the adsorbate and substrate. The nature of this bond may lie anywhere between the extremes of virtually complete ionic or complete covalent character. Foreign gas atoms that strike the surface may bind to one of the surface sites through formation of a surface chemical bond. If the foreign gas atoms are adsorbing to the surface through chemisorption, the photoemission spectra peak position should be different with the reference data and changing because the binding circumstance is changing as the coverage increasing. In our case, as the coverage of C_{60}

increased, both the peak positions of C *1s* and P *2p* have been changed. Detailed results can be found in section 3.3.

Furthermore, the non-rigid band shift in valence band is a signature of chemical bond formation, in particular hybridisation, between the substrate and adsorbed fullerene molecules. Comparing submonolayer with multilayer spectra, we notice that the position of the highest occupied molecular orbital (HOMO) stays constant, while the HOMO-1 shifts to higher binding energies—non-rigid shift, see section 3.3.

3.3 The evolution of core levels and valence band as C₆₀ coverage

From the core level C *1s*, P *2p* and valence band spectra acquired in different C₆₀ coverage, we can get information about the growth type and bonding type on the substrate.

3.3.1 The evolution of C *1s* as C₆₀ coverage

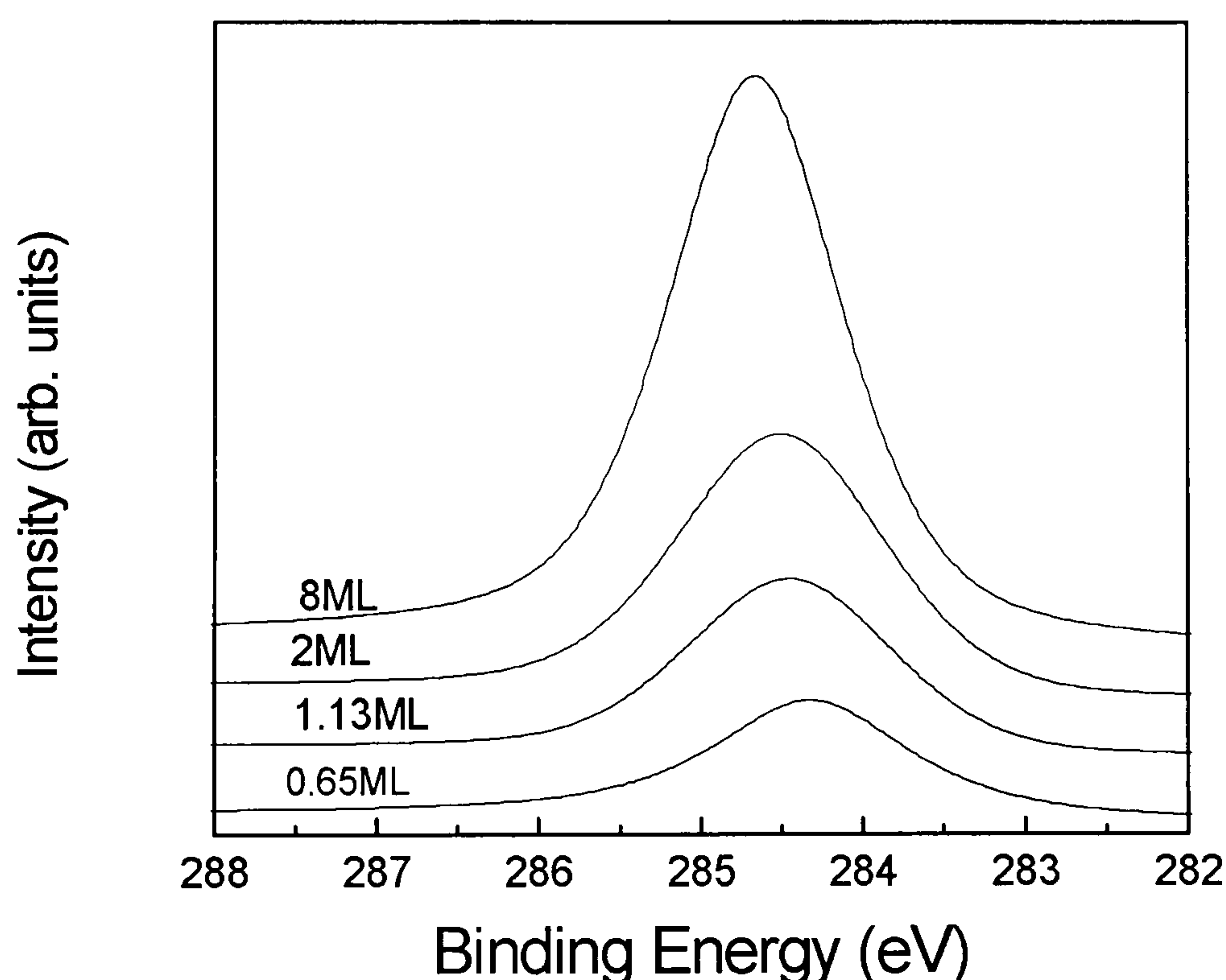


Fig. 3. 3 C *1s* photoemission spectra ($h\nu=1253.6\text{eV}$) for 0.65 ML and 1.13, 2, and 8 ML of C₆₀ on InP (100) [4].

Fig. 3.3 presents spectra for a range of coverages of C_{60} on InP (100) and the Fig. 3.4 shows the C $1s$ peak position vs. coverage. With increasing coverage, the C $1s$ binding energy (E_B) is shifted to higher binding energies. The C $1s$ binding energy for 0.65 ML is 0.34 eV lower than that for 8 ML, which is located at 284.65 eV. This shift is mainly due to reduced image screening for molecules in the multilayer [7]. In addition, the full width at half maximum (FWHM) of the C $1s$ line at submonolayer coverages is increased to 1.46 eV in comparison to a FWHM of 1.27 eV at coverage of 8 ML. An asymmetric lineshape is observed even above monolayer coverage resulting from the 3-D growth mode at room temperature, because molecules in several incomplete layers are probed, the core hole in each layer experiencing a different degree of screening and hence displaying slightly different binding energies [7]. A very small broadening of ~ 0.1 eV of the C $1s$ line was reported for C_{60} adsorbed on GaAs (110) [8].

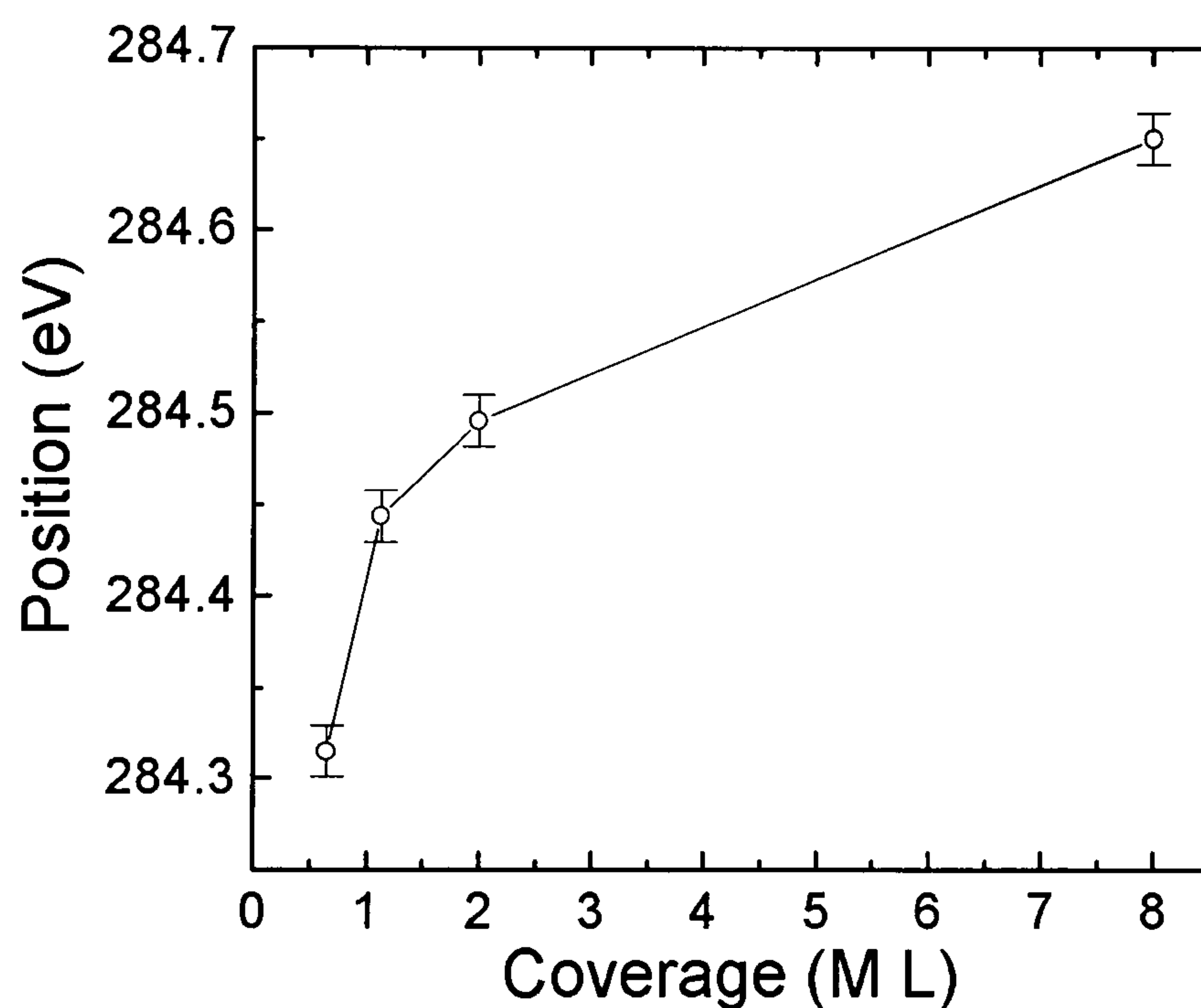


Fig. 3. 4 The relationship between C $1s$ peak position and C_{60} coverage [4]

3.3.2 The evolution of valence band as C_{60} coverage

Changes in the electronic structure of C_{60} brought about by adsorption can be further assessed by comparing valence-band spectra of 1.13 ML C_{60} /InP (100) with those of submonolayer (0.26 ML, 0.65 ML) and multilayer (2 ML, 8 ML) films on the same

substrate, as shown in Fig. 3.5. Comparing submonolayer with multilayer spectra, we notice that the position of the highest occupied molecular orbital (HOMO) stays constant, while the HOMO-1 shifts to higher binding energies, shown in Fig.3.6. This non-rigid band shift is a signature of chemical bond formation, in particular hybridisation, between the substrate and adsorbed fullerene molecules, although it is usually accompanied by significant extra broadening [9, 10] of the HOMO-1 related feature, absent in this case.

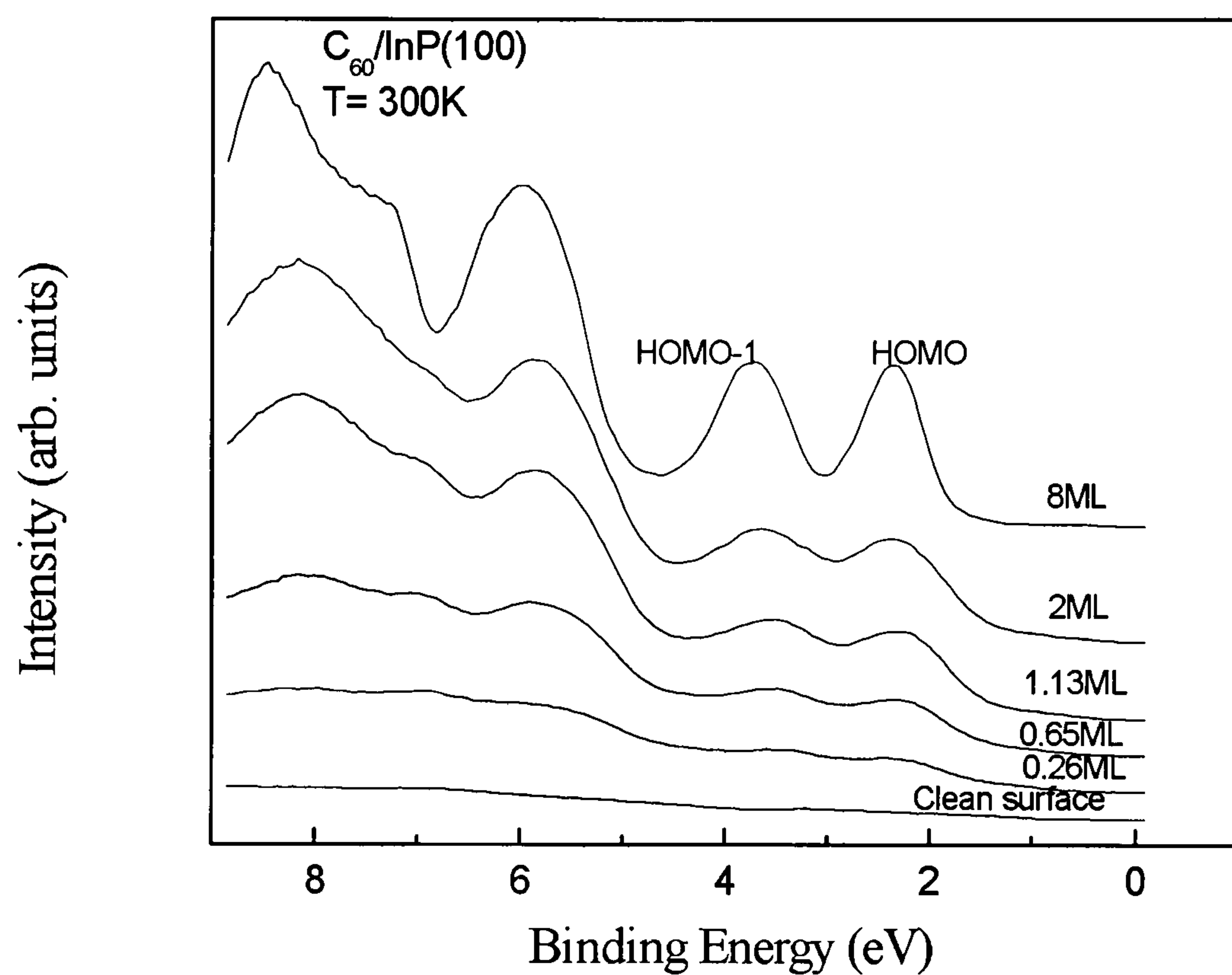


Fig. 3. 5 Valence band photoemission spectra ($h\nu=21.2\text{eV}$) collected for 0.26, 0.65, 1.13, and 8 ML of C₆₀ on InP (100) [4].

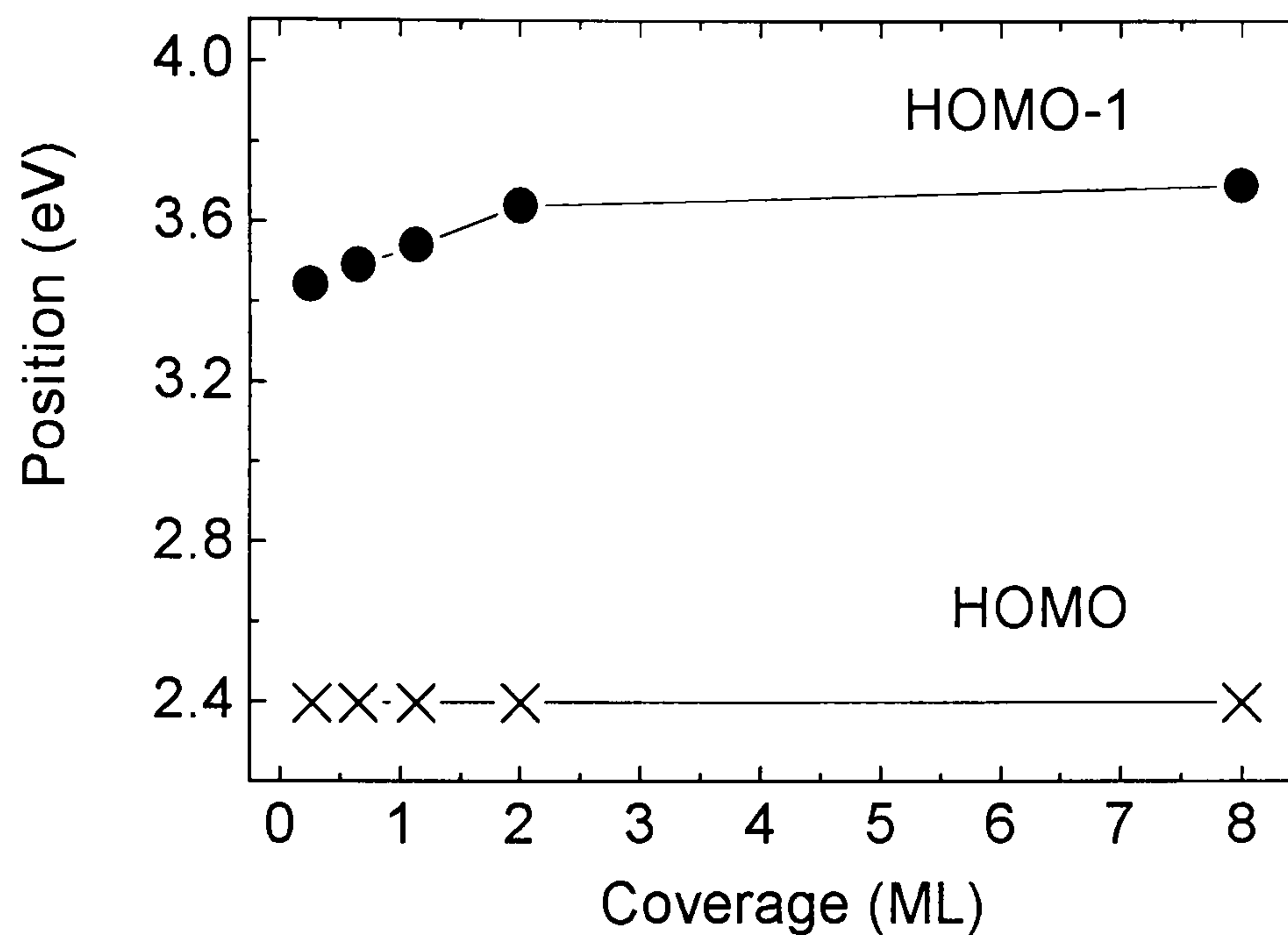


Fig. 3. 6 The HOMO and HOMO-1 peak position vs. coverage; the error bars are within the size of the dots [4].

3.3.3 The evolution of P $2p$ as coverage of C_{60}

To determine more about the nature of the substrate-adsorbate bond we recorded P $2p$ core level XPS spectra and In $4d$ UPS spectra with different C_{60} coverages. Fig 3.7 shows P $2p$ core levels for a range of coverages of C_{60} on InP (100). The Fig. 3.8 shows the P $2p$ peak of clean InP, and with C_{60} coverages of 0.65 ML and 8ML, all normalised to the same peak height after subtraction of the background. It is clear from Fig. 3.8 that there is a small shift in line position and corresponding change in lineshape with C_{60} coverage, which can be associated with a shift of a surface-related component of the P $2p$ line. The three-dimensional growth results in changes to the P $2p$ lineshape even above a nominal 1 ML coverage.

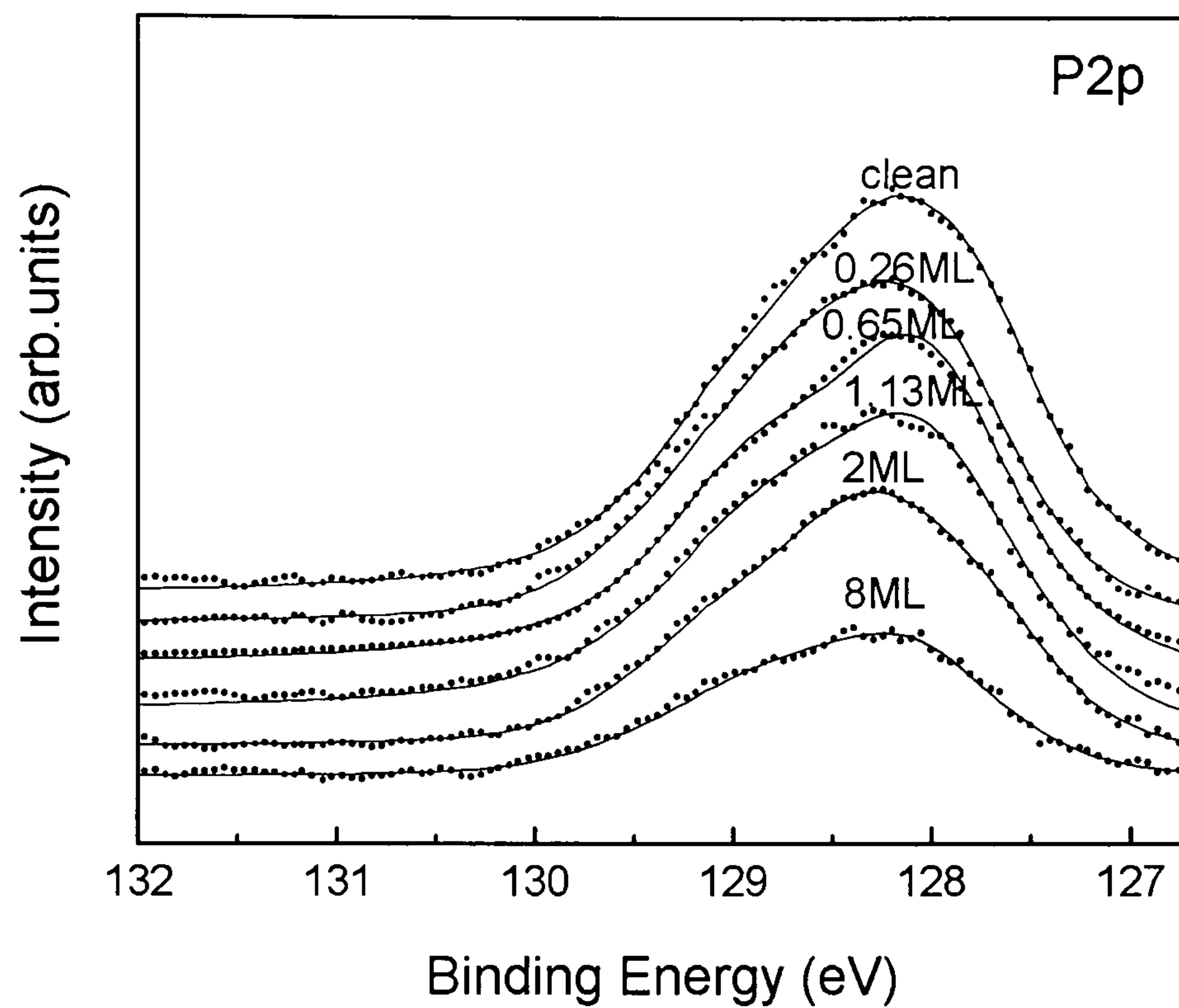


Fig. 3. 7 P 2*p* core level photoemission spectra ($h\nu= 1253.6$ eV) of C₆₀ on InP (100) [4].

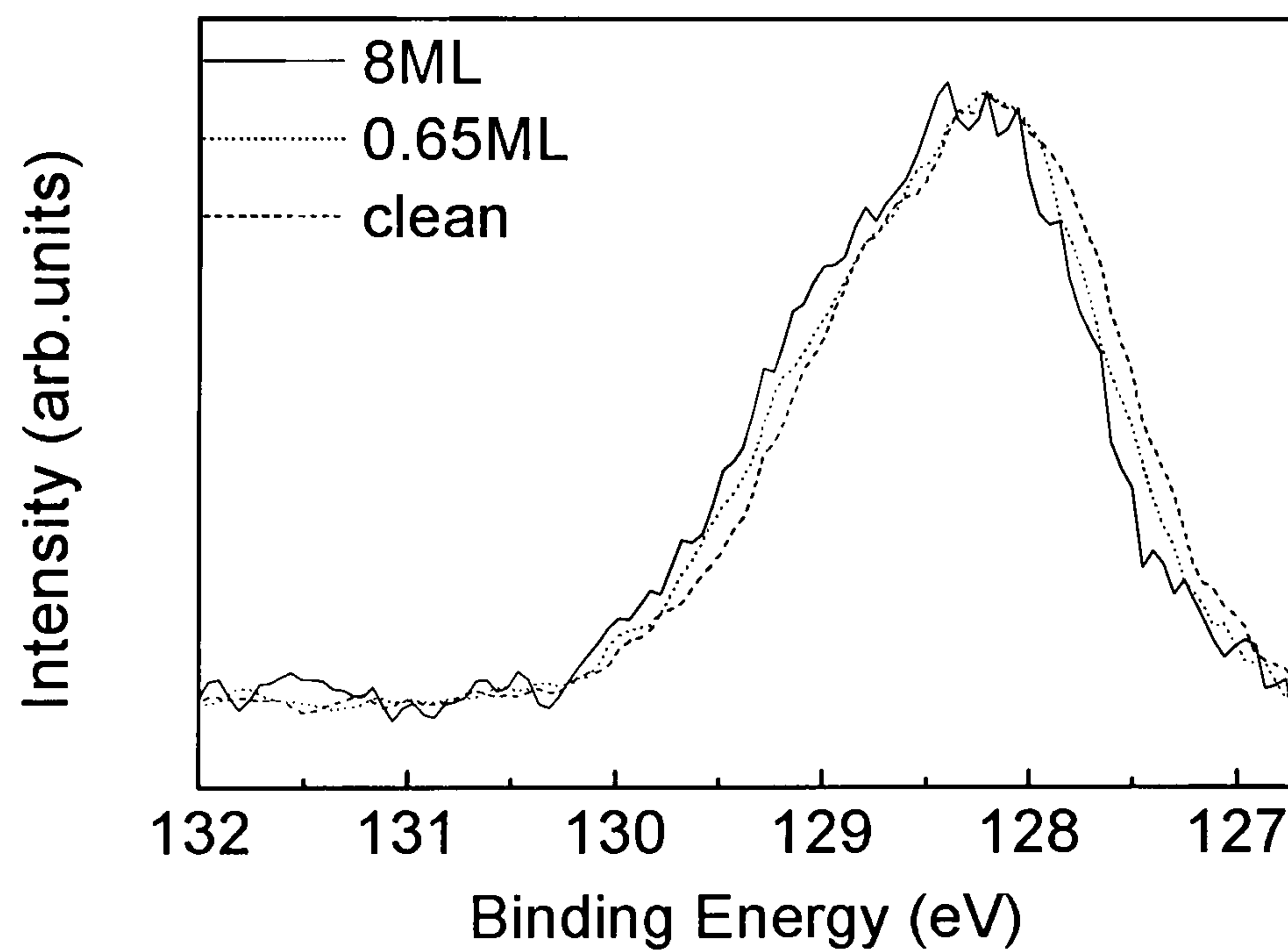


Fig. 3. 8 Re-scaled spectra of clean InP, and with C₆₀ coverages of 0.65 and 8 ML with backgrounds subtracted [4]

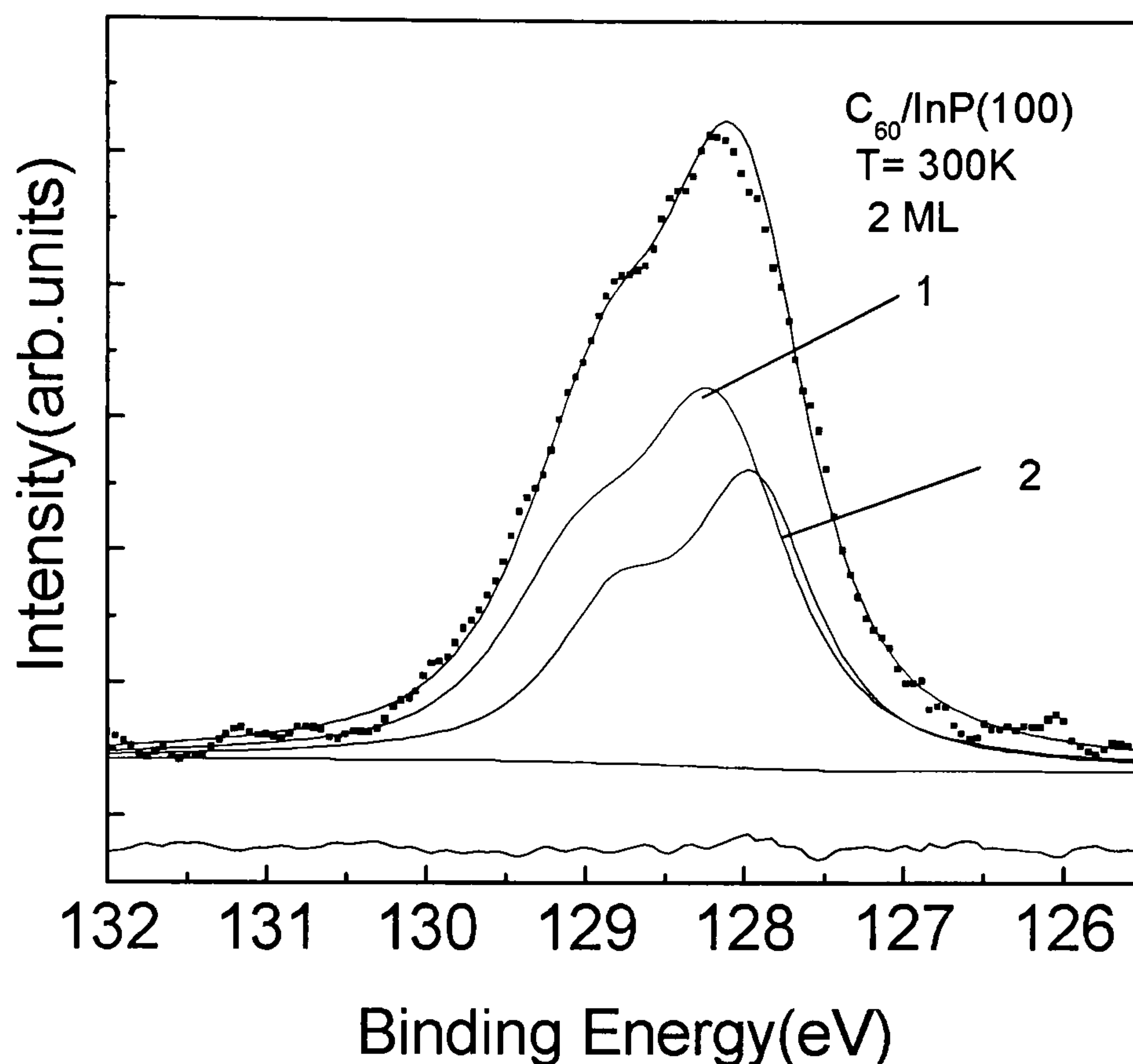


Fig. 3. 9 The P $2p$ core level photoemission spectrum ($h\nu= 1253.6$ eV) of 2 ML C_{60} on InP (100). Experimental spectrum (dotted line) was fitted to a Shirley background and two mixed doublet components: bulk (1) and surface (2) components [4].

Fig. 3.9 shows the lineshape analysis of the P $2p$ core level photoemission spectrum of 2 ML C_{60} on InP (100); this was fitted to two mixed doublets and a Shirley background. During the fitting procedure the spin-orbit splitting was kept fixed at 0.86 eV and the branching ratio set to 0.5 [11]. The Fig. 3.10 shows P $2p$ surface component peak position vs. coverage. With increasing coverage, the P $2p$ surface component peak position shifts to higher binding energies. This is indicative of a chemisorption bond between C_{60} molecules and P atoms.

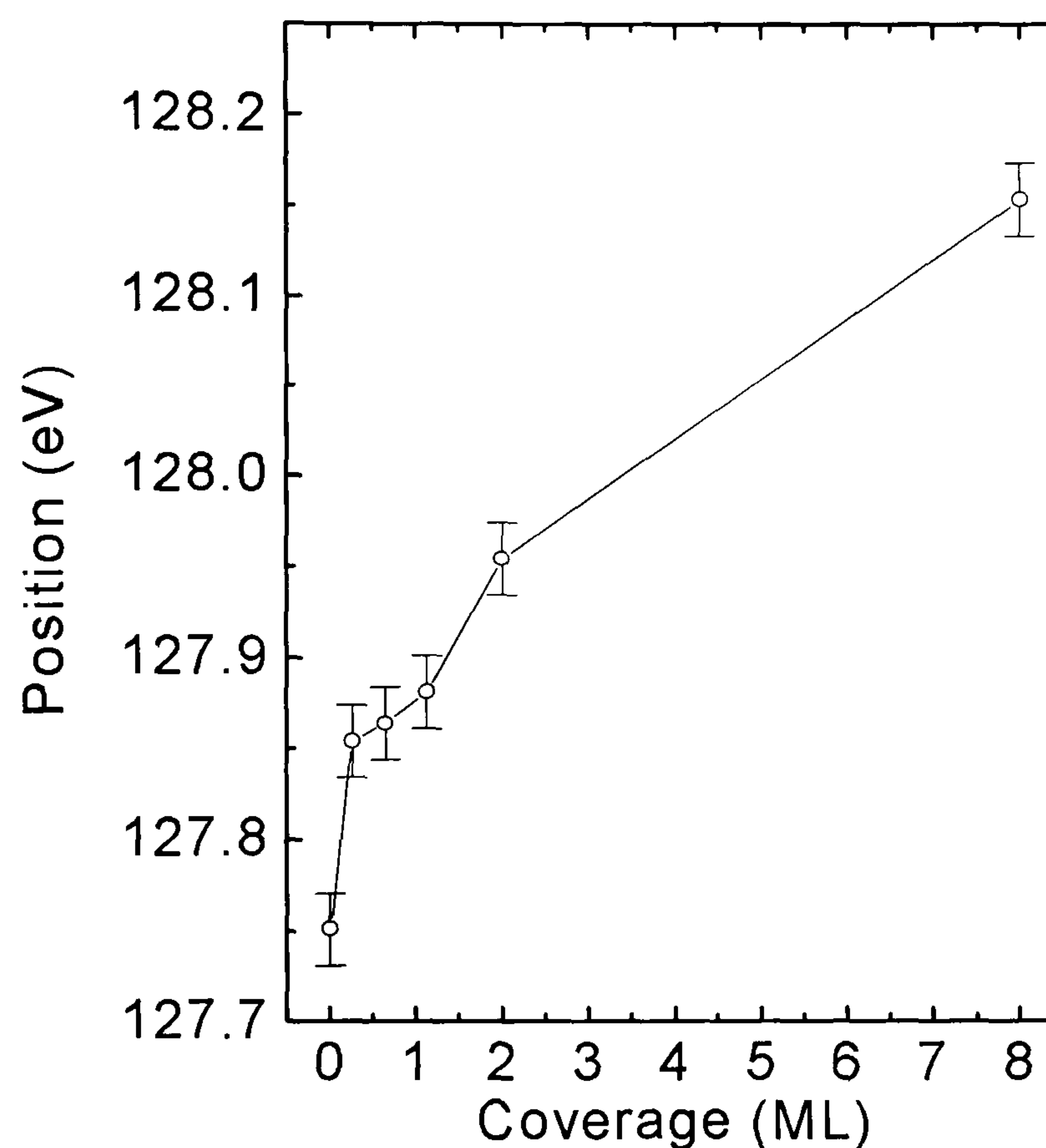


Fig. 3. 10 The surface component peak position of the P $2p$ vs. coverage [4].

3.3.4 The In $4d$ core level spectra in different C₆₀ coverage

For In $4d$ UPS ($h\nu = 40.8$ eV) spectra, the line was fitted with 3 mixed doublets and a Shirley background. Surface component (3) is attributed to the In-P bond [11-14], while the surface component (2) is still not uniquely assigned [12, 13]. During the fitting procedure, spin-orbit splitting was kept fixed at 0.86 eV; the branching ratios were 0.65 [11]. Fig. 3.11 shows the lineshape analysis of the In $4d$ photoemission spectrum ($h\nu = 40.8$ eV) of 0.26 ML C₆₀ on InP (100). Fig. 3.12 shows the binding energy of the surface component (3) of the In $4d$ line as a function of C₆₀ coverage. It is clear that there is no change in binding energy over the coverage range studied nor after annealing (open circle). The same observation is made for the surface component (2). This implies that there is no significant perturbation of the surface In atoms by the adsorbed C₆₀ and that consequently bonding is localised between the adsorbed C₆₀ and the surface P atoms.

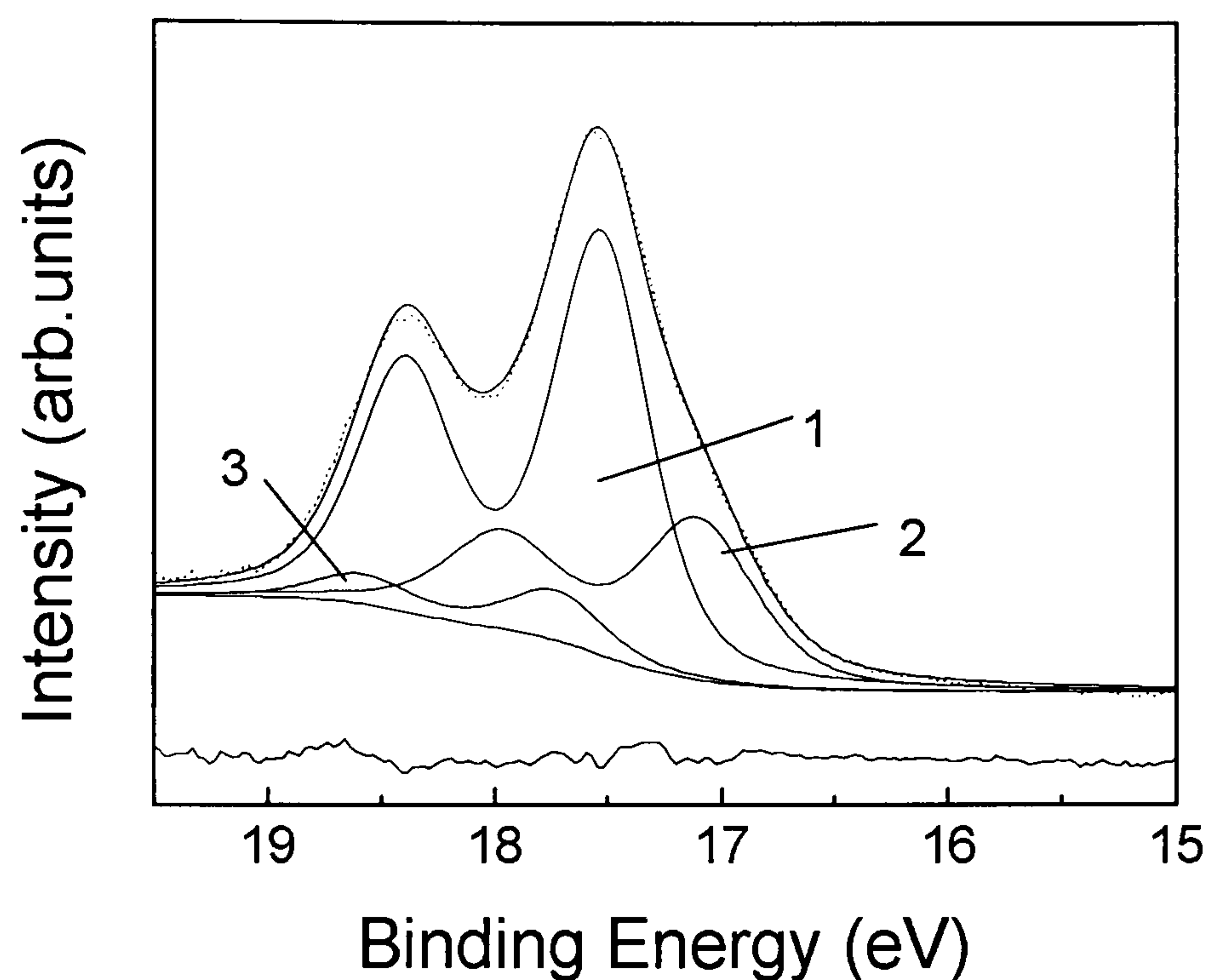


Fig. 3. 11 The In 4*d* photoemission spectrum ($h\nu= 40.8$ eV) of 0.26 ML C_{60} on InP (100). The experimental spectrum (dotted line) was fitted to a Shirley background and three mixed doublet components: bulk (1) and surface (2 & 3) components [4].

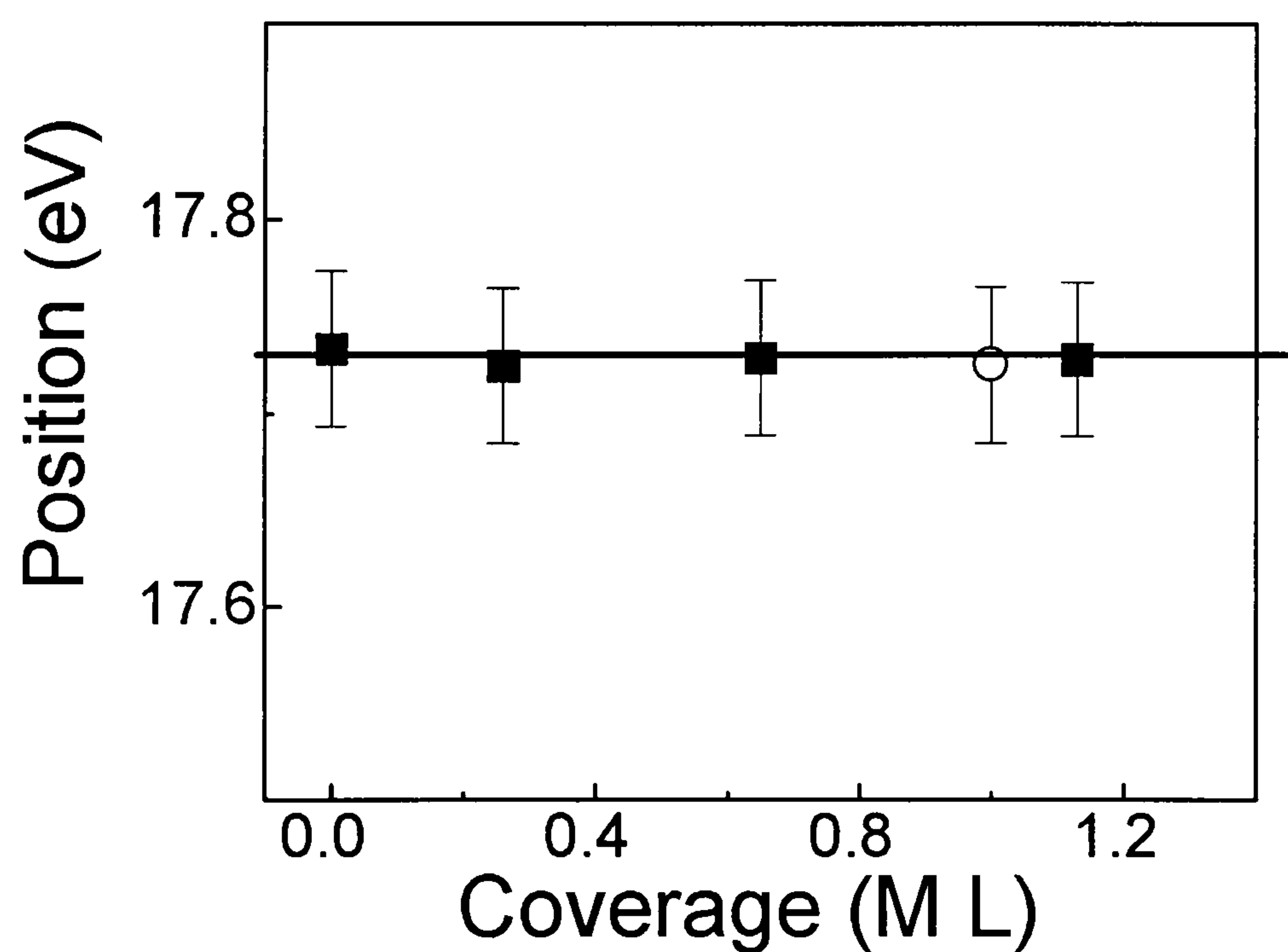


Fig. 3. 12 The indium surface component (3) of In 4*d* peak position vs. coverage (■), in comparison with that of 1ML of C_{60} on InP (100) after annealing at 600 K (○) [4].

3.4 The evolution of core levels and valence band as annealing temperature

The localization of chemical bonding between the C₆₀ and P is indicative of a primarily covalent interaction between the adsorbed C₆₀ and the InP (100) surface – charge transfer interactions are generally delocalised and would be expected to perturb *both* the In and P core lines contrary to our observations. The absence of appreciable charge transfer is reflected in the valence band spectra of Fig. 3.13. Any transferred charge would have to be accommodated in the normally empty t_{1u} lowest unoccupied molecular orbital which can result in the presence of fullerene-related photoemission features near the Fermi level (E_F) [15, 16]. Such features are noticeably absent from our valence band spectra at all C₆₀ coverages and under all annealing conditions used.

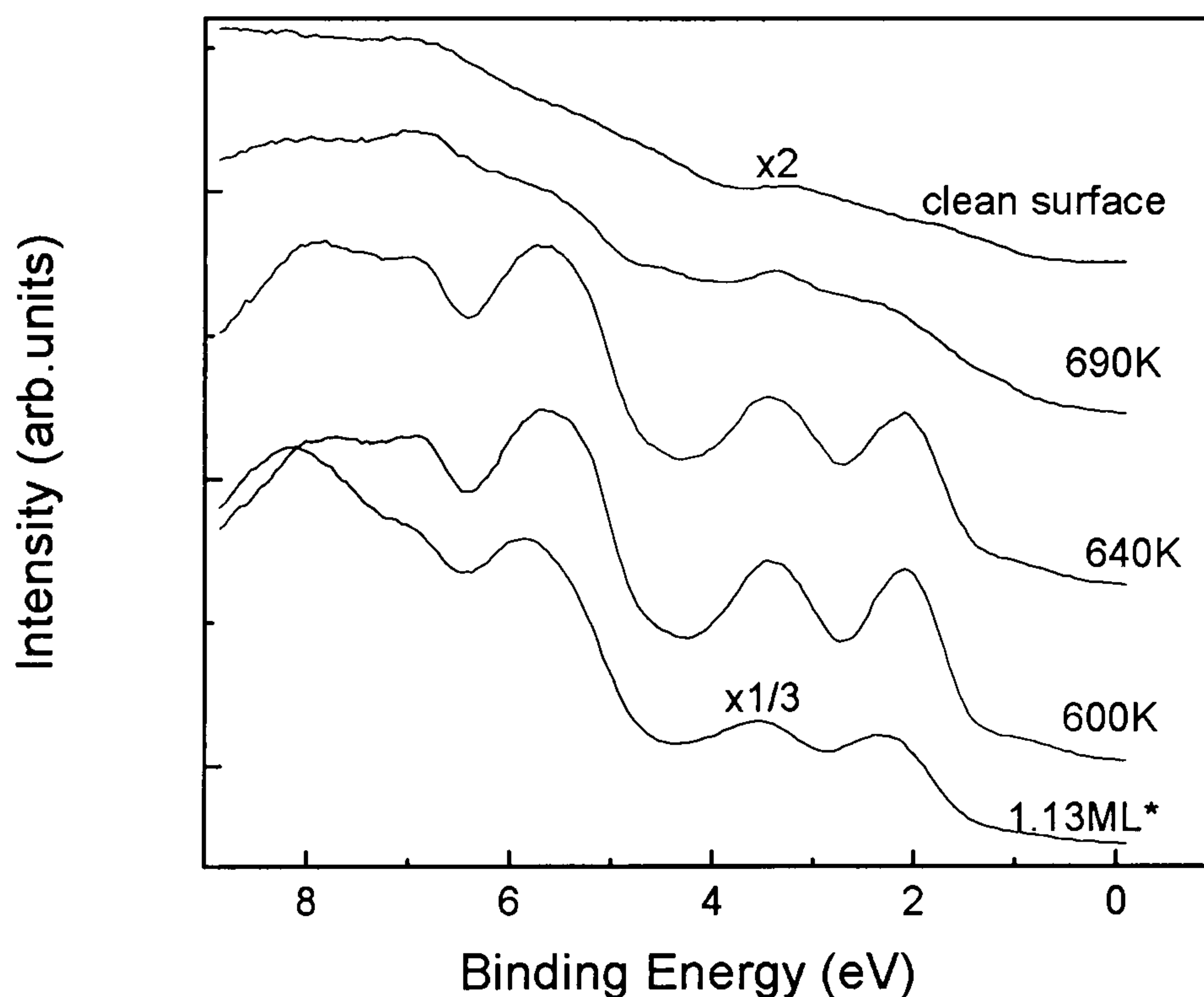


Fig. 3. 13 Valence-band spectra ($h\nu = 21.2$ eV) collected for C₆₀ on InP (100) as deposited at RT and after various annealing steps. Spectra from the clean surface and a coverage of 1.13 ML C₆₀/InP (100) before annealing are plotted for comparison [4].

3.4.1 The evolution of core level C *1s* and valence band as annealing temperature

To follow changes in the adsorbed C₆₀ layers upon annealing, we recorded C *1s* XPS after annealing at 600 K, 640 K, 690 K and 740 K. The results are shown in Fig. 3.14 together with a spectrum from RT-grown 1.13 ML C₆₀/InP (100). Annealing to 640 K causes the core line shifted by 0.1 eV to lower binding energy, and further, a small narrowing (~ 0.05 eV) of the C *1s* line is observed. After annealing cycles at 600 K and 640 K, the ratio of C *1s* to In *3d* peak height is found to be unchanged, indicating that desorption of less strongly bound molecules cannot account for the narrowing of the C *1s* line. Therefore, the narrowing probably arises from changes in adsorption state and or better ordering of the fullerene molecules in the film. These changes are reflected in the valence band UPS spectra from the same surfaces. The results are shown in Fig. 3.13, together with a spectrum from RT-grown 1.13 ML C₆₀/InP (100) and a spectrum from the clean InP (100) surface.

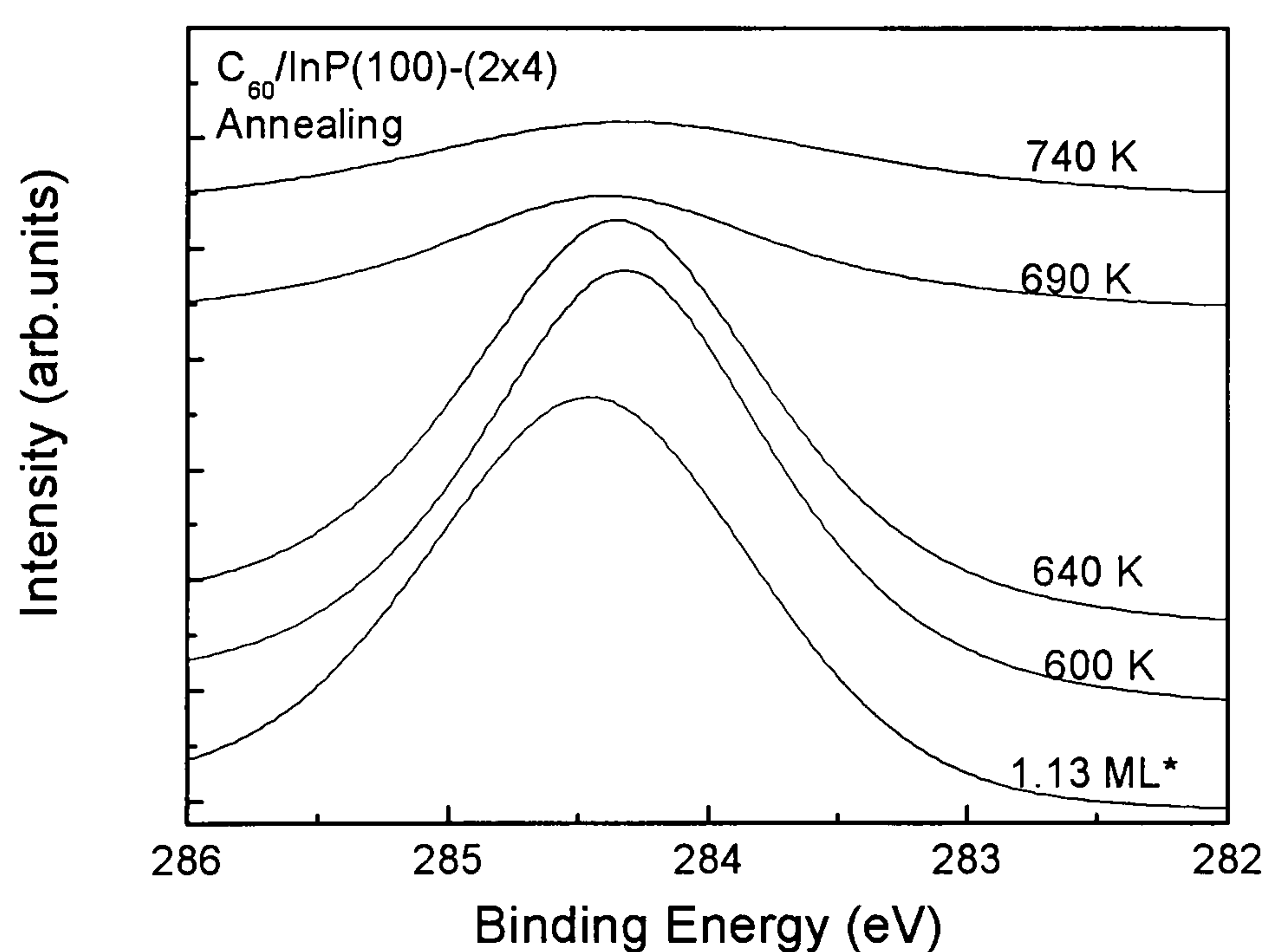


Fig. 3. 14 C *1s* photoemission spectra ($h\nu = 1253.6$ eV) of C₆₀ on InP as deposited at RT and after various annealing steps. Also plotted, for comparison, is the C *1s* spectrum of 1.13 ML C₆₀/InP (100) before annealing [4].

3.4.2 The components of core level In *4d* spectrum at high annealing temperature

Annealing to 640 K causes HOMO peak position shifted by 0.3 eV and HOMO-1 shifted by 0.1 eV towards higher binding energy. After annealing to 690 K, substantial desorption of carbon is observed and the ratio of C *1s* to In *3d* peak height is reduced by about one third. Further broadening of the valence band features is observed at this temperature with the fullerene-related signal superimposed on a strong background from the InP surface.

It is found that, with increasing annealing temperature to 640 K, there is a small metallic component in the In *4d* core level photoemission spectrum appears, which indicates the presence of metallic indium clusters. Previous work on sputtering of InP [17] shows a similar component which arises due to the preferential sputtering of phosphorous. Thus, the metallic indium component is a characteristic signature of phosphorous desorption from the InP (100) surface. The intensity of metallic indium component rises with increasing temperature, while intensity of both C *1s* and P *2p* peaks falls. This indicates that C₆₀ and phosphorous might desorb together from the surface and thus this could be a further support for the conclusion that bonding between C₆₀ and InP (100) is mediated by covalent bonding with surface P atoms, the surface In atoms playing a passive role. Fig. 3.15 shows the In *4d* photoemission spectrum ($h\nu = 40.8$ eV) after annealing to 740 K. The experimental spectrum (dotted line) was fitted to Shirley background and four doublet components: bulk (1), 2 surface (2, 3) and metallic indium (4) components. The metallic In component is clearly visible and is at a different binding energy to the surface component (2), enabling a clear differentiation between the two In species [14]. The detailed discussion on this metallic indium component—indium cluster can be found in next chapter.

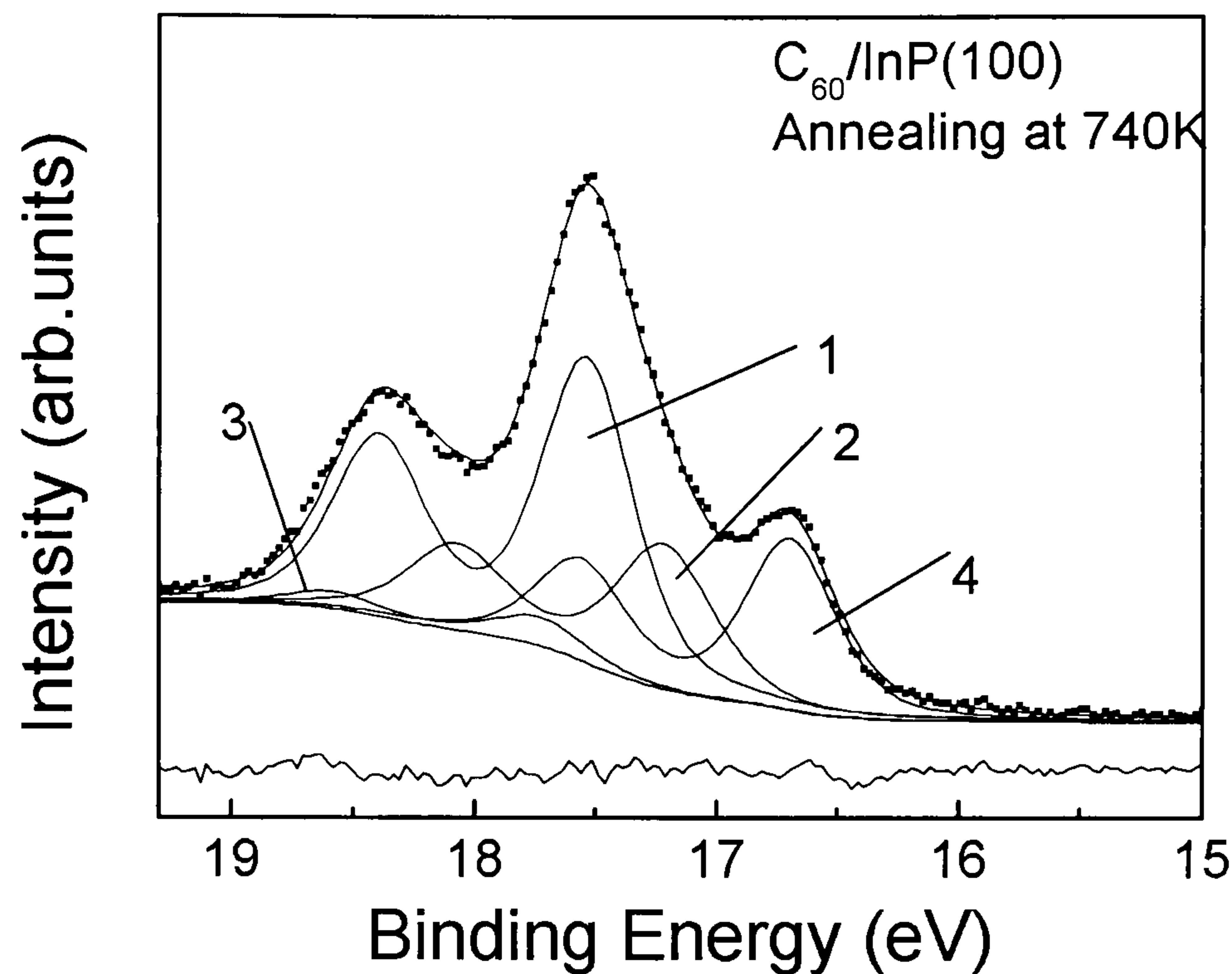


Fig. 3. 15 The In $4d$ photoemission spectrum ($h\nu = 40.8\text{eV}$) after annealing to 740 K. The experimental spectrum (dotted line) was fitted to a Shirley background and four mixed doublet components: bulk (1), surface (2 & 3) and metallic indium (4) components [4].

The possible reconstruction models for the In rich (2×4) InP (100) surface are shown in Fig. 3.16, (a) P-trimer, (b) In-trimer, (c) P-dimer, (d) In-dimer, (e) In and P mixed-dimer. The presence of P at the outermost surface is necessary for C₆₀ to bond to the phosphorous. Normally, isolated P behaves as an electron donor and C₆₀ as an acceptor. If a P-P dimer is formed on the InP (100) surface a dangling p-orbital is present, or for the case of the In-P mixed dimer a σ -like bond is formed by in plane In sp^2 hybrids and a P p-orbital [21]. Since we did not observe any significant changes in the In $4d$ surface components within our resolution, there is a strong possibility that P-P dimers are present on the InP (100)- (2×4) surface. However, it is also possible (although unlikely given the lack of change in the surface components of the In $4d$ line) that the adsorption of C₆₀ may lead to a new surface reconstruction, which involves the presence of surface

phosphorous dimers. Further experimental investigations are necessary to fully resolve this issue.

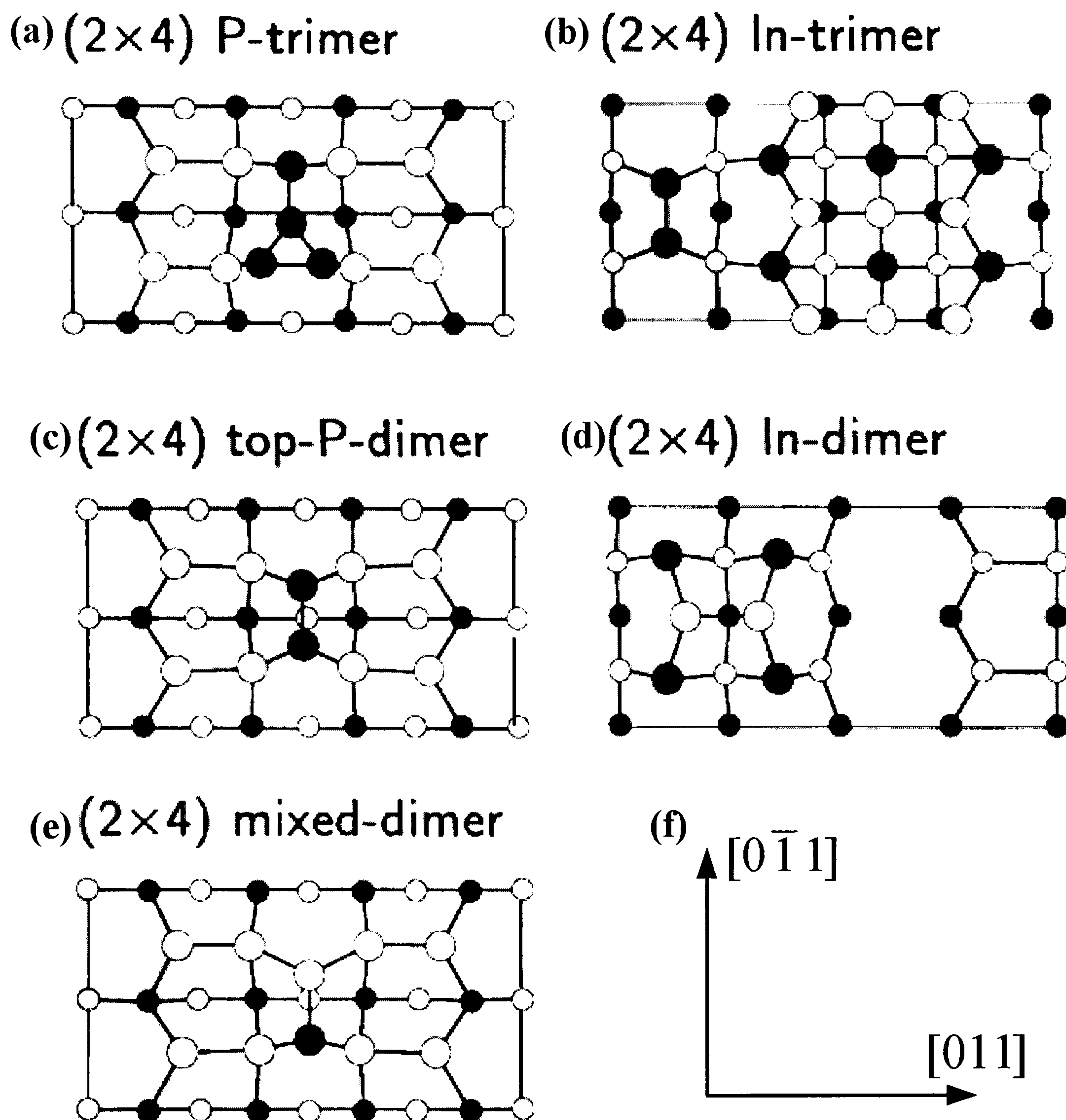


Fig. 3. 16 Top view of InP (100) (2×4) surface reconstruction models. Empty (filled) circles represent In (P) atoms. Large (small) symbols indicate positions in the first and second (third and fourth) atomic layers [20].

3.5 Summary

The growth models and criteria of chemisorption are described. The evolution of core level and valence band as function of C_{60} coverage/annealing temperature is discussed. The growth model and electronic structure of C_{60} molecules adsorbed on InP (100) were studied by X-ray photoemission spectroscopy (XPS) and ultraviolet photoemission spectroscopy (UPS) as a function of coverage and annealing temperature. We have found [4] that C_{60} molecules adsorbed on InP (100) at room temperature form a chemical bond with the substrate, but without any observable charge transfer into the lowest unoccupied molecular orbital (LUMO) of the C_{60} molecule from the substrate. The resulting covalent bonds are localized between the C_{60} molecules and surface phosphorus atoms. This assertion is supported by evidence from annealing experiments which show simultaneous desorption of carbon and phosphorous. Careful analysis of In $4d$ core level spectra indicate that there is no detectable interaction between the C_{60} and surface In atoms, suggesting the presence of P-P or mixed In-P dimers in the surface reconstruction of the substrate.

3.6 Reference:

- [1] J.B. Howard, J.T. McKinmon, Y. Marazkovsky, A.L. Lafleur, and M. E. Johnson, *Nature* **352**, 139 (1994).
- [2] L. Becker, J.L. Bada, R.E. Winans, J.E. Hunt, T.E. Bunch, and B. M. French, *Science* **265**, 642 (1994).
- [3] D. Heymann, L.P.F. Chibante, R.P. Brooks, W.S. Wolbach, and E. Smalley, *Science* **265**, 645 (1994).
- [4] Y. Chao, K. Svensson, D. Radosavkic, V. R. Dhanak, L. Šiller, and M. R. C. Hunt, *Phys. Rev. B* **64**, 235331 (2001).
- [5] A. Zangwill, *Physics at Surfaces* (Cambridge University Press, 1988).
- [6] J. C. Duphy, D. Klyachko, H. Xu, and D. M. Chen, *Surf. Sci.* **383**, L760 (1997).
- [7] A. J. Maxwell, P. A. Bruhwiler, D. Arvanitis, J. Hasselstom, and N. Martensson, *Chem. Phys. Lett.* **260**, 71 (1996).
- [8] T. R. Ohno, Y. Chen, S. E. Harvey, G. H. Kroll, J. H. Weaver, R. E. Haufler, and R. E. Smalley, *Phys. Rev. B* **44**, 13747 (1991).
- [9] M. R. C. Hunt, A. Rajogopal, R. Caudano, and P. Rudolf, *Surf. Sci.* **454-456**, 267 (2000).
- [10] A. J. Maxwell, P. A. Bruhwiler, D. Arvanitis, J. Hasselston, M. K.-J. Johansson, and N. Martensson, *Phys. Rev. B* **57**, 7312 (1998).
- [11] R. K. Gebhardt, S. Sloboshanin, J. A. Schaefer, and T. Chasse, *Appl. Surf. Sci.* **142**, 94 (1999).

- [12] M. Shimomura, N. Sanada, S. Ichikawa, Y. Fukuda, Nagoshi, and P. J. Moller, J. Appl. Phys. **83**, 3071 (1998).
- [13] W. R. A. Huff, M. Shimomura, N. Sanada, G. Kaneda, Y. Suzuki, H. W. Yeom, T. Abukawa, S. Kono, and Y. Fukuda, Phys. Rev. B **57**, 10132 (1998).
- [14] W. G. Schmidt, F. Bechstedt, N. Esser, M. Pristovsek, C. Schultz, and W. Richter, Phys. Rev. B **57**, 14596 (1998).
- [15] A. J. Maxwell, P. A. Bruhwiler, S. Andersson, N. Martensson, and P. Rudolf, Chem. Phys. Lett. **247**, 257 (1995).
- [16] P. J. Benning, F. Stepinak, and J. H. Weaver, Phys. Rev. B **48**, 9086 (1993).
- [17] W. M. Lau, R. N. S. Sodhi, B. J. Finn, K. H. Tan, and G. M. Bancroft, Appl. Phys. Lett. **51**, 177 (1987).
- [18] Q. Guo, M. E. Pemble, and E. M. Williams, Surf. Sci. **433-435**, 410 (1999).
- [19] M. Shimomura, N. Sanada, Y. Fukuda, and P. J. Moller, Surf. Sci. **359**, L451 (1996).
- [20] W. G. Schmidt and F. Bechstedt, Surf. Sci. **409**, 474 (1998).
- [21] A. M. Frisch, P. Vogt, S. Visbeck, T. Hannappel, F. Willig, W. Braun, W. Richter, J. Bernholc, W. G. Schmidt, and N. Esser, Appl. Surf. Sci. **166**, 224 (2000).
- [22] W. G. Schmidt, E. L. Briggs, J. Bernholc, and F. Bechstedt, Phys. Rev. B **59**, 2234 (1999).

Chapter 4 Nanometre scale Indium clusters on InP (100) surface

The evolution of clean, In-terminated InP (100)-(2 × 4) surfaces is investigated by synchrotron-radiation-excited photoemission spectroscopy (SRPES) as a function of annealing temperature. As-prepared InP (100)-(2 × 4) surface are found to be free of metallic indium, and the In4d core level shows two clear surface components. A third, indium-cluster-related component appears after annealing above 360 ± 10 °C, due to phosphorous desorption, and is accompanied by a corresponding reduction in intensity in the In-P surface component. Further annealing leads to a decrease in binding energy of the indium cluster related peak due to increased metallicity and hence core-hole screening in the clusters. The increasingly metallic nature of the indium clusters is also revealed by the appearance and growth of a Fermi edge in valence band spectra. Some ARPES results and AFM images are also given.

4.1	The evolution of In-terminated InP (100)-(2 × 4) as a function of temperature.....	106
4.2	In 4d components: bulk, surface and Indium clusters	108
4.3	The evolution of components as a function of temperature	112
4.4	Valence band evolution	114
4.5	Angle Resolved Photoemission Spectroscopy of Indium clusters.....	116
4.6	AFM images of indium clusters.....	124
4.7	Summary	126
4.8	References.....	127

Nanoscaled clusters study is on its way to a new climax [1-4] because cluster matter as a representative of novel materials has been indispensable in understanding the transition from the atomic to bulk solid state [5], and has plenty of future potential applications, such as heterogeneous catalysis [6], nonlinearoptics [7, 8], and nanoscale electronics [9, 10]. Indium clusters might have important role in formation InO_x thin films [11, 12], known as sensor elements. It has been found that indium cluster is a liquid-like structure but a solid-like structure for aluminium clusters [13].

Samples were mounted on a Ta plate and, in general, evenly heated by electron bombardment. However, one of the samples was unevenly heated in order to get a full temperature gradient across the surface. This was achieved by fixing one end of the sample tightly to the sample holder while the other end was loosely held (henceforth we will call this the ‘temperature gradient heated sample’). All the data presented in this work correspond were obtained from the evenly heated samples unless explicitly stated otherwise. Sample temperatures were measured by K-type thermo-couple in close proximity to the sample holder, using slow heating and cooling to ensure proper temperature equilibration. The sample preparation can be found in section 2.4.1. The experimental resolution was 0.3 eV [14, 15]. Binding energy calibration can be found in section 2.3.2.

The temperatures of the temperature gradient heated sample were calibrated by comparing area ratios of all components with those of other spectra that were taken from evenly heated samples (in all cases the samples were heated for an equal time of 2 min). The separation of selected adjacent points was ~ 3 mm, and the corresponding temperature difference was no more than 20°C , thus we estimate that the temperature variation across the spot exposed to synchrotron light (~ 1 mm) on the temperature gradient heated sample was not more than 10°C . Area ratios for a given component are defined as the sum of the $\text{In}4d_{3/2}$ and $4d_{5/2}$ peak areas for that component divided by the total area of the core line (sum of all components).

4.1 The evolution of In-terminated InP (100)-(2 × 4) as a function of temperature

Fig.4.1 shows In4*d* core level photoemission spectra obtained with 50 eV photon energy from clean and evenly heated samples. Each curve indicates a new sample evenly heated to the labelled temperature. One can see a rise in the shoulder on the low binding energy side of the In4*d* core line, associated with formation of indium clusters due to the loss of phosphorus [16]. As the temperature of the surface becomes higher, the number and/or size of the clusters increases. Exactly the same behaviour was observed on the temperature gradient heated sample: see Fig. 4.2.

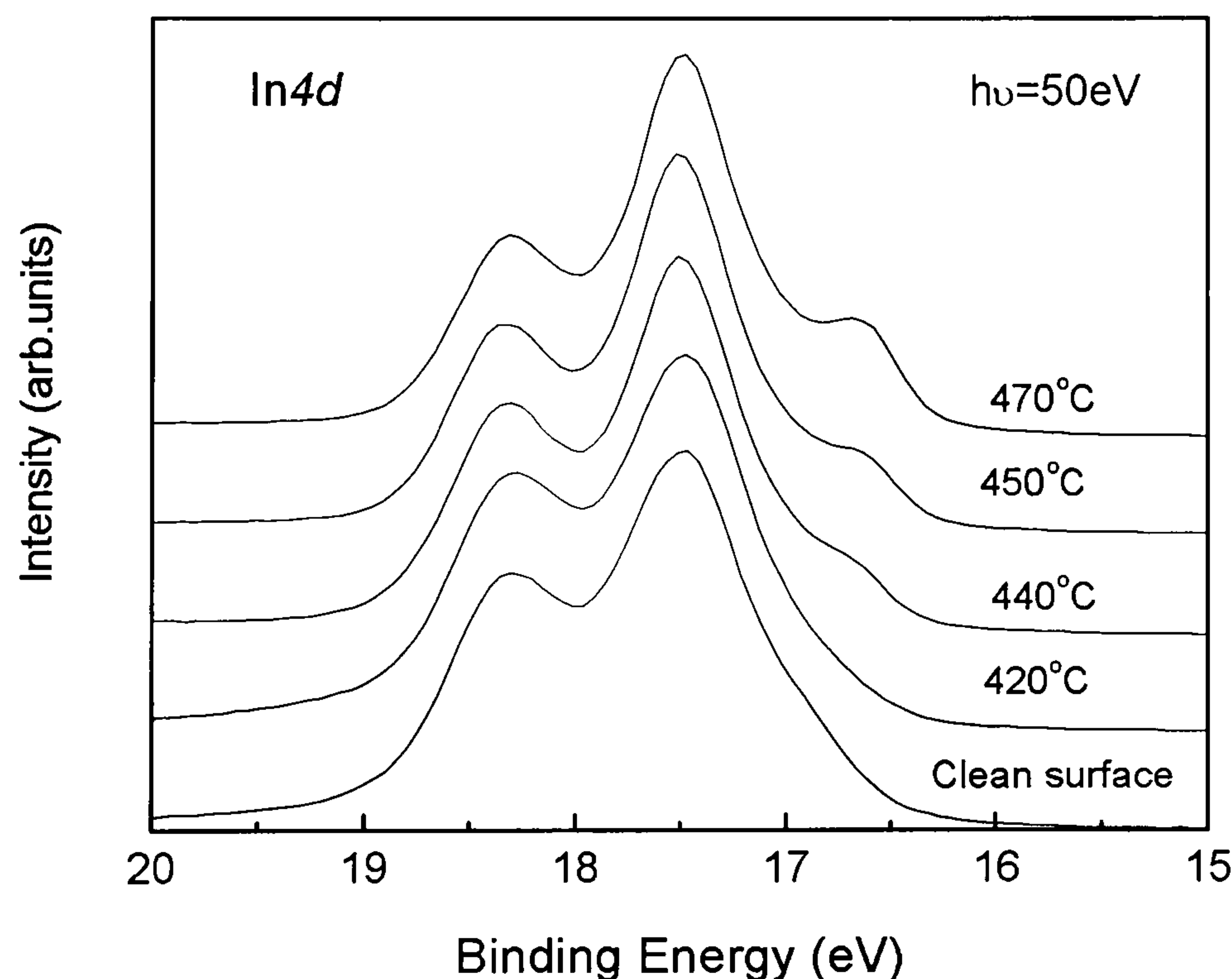


Fig. 4. 1 In4*d* photoemission spectra ($h\nu= 50\text{eV}$) of the cluster-free InP (100)-(2×4) surface and of four samples heated to the temperatures denoted in the figure. A clear rise of the shoulder on the low binding energy side is observed [15].

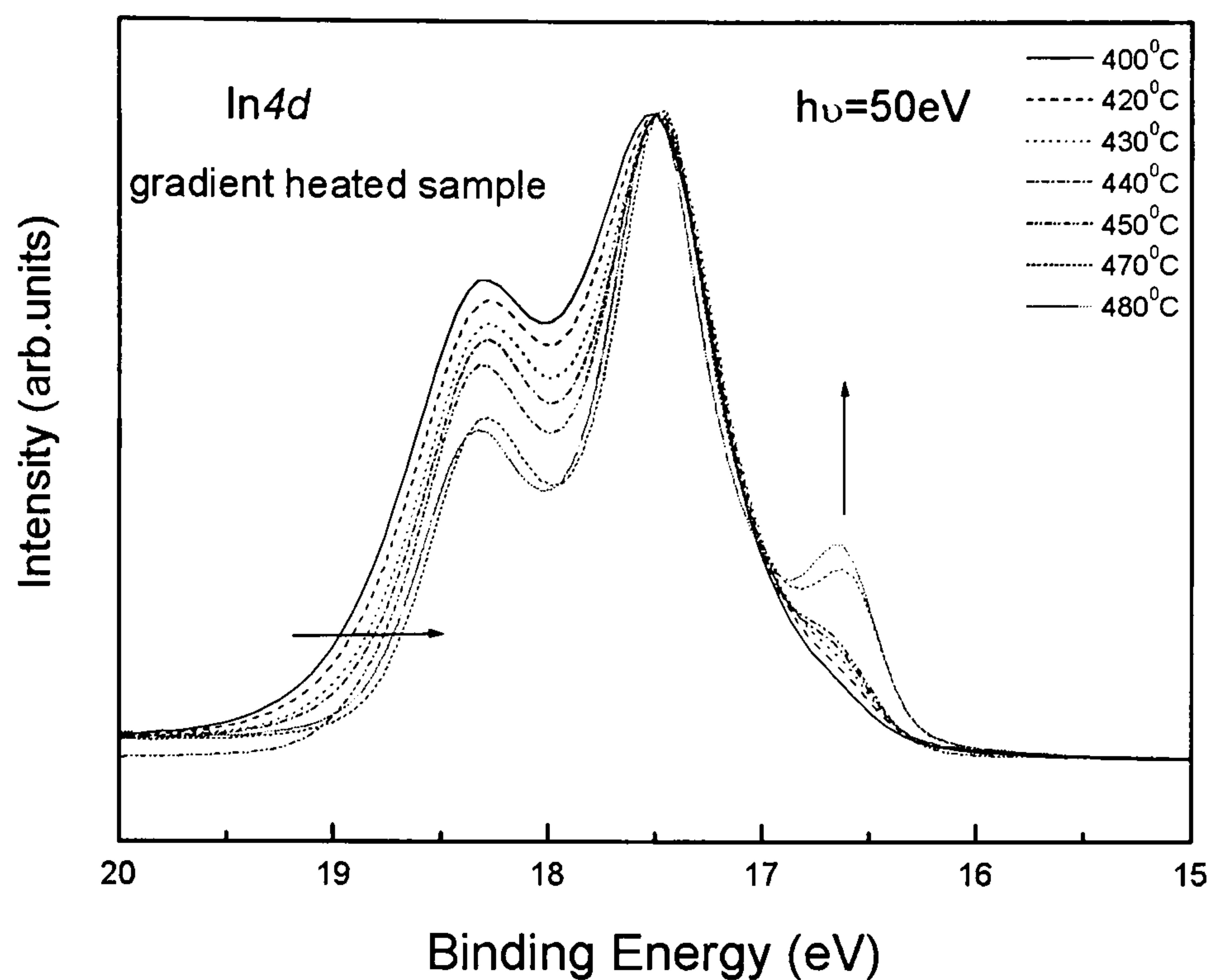


Fig. 4. 2 $\text{In}4d$ photoemission spectra ($h\nu = 50\text{eV}$) of the temperature-gradient-heated sample [15].

In addition to the obvious growth of the cluster-related component as we scan from the end annealed at the lower temperature to the higher, one can see an additional effect, an asymmetric narrowing of the $\text{In}4d$ line on the higher binding energy side (indicated with an arrow in Figure 4.2).

Initial atomic force microscopy (AFM) measurements of a gradient heated sample, across the whole length of the surface indicated the presence of a large number of clusters with strong increase in cluster coverage with temperature, see section 4.6.

4.2 In4*d* components: bulk, surface and Indium clusters

In order to understand this behaviour and follow the cluster growth mechanism further, we studied the evolution of the shape of the In4*d* core levels for both evenly heated samples and the temperature gradient heated sample in detail. Figs. 4.3 and 4.4 show the In4*d* photoemission spectra of the clean surface and after annealing at 470°C respectively. The experimental spectrum was fitted to three (for the clean surface) or four (for the annealed surface) mixed doublets with a Shirley background. During the fitting procedure, spin-orbit splitting was kept fixed at 0.86 eV; the branching ratio was 0.65. The position of the bulk component was kept fixed within ± 0.02 eV, and the width was allowed to vary by ± 0.05 eV. The initial parameters for fitting the In4*d* core lines were obtained from fits to spectra of the clean InP (100)-(2×4) surface [14] obtained with HeII radiation – these spectra were acquired at an improved resolution of 0.09 eV, but at the expense of enormously increased acquisition time. The clean surface was fitted to three rather than four components since the addition of a fourth component led to no significant increase in the quality of the fit, as would be expected if a fourth doublet was genuinely present. It should be noted that the FWHM of the In4*d* lines is slightly larger for the clean (2×4) surface than for the annealed surface (0.60 and 0.53 eV respectively) we attribute this difference to the presence of defects on the as prepared (2×4) surface, which are subsequently reduced in density by the annealing procedure. Table 4.1 and 4.2 give the fitting parameters of the clean surface and annealed surface.

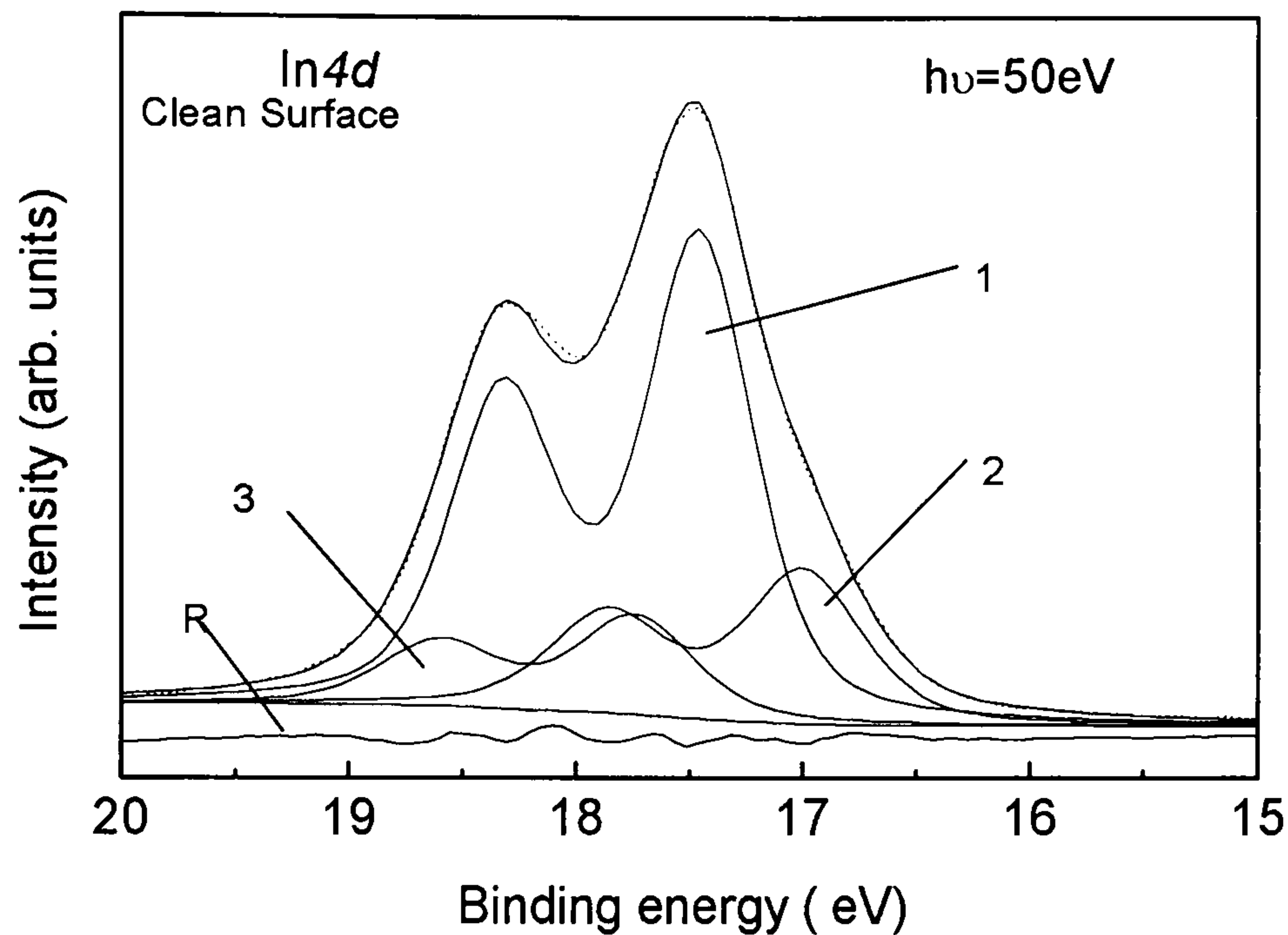


Fig. 4. 3 In4*d* photoemission spectrum ($h\nu= 50\text{eV}$) of clean InP (100)-(2 × 4). The experimental spectrum (dotted line) was fitted to a Shirley background and three mixed doublet components: bulk (1) and surface (2 & 3) components. The line marked 'R' shows the residuals of the fit [15].

The In4*d* core level spectrum of the clean surface can be decomposed into a bulk-related doublet (In-1) and two surface contributions (In-2 and In-3), which exhibit core level shifts compared to the dominant bulk component of $+0.40 \pm 0.03\text{eV}$ and $-0.30 \pm 0.03\text{ eV}$ respectively, which is consistent with previous studies [17-19]. The In-3 component has been attributed to three-fold coordinated Indium surface atoms, which exhibit charge transfer to three-fold coordinated P surface atoms [19, 20]. The component labelled In-2 might be associated with four-fold coordinated surface indium atoms, which are characterized by charge accumulation [19]. After the sample was heated above 360°C , the surface showed thermal decomposition, as a result of which the In4*d* spectra had to be fitted with four doublets and a Shirley background [21, 22]. The fourth doublet (In-4) we relate to contributions from metallic indium clusters, formed from surface indium liberated during the annealing process.

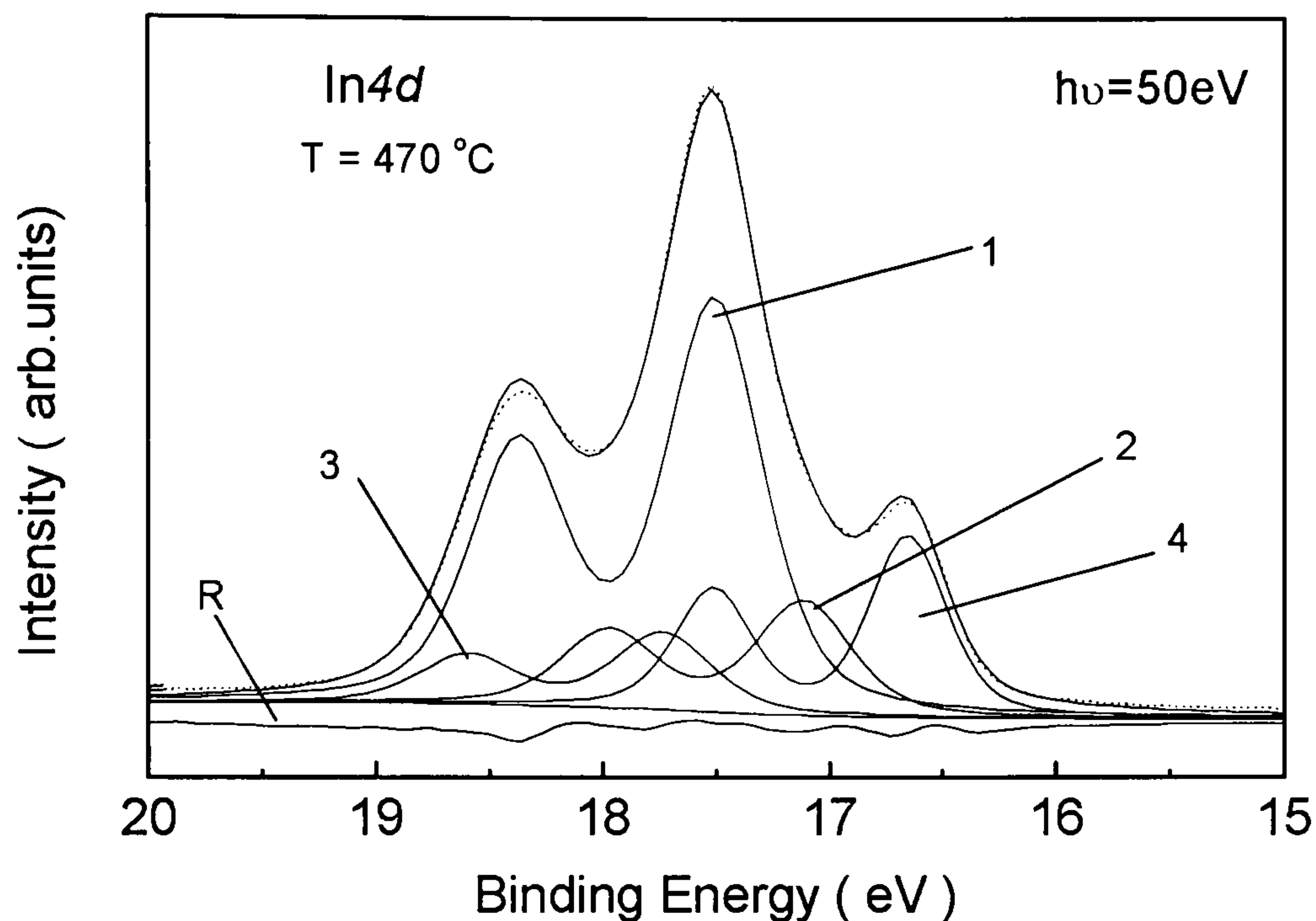


Fig. 4. 4 In4d photoemission spectrum ($h\nu= 50\text{eV}$) obtained after annealing a clean surface at 470°C . The experimental spectrum (dotted line) was fitted with a Shirley background and four mixed doublet components: bulk (1), surface (2 & 3) and indium cluster (4) components. The line marked 'R' shows the residuals of the fitting [15].

It is worth mentioning the differences in In4d fitting procedures between our work and that of others. Some groups fit the In4d photoemission spectrum of the *cluster-free* InP (100) surface with four doublets and a Shirley background [7, 8] and others with three doublets and a Shirley background [17-19, 23]. After experimentation with fitting parameters we found that three doublets (one bulk and two surface components) were enough; after annealing to temperatures beyond the P thermal desorption point, metallic indium appeared on the surface, requiring a fourth doublet. During the fitting procedure, the branching ratio and spin-orbit splitting should be kept fixed for all components, though in ref. ([21]), the branching ratio was allowed to vary considerably.

Table 4.1 The fitting parameters of the clean surface

Component	B	S1	S2
Shift relative to bulk (eV)	0	-0.30	+0.40
Width (eV)	0.60	0.60	0.60
Spin-orbit splitting (eV)	0.86	0.86	0.86
Branching ratio	0.65	0.65	0.65

Table 4.2 The fitting parameters of the surface annealed at 470°C

Components	B	S1	S2	C
Shift relative to bulk (eV)	0	-0.39	+0.16	-0.82
Width (eV)	0.53	0.53	0.53	0.53
Spin-orbit splitting (eV)	0.86	0.86	0.86	0.86
Branching ratio	0.65	0.65	0.65	0.65

4.3 The evolution of components as a function of temperature

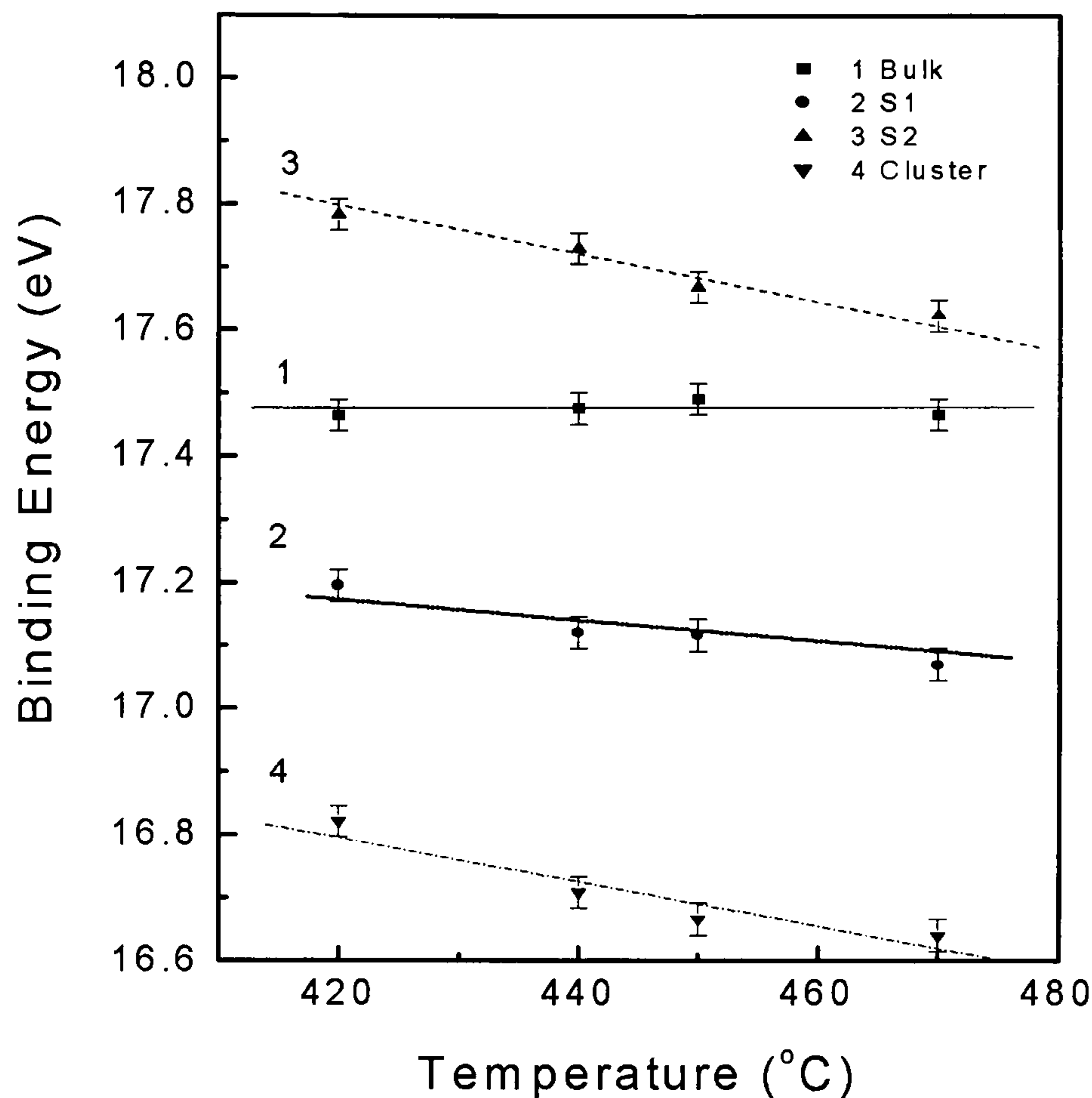


Fig. 4. 5 Binding energy positions of all components for evenly heated samples [15].

In Fig. 4.5 we show the general trend of all four components for evenly heated samples. It is obvious that a shift in the both surface components and the cluster-related component is observed. Since the In-3 (second surface component, S2) is related to charge exchange between the indium and phosphorus [19], it is to be expected that, as one begins to lose phosphorus atoms, this component will become weaker and probably some redistribution of charge will occur. The reduction in intensity of this component is the main reason for the apparent narrowing of the In4*d* with temperature in Fig. 4.2.

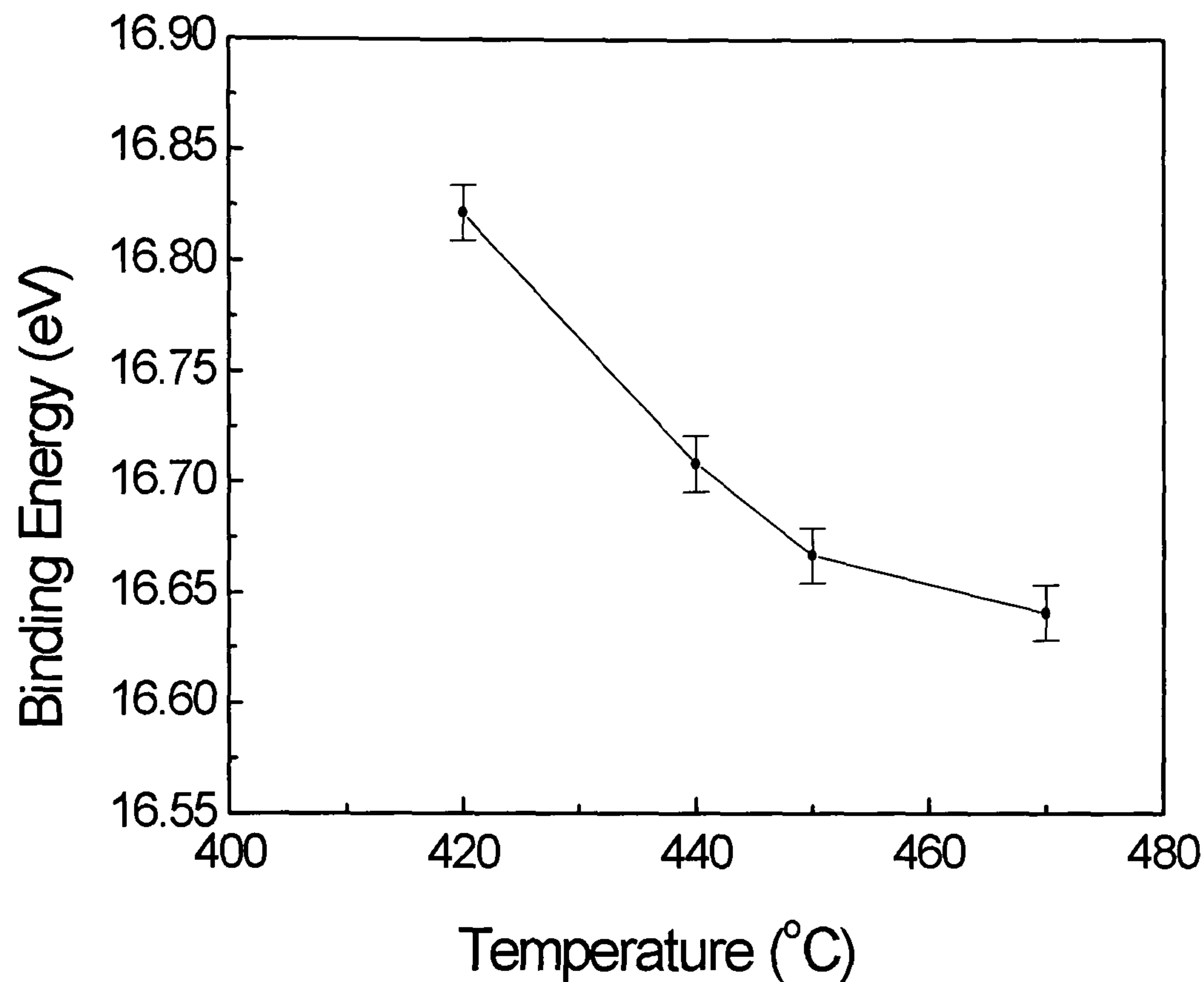


Fig. 4. 6 Binding energy position of the indium cluster related component against temperature for evenly heated samples [15].

Fig. 4.6 shows in greater detail how the position of the cluster-related spectral component of the evenly heated samples shifts with annealing temperature. When the annealing temperature is increased gradually from 420°C to 470°C, the cluster-related component position shifts to lower binding energy by 0.2 eV. Examination of the coverage dependence of core electron photoemission intensity and binding energy for simple, noble, and transition-metal clusters supported on amorphous carbon [3], has shown that very small metal-atom clusters, containing fewer than 30 atoms, are not fully metallic and final-state core holes are screened by polarisation of neighbouring atoms. Consequently, the binding energy depends only weakly on the cluster size [3]. In larger metallic clusters, conduction electrons screen the hole, with the missing charge appearing at the surface of the cluster. In this regime, the core electron binding energy shifts to lower values with increasing cluster size [3, 10]. The variation in binding energy of the cluster-related component of the In 4*d* line indicates that, for temperatures above 420°C, the indium clusters fall into the latter regime.

4.4 Valence band evolution

To further investigate the evolution of the InP surface during annealing, we recorded valence band spectra after annealing at each temperature. Fig. 4.7 shows the normalised valence band spectra. After annealing to $440 \pm 10^\circ\text{C}$ and above, a Fermi edge begins to become apparent in the spectra, indicating that the indium clusters, or a proportion thereof, have become fully metallic. By carefully inspecting the features of the valence band, one can also find that the highest surface state peak position shifts from 1.70 eV to 2.05 eV when the annealing temperature is increased from 400°C to 500°C .

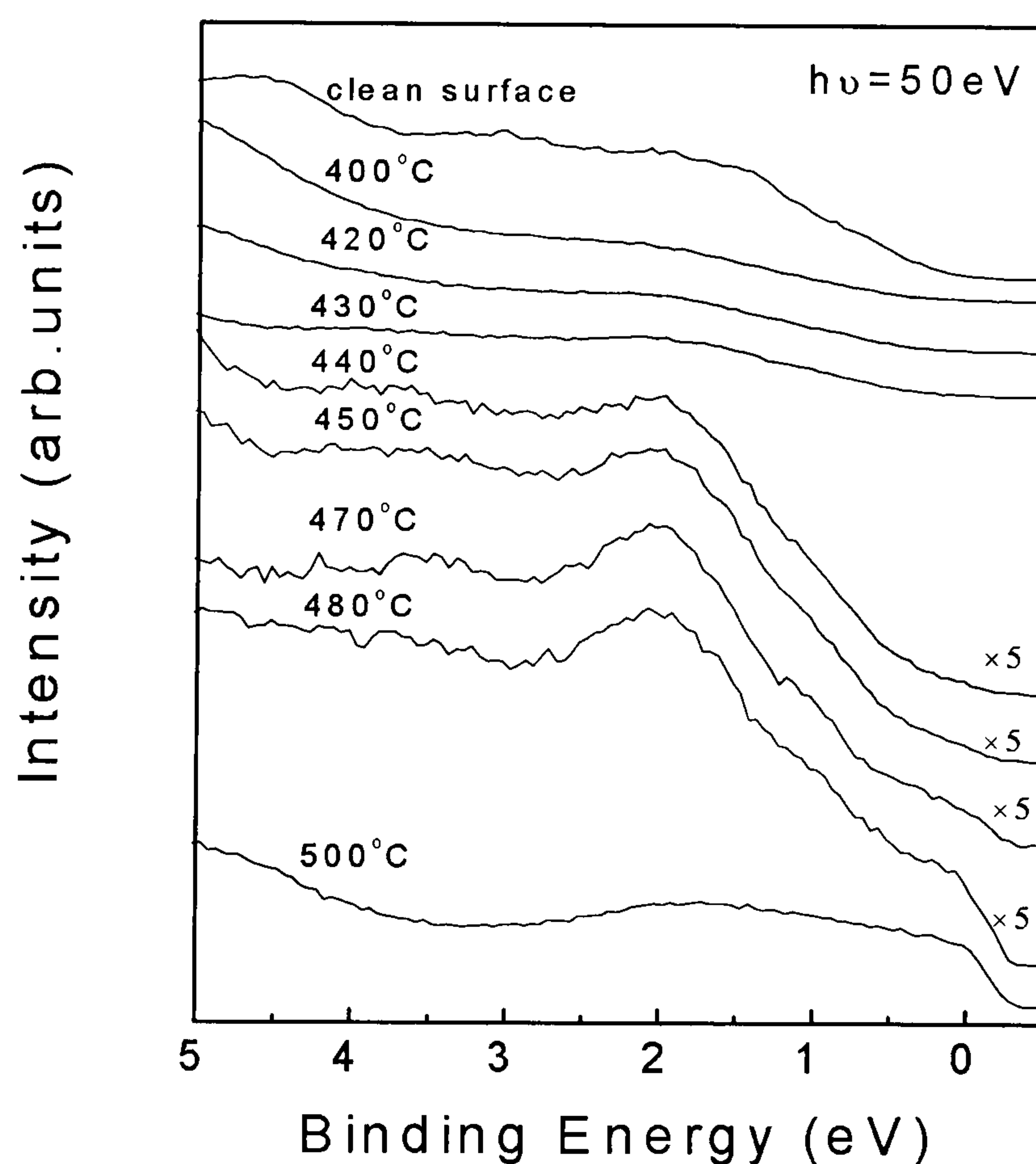


Fig. 4. 7 Valence-band spectra ($h\nu = 50\text{eV}$) collected at normal emission from InP(100)-(2 \times 4) surfaces after various annealing steps [15].

This might be interpreted as the appearance of new donor states in the gap during the annealing procedure, which donate electrons and shift E_F closer to vacuum level. This appears as a shift of the valence-band to a higher binding energy. Fig. 4.8 schematically illustrates the band structure change after annealing.

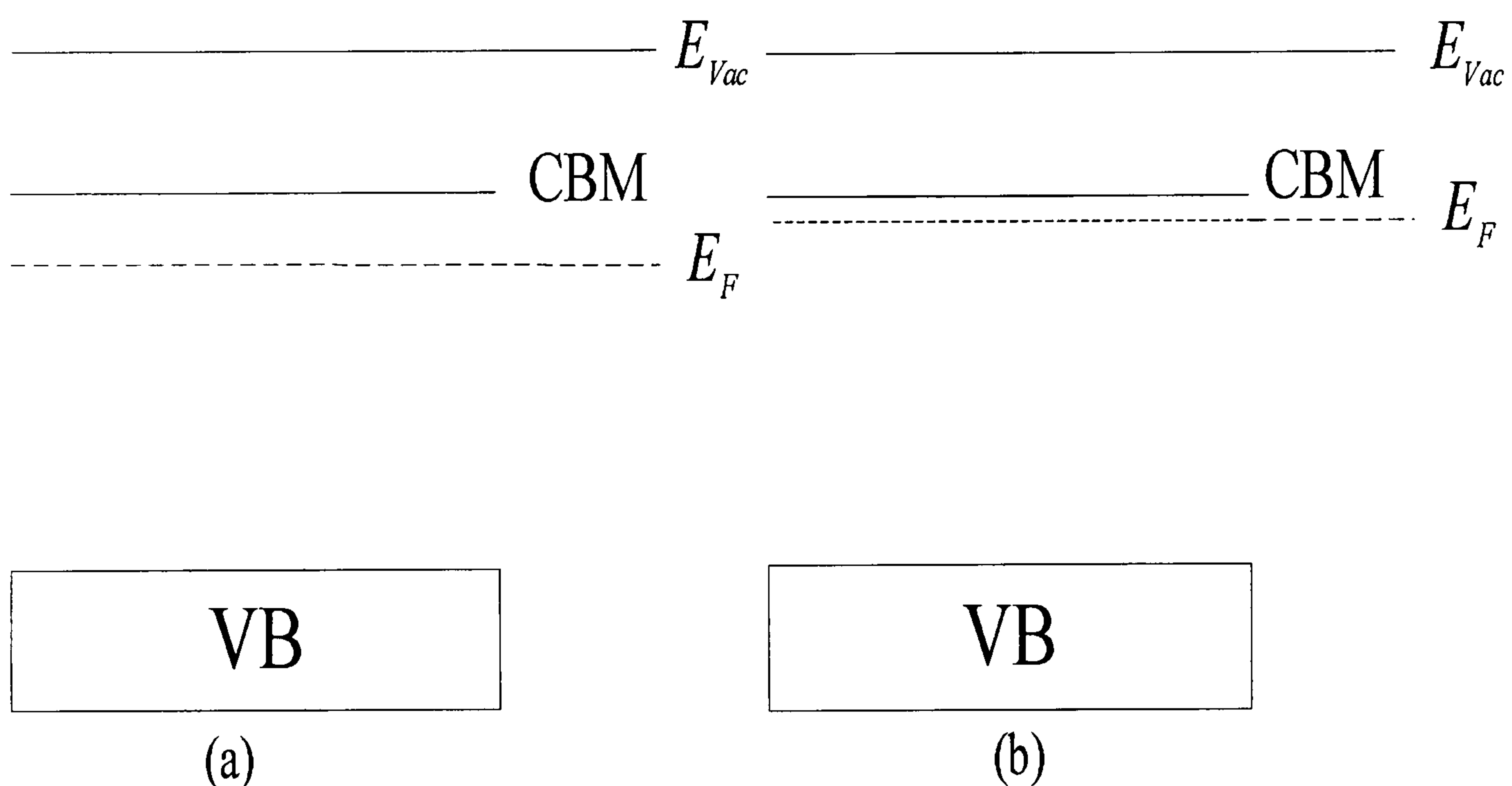


Fig. 4. 8 Comparison of band structure: (a) before annealing and (b) after annealing. During the annealing procedure, appearance of new donor states in the gap donate electrons and shift Fermi edge closer to vacuum level, which is the reason why highest surface state peak position shifts to higher binding energy. CB—conduction band; VB—valence band.

4.5 Angle Resolved Photoemission Spectroscopy of Indium clusters

The angle resolved photoemission spectroscopy of the clean surface InP (100) has been done by two groups [24, 25]. But, to our knowledge, no work has been done on the surface band structure of indium clusters with cluster free In-terminated InP (100)-(2×4) surface. In this work we acquired the angle resolved valence band spectra from the surfaces resulted from heating a perfect (to within experimental sensitivity) InP (100) - (2×4) surface at temperature 470°C and 490°C, and present a detailed analysis of the changes induced in surface band structure.

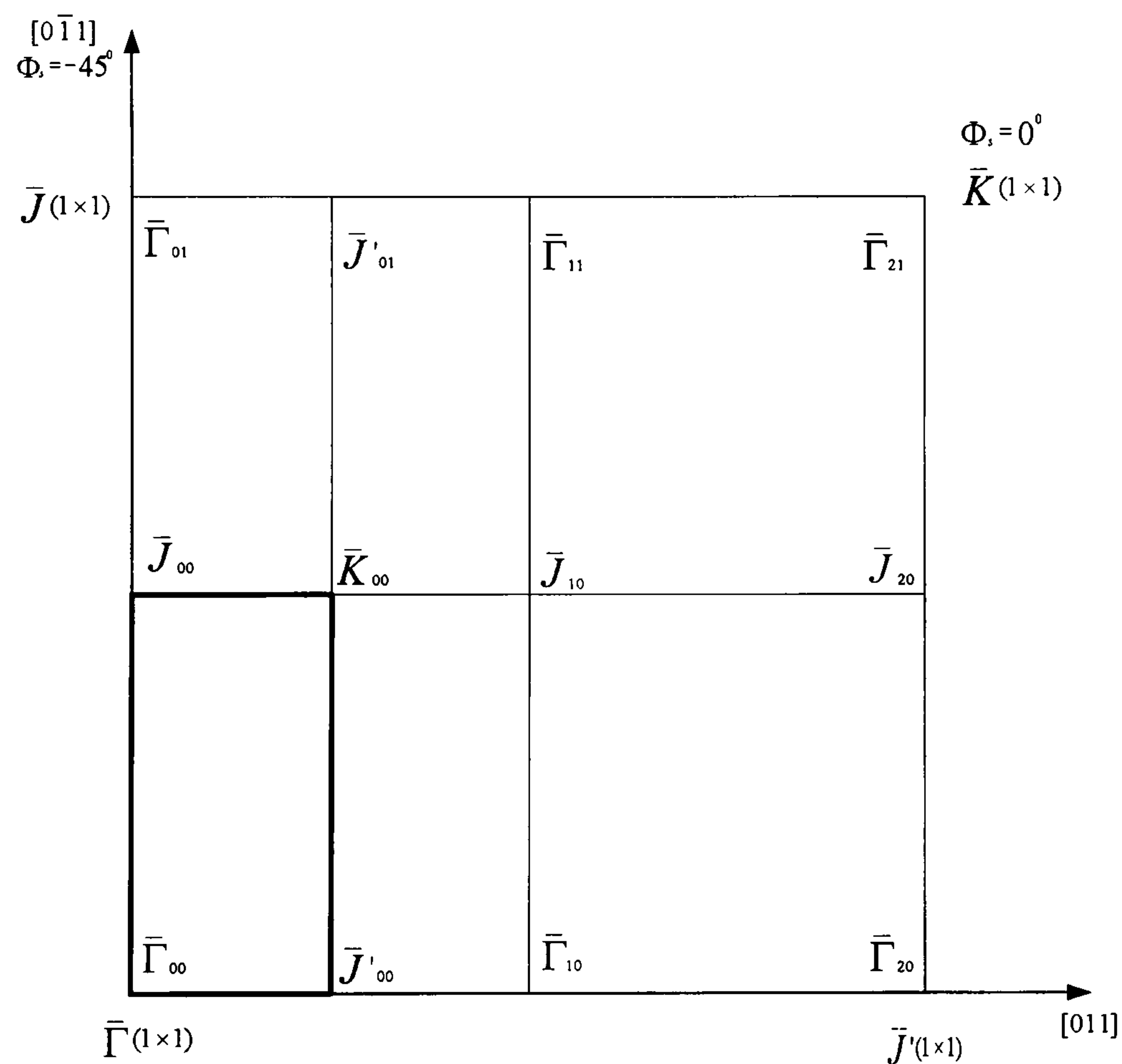


Fig. 4. 9 Schematic drawing of the (1×1) irreducible SBZ with the (2×4) SBZ superimposed (irreducible part in bold) [26]

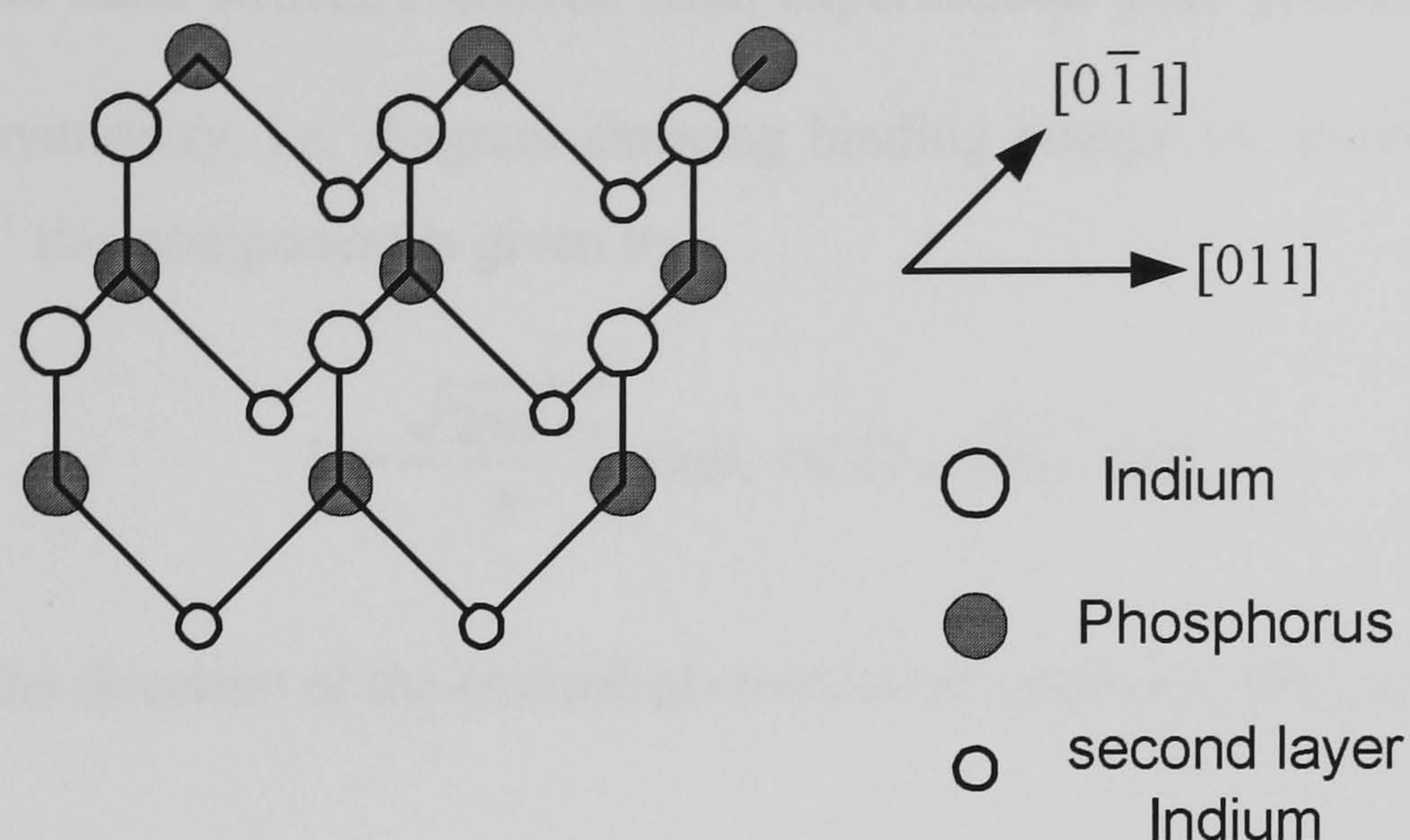


Fig. 4. 10 the ideal (1×1) surface illustrating the $[011]$ and $[0\bar{1}1]$ directions [26]

The schematic of the experimental geometry is illustrated in Fig. 2.12, Chapter 2. All the angles are measured relative to the surface normal. The sample was aligned to the plane defined by incident photon beam $h\nu$ and the photon polarization vector \vec{E} . The surface normal and the photoemission direction \vec{k} were maintained in the same plane. The dispersions were measured along the various symmetry axes by rotating the sample to change the photoemission angle θ_e and by adjusting the sample azimuth ϕ_s . Binding energies for valence band spectra were referenced to the Fermi level of a Ta plate at the base of, and in electrical contact with, the sample holder. Annealing of samples was performed by thermal heating from the backside. Fig. 4.9 is the schematic drawing of the (1×1) irreducible SBZ with the (2×4) SBZ superimposed (irreducible part in bold), and Fig. 4.10 the ideal (1×1) surface illustrating the $[011]$ and $[0\bar{1}1]$ directions. Note that our definition of \bar{J} and \bar{J}' is consistent with that of Ivanov, Mazur and Pollmann [27].

Fig. 4.11 shows row valence band photoemission spectra of clean surface InP (100) - (2×4) collected at photon energy of 24 eV in three azimuth of the sample. Fig. 4.12

shows surface band structure derived from experimental peak positions along the $\bar{\Gamma} - \bar{J}$ and $\bar{\Gamma} - \bar{J}'$ symmetry, i.e. diagram showing binding energy vs. momentum component. In unit of \AA^{-1} this component is given by

$$k_{\parallel} = \frac{\sqrt{2mE_{kin}}}{\hbar} \sin\theta_e = 0.512 \sqrt{E_{kin}} \sin\theta_e \quad (4.1)$$

where θ_e is the direction of the emitted photoelectron relative to the surface normal [28].

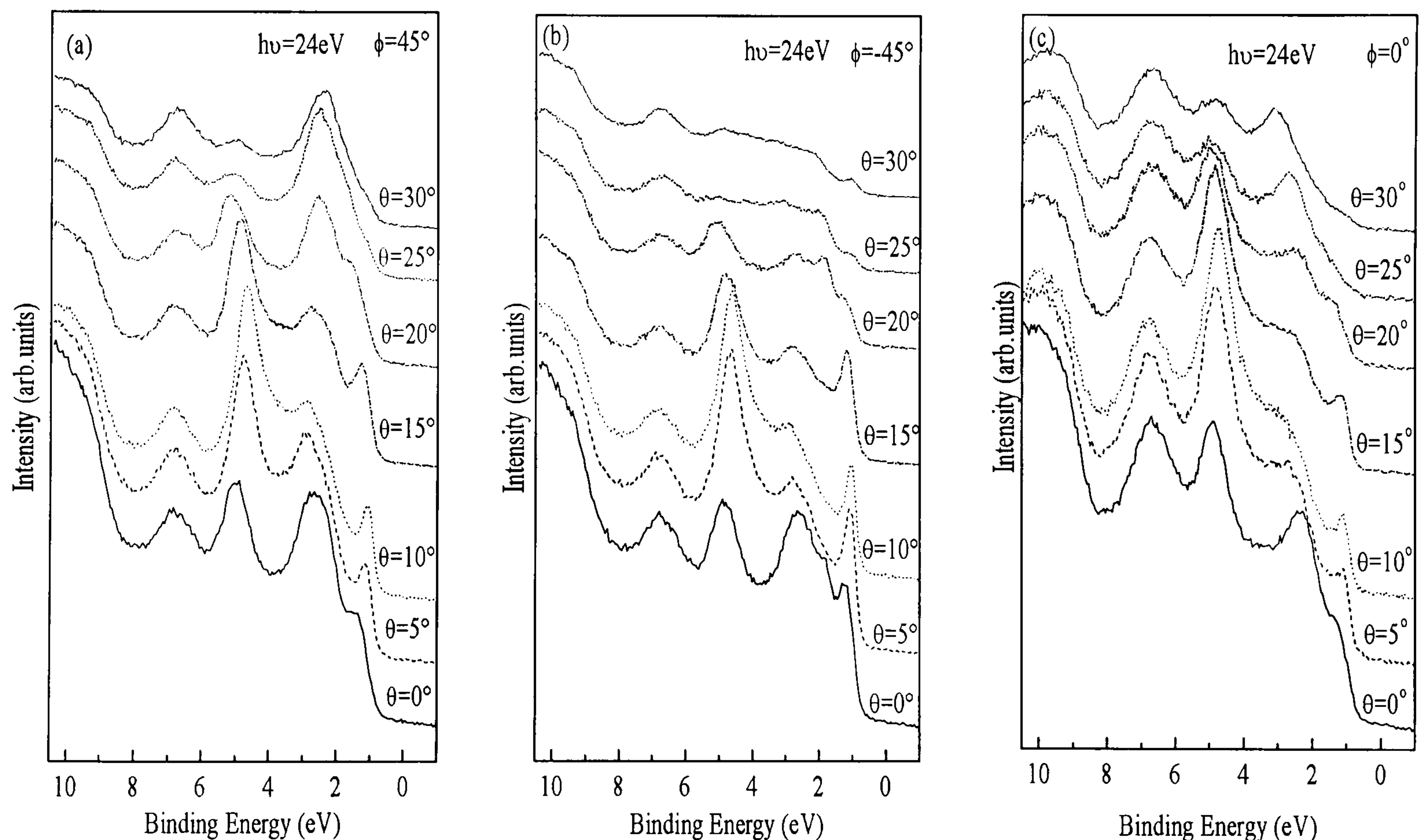


Fig. 4. 11 Valence band photoemission spectra of clean surface InP (100)-(2×4) collected at photon energy of 24 eV in three azimuth of the sample: (a) $\Phi = 45^\circ$, (b) $\Phi = -45^\circ$, (c) $\Phi = 0^\circ$

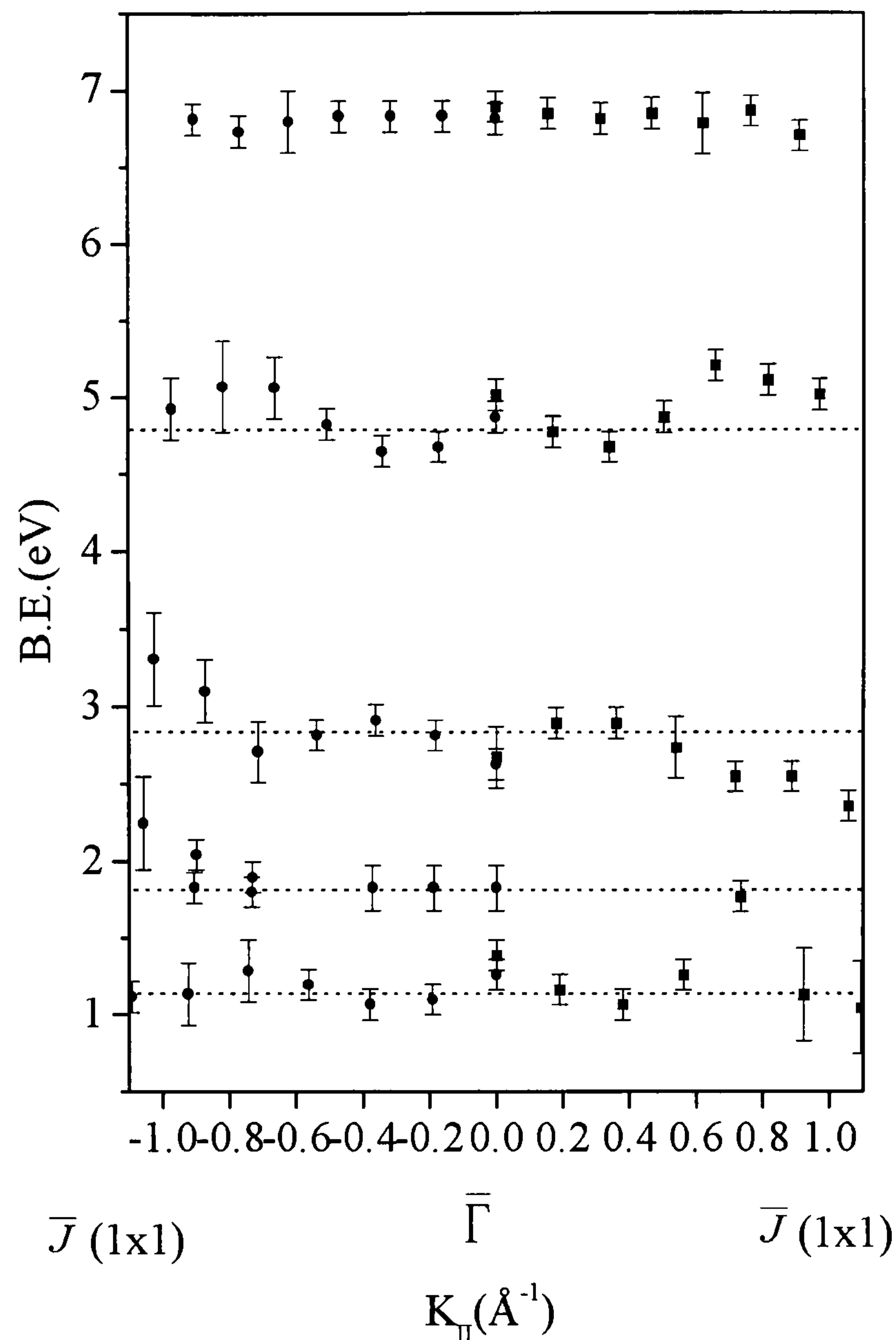


Fig. 4. 12 Surface band structure derived from experimental peak positions on valence band spectra of clean surface InP(100)-(2×4) along the $\bar{\Gamma} - \bar{J}$ and $\bar{\Gamma} - \bar{J}'$ symmetry

In ref. ([26]) three surface states, located at binding energy $E_B = 1.0$ eV, 1.8 eV and 4.3 eV, have been reported. In Fig. 4.12, we got the results at binding energy $E_B = 1.14$ eV, 1.81 eV, 2.84 eV and 4.79 eV respectively.

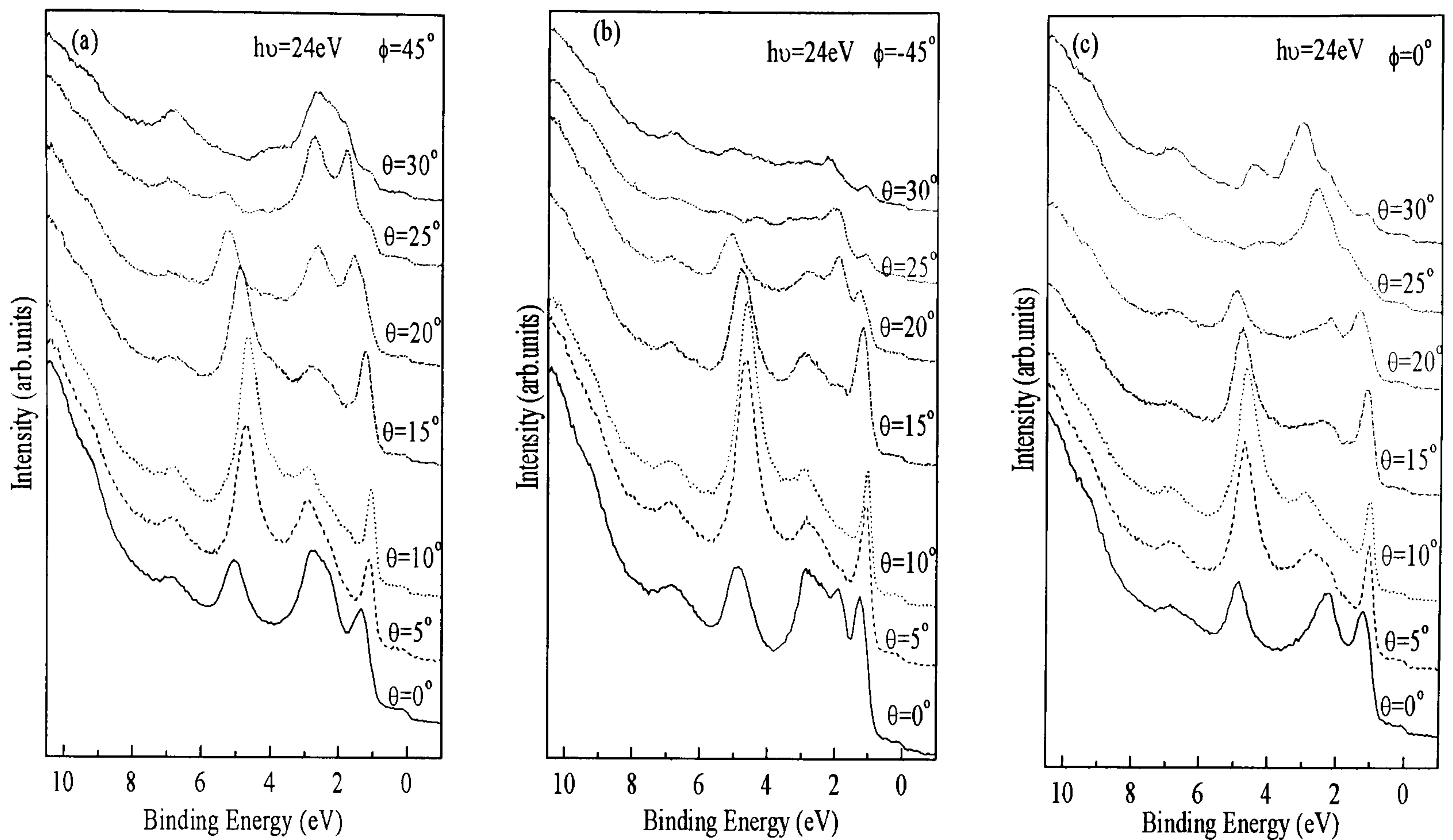


Fig. 4. 13 Valence band photoemission spectra of InP (100) surface after annealed at 470°C, collected at photon energy of 24 eV in three azimuth of the sample: (a) $\Phi = 45^\circ$, (b) $\Phi = -45^\circ$, (c) $\Phi = 0^\circ$

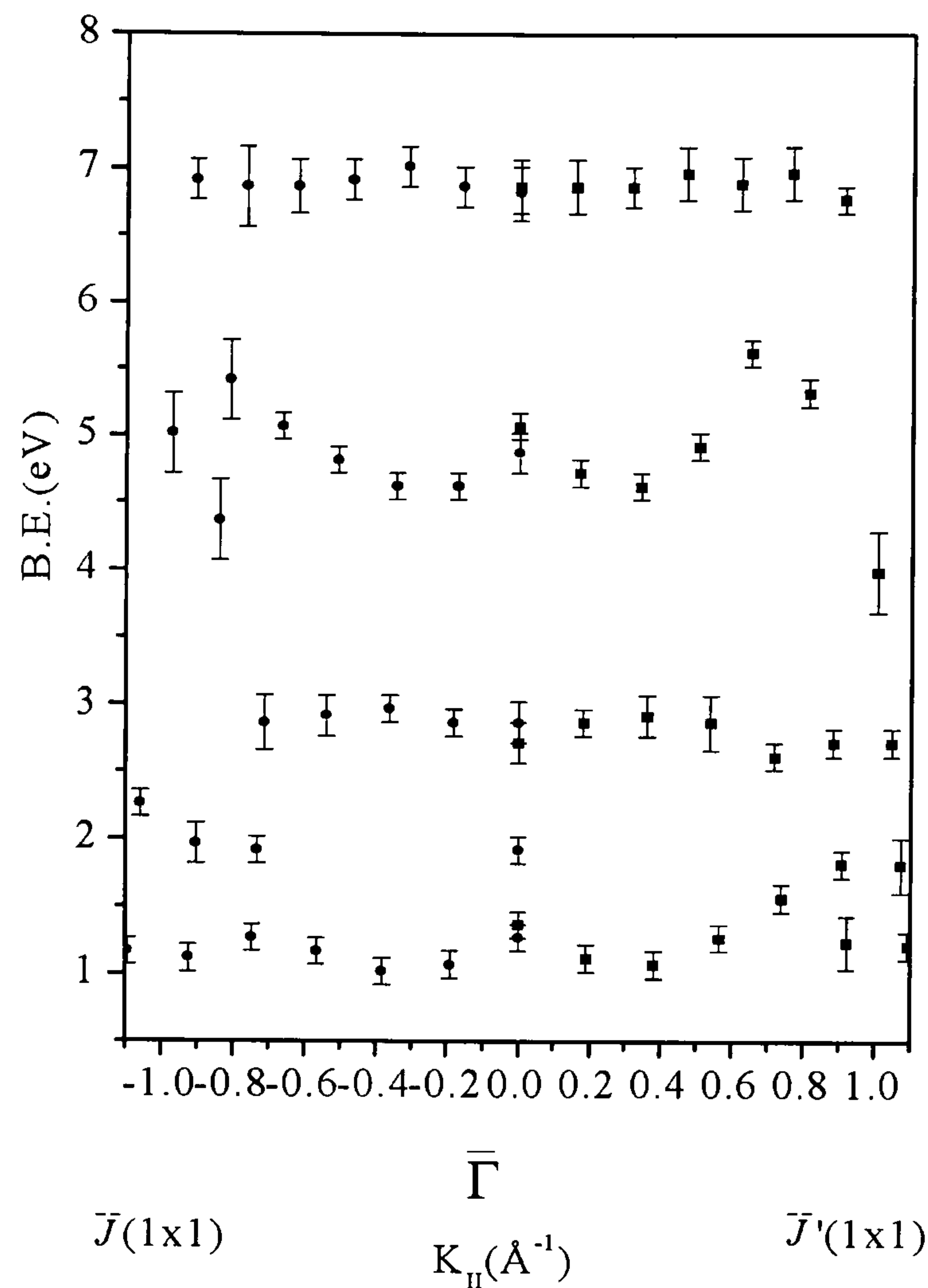


Fig. 4. 14 Surface band structure derived from experimental peak positions on the valence band spectra along the $\bar{\Gamma} - \bar{J}$ and $\bar{\Gamma} - \bar{J}'$ symmetry, sample was annealed at 470°C.

Fig. 4.13 shows valence band photoemission spectra of InP (100) surface after heated at 470°C, collected at photon energy of 24 eV in three azimuth of the sample. Fig. 4.14 shows surface band structure derived from experimental peak positions along the $\bar{\Gamma} - \bar{J}$ and $\bar{\Gamma} - \bar{J}'$ symmetry. Comparing Fig. 4.13 to Fig. 4.11, $\phi_s = 45^\circ$, $\theta_e = 25^\circ$ and 30° one can see the states at binding energy 1.81 eV very clear, which does not exist in Fig. 4.11, $\phi_s = 45^\circ$; in $\phi_s = 45^\circ$, $\theta_e = 30^\circ$, the peak at 5.03 eV shifted to 3.97 eV. In Fig. 4.13 the Fermi edge is clearly visible.

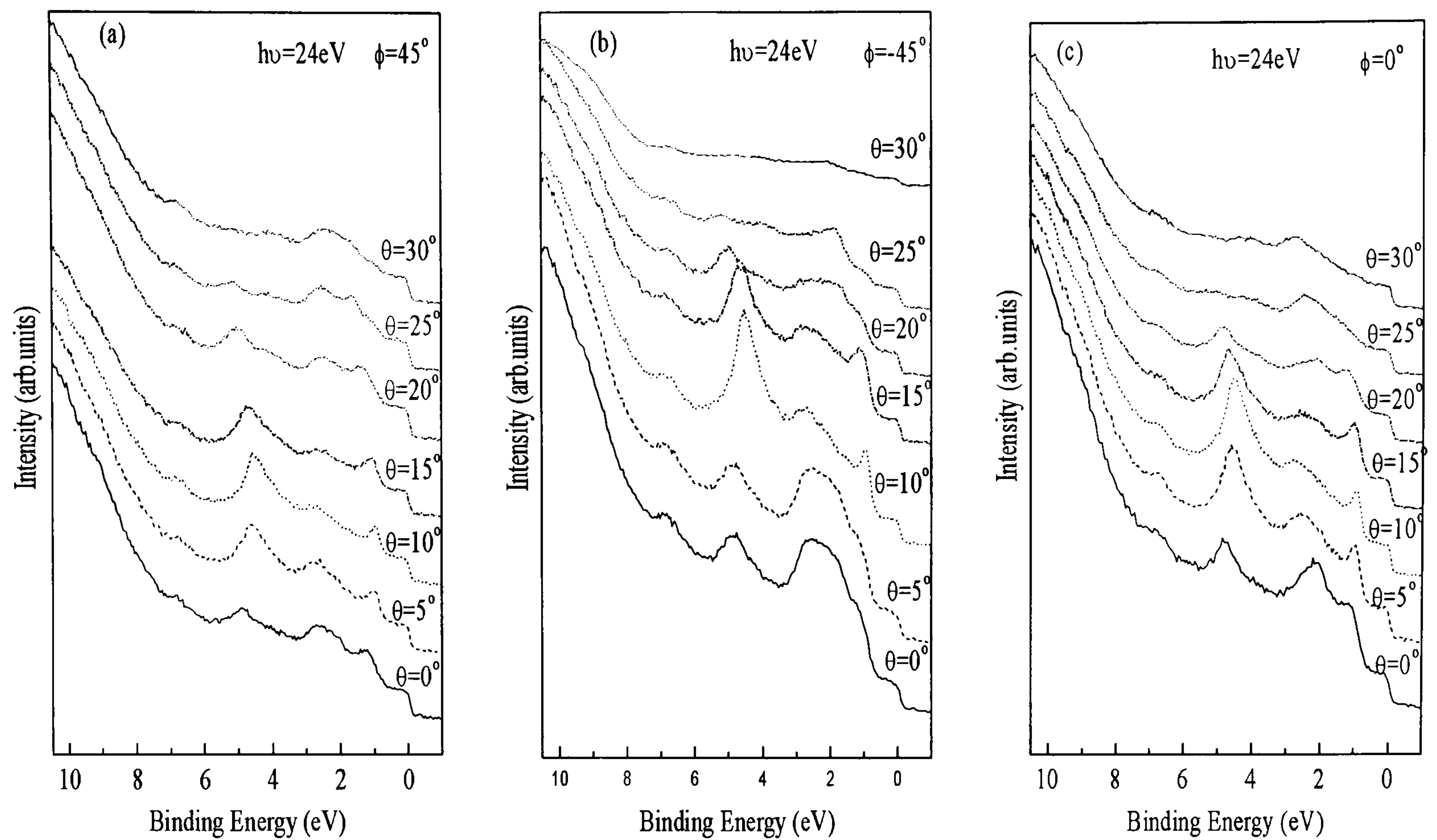


Fig. 4. 15 Valence band photoemission spectra of InP (100) surface after annealed at 490°C, collected at photon energy of 24 eV in three azimuth of the sample: (a) $\Phi = 45^\circ$, (b) $\Phi = -45^\circ$, (c) $\Phi = 0^\circ$.

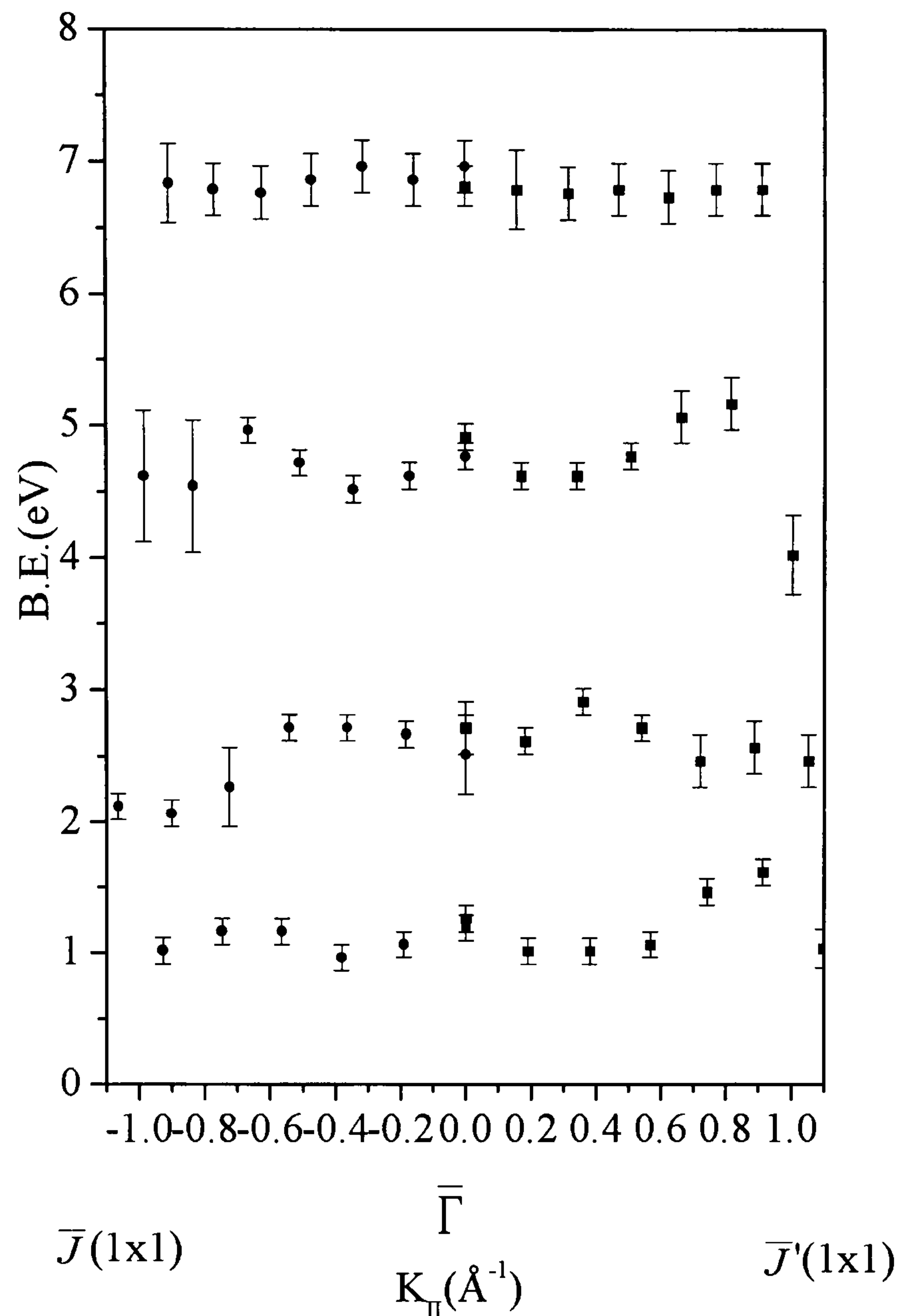


Fig. 4. 16 Surface band structure derived from experimental peak positions on the valence band spectra along the $\bar{\Gamma}$ - \bar{J} and $\bar{\Gamma}$ - \bar{J}' symmetry, sample was annealed at 490 °C.

Fig. 4.15 shows valence band photoemission spectra of InP (100) surface after heated at 490 °C, collected at photon energy of 24 eV in three azimuth of the sample. Fig. 4.16 shows Surface band structure derived from experimental peak positions along the $\bar{\Gamma}$ - \bar{J} and $\bar{\Gamma}$ - \bar{J}' symmetry. Also the Fermi edge is clearly visible.

4.6 AFM images of indium clusters

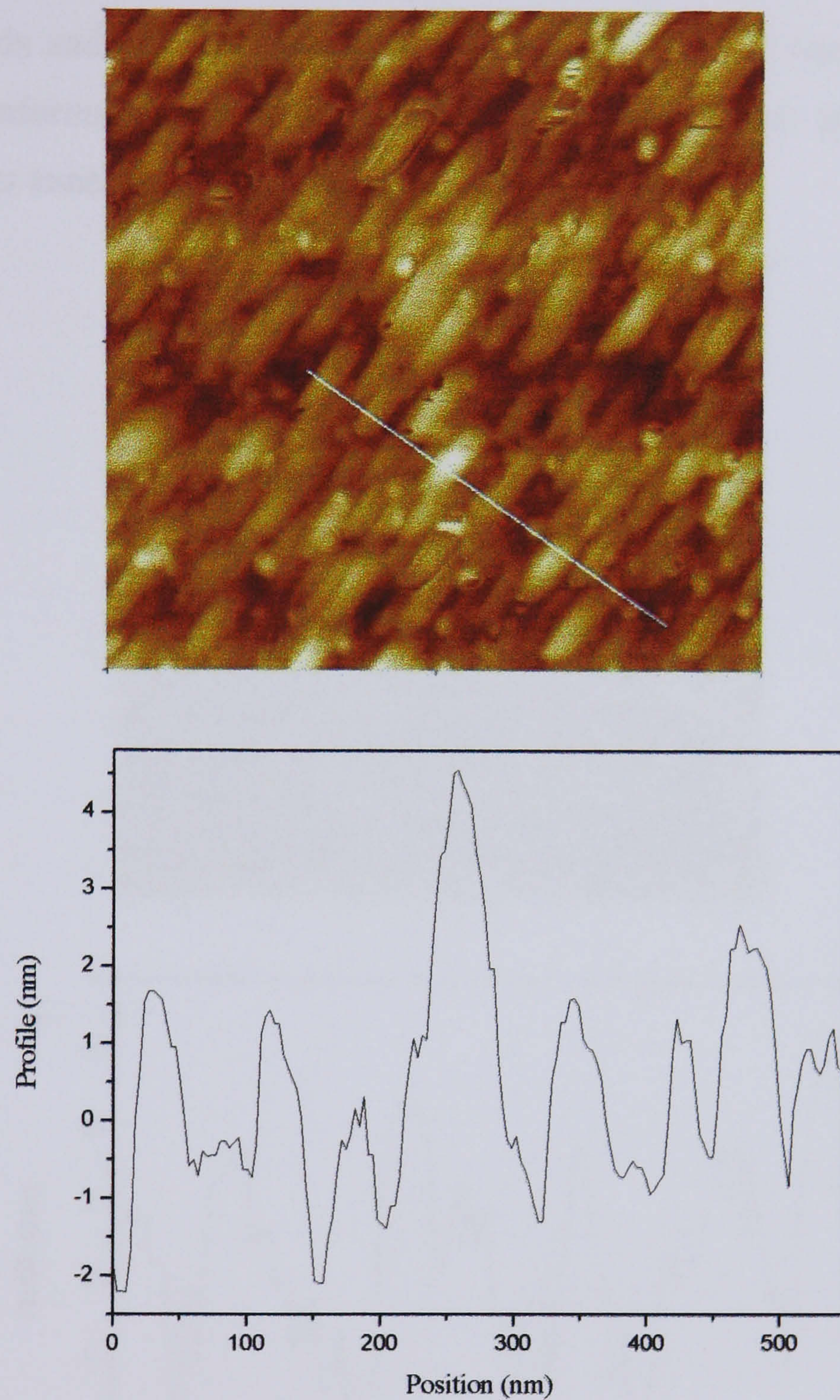


Fig. 4. 17 AFM image from the sample evenly heated at 440 °C, scan area $1 \times 1 \mu\text{m}$, scan speed $4 \mu\text{m}$ per second. The profile was taken along the white line.

After the PES experiments in UHV we took the sample out and checked in air with AFM described in Chapter 2. The AFM images for both evenly heated and temperature-gradient-heated samples are shown in Fig. 4.17 and Fig. 4.18. The both

images were obtained for the same scan area, $1 \times 1 \mu\text{m}$, and the profiles obtained along the line cross part of the image. By comparing the both images, one can see well developed rectangular islands and many larger circular islands in Fig. 4.18 than in Fig. 4.17. This might give the information on indium cluster development level: the scan area in Fig. 4.18 was at higher annealing temperature.

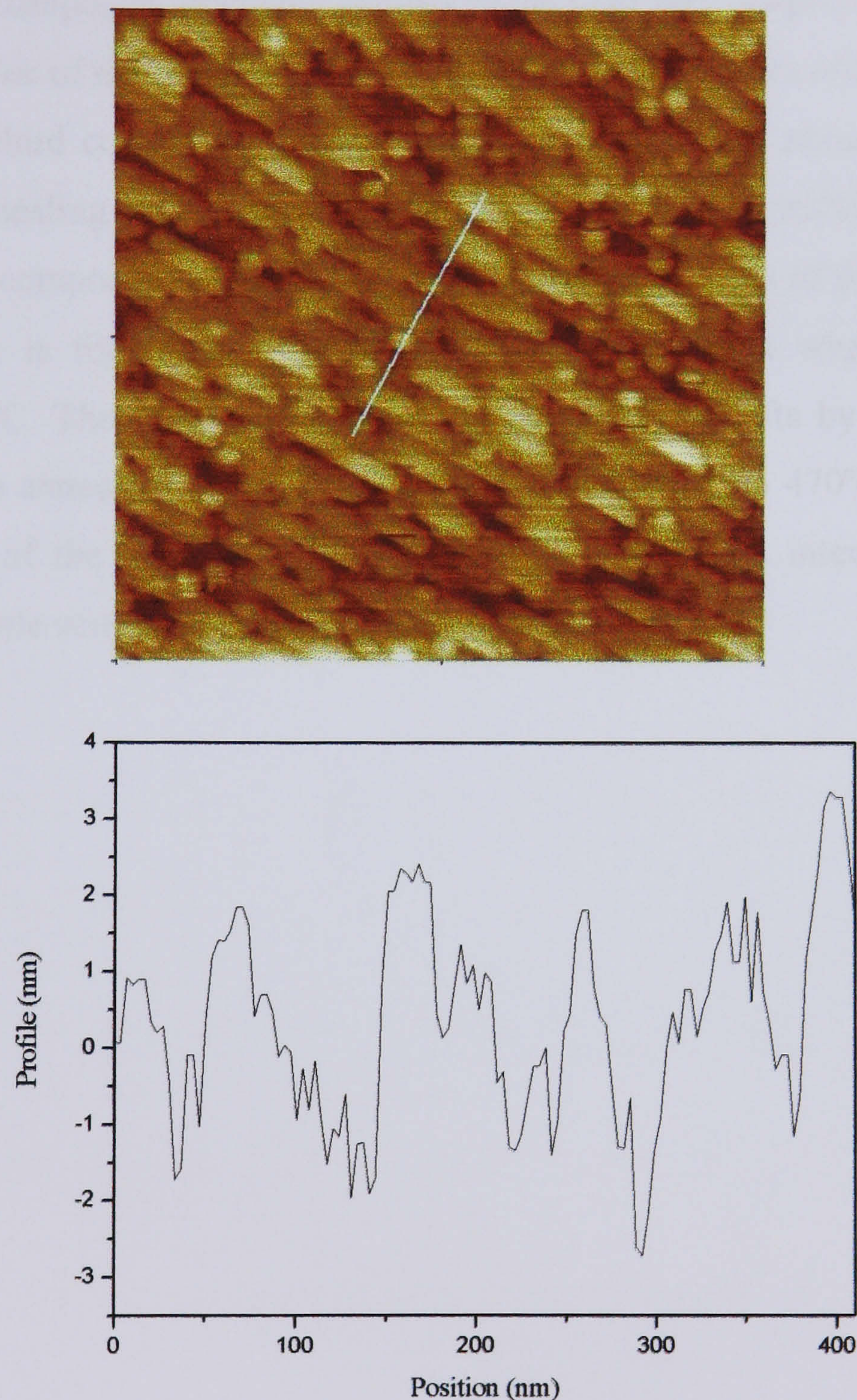


Fig. 4. 18 AFM image from the temperature-gradient-heated sample, scan area $1 \times 1 \mu\text{m}$, scan speed $4 \mu\text{m}$ per second, scan at 90° direction, indicated the features are real. The profile was taken along the white line.

4.7 Summary

In conclusion, the annealing of clean InP (100)-(2 × 4) surfaces, free from excess indium, was investigated by PES, ARPES and AFM.

Above the thermal desorption temperature of phosphorous (360°C) [11, 29] a metallic indium component gradually appears in the In4*d* line. As-prepared InP (100)-(2 × 4) surfaces are free of metallic indium and the 4*d* core level shows only two clear surface components. A third component, indium cluster-related, due to phosphorous desorption appears after annealing and is accompanied by a corresponding reduction in intensity in the In-P surface component. By careful inspection of the features of the In4*d* and valence band spectra, it is found that a visible Fermi edge appears when the temperature approaches 440°C. The cluster component of the In4*d* line shifts by 0.2 eV in binding energy when the annealing temperature is raised from 420°C to 470°C. This shift in the binding energy of the cluster-related core level component is interpreted in terms of improved core hole screening with increasing cluster size.

4.8 References

- [1] D. Dalacu, E. Jolanta, E. Klemberg-Sapieha, and L. Martinu, *Surf. Sci.* **472**, 33 (2001).
- [2] T. D. Lowes and M. Zinke-Allmang, *Phys. Rev. B* **49**, 16678 (1994).
- [3] G. K. Wertheim and S. B. DiCenzo, *phys.Rev. B* **37**, 844 (1988).
- [4] G. K. Wertheim, S. B. Dicenszo, and D. N. E. Buchanan, *Phys. Rev. B* **33**, 5384 (1986).
- [5] W. A. de Heer, *Rev. Mod. Phys.* **65**, 611 (1993).
- [6] M. Valdem, X. Lai, and D. W. Goodman, *Science* **281**, 1647 (1998).
- [7] H. B. Liao, R. F. Xiao, J. S. Fu, H. Wang, K. S. Wong, and G. K. L. Wong, *Opt. Lett.* **23**, 388 (1998).
- [8] D. Ricard, P. Roussignol, and C. Flytzanis, *Opt. Lett.* **10**, 511 (1985).
- [9] S. H. M. Persson and L. Olofsson, *Appl. Phys. Lett.* **74**, 2546 (1999).
- [10] U. Kreibig and M. Vollmer, *Optical Properties of Metal Clusters* (Springer-Verlag, 1995).
- [11] H. Yamaura, T. Jinkawa, J. Tamaki, K. Moroya, N. Miura, and N. Yamazoe, *Sensors and Actuators B* **35-36**, 325 (1996).

- [12] N. G. Patel, K. K. Makhija, C. J. Panchal, D. B. Dave, and V. S. Vaishnav, *Sensors and Actuators B* **23**, 49 (1995).
- [13] M. Broyer, *J. Non-Crystalline Solids* **156**, 787 (1993).
- [14] Y. Chao, K. Svensson, D. Radosavkic, V. R. Dhanak, L. Šiller, and M. R. C. Hunt, *Phys. Rev. B* **64**, 235331 (2001).
- [15] Y. Chao, K. Svensson, D. Radosavkic, V. R. Dhanak, M. R. C. Hunt, and L. Šiller, *Phys. Rev. B* **66**, 075323 (2002).
- [16] W. M. Lau, R. N. S. Sodhi, B. J. Finn, K. H. Tan, and G. M. Bancroft, *Appl. Phys. Lett.* **51**, 177 (1987).
- [17] R. K. Gebhardt, A. B. Preobrajenski, and T. Chasse, *Phys. Rev. B* **61**, 9997 (2000).
- [18] S. Sloboshanin, R. K. Gebhardt, J. A. Schaefer, and T. Chasse, *Surf. Sci.* **431**, 252 (1999).
- [19] R. K. Gebhardt, S. Sloboshanin, J. A. Schaefer, and T. Chasse, *Appl. Surf. Sci.* **142**, 94 (1999).
- [20] W. G. Schmidt, F. Bechstedt, N. Esser, M. Pristovsek, C. Schultz, and W. Richter, *Phys. Rev. B* **57**, 14596 (1998).

- [21] M. Shimomura, N. Sanada, G. Kaneda, T. Takeuchi, Y. Suzuki, Y. Fukuda, W. R. A. Huff, T. Abukawa, S. Kono, H. W. Yeom, and A. Kakizaki, *Surf. Sci.* **413**, 625 (1998).
- [22] V. Chab, L. Pekarek, I. Ulrych, J. Suchy, K. C. Prince, M. Peloi, M. Evans, C. Comicioli, M. Zacchigna, and C. Crotti, *Surf. Sci.* **377**, 261 (1997).
- [23] C. Schultz, A. M. Frisch, K. Hinrichs, J. Kinsky, T. Herrmann, U. Rossow, N. Esser, and W. Richter, *J. Vac. Sci. Technol. B* **15**, 1260 (1997).
- [24] A. M. Frisch, P. Vogt, S. Visbeck, T. Hannappel, F. Willing, W. Braun, W. Richter, J. Bernholc, W. G. Schmidt, and N. Esser, *Surf. Sci.* **166**, 224 (2000).
- [25] W. R. A. Huff, M. Shimomura, N. Sanada, G. Kaneda, T. Takeuchi, Y. Suzuki, H. W. Yeom, T. Abukawa, S. Kono, and Y. Fukuda, *J. Electron Spectrosc. Relat. Phenom.* **88**, 609 (1998).
- [26] W. R. A. Huff, M. Shimomura, N. Sanada, G. Kaneda, Y. Suzuki, H. W. Yeom, T. Abukawa, S. Kono, and Y. Fukuda, *Phys. Rev. B* **57**, 10132 (1998).
- [27] I. Ivanov, A. Mazur, and J. Pollmann, *Surf. Sci.* **92**, 365 (1980).
- [28] M. C. Hkansson, L. S. O. Johansson, C. B. M. Andersson, U. O. Karlsson, L. O. Olsson, L. Ilver, J. Kanski, and P. O. Nilsson, *Surf. Sci.* **374**, 73 (1997).
- [29] M. GajdardziskaJosifovska, M. H. Malay, and D. J. Smith, *Surf. Rev. Lett.* **4**, 655 (1997).

Chapter 5 Luminescent Alkylated Si Quantum Dots

Alkyl-modified silicon nanocrystallites are efficient fluorophores which are of interest for fundamental spectroscopic studies and as luminescent probes in biology because of their stability in aqueous media. In this work we have investigated these particles using scanning tunnelling microscopy (STM), synchrotron radiation excited photoemission spectroscopy (SRPES) and X-ray excited optical luminescence (XEOL). During the course of illumination with 145 eV photons we have monitored the evolution of the Si 2p core level, and observed in real time a splitting and growth of a new Si 2p component assigned to the Si^{4+} oxidation state of Si. This new peak is attributed to in situ oxidation of Si nanocrystallites caused by photo-induced reaction, possibly with multilayers of water present on the surface of the quantum dots. XEOL reveals that three emission bands are active upon soft X-ray photon excitation. An interesting reversible ageing phenomenon of photoluminescence is observed upon exposure to the X-rays which is possibly due to prolonged trapping of charge in the alkyl chains attached to the Si/SiO_x core.

5.1	Some aspects of silicon quantum dots synthesis and STM image	131
5.2	Core level spectra: line shape and shift	139
5.3	NEXAFS of Alkylated silicon quantum dots.....	151
5.4	Photoluminescence Spectra	152
5.5	Summary	156
5.6	References.....	157

The current microelectronic technology should reach feature sizes on chip of about 20-30 nm by the year 2016. Below this limit the transport, electronic, and optical properties of bulk silicon start to be influenced significantly by quantum confinement effects. Therefore, it is desirable to develop techniques of fabrication of silicon NCs (Si-NCs) and study their physical properties. The second reason for intensive investigation of Si nanostructures is their potential application in light-emitting devices integrated on a chip. Compared to the weak IR luminescence of bulk silicon (observed only at low temperatures), the efficiency of photoluminescence (PL) from Si nanostructures is increased enormously.

Sample preparation can be found in section 2.4.2, Soft X-ray photoemission spectra were acquired at beamline I-511 of MAXLab, Lund, Sweden and both photoemission and XEOL spectra were measured at beamline 4.1 of the synchrotron radiation source (SRS), Daresbury UK. The XEOL measurement details can be found in section 2.7. All the binding energy calibration can be found in section 2.3.2. It should be noted that all the films measured display some degree of charging, ultimately reaching an equilibrium state, as discussed below. Consequently, the “binding energies” quoted do not reflect the true binding energies of the core level photoelectrons, but incorporates the energy required for the electrons to escape the surface charge distribution. However, the degree of charging is small and does not prevent identification of the elemental composition and chemical state of the silicon nanocrystallites, which are considered later.

5.1 Some aspects of silicon quantum dots synthesis and STM image

To obtain silicon quantum dots first step [1] is electrochemical etching silicon chip to get porous silicon layer. Porous Si (designated π -Si as the similar pronunciation) was discovered in 1956 [2]. The visible luminescence of porous Si was observed more recently by L. T. Canham [3]. The porous layer is created by electrochemical dissolution (anodization or etching) in HF-based electrolytes. Fig. 2.13 and Fig. 2.14 show the schematic of porous silicon fabrication cell and the specific processes involved in anodic etching at and close to the pore. It is based on the fact that holes are necessary for the

electrochemical dissolution process of Si. Holes (h^+) arriving at the Si:HF solution interface etch the Si lattice



Etching creates a rough surface. Since bandgap in π -Si increases compared with bulk c-Si due to the quantum confinement effect [4], holes need the additional energy E_q to penetrate into the porous layer. If E_q is larger than the bias, porous layer becomes depleted of holes and further dissolution is stopped. Since E_q is a function of the size of the nanocrystals, one can conclude that an increase in the formation bias will result in an increase in bandgap energy and a decrease in crystallite size in the porous layer. This process is self adjusting. Quantum confinement effect limits the size of the nanocrystals [5]. Fig. 5.1 schematically illustrates π -Si fabrication, the chemical process in anodic etching near the pore tip and the band diagram for silicon-electrolyte transition at the pore tip and between the bulk and π -Si.

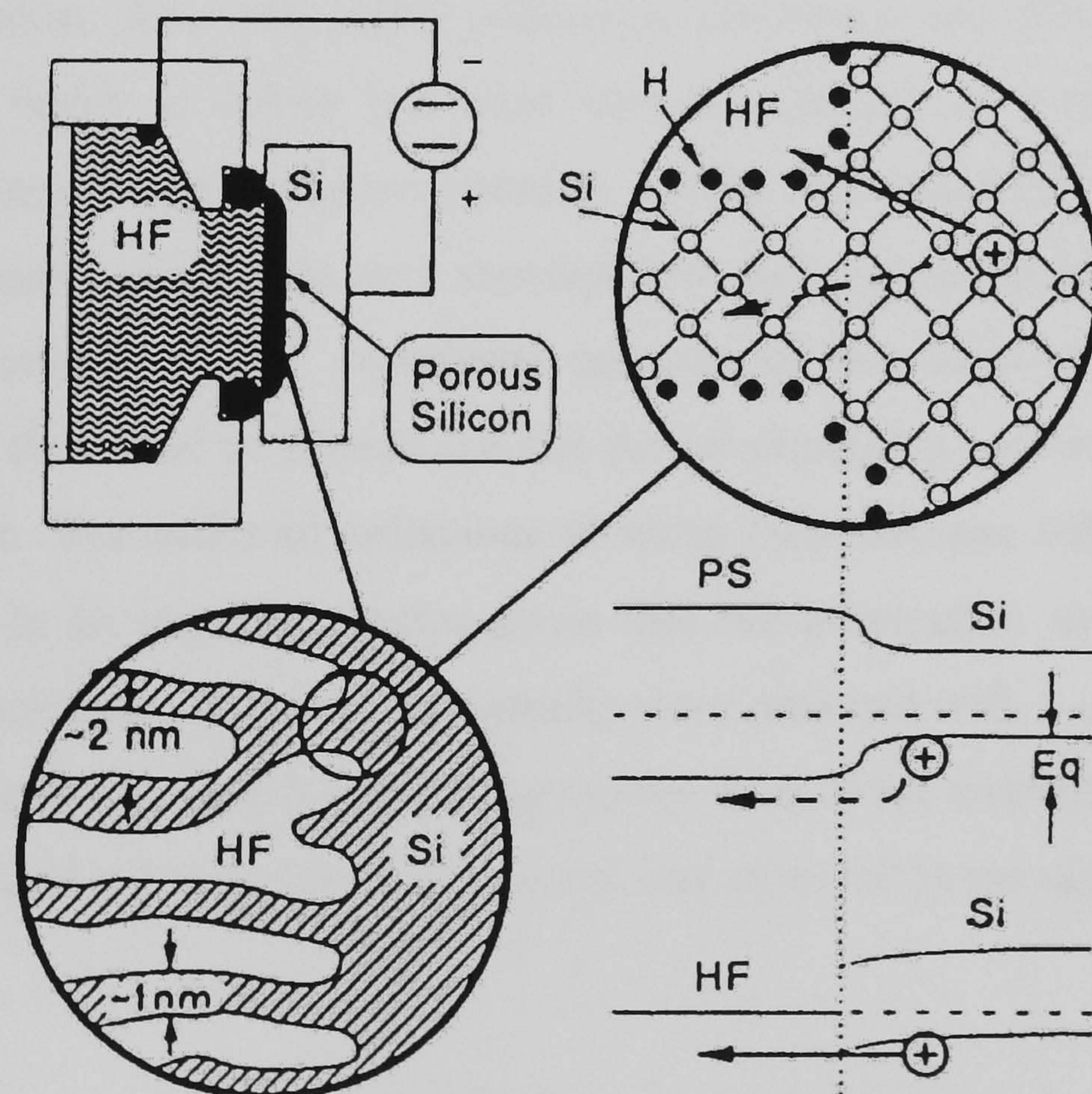


Fig. 5. 1 Schematic of π -Si fabrication, the chemical process in anodic etching near the pore tip and the band diagram for silicon-electrolyte transition at the pore tip and between the bulk and π -Si [4]

Different etching current densities were used to investigate the current effect to the quality of quantum dots [6]. Fig. 5.2 shows the silicon chips surface aspect after electrochemical etching at different current densities. To obtain high quality luminescent silicon quantum dots, higher current density is needed.

After cleaving the porous silicon layer from the substrate wafer by the high current density “electro-polishing” step, a fluorescing powder was formed. The colour of the fluorescence under illumination from a handheld mercury lamp was dependent on the current density used to prepare the porous silicon and varied from red to orange as the current density was increased; this effect is well-known in studies of porous silicon film [7-9]. The powder, which was loosely bound in small clumps of ca. 0.1—1 mm diameter, showed the same red fluorescence in EtOH + HF etch solution as in dry toluene or after drying on a filter paper. Refluxing the powder in pure dry toluene overnight had no effect, but if an alkene (1-octene, 1-undecene, 1-undecene-11-ODMT, or 1, 9-decadiene) was added to the reflux, most of the clumps of silicon powder appeared to dissolve to form a luminescent solution. After this reflux procedure, the liquid was observed to be a pale yellow and the depth of colour increased with the amount of powder dissolved. A comparison between three 1-alkenes (hexene, octane and undecene) revealed that the solution forms easily with undecene, incompletely with octene and hardly at all with hexene. In the case of octene, significant amounts of powdered porous silicon were undissolved, but this could be filtered out and the sol remaining was transparent as in the case of undecene. The different behaviour of these three alkenes reflects their relative volatility which is an important factor given that the preparation involves reaction in boiling toluene solutions. Since the best results were obtained with 1-undecene, we have concentrated on sols prepared from 1-undecene for most of the characterisations reported below although similar luminescence behaviour was observed in the case of 1-octene.

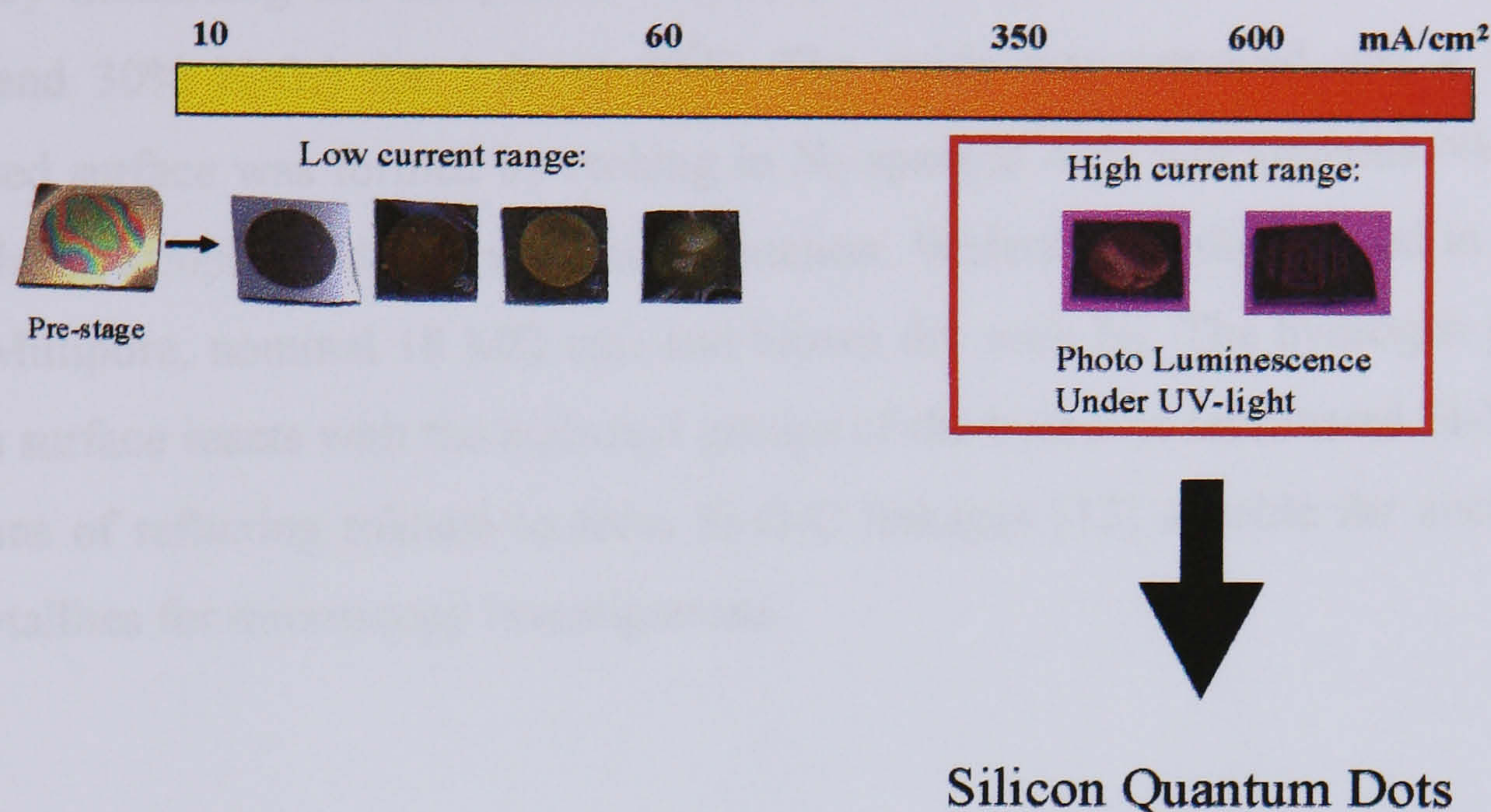


Fig. 5. 2 the silicon chip surface aspects after electrochemical etching at different current densities, higher current density needed for preparing luminescent silicon quantum dots

Fig. 5.3 shows the schematic structure of the prepared silicon quantum dots. The estimated size of Q-dot is 1.3-1.7 nm [6]. High resolution transmission electron microscopy (HRTEM) studies of the resulting material indicate that the nanocrystallites are certainly smaller than 6 nm – difficulties in dispersion of the particles, probably due to their very small size, make a more accurate diameter determination difficult [10].

To obtain a more accurate measure of the diameter of the nanocrystallites, scanning tunnelling microscopy (STM) measurements of hydroxyl-terminated nanocrystallites dispersed on a hydrogen passivated Si (111) surface has been made [11]. Hydroxyl-terminated nanocrystallites were prepared using dimethoxytrityl-protected undecenol in the hydrosilation procedure for formation of the nanocrystallites. The hydroxyl groups were exposed by cleaving the trityl protecting group in HF/EtOH from the porous silicon etch prior to cleaving the nanocrystallites from the porous silicon surface. The hydrogen passivated Si(111) surface was prepared by a deoxygenated NH_4F etch in which $\langle 111 \rangle$ oriented silicon wafers (phosphorus-doped, n-type, 1-20 Ω cm resistivity, < 0.1 degree miscut, Compart Technology, Peterborough, UK) were first cut into 1 cm^2 square pieces and then degreased with trichloroethylene followed by acetone. An oxide layer was

formed by immersing the samples in freshly prepared 'piranha' solution (1:4 v/v conc. H_2SO_4 and 30% H_2O_2) for 1 h. at 80°C . The oxide was removed and a hydrogen-terminated surface was formed by etching in N_2 -sparged 40% w/v aqueous NH_4F for 20 min with the sample held in a vertical orientation. Wafers were then rinsed in deionized water (Millipore, nominal $18\text{ M}\Omega\text{ cm}$) and blown dry with N_2 . The hydrogen passivated Si (111) surface reacts with the hydroxyl groups of the hydroxyl terminated Si-NCs under conditions of refluxing toluene to form Si-O-C linkages [12] suitable for anchoring the nanocrystallites for microscopy investigations.

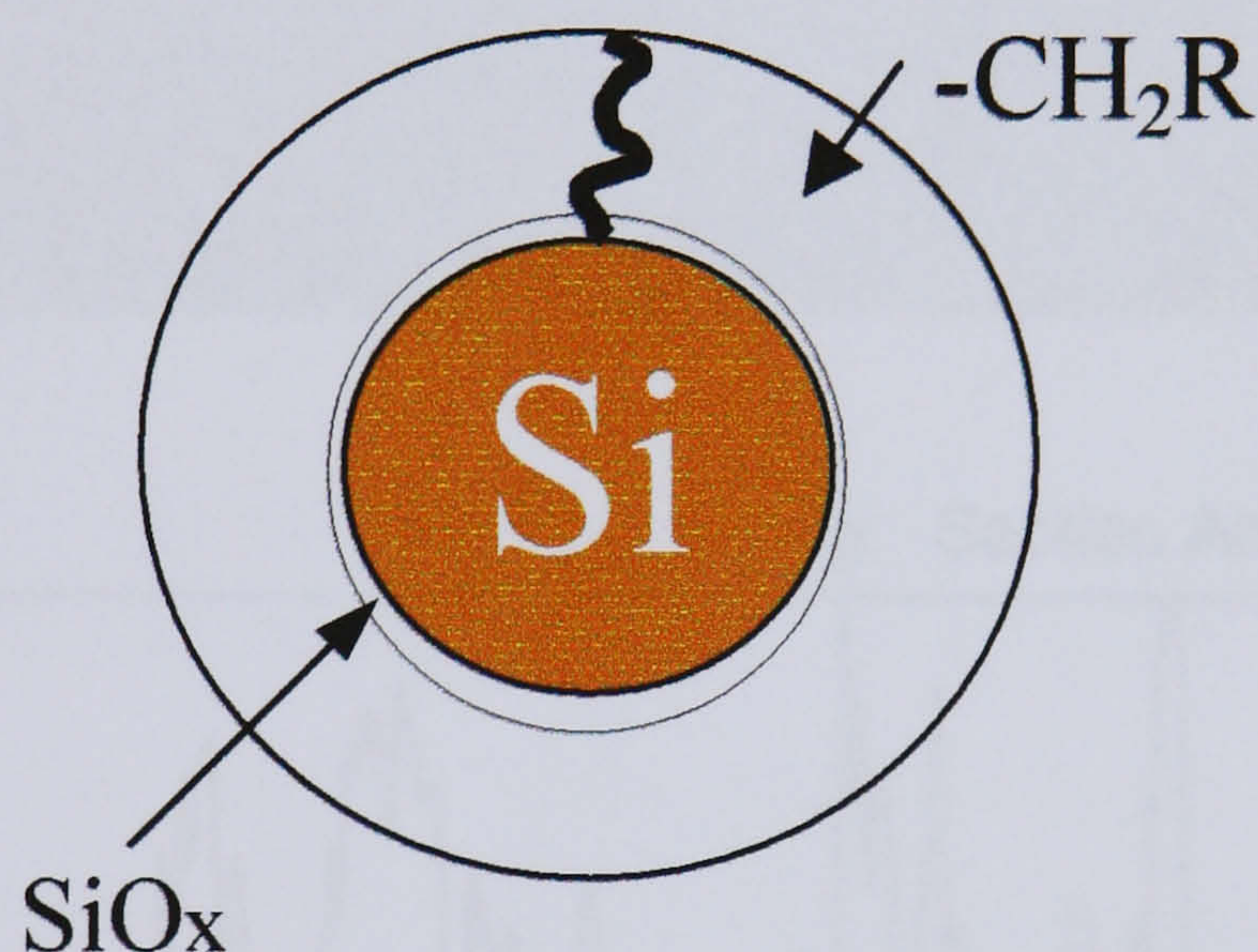


Fig. 5. 3 Prepared silicon quantum dots structure: silicon core with thin layer of SiO_x and hydrocarbon chain around

Figure 5.4 (a) show an STM image of silicon nanocrystallites dispersed on the passivated Si (111) surfaces. The tunnelling current was 66 pA with a bias voltage of 1.5 V, and the samples were imaged under ambient conditions. The STM images show evidence for clustering of the nanocrystallites, reflected in differing lateral extent of the raised topographic features. However, the height of these features is ca. 4 - 5 nm (see figure 5.4 (b)) which is in rough agreement with previous estimates of the Si core from Raman spectroscopy (2.5 nm, [13]) plus the thickness of the C_{11} alkyl chains.

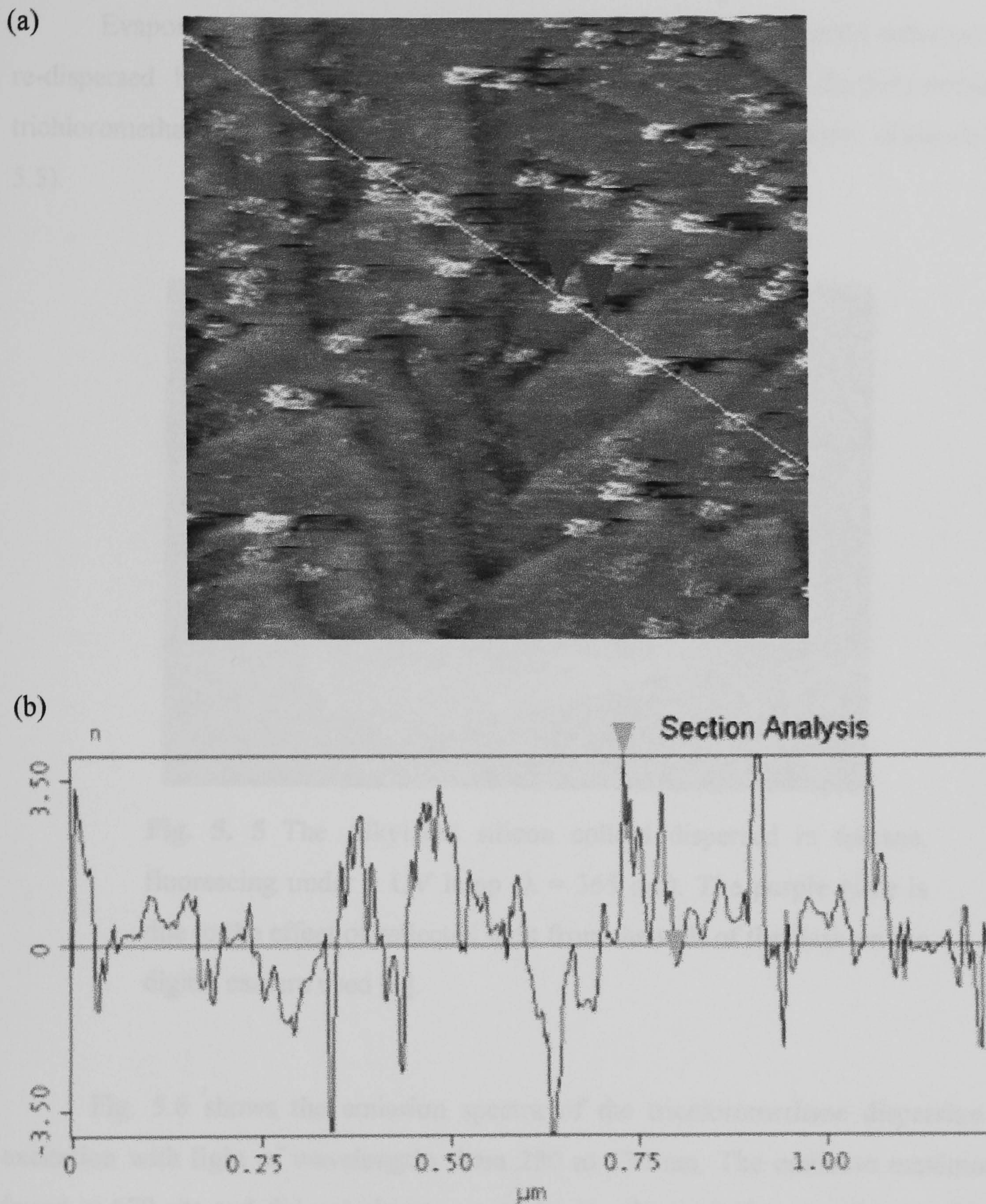


Fig. 5. 4 (a) $1 \times 1 \mu\text{m}$ STM image of silicon nanocrystals dispersed on hydrogen passivated Si(111). The sample was prepared by refluxing -OH terminated Si-NCs with hydrogen-terminated Si (111). The tunnelling current was 66 pA and the bias voltage was 1.5 V. The sample was imaged in air. (b) Line profile across the diagonal of the STM image in (a) [11].

Evaporation to dryness produced a yellow powder which could subsequently be re-dispersed by stirring in organic solvents such as toluene, dichloromethane and trichloromethane to produce similarly stable, non-turbid, fluorescent dispersions (Fig. 5.5).

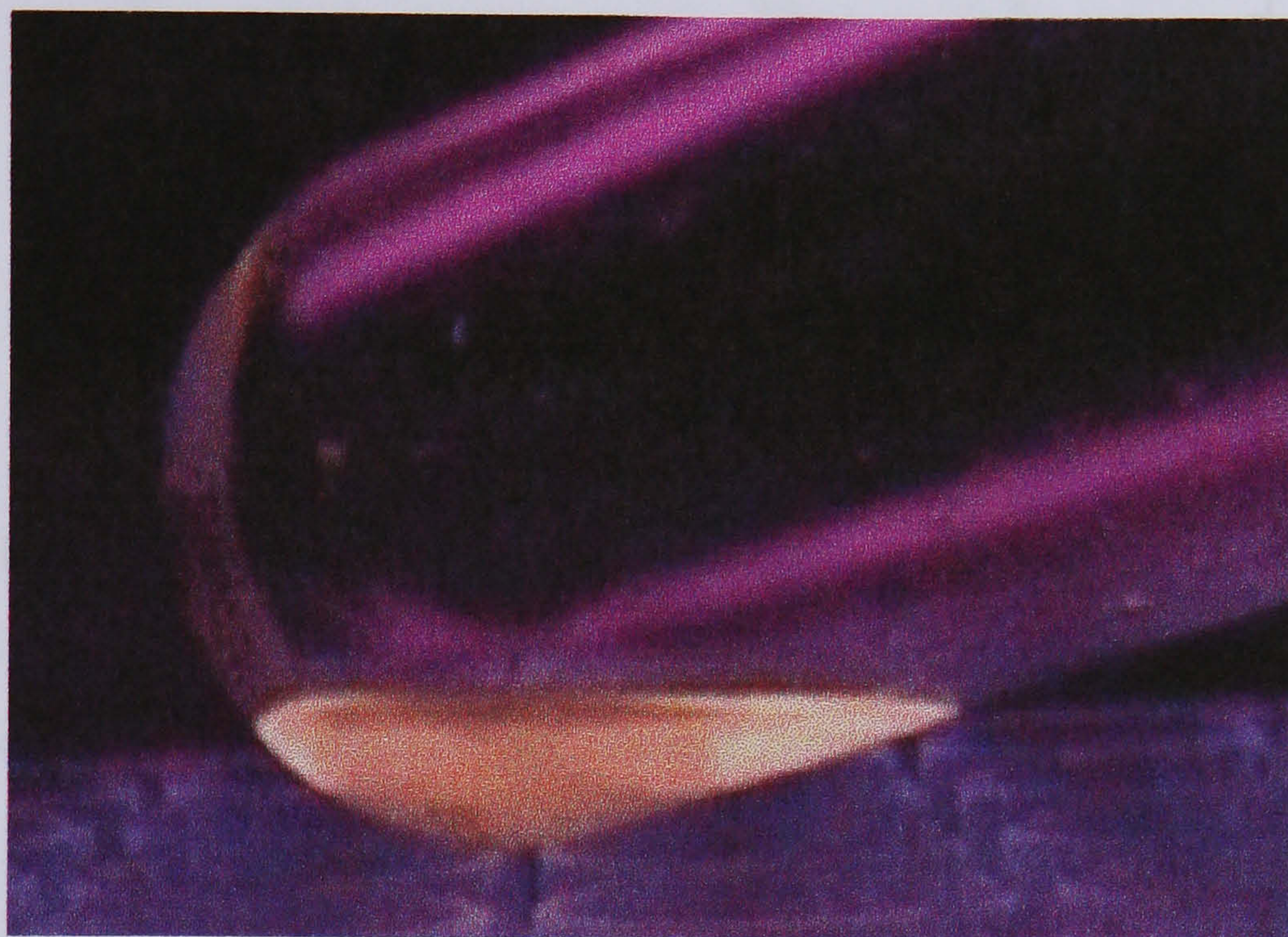


Fig. 5. 5 The Alkylated silicon colloid dispersed in toluene, fluorescing under a UV lamp ($\lambda = 365$ nm). The purple glare is due to the effect of reflected light from the wall of the flask on the digital camera used [6].

Fig. 5.6 shows the emission spectra of the trichloromethane dispersion under excitation with light of wavelengths from 280 to 370 nm. The emission maximum was found at 670 nm and did not change upon altering the excitation wavelength. On fixing the detection wavelength at 670 nm and scanning the excitation wavelength, an excitation spectrum corresponding closely to the absorption spectrum was obtained after correction for the inner filter effect. See Fig. 5.7.

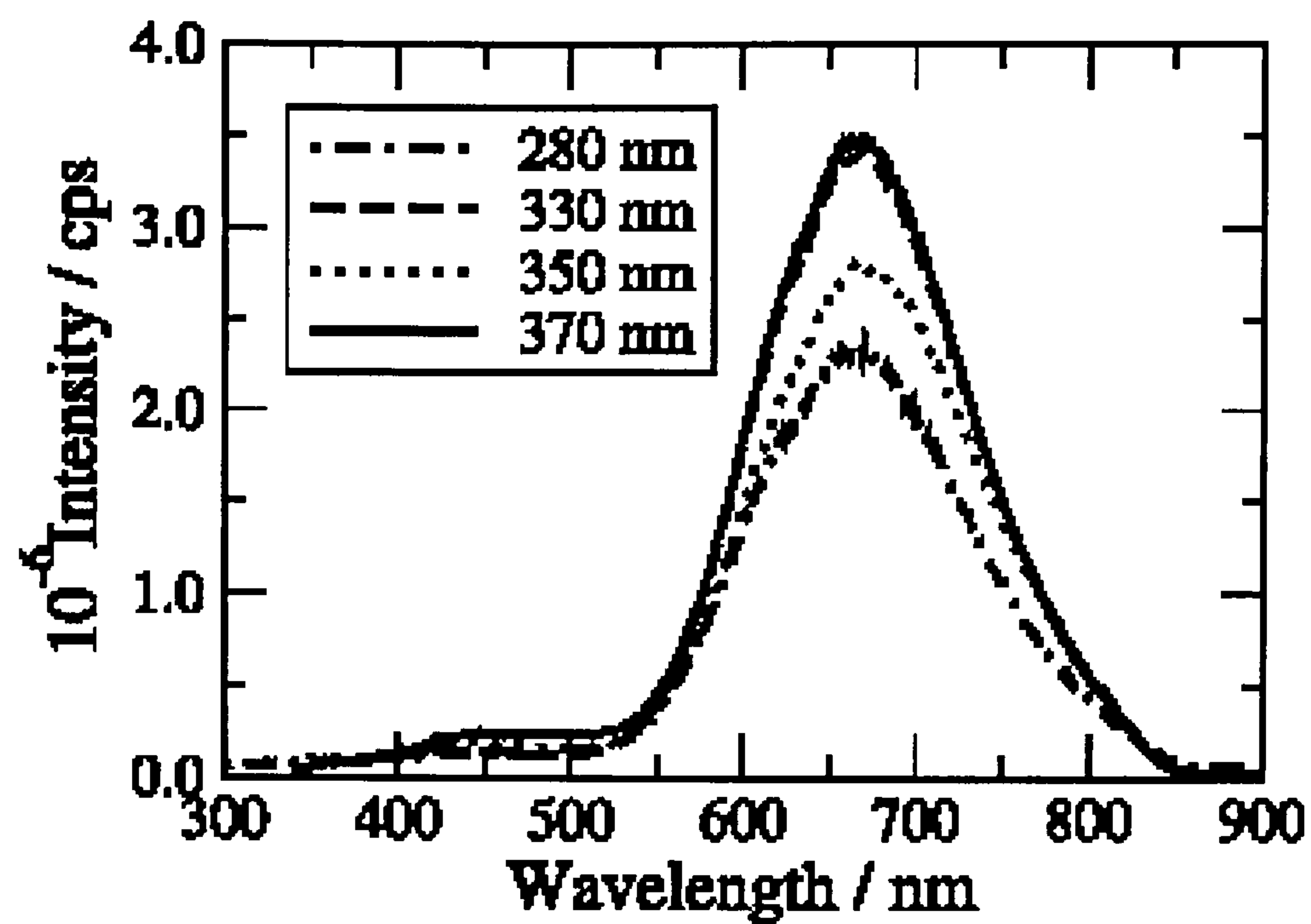


Fig. 5. 6 Fluorescence emission spectra of the silicon colloidal dispersed in trichloromethane (uncorrected). The corresponding excitation wavelengths are marked in nm [6].

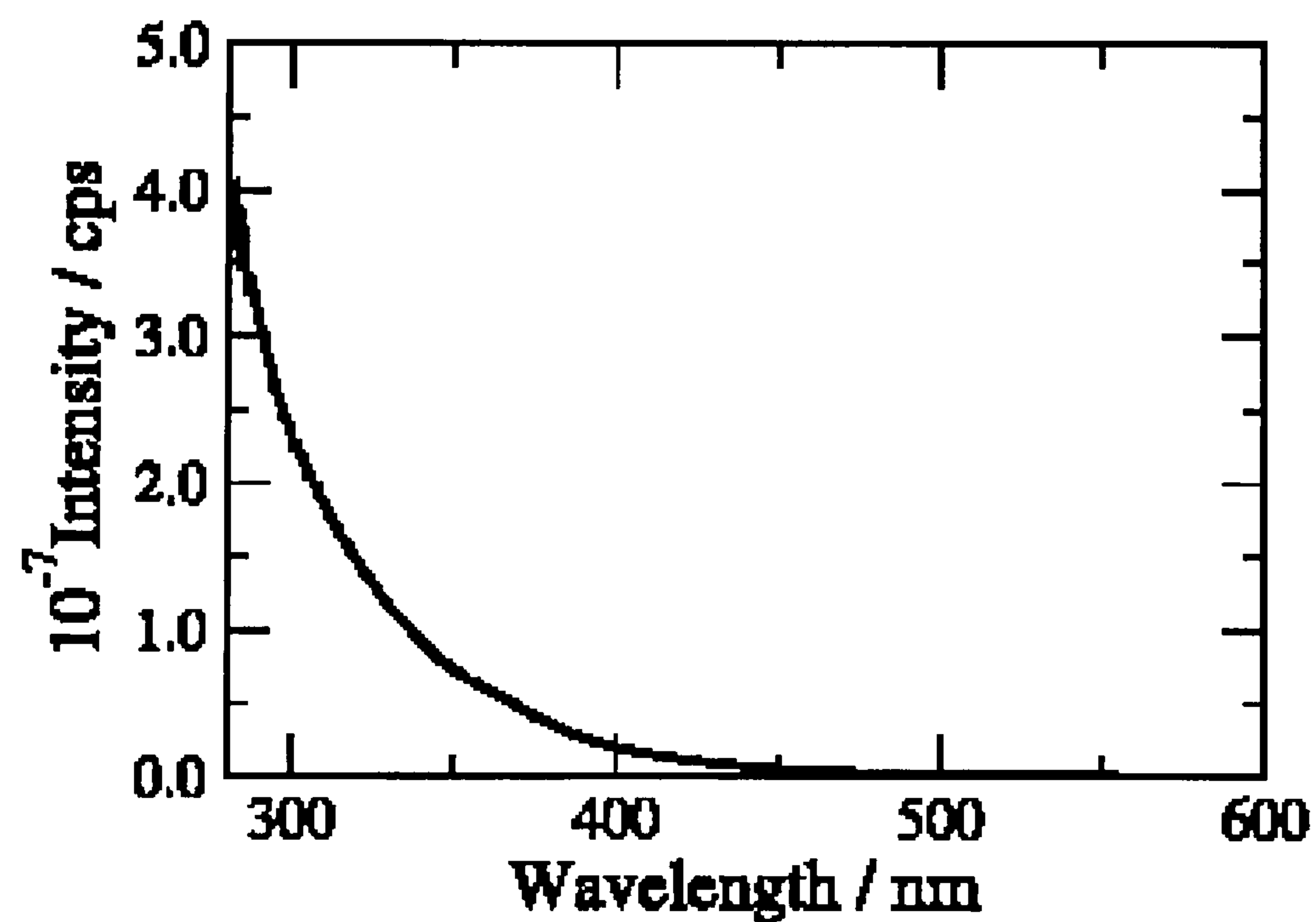


Fig. 5. 7 Excitation spectrum of the silicon colloid corresponding to the emission at 670 nm in Fig. 5.6 [6].

5.2 Core level spectra: line shape and shift

Two types of samples were studied, differing in their history: the first one was rapidly inserted into the ultra high vacuum (UHV) chamber whereas the second type of samples kept in air for several hours before introduction into the vacuum, we refer to these as the “fast” and “slow” samples respectively.

Fig. 5.8 shows the development of Si $2p$ spectra obtained in normal emission, with $h\nu=145$ eV photons, for a sample that had been exposed to the air for several hours (‘slow’ sample). The spectra are normalized to photon flux. Initially a single peak (denoted as A) is observed at a nominal binding energy of 103.5 ± 0.1 eV. However, upon irradiation this peak decreases in intensity and shifts to higher binding energy. The change in position and intensity of the peak at 103.5 eV is accompanied by the growth of a ‘tail’ at higher binding energy which also grows in relative intensity and moves progressively to higher binding energy. Eventually the tail develops into a clear peak (denoted as B) at a final binding energy of approximately 106.8 ± 0.1 eV. The data were fitted to mixed (Gaussian-Lorentzian) doublets with a Shirley background; the width and position were allowed to vary.

Fig. 5.9 shows the development of the intensity of both peaks with irradiation, measured in terms of flux \times time. The decay of the intensity of the peak initially located at 103.5 ± 0.1 eV binding energy (I_{PES}) may be fitted to an exponential function:

$$I_{PES} = 26600 \bullet \exp (-x/44) + 2200, \text{ where } x = \text{flux} \bullet \text{time (nA} \bullet \text{s)}. \quad (5. 2)$$

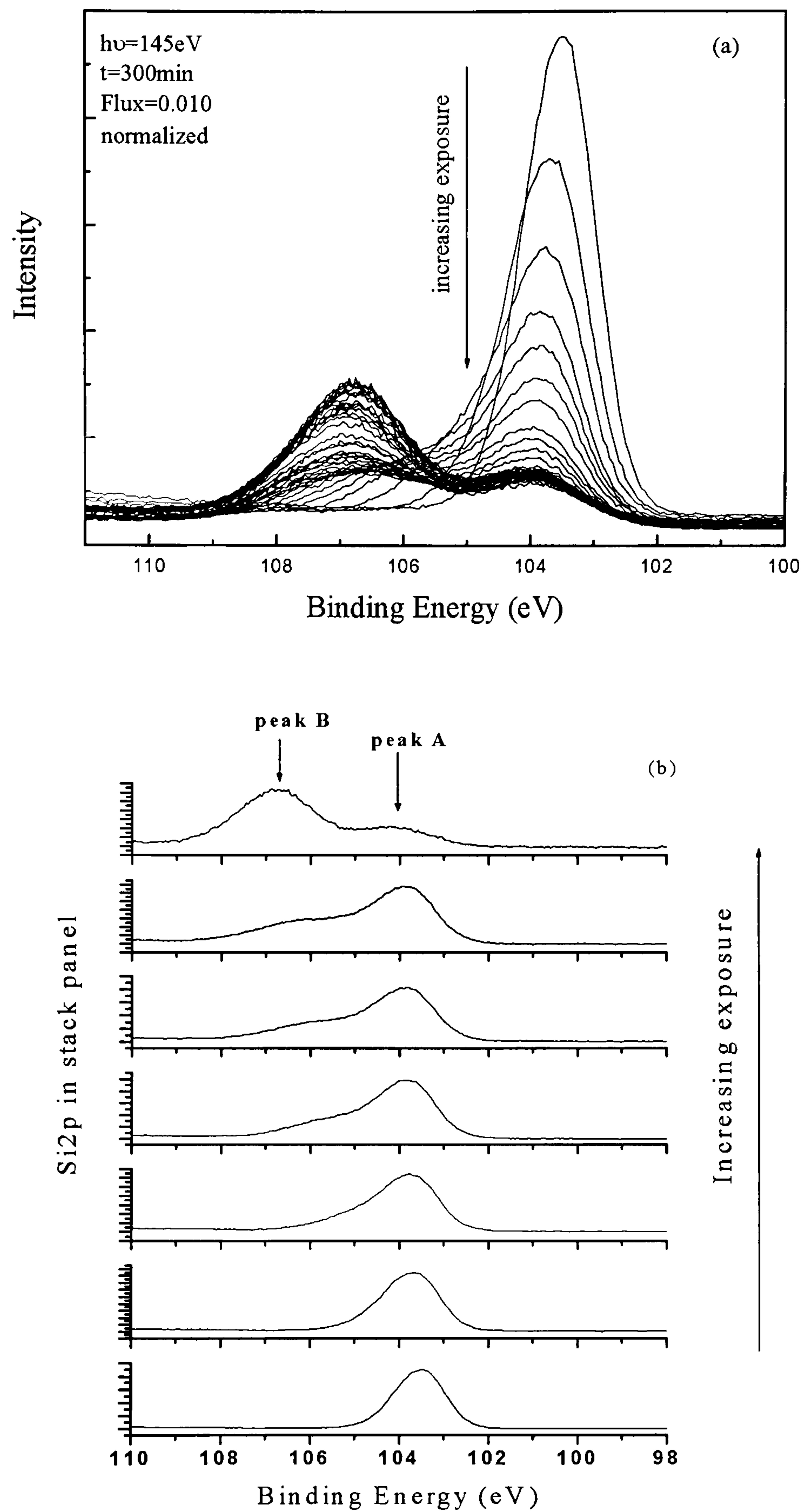


Fig. 5. 8 With the exposure increased to 400nA•s, the evolution of normalized Si 2p spectra, obtained in normal emission with $h\nu=145$ eV photons from a Si nanocrystallites film exposed to air for several hours (“slow sample”). The whole set of spectra showed in (a), while part of spectra showed in stack panel (b), slow sample [11]

The incident photon flux was measured with a gold grid held immediately before the main experimental chamber, and although the scale is internally consistent, we cannot convert the exposure simply into the number of photons per square meter because we do not exactly know the solid angle and distance between the mesh and the sample, and thus the lifetime determined from the fitting is only a qualitative measure. As this initial peak decays the second peak is seen to continuously rise during the course of the irradiation.

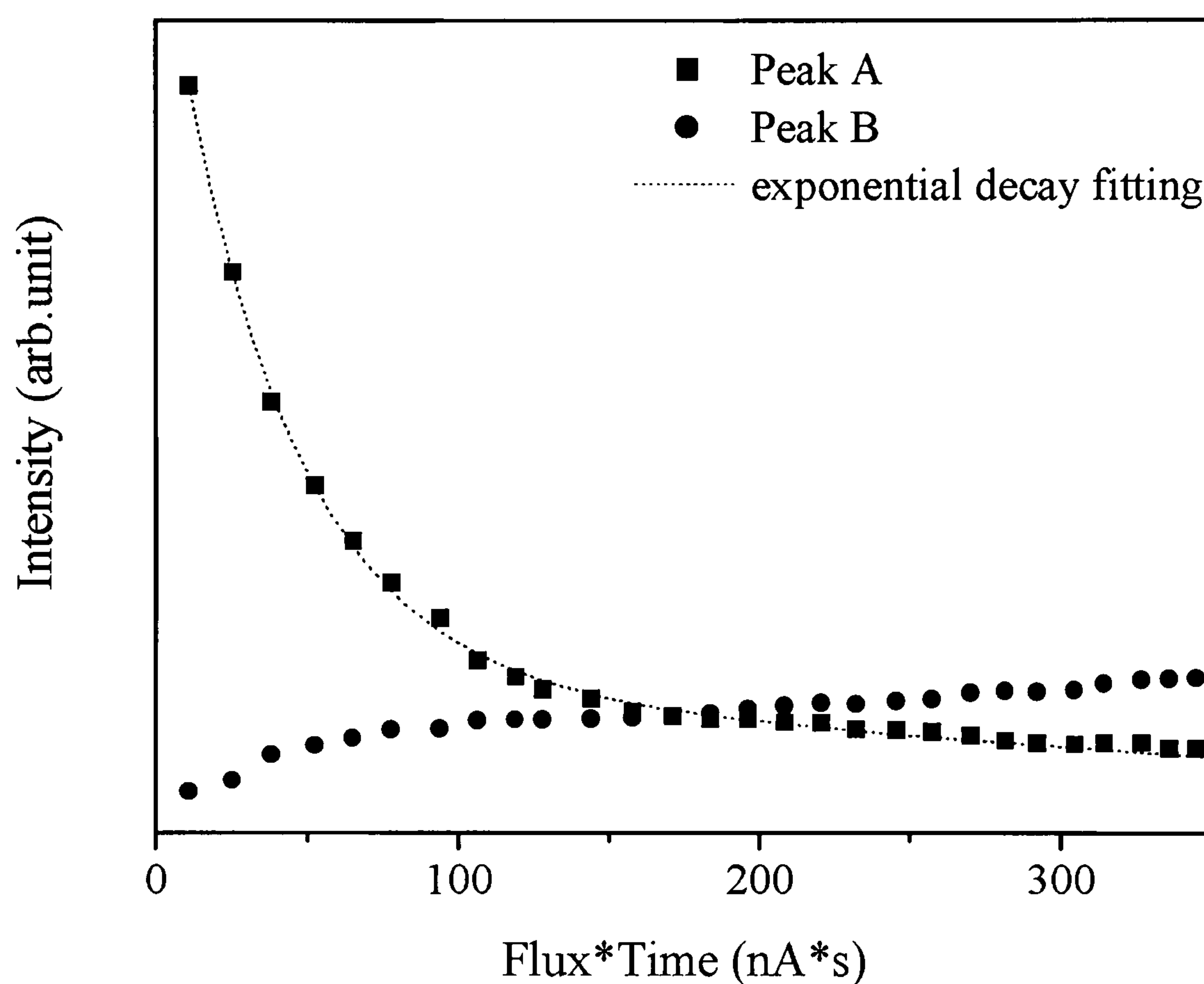


Fig. 5. 9 Plot of the intensity evolution of low (Peak A) and high (Peak B) binding energy Si $2p$ peaks as a function of photon irradiation. The decay in intensity of peak A is fitted with an exponential decay (dotted line), slow sample [11]

Fig. 5.10 shows the development of the binding energy of two peaks during the exposure to the synchrotron radiation. The peak initially observed in the spectra moves from its initial position of 103.5 ± 0.1 eV to saturating at a binding energy of 104.0 ± 0.1 eV, while the second peak position also shifts, from 106.2 ± 0.2 eV to a saturation binding energy of 106.8 ± 0.1 eV.

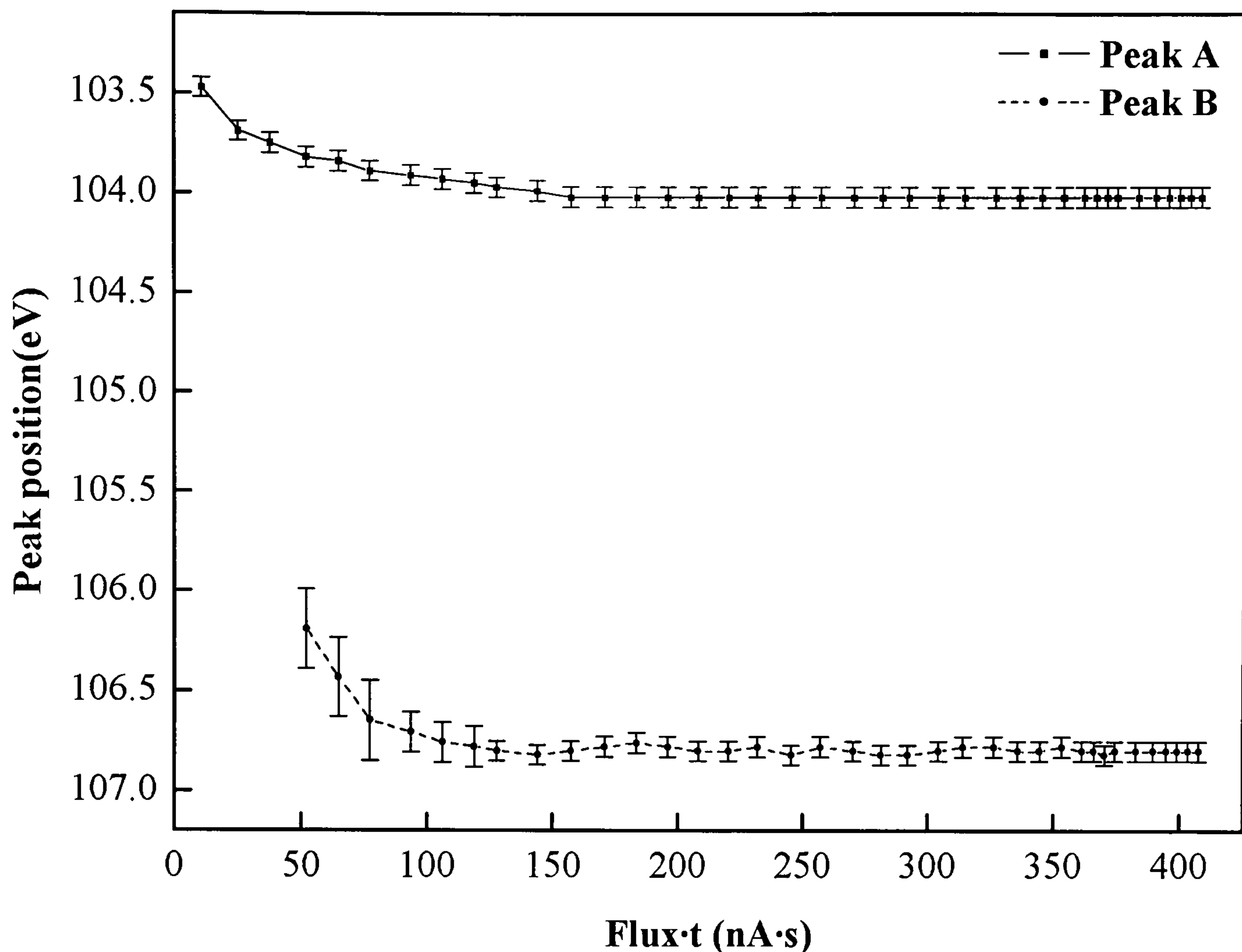


Fig. 5. 10 The evolution of the binding energies of the two Si 2*p* peaks as a function of photon exposure ('slow' sample) [11].

Two possible mechanisms can be responsible for this behaviour; the first is that an irreversible chemical reaction occurs during irradiation. The alternative is that these changes are due to charging, which occurs because the Si-NCs are surrounded with alkyl chains and thus are highly insulating. This second process is ultimately reversible. In addition the thickness of film is inhomogeneous, so different parts of the surface can charge with different rates. In order to check reversibility of the observed changes in the photoemission spectra we have waited for 7 hours after irradiating the sample and in Figure 5.11, spectrum b), we see that the intensity of both peaks A and B has partially recovered, but with relative better recovery for peak A (compare intensity of A over B in spectrum a) and spectrum b)). However, the peak B has a similar position as after initial irradiation, which suggests that it arises from a chemical reaction which occurs during the

procedure of exposure to synchrotron radiation. We conclude that the decay of the intensity of the first peak with irradiation time and the observed shift in binding energies of the peaks indicates that charging of the Si-NCs is a second process that develops in tandem with a photo-induced reaction as irradiation proceeds.

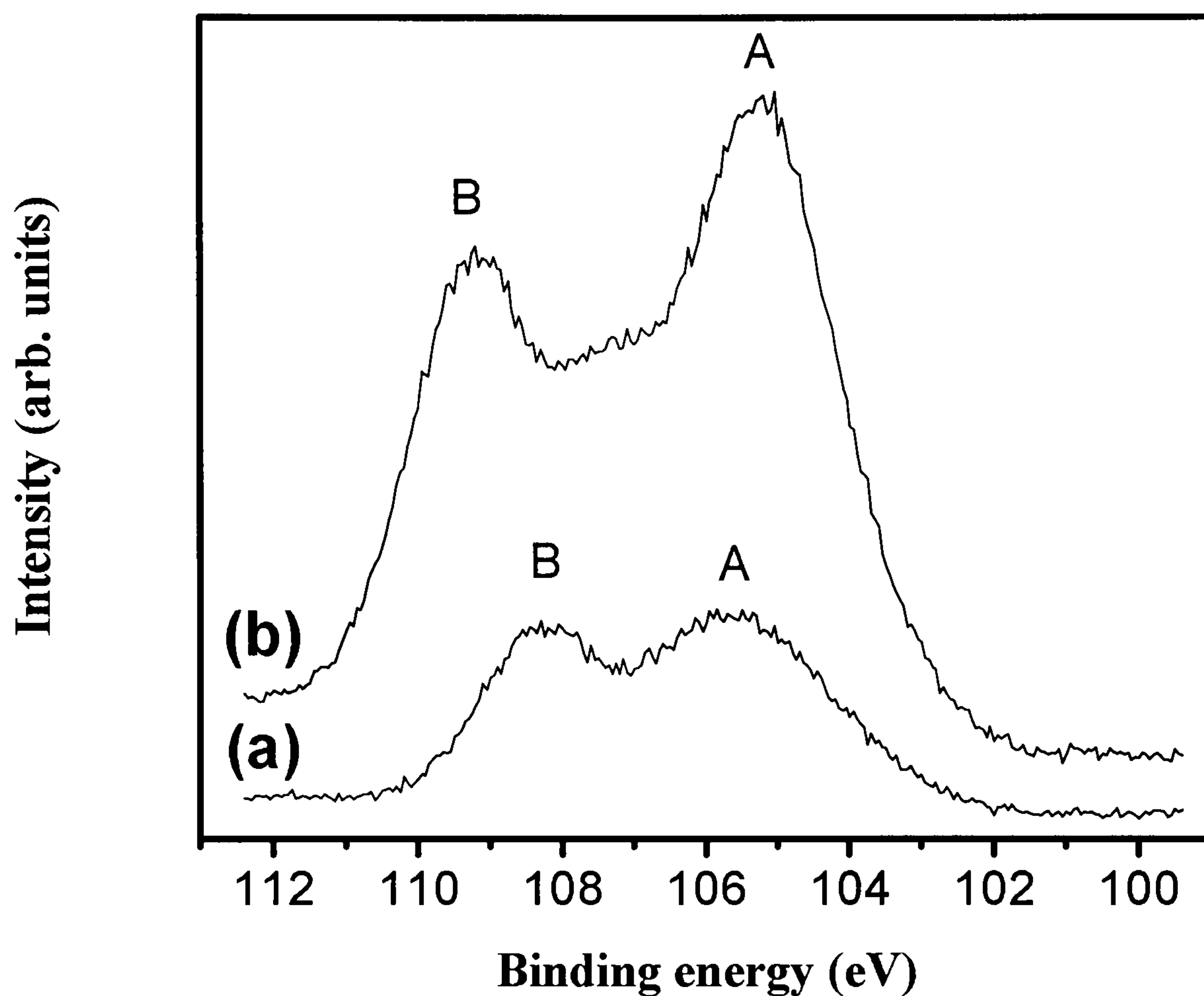


Fig. 5. 11 (a) Si 2*p* spectra, obtained at normal emission with 145 eV photons from a Si-nanocrystallite film exposed to air for several hours ('slow' sample) and exposed to ~ 2 hours of irradiation. (b) The same as above but after irradiation, the beam was stopped and the waiting time without irradiation was 7 hours.

Figure 5.12 shows the development of normalized Si 2*p* spectra obtained under identical conditions for a sample which was introduced rapidly (the 'fast' sample). A single peak is observed over the whole dose range studied initially located at a binding energy of 102.6 ± 0.1 eV to the peak moves upwards in binding energy to 103.1 ± 0.1 eV after irradiation. The initial peak position and the magnitude of the shift of this peak are

slightly different from that of the ‘slow’ sample. However, slightly different binding energy values are expected since the thickness of the film may vary in each deposition from the solution of quantum dots affecting the degree of charging within the film. It is notable that even after several hours of photo-irradiation no new peak is observed, contrary to the behaviour of the ‘slow’ sample. The variation of the intensity of the Si 2p peak with photon exposure is plotted in Figure 5.13.

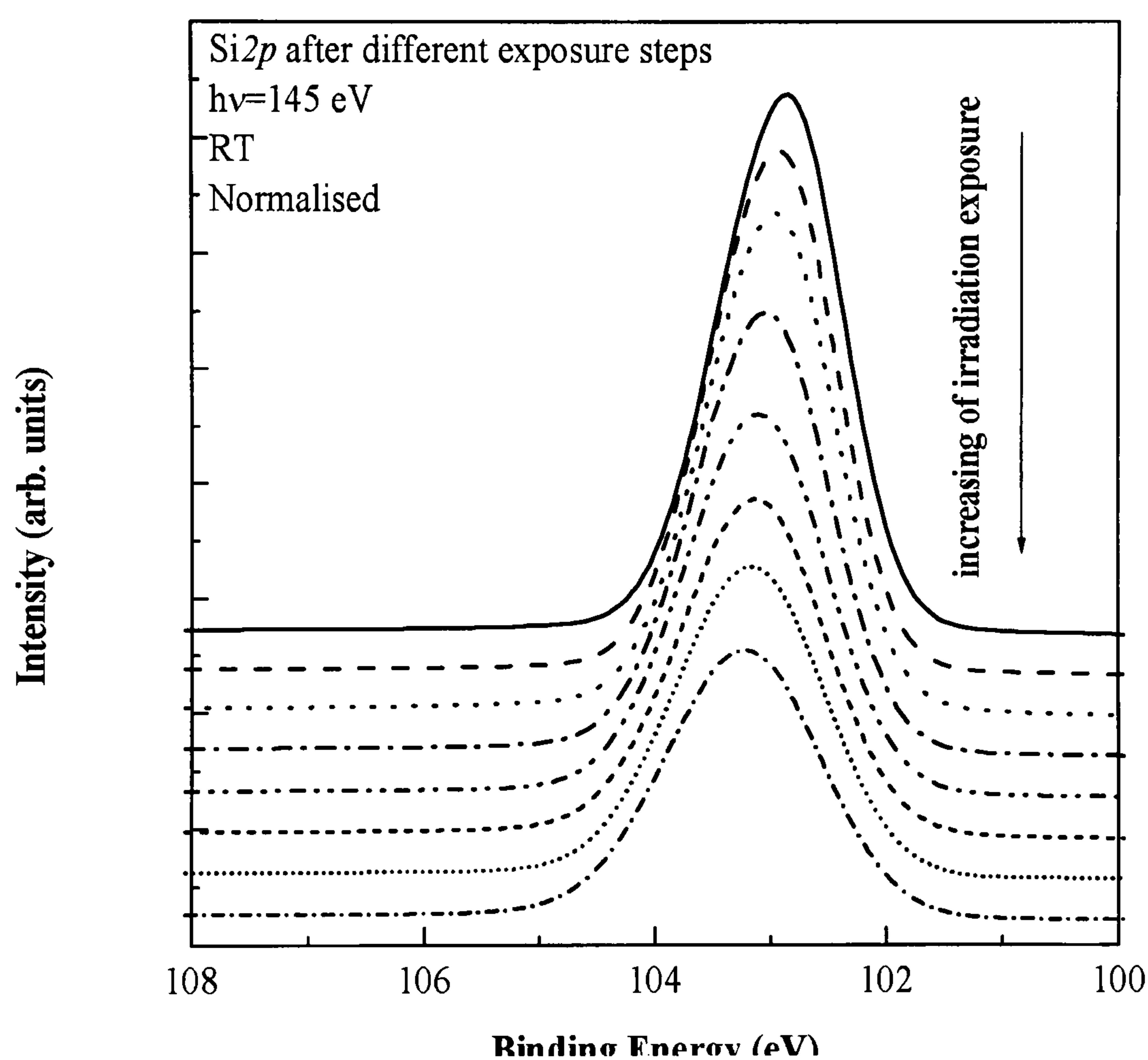


Fig. 5. 12 The evolution of normalized Si 2p spectra obtained at normal emission with $h\nu=145$ eV photons from a Si-nanocrystallites film rapidly introduced into vacuum chamber (“fast sample”) [11]

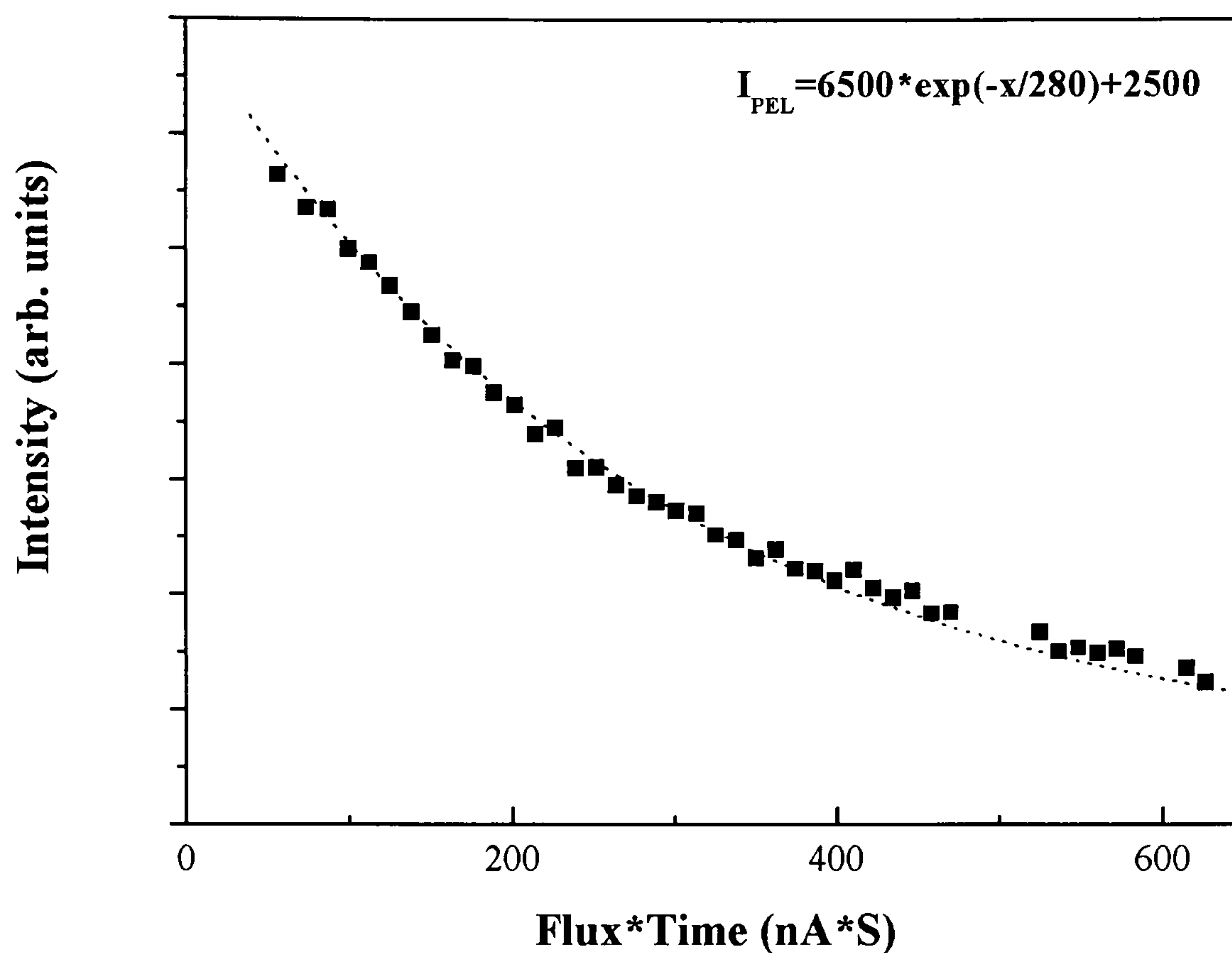


Fig. 5. 13 The intensity of the Si 2*p* peak as a function of irradiation, the dotted line is an exponential decay fitted to the data, “fast sample” [11]

As previously we see that the intensity falls exponentially, and here it can be modelled by the relationship:

$$I_{PEL} = 6500 \exp(-x/280) + 2500, \text{ where } x = \text{flux} \cdot \text{time (nA} \cdot \text{s)}. \quad (5.3)$$

In Fig. 5.14 the variation in the peak width (full width at half maximum) is plotted as a function of exposure. The width of the peak increases with irradiation and follows a logarithmic function:

$$FWHM = \ln \{(x+200)/12\}/3, \text{ where } x = \text{flux} \cdot \text{time (nA} \cdot \text{s)}. \quad (5.4)$$

The evolution of Si 2*p* peak position as a function of irradiation is plotted in Fig. 5.15.

Figure 5.16 shows Si $2p$ spectra obtained after exposure to ~ 2 hours of continuous irradiation (a) and its recovery after waited 11 hours without beam irradiation. We see that the peak intensity has recovered and the width of the peak has decreased. Again this indicates that the charging is the main mechanism responsible for the observed changes.

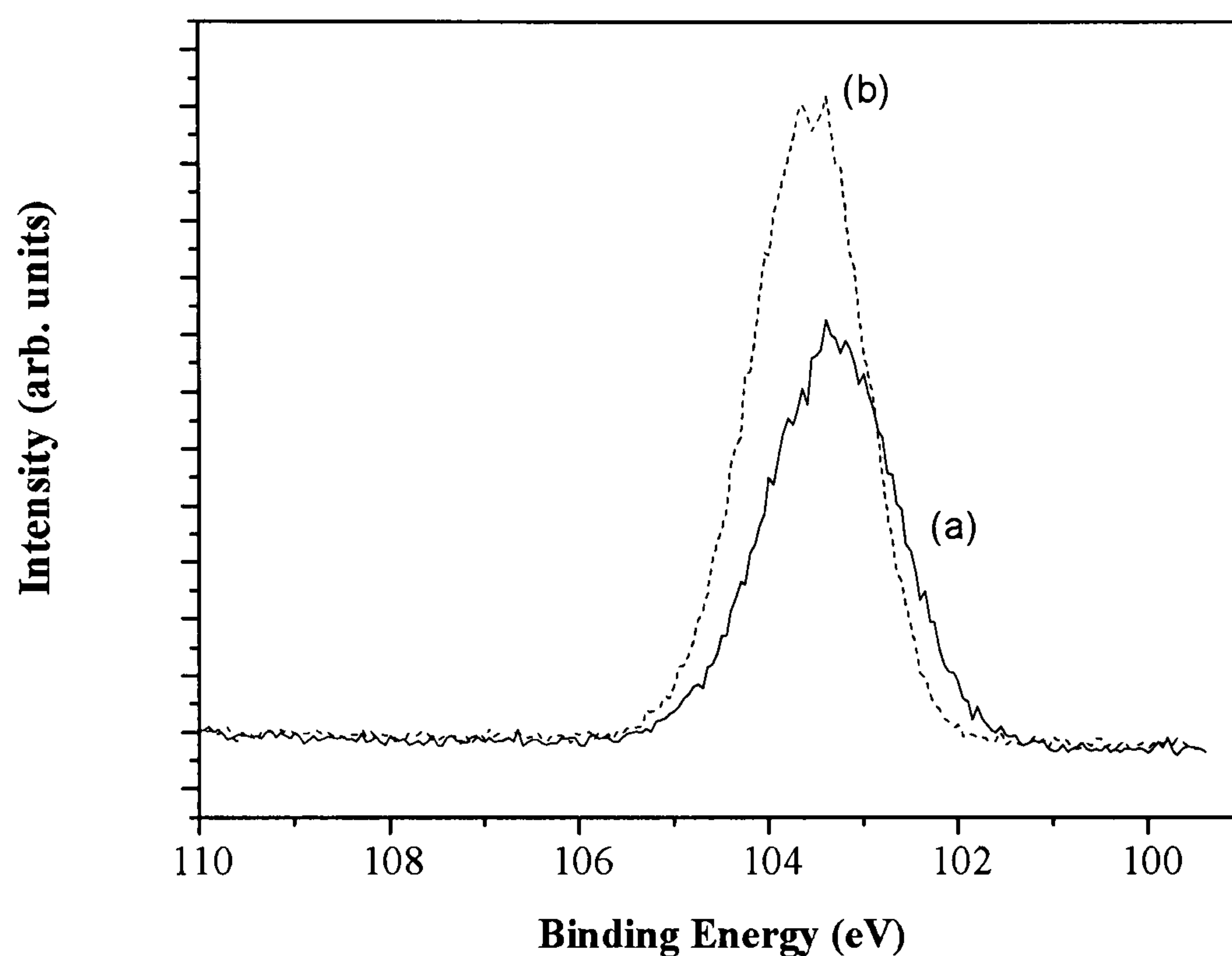


Fig. 5. 16 (a) Si $2p$ spectrum obtained at normal emission with 145 eV photons from a Si-nanocrystallite film ('fast' sample) and exposed to ~ 2 hours of irradiation. (b) The same as above but after irradiation, the beam was stopped and the waiting time without irradiation was 11 hours [11].

In Fig. 5.17 we plot the Si $2p$ region of a 'fast' sample (in the spectra shown the nanocrystallite film was deposited on a HOPG substrate) at room temperature, spectrum (A), and after heating to ~ 275 °C for 5 minutes, spectrum (B). Valence band spectra (not shown here) demonstrate emission from the substrate after annealing, leading to the conclusion that upon annealing at temperatures of ~ 275 °C the Si-NCs begin to desorb

from graphite. In particular, the desorption leads to a thinning of the Si-NC film and a reduction in charging due to the proximity of the graphite surface to the remaining Si-NC material (i.e., screening and neutralisation by the substrate is more effective in the thinner film). This is reflected in a shift of the Si $2p$ peak to lower binding energy, from 102.9 ± 0.1 eV in the as-introduced film to 101.8 ± 0.1 eV after annealing. The energy position of 101.8 eV is still far from the known position for Si-Si bond, 99.5 eV [14], which indicates that even in a thin film there is still considerable charge trapping in the film as soon as irradiation starts, as we discuss below. The continued presence of charge trapping arises from the passivation of the Si-NCs by the long alkyl chains and may be further contributed to by the likelihood that the nanocrystallites are still in the form of agglomerated clusters rather than dispersed as individual particles.

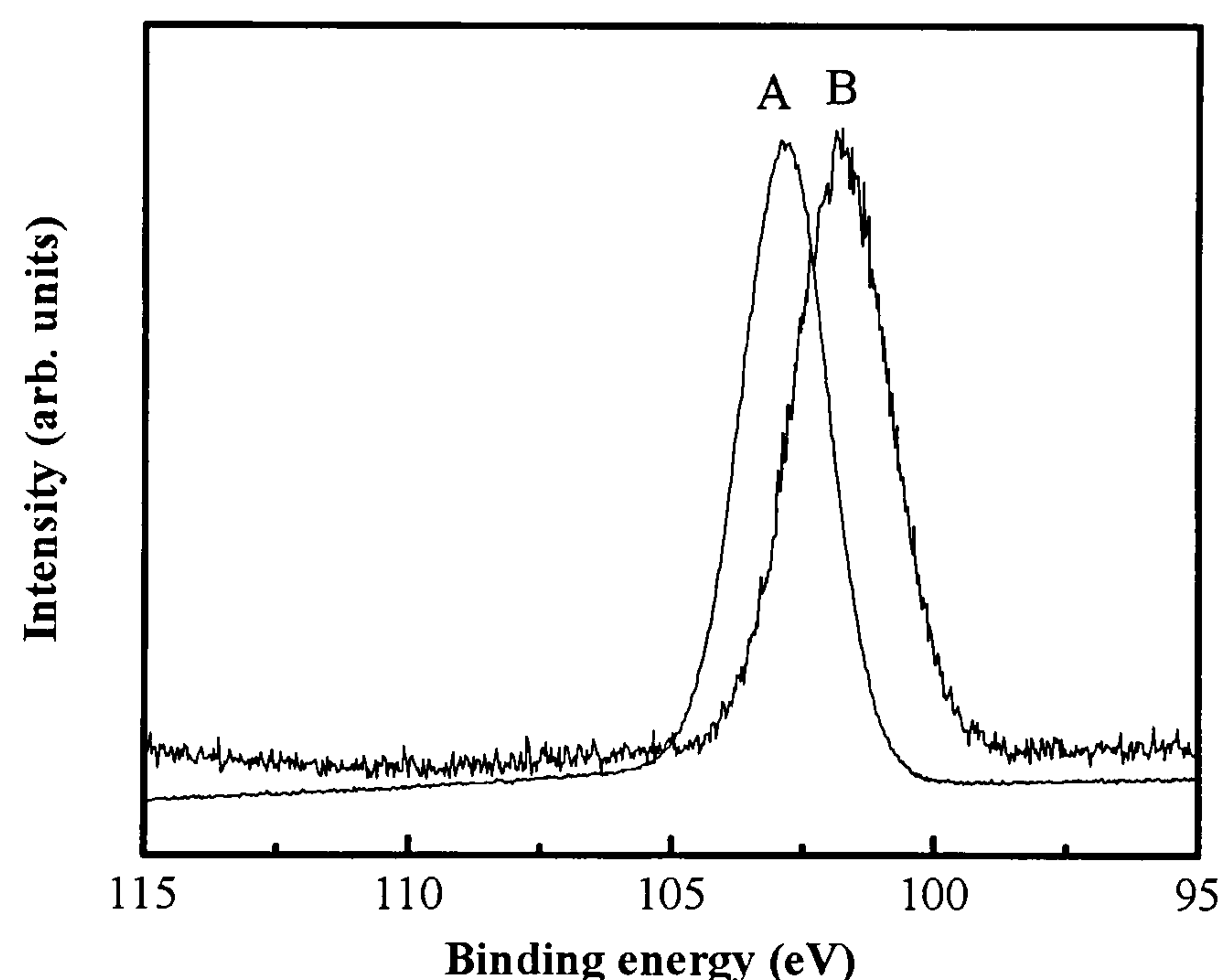


Fig. 5. 17 Si $2p$ spectrum obtained at normal emission with 145 eV photons at room temperature. Showing a ‘fast’ sample as introduced (peak (A)) and after annealing to 275°C for 5 minutes (peak B).

In Fig. 5.18 a survey spectrum obtained at a photon energy of 633 eV is plotted, Si $2p$, O $1s$ and C $1s$ core lines are clearly visible, supporting previous infrared (IR) studies, which indicate the presence of both Si-C (anchoring the alkyl chains to the dot) and Si-O

bonds from oxidation of unalkylated Si-H [6]. Taken together, the data indicate that the silicon nanocrystallites are encapsulated with a combination of surface (sub-) oxides and alkyl chains.

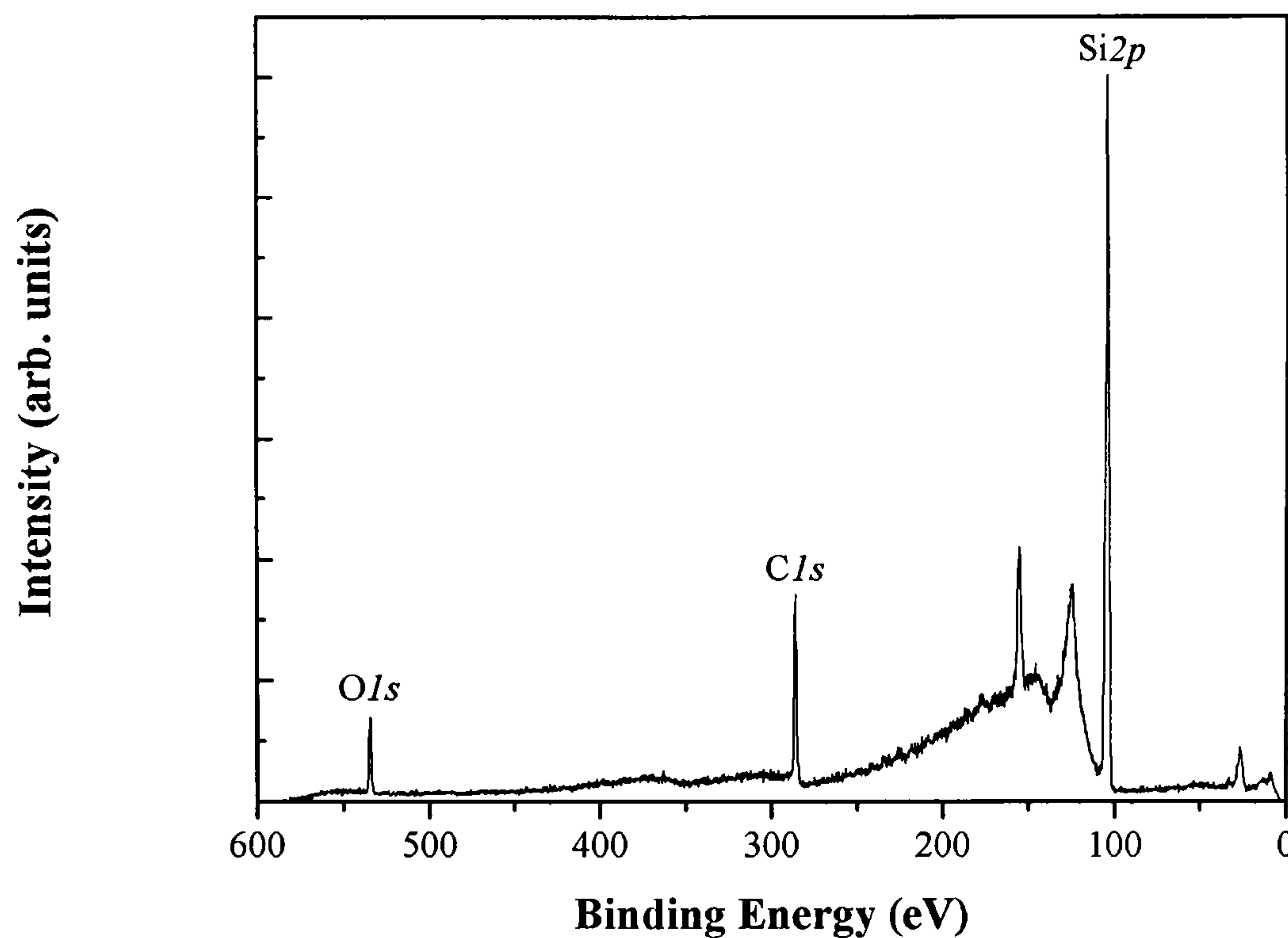


Fig. 5. 18 X-ray overview of fast sample measured at normal emission with $h\nu = 633$ eV photons after annealing to $\sim 275^\circ\text{C}$ for 5 minutes [11].

We interpret the initial change in Si 2*p* binding energies, their final saturation, and the dependence of the binding energy on film thickness as a signature of charging within the film. In consequence, as mentioned earlier, the ‘binding energies’ quoted do not reflect the real binding energy of the core level in question, but include the energy barrier due to local charge-induced fields that the photoelectron must overcome in order to escape from the surface of the nanocrystallite film. In the ‘slow’ sample two Si 2*p* components can be observed which, at the highest photon doses, are separated by 3.5 eV. Survey spectra indicate that only Si, C, and O are present in the films (there may also be some hydrogen, which it is not possible to detect directly by photoemission). We attribute the low binding energy Si 2*p* core line at 103.5 eV in the thick film (or 101.8 eV in the thin film) to a multicomponent peak consisting of ‘bulk’ Si, and/or one or both of Si-C and Si¹⁺ - in which one Si-Si bond has been replaced by an Si-O bond [15] (the reported

value for the Si $2p$ binding energy in SiC is at 100.4 eV [16]). As mentioned, the presence of a Si-C component in the Si $2p$ line would be consistent with recent IR studies of the silicon nanocrystallites, which reveal formation of SiC bond [6], so the presence of such a component in the low binding energy peak cannot be ruled out). The multicomponent nature of the low binding energy peak prevents a clear observation of the spin-orbit splitting which would be expected from the Si $2p$ core level.

The second peak, observed in this work at 106.8 eV is attributed to the photon-induced formation of a second oxide such as SiO_x , where $x \sim 2$, because both the energy separation between first and second peak is similar to that reported for oxidation of Si(100) and Si (111) single crystal – 3.5 eV in this work compared to 3.2 eV in Ref.[14, 17]. Two strong components has been also observed, similarly to our experiment, when nanocrystalline silicon was embedded into a silicon-oxide thin film, Si $2p$ core level spectra for the as deposited sample and a sample after annealing at 900 °C have shown a substantial increase of Si^{+4} component, which has been interpreted the further oxidation of silicon and the transformation from suboxide states to Si^{+4} state [18]. Recently a vacuum ultraviolet (VUV) surface photochemistry of water adsorbed on graphite [16] and CO_2 ice [19] have shown that only $\text{H}^+(\text{D}^+)$ and $\text{H}_3\text{O}^+(\text{D}_3\text{O}^+)$ ion fragments can readily desorb into vacuum, leaving OH species trapped at the surface and thus available for silicon oxidation, which may be the mechanism by which oxidation occurs in this work.

The absence of the second, oxide, peak in ‘fast’ sample, comparing Fig. 5.8 and Fig. 5.12, can be explained by the time required for diffusion of water (and/or oxygen) into the samples from the ambient atmosphere. It must be borne in mind that the as-prepared samples contain significant quantities of the original solvent which must diffuse out or undergo exchange with water during atmospheric exposure in order for there to be sufficient concentration within the film to enable photo-induced oxidation to occur.

5.3 NEXAFS of Alkylated silicon quantum dots

To investigate the mechanism of photoluminescence of silicon quantum dots, we acquired near edge X-ray absorption fine structure (NEXAFS) spectra to get the absorption peak photon energy. Fig. 5.19 shows the partial electron yield (PEY) NEXAFS spectrum of the Alkylated silicon quantum dots, which is peaked at ~ 106.5 eV. The data on NEXAFS were used later by Krishnamurthy to measure PL on new PL station MoLES at beamline 6.1, Daresbury. Data obtained by Krishnamurthy [20] revealed the origin of the orange light is from the Si-Si bond; see Fig. 5.20 and Fig. 5.21. Initially we used this photon energy to obtain the photon luminescence spectrum, showed in Fig. 5.20. There are three light bands in the spectrum: blue, green and orange.

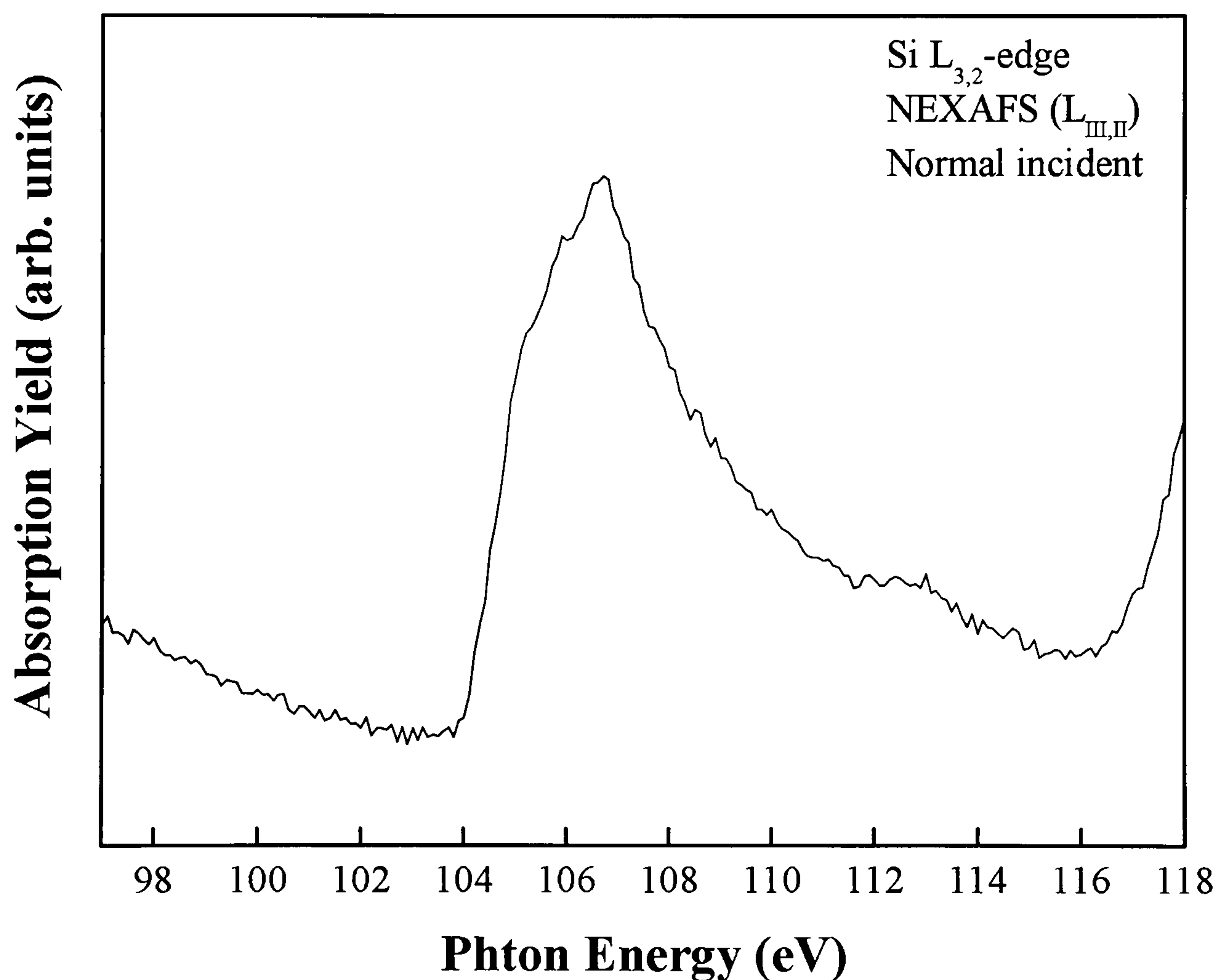


Fig. 5. 19 Si L_{3, 2} -edge X-ray absorption fine structure (NEXAFS) spectrum of alkylated Si quantum dots [11].

5.4 Photoluminescence Spectra

Fig. 5.20 shows the room temperature photoluminescence spectrum of the ‘fast’ sample excited by synchrotron radiation at $h\nu=106.5\text{eV}$, which is the peak photon energy in the near edge X-ray absorption fine structure (NEXAFS) of this Si-QD (See Fig. 5.19). The spectrum exhibits three bands of luminescence: blue $390 \pm 20\text{ nm}$, green $480 \pm 20\text{ nm}$ and red-orange $750 \pm 10\text{ nm}$, respectively.

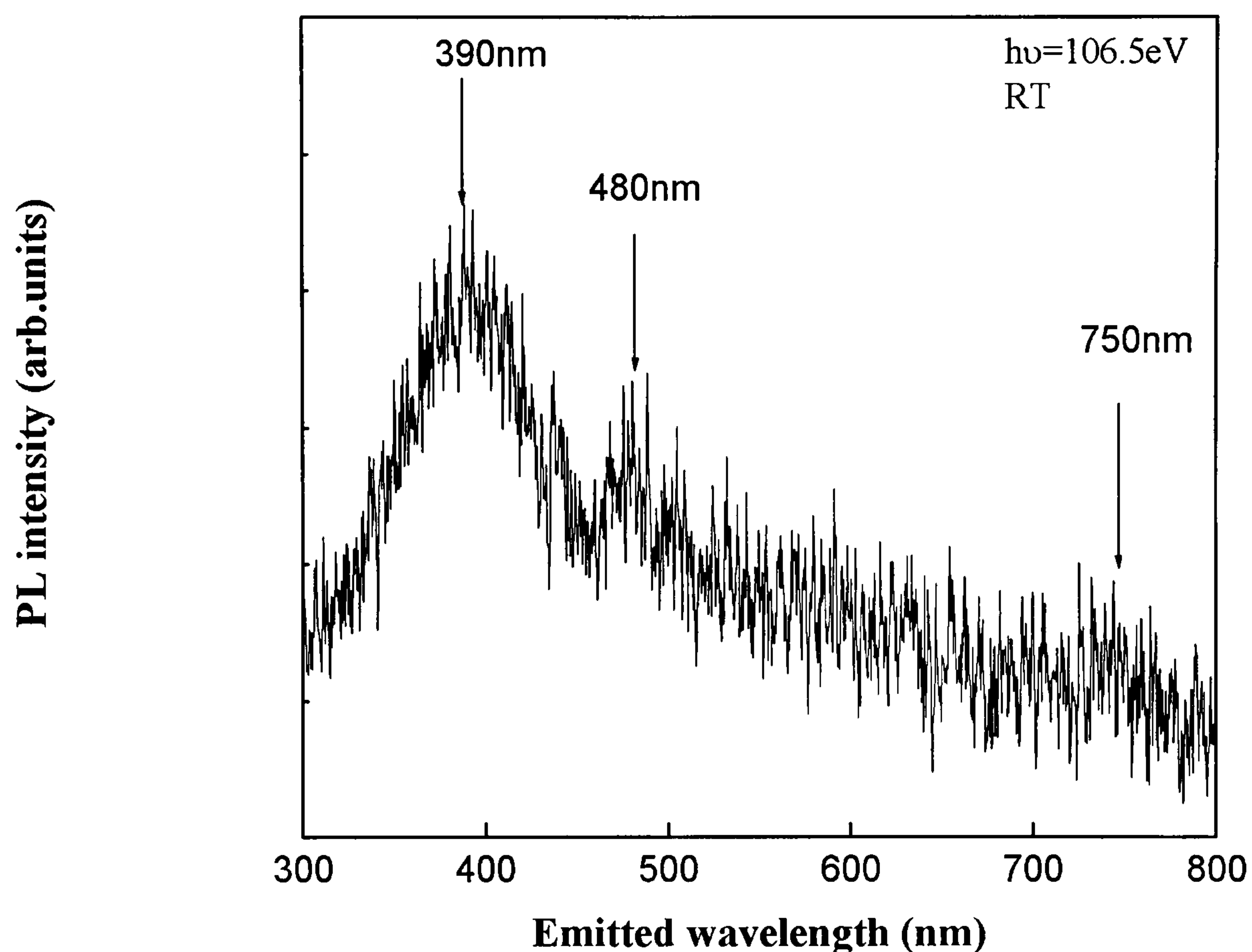


Fig. 5. 20 Room temperature photoluminescence (PL) spectrum excited by synchrotron radiation at $h\nu=106.5\text{ eV}$, three peaks are clearly displayed: $390 \pm 20\text{ nm}$, $480 \pm 20\text{ nm}$ and $750 \pm 10\text{ nm}$ [11]

Fig. 5.21 shows the narrow region (blue peak) room temperature PL spectra taken during the procedure of exposure to synchrotron radiation at $h\nu=106.5\text{eV}$. From bottom to top panel, each spectrum obtained in one scan and one by one, about 5 min each. Fig. 5.22 shows the decay of room temperature PL intensity of blue peak at 390 nm as

exposed to synchrotron radiation at $h\nu=106.5\text{eV}$. The intensity (I_{PL}) decay curve was fitted by exponential decay function:

$$I_{PL} = 0.72 \cdot \exp(-x/1900), \text{ where } x = \text{flux} \cdot \text{time (nA} \cdot \text{s)}. \quad (5.5)$$

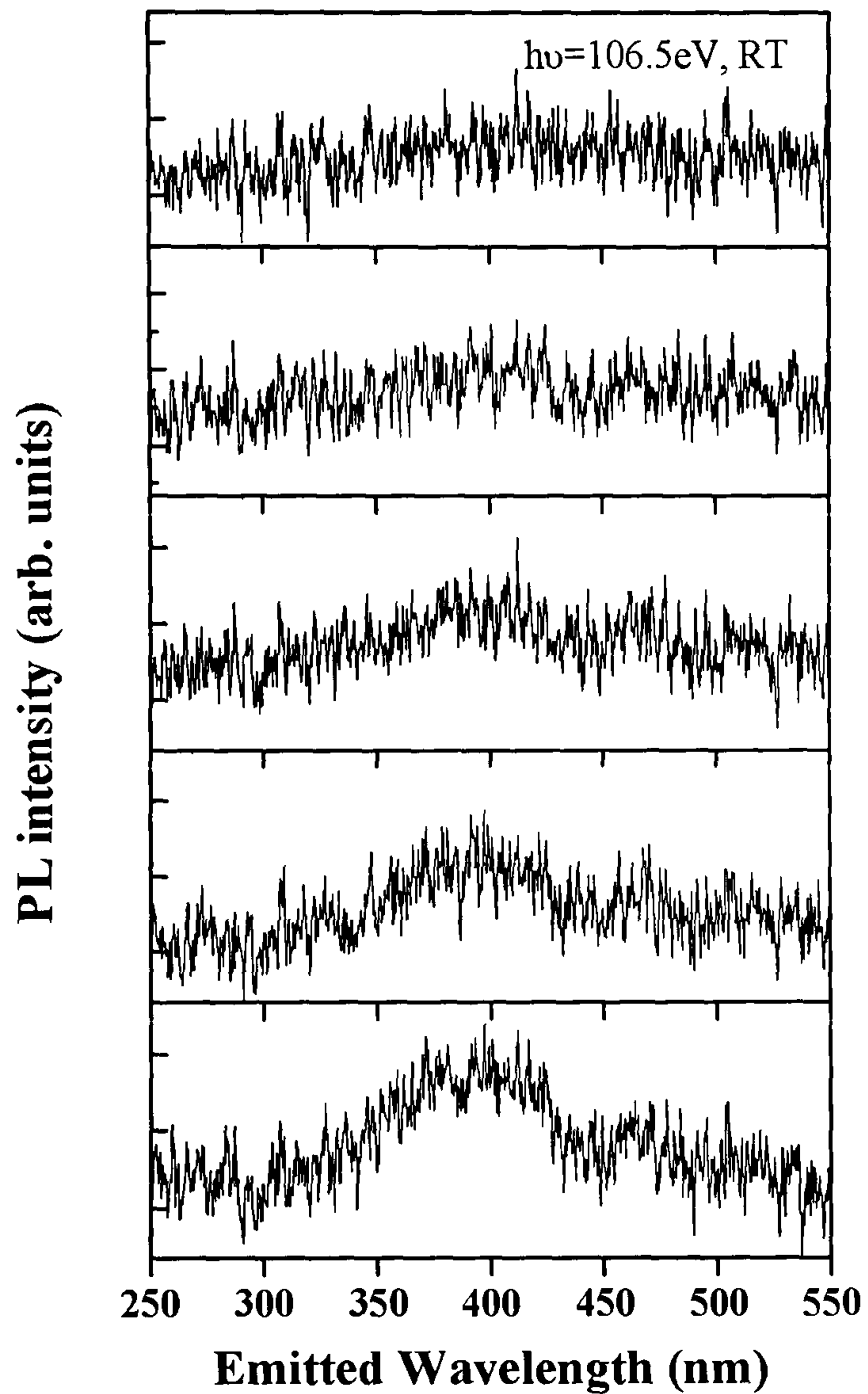


Fig. 5. 21 Room temperature PL spectra taken during the step of exposure to synchrotron radiation at $h\nu=106.5\text{eV}$, from bottom to top, exposure increased from 939 to 4593 nA·s [11]

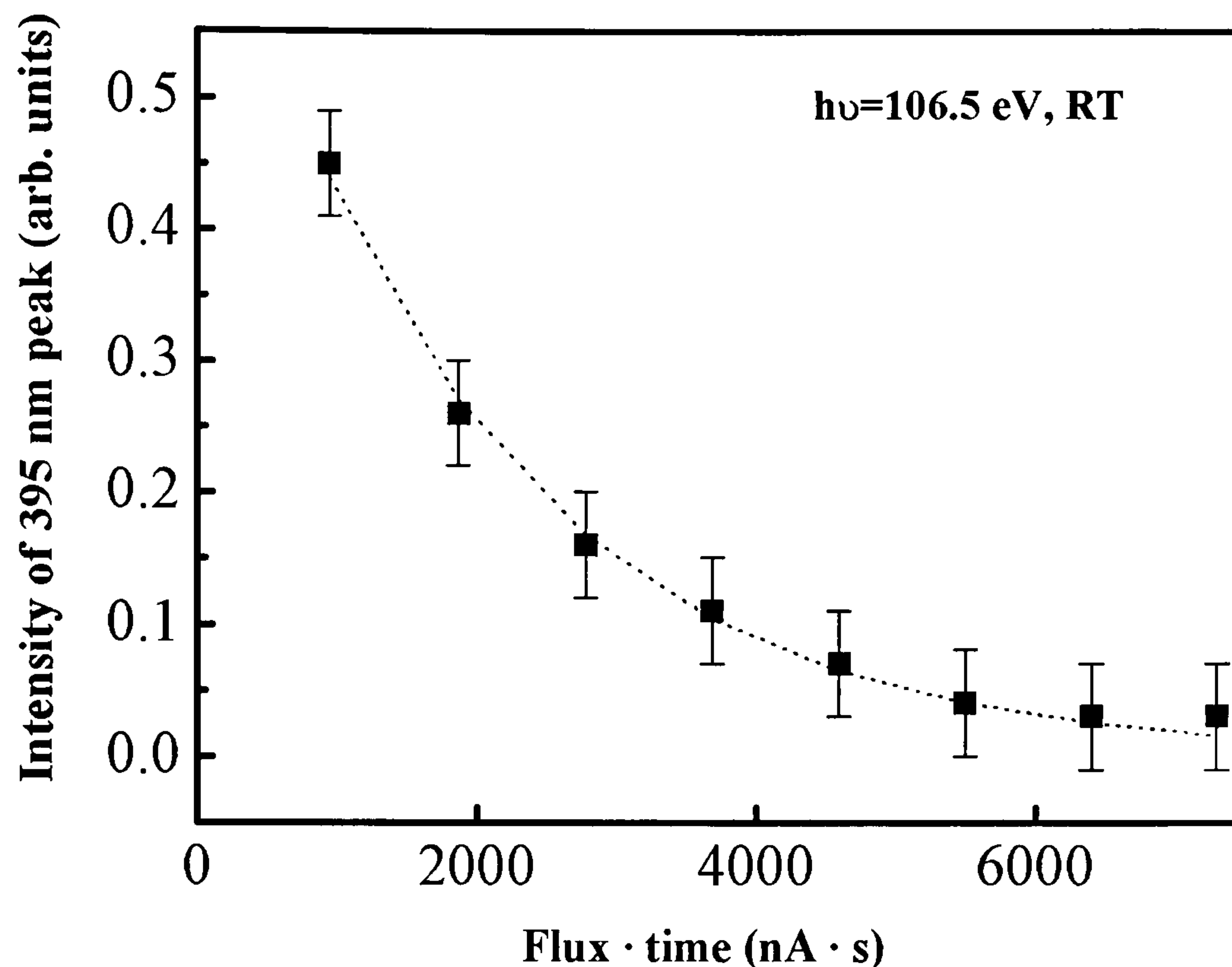


Fig. 5. 22 Decay in PL intensity of the blue peak at 390nm, measured at room temperature as a function of exposure to synchrotron radiation and its fitting by $I_{PL} = 0.72 \exp(-x/1900)$, (where $x = \text{flux} \cdot \text{time (nA} \cdot \text{s)}$) [11].

It's a pure exponential decay function rather than a stretched exponential function suggested by Kanemitsu [21]. The similar behaviour observed in both type samples. This behaviour indicates that the decay of PL intensity might be related to the decay of intensity of the low binding energy peak in the Si $2p$ photoemission spectra since both vary exponentially. Such an agreement suggests that the decay of PL intensity is likely related to charge trapping phenomena rather than being brought about by the oxidation reaction. The fact that we did not observe any oxidation on the 'fast' sample is a sufficient proof of this, but in addition, the oxidation reaction exhibits a non-exponential growth: see peak B in Fig. 5.8 and Fig. 5.9, for the 'slow' sample.

It is interesting to note that the same sample exhibits orange luminescence at 670 nm when it's excited with 280 nm excitation energy of the laser. See Fig. 5.6 and Fig. 5.7. One possibility is that at higher excitation energies the energy of excitation resonates with direct transition within Si crystal while with lower excitation energies, mostly passivation

layer and defect sites of the surface of the silicon nanocrystals are responsible for the photoluminescence. This mechanism has been suggested by Wolkin [22] and Ding [23], but the decay of the orange light is much faster than that of the blue light. The detection time in this work is rather slow, it takes 10 minutes to acquire one scan, this means that by the time the monochromator detects the orange light, the big proportion has already been quenched. Probably the main reason for this quenching is attributed to the presence of the local defect states which they fall into band gap and which are very quickly populated by low energy secondary electrons generated by a VUV irradiation.

The recent results [20] obtained at Beamline 6.1 shows clear two photoluminescence bands, orange and blue, showed in Fig. 5.23. Further study indicated that the orange light is from Si-Si bond, and blue light from Si-C bond. As we mentioned the alkylated silicon quantum dots surrounded by carbon chain, see Fig. 5.3.

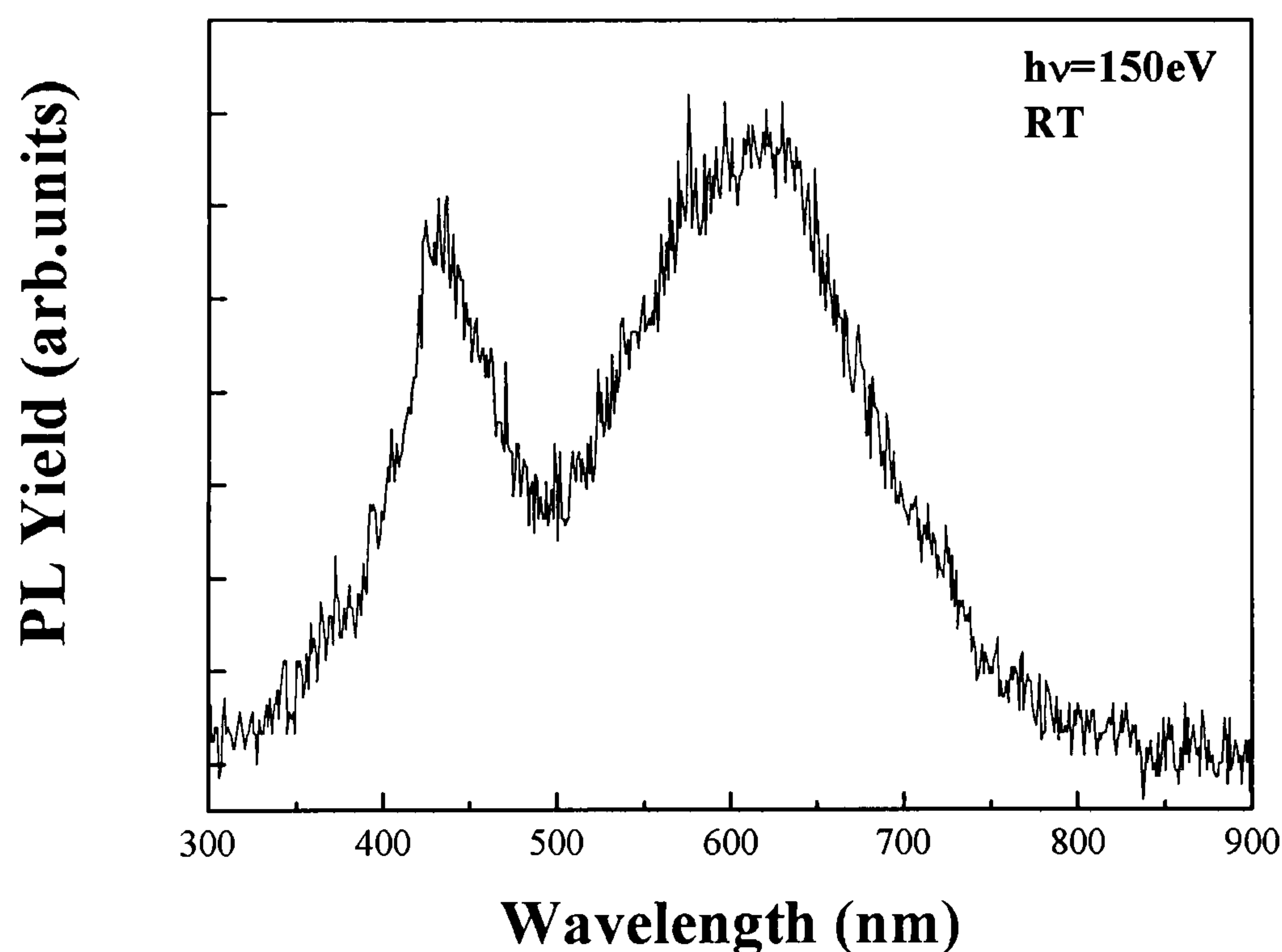


Fig. 5. 23 Photoluminescence spectrum acquired at beamline 6.1, Daresbury. There are two clear luminescent bands with excitation energy $h\nu=150$ eV at room temperature [20].

5.5 Summary

Recently, it has been shown that an alkyl-modified silicon core is an efficient fluorophore which is stable in aqueous/biological media, non-toxic, and emits photons (wavelength 600-700 nm with 513 nm excitation; two bands X-ray excited optical luminescence (XEOL) with soft X-ray) which do not interact strongly with most biological molecules [6]. Thus, it might be potentially important as nanoscale sensors inside living cells.

Scanning tunnelling microscopy (STM), synchrotron radiation excited photoemission (SRPES) and X-ray excited optical luminescences (XEOL) have been performed. During the course of illumination with 145 eV photons we have monitored the evolution of the Si 2*p* core level, and observed in real time a splitting and growth of a new Si 2*p* component assigned to the Si⁴⁺ oxidation state of Si. This new peak is attributed to *in situ* oxidation of Si quantum dots caused by photo-induced reaction, possibly with multilayer of water present on the surface of the as-introduced quantum dots. XEOL reveals that three emission bands are active upon soft X-ray photon excitation. Surprisingly the 390 nm band (blue light) is the most intense, which is quite different to the result for UV photo-excitation, where the 600-700 nm band is the most prominent one (orange light). The orange light originated from Si-Si bond, blue light from Si-C bond. An interesting ageing phenomenon of photoluminescence is observed upon exposure to the X-ray which is possibly due to prolonged trapping of charge in the alkyl chains attached to the Si/SiO_x core.

5.6 References

- [1] L. H. Lie, S. N. Patole, A. R. Pike, L. C. Ryder, B. A. Connolly, A. D. Ward, E. M. Tuite, A. Houlton, and B. R. Horrocks, *Faraday. Discuss.* **125**, in press (2003).
- [2] J. A. Uhler, *Bell Syst. Tech. J.* **35**, 333 (1956).
- [3] L. T. Canham, *Appl. Phys. Lett.* **57**, 1046 (1990).
- [4] Y. Kanemitsu, in *Light Emission in Silicon From Physics to Devices*, edited by D. J. Lockwood (Academic Press, New York, 1998), Vol. 49, p. 164.
- [5] V. Lehmann and U. Gosele, *Appl. Phys. Lett.* **58**, 856 (1991).
- [6] L. H. Lie, M. Duerdin, E. M. Tuite, A. Houlton, and B. R. Horrocks, *J. Electroanal. Chem.* **538**, 183 (2002).
- [7] M. J. Sailor, J. L. Heinrich, and J. M. Lauerhaas, *Studies Sur. Sci. Catal.* **103**, 209 (1997).
- [8] M. J. Sailor and E. J. Lee, *Adv. Mater.* **9**, 783 (1997).
- [9] D. J. Norris, M. G. Bawendi, and L. E. Brus, in *IUPAC*, edited by J. Jortner and M. A. Ratner (Blackwell Science, Oxford, 1997), p. 281.
- [10] Y. Butenko, V. Kuznetsov, and L. Siller, unpublished.

- [11] Y. Chao, S. Krishnamurthy, M. Montalti, L. H. Lie, A. Houlton, B. R. Horrocks, L. Kjeldgaard, V. R. Dhanak, M. R. C. Hunt, and L. Šiller, J. Chem. Phys. **submitted** (2003).
- [12] C. G. Cleland, B. R. Horrocks, and A. Houlton, Journal of the Chemical Society-Faraday Transactions **91**, 4001 (1995).
- [13] L. H. Lie, S. N. Patole, A. R. Pike, L. C. Ryder, B. A. Connolly, A. D. Ward, E. M. Tuite, A. Houlton, and B. R. Horrocks, Faraday. Discuss. **125**, in press (2003).
- [14] T. Giaddui, L. G. Earwaker, K. S. Forcey, A. Loni, and L. T. Canham, J. Phys. D-Appl. Phys. **31**, 1131 (1998).
- [15] F. J. Himpsel, F. R. McFeely, A. Taleb-Ibrahimi, J. A. Yarmoff, and G. Hollinger, Phys. Rev. B **38**, 6084 (1988).
- [16] S. R. Baggott, K. W. Kolasinski, L. M. A. Perdigao, D. Riedel, Q. M. Guo, and R. E. Palmer, J. Chem. Phys. **117**, 6667 (2002).
- [17] F. G. Bell and L. Ley, Phys. Rev. B **37**, 8383 (1988).
- [18] M. Zhu, G. Chen, and P. Chen, Appl. Phys. A **65**, 195 (1997).
- [19] L. Siller, M. T. Sieger, and T. M. Orlando, Journal of Chemical Physics **118**, 8898 (2003).
- [20] S. Krishnamurthy, in *School of Chemical Engineering and Advanced Materials* (Newcastle University, Newcastle, 2003).

- [21] Y. Kanemitsu, T. Ogawa, K. Shiraishi, and K. Takeda, *Phys. Rev. B* **48**, 4883 (1993).
- [22] M. V. Wolkin, J. Jorne, P. M. Fauchet, G. Allan, and C. Delerue, *Phys. Rev. Lett.* **82**, 197 (1999).
- [23] Z. Ding, B. M. Quinn, S. K. Haram, L. E. Pell, B. A. Korgel, and A. J. Bard, *Science* **296**, 1293 (2002).

Chapter 6 Future Work

In this chapter the future work is proposed: intensive investigation on unique optical property related electronic structure of Si-QDs; evolution of indium clusters electronic structure during the annealing steps; investigation of reconstruction of InP (100) (2× 4) when C₆₀ on the surface .

6.1	Intensive investigation on unique optical property related electronic structure of Si-QDs	161
6.2	Evolution of Indium clusters electronic structure as a function of annealing temperature—at different cluster size	162
6.3	Reconstructure of InP (100) (2 × 4) with C ₆₀ on the surface.....	162
6.4	References	163

The future work could be divided into three parts. Firstly, intensive investigation on unique optical property related electronic structure of Si-QDs, which is still focus on the sample preparation and the fundamental properties of the Si-QDs. Total fluorescence yield (TFY), is proposed for the NEXAFS measurement of living cell. Secondly, evolution of indium clusters electronic structure during the annealing steps, i.e. the relationship between bandgap and clusters size. Thirdly, the investigation of reconstruction of InP (100) (2×4) with C_{60} on the surface.

6.1 Intensive investigation on unique optical property related electronic structure of Si-QDs

Although the Stokes shift exists, the photoluminescence wave length is related to the bandgap of Si-QDs, thus it's very meaningful to probe this parameter. To get the proper data, one should measure the distance between the bottom of conduction band and top of the valence band. Unfortunately both these positions are changing due to quantum confinement. One would expect valence band recedes and conduction band edge rises. Thus, the separation between the top of the valence band and the Si2p level is smaller than in bulk Si. One can get ΔE_{vb} by measure this separation difference, ΔE_{cb} by the shift in NEXAFS Si-L edge [1, 2]. Then the bandgap of the Si-QDs, as shown in Fig. 1.15, is given by

$$E_{gap} = \Delta E_{vb} + \Delta E_{cb} + 1.1 \text{ eV} \quad (6.1)$$

Since total fluorescence yield (TFY) can reach considerably larger probe depths (on the order of 1000\AA) and is less sensitive to possible surface contamination as discussed in Chapter 1, it can be used to measure absorption in buried layers, especially in the case of Si-QDs sensor in the living cell.

Furthermore, as it's mentioned in Chapter 5, the decay of photoluminescence intensity is quite different with the result of porous Si in literature [3]. The reason is our detector worked so extremely "SLOW" that it takes 10 minutes to acquire one scan. If time resolved photoluminescence in nanosecond, even in femtosencond or attosencond, is

available, it should be very nice to acquire the spectra and analyse the decay behaviour, and helpful to understand the mechanism of photoluminescence of Si-QDs.

The PL mechanism in Si-QD has been intensively debated and several models proposed. Detailed studies are, however, hampered by the broad PL band resulting from inhomogeneous broadening, omnipresent in ensembles of QDs. Although certain improvement can be achieved by size selection methods [4], single-dot spectroscopy techniques would be needed to reveal the PL mechanism. These methods are widely applied to study individual QDs of III–V and II–VI semiconductors [5] but have only scarcely been used to study light emission from silicon QDs [6, 7]. Two main difficulties are the low emission rate from the Si-QDs (long radiation lifetime resulting from the indirect transition) and the complicated preparation of diluted and well-defined systems of Si-QDs [8]. It also could be an exciting challenge.

6.2 Evolution of Indium clusters electronic structure as a function of annealing temperature—at different cluster size

In Chapter 4 the evolution of indium clusters core level as a function of annealing temperature has been investigated. It is also possible to investigate the evolution of bandgap which is the distance between the bottom of conduction band and the top of valence band. As we already know the indium clusters appear on the InP (100) surface after annealing to the desorption temperature of phosphorous, further annealing could enlarge the clusters size, until entirely metallic indium covers the surface.

6.3 Reconstruction of InP (100) (2×4) with C_{60} on the surface

As mentioned in Chapter 3, the construction of InP (100) surface is a very important issue, and STM investigation is possible for the reconstruction procedure [9, 10]. Since Omicron UHV Nanoprobe, an instrument unique to a European University, is available at the Institute for Nanoscience and Nanotechnology at the University of Newcastle, we could investigate the effect of C_{60} on the reconstruction of InP (100) surface.

6.4 References

- [1] T. van Buuren and T. Tiedje, Appl. Phys. Lett. **63**, 2911 (1993).
- [2] T. van Buuren, L. N. Dinh, L. L. Chase, W. J. Siekhaus, and L. J. Terminello, Phys. Rev. Lett. **80**, 3803 (1998).
- [3] Y. Kanemitsu, T. Ogawa, K. Shiraishi, and K. Takeda, Phys. Rev. B **48**, 4883 (1993).
- [4] W. L. Wilson, P. F. Szajowski, and L. E. Brus, Science **262**, 1242 (1993).
- [5] A. Gustafsson, M. Pistol, -E., L. Montellius, and L. Samuelson, J. Appl. Phys. **84**, 1715 (1998).
- [6] J. K. Rogers, F. Seiferth, and M. Vaez-Iravani, Appl. Phys. Lett. **66**, 3260 (1995).
- [7] M. D. Mason, G. M. Credo, K. D. Weston, and S. K. Buratto, Phys. Rev. Lett. **80**, 5405 (1998).
- [8] J. Valenta, R. Juhasz, and J. Linnros, Appl. Phys. Lett. **80**, 1070 (2002).
- [9] Q. Guo, M. E. Pemble, and E. M. Williams, Surf. Sci. **433-435**, 410 (1999).
- [10] M. Shimomura, N. Sanada, Y. Fukuda, and P. J. Moller, Surf. Sci. **359**, L451 (1996).

Appendix A: Fittings parameters of core level spectra

All the fittings of core level spectra were fitted in Winspec program and plotted with Origin program.

1. Fitting Parameters of C1s

To get the detailed information of C1s core level spectra, such as peak position and FWHM, I fitted C1s spectrum with one mixed singlet and Shirley background.

Table 3.1 Fitting Parameters of C1s in different coverage

Coverage (ML)	Position (eV)	Width (eV)
0.65	284.32	1.457
1.13	284.44	1.479
2	284.50	1.497
8	284.65	1.271

Table 3.2 Fitting parameters of C1s after various annealing steps

Temperature (K)	Position (eV)	Width (eV)
600	284.32	1.363
640	284.34	1.416
690	284.40	1.674
740	284.34	2.078

2. Fitting Parameters of P2p

The P2p core level spectra were fitted with two mixed doublets and one Shirley background. One doublet is bulk-related; another one is surface-related. For bulk component the peak position was kept fixed at 128.194eV, branching intensity ratio 0.5, and spin-orbit splitting 0.86eV. For surface component the intensity ratio and splitting were also kept same as bulk component. But at different coverage, the different surface peak position applied. Table 3.3 gives the details.

Table 3.3 P2p surface peak position at different coverage

Coverage (ML)	0	0.26	0.65	1	1.13	2	8
Position (eV)	127.75	127.85	127.86	127.87	127.88	127.95	128.153

3. Fitting Parameters of In4d

The In4d core level spectra were fitted with three mixed doublets and one Shirley background. One doublet is bulk-related and other two are surface-related.

The bulk component peak position was kept fixed at 17.50 ± 0.02 eV. The spin-orbit splitting was kept fixed at 0.86 eV and the branching ratio was 0.65. For the two surface components, the spin-orbit splitting and branching ratio were kept fixed same as those of bulk component.

After annealing to 640K, to get a quality fitting, I have to use four doublets and one Shirley background. The forth doublet is related to metallic indium which exhibits on the surface after phosphorus desorbed at high temperature. Detailed discussion about the metallic indium clusters behaviour can be found in Chapter 4.

Appendix B: List of papers

- 1. During my Ph D experience, the following eight papers have been emerged.
The work in this thesis is based on the first four given below.**

I. A photoemission study of chemisorption of C₆₀ on InP (100)

Y. Chao, K. Svensson, D. Radosavkić, V.R. Dhanak, L. Šiller and M.R.C. Hunt

[Phys. Rev. B 64, 235331 \(2001\)](#)

II. Photoemission spectroscopy of the evolution of In-terminated InP (100)-(2 × 4) as
a function of temperature: surface and cluster related In4*d* lines

Y. Chao, K. Svensson, D. Radosavkić, V.R. Dhanak, M.R.C. Hunt and L. Šiller

[Phys. Rev. B 66, 075323 \(2002\)](#)

III. Reactions and luminescence in alkylated Si nanocrystallites induced by
VUV/XUV photons

Y. Chao, S. Krishnamurthy, M. Momtalti, L. Kjeldgaard, L. H. Lie, A. Houlton, B. R.
Horrocks, V.R. Dhanak, M.R.C. Hunt and L. Šiller

(Accepted by J. Chem. Phys.)

IV. Angle resolved photoemission spectra of indium clusters on InP (100))

Y. Chao, K. Svensson, D. Radosavkić, V.R. Dhanak, M.R.C. Hunt and L. Šiller

(In manuscript)

2. Other works I have been deeply involved but I did not put them into this thesis:

V. Photoemission spectroscopy of clean and potassium intercalated carbon onions

M. Montalti, S. Krishnamurthy, Y. Chao, Yu.V. Butenko, V.L. Kuznetsov, V.R.Dhanak, M.R.C. Hunt and L. Šiller

[Phys. Rev. B 67 113401 \(2003\)](#)

VI. Thermally induced decomposition of single wall carbon nanotubes adsorbed on H/Si (111)

Michael R.C. Hunt, Massimo Montalti, Yimin Chao, Satheesh Krishnamurthy, Vinod R. Dhanak, and Lidija Šiller

[Appl. Phys. Lett. 81,4847\(2002\)](#)

VII. Multi-wall and single-wall carbon nanotubes: Fermi liquid and Luttinger liquid

Michael R.C. Hunt, Massimo Montalti, Yimin Chao, Satheesh Krishnamurthy, Vinod R. Dhanak, and Lidija Šiller (Submitted to Phys. Rev. Lett.)

VIII. Gold nitride—novel material

S. Krishnamurthy, Y. Chao, M. Montalti, M.G.Wardle,M.J. Shaw, P.R. Briddon, K. Svennson, M.R.C. Hunt and L. Šiller (Submitted to Phys. Rev. B)

Patent:

National patent number: GB0313895.5, Title: method of producing gold nitride